

Habilitation Thesis

**Modeling and Numerical Simulation  
of complex technical flows**

by

**Helfried Steiner**

Institute of Fluid Mechanics and Heat Transfer  
Graz University of Technology

submitted to

Graz University of Technology

for receiving a

venia docendi

Graz, October 2006

# Abstract

The numerical flow simulation has become an indispensable tool in all fields of academic research as well as industrial design and development. Despite the rapid increase of the available computational resources, the concept of resolving directly all relevant physical/chemical effects will remain an unfeasible approach due to its unaffordable computational costs. There remains a substantial need for a reliable modeling of the numerically unresolved, small-scale phenomena. The present work exemplarily considers the simulation and modeling of two highly complex flows with strong relevance for many engineering devices involving the conversion and transmission of energy: the Large-Eddy Simulation (LES) of non-premixed combustion and the modeling of subcooled boiling flow. For both cases, several well-established model approaches are reviewed. The underlying strategies are outlined, and their ranges of applicability, predictive capabilities, major limitations, and possible further developments are commented on.

It is shown that in the field of LES of non-premixed combustion the state-of-the-art combustion models have already reached a very advanced level. Using comprehensive combustion models involving more than one quantity to parameterize the flame, produces very accurate predictions for the reactive species concentrations. Highly unsteady phenomena like extinction and re-ignition can be captured as well. An efficient mapping between the flame structure in the parameter space and the reactive flow field in the physical space represents a major issue for further development in this field.

In the case of subcooled boiling flow, there is still much uncertainty about the underlying physics, especially concerning the process of bubble nucleation. Today's widely used model correlations, which are discussed in the present work, involve therefore much empiricism in terms of adjustable constants. This leads to a loss of generality of the individual correlations. Providing mostly global information on the resulting wall heat transfer rates, the applicability of most approaches in the numerical simulation of subcooled boiling flow is limited, as this requires a more local description.

Key words: Large-Eddy Simulation, non-premixed combustion, subcooled boiling flow.

## *Preface*

The present work encompasses a substantial part of my post-doctoral research work, which I performed at the Institute of Fluid Mechanics and Heat Transfer at Graz University of Technology, as well as during a two years research visit to the Center for Turbulence Research at Stanford University. I am especially indebted to the present head of the institute, Prof. Günter Brenn, as well as his predecessors, Prof. Walter Gretler and Prof. Uwe Schafflinger, for giving me always support, motivation and guidance in all my research activities. I thankfully acknowledge my friends and colleagues Kendal Bushe, Heinz Pitsch, Bendiks Boersma, and Peymann Givi, who have amply contributed to my work as collaborators or in various fruitful discussions. The present work would also not have been possible without the thesis work of the students Bernd Breitschädel, Alexander Kobor, Ludwig Gebhard and Franz Ramstorfer, whose important contributions are gratefully mentioned here. I further thankfully mention all my colleagues at the institute including the scientific staff as well as the workshop members, who all created a pleasant, team-based working atmosphere, which was highly supportive to my activities.

Helfried Steiner

# Contents

<b>1</b>	<b>General Introduction</b>	<b>1</b>
<b>2</b>	<b>Large-Eddy Simulation of non-premixed flames</b>	<b>5</b>
2.1	Introduction . . . . .	5
2.2	Formulation in LES . . . . .	6
2.3	Subgrid-scale modeling of non-premixed combustion . . . . .	9
2.4	Mixture fraction based models . . . . .	12
2.4.1	Chemical equilibrium models . . . . .	13
2.4.2	Laminar Flamelet Model . . . . .	17
2.4.3	Conditional Moment Closure . . . . .	21
2.5	Concluding remarks . . . . .	26
<b>3</b>	<b>Modeling of subcooled boiling flow</b>	<b>28</b>
3.1	Introduction . . . . .	28
3.2	Basic model considerations . . . . .	30
3.2.1	Onset of nucleate boiling (ONB) . . . . .	32
3.2.2	Transition from partially developed (PDB) to fully developed boiling (FDB) . . . . .	35
3.3	Models for the wall heat flux . . . . .	36
3.3.1	General empirical correlations . . . . .	36
3.3.2	Mechanistic models . . . . .	38
3.3.3	Accuracy limiting effects in technical flows . . . . .	47
3.4	Concluding remarks . . . . .	54
<b>4</b>	<b>Conclusions</b>	<b>56</b>
	REFERENCES	<b>58</b>
	APPENDIX-PAPERS	<b>67</b>

# 1 General Introduction

During the last decades the numerical flow simulation, commonly termed *Computational Fluid Dynamics (CFD)*, has become an indispensable tool in the design and development of engineering devices. The steady improvements and further refinements of the employed numerical methods together with the substantial increase in the available computer power made ever more complex problems accessible to the numerical approach. The considered problems may involve complicated flow geometries, physically complex flow phenomena such as turbulence, shocks and contact surface discontinuities, or thermodynamic processes such as phase change, or chemical reactions. Despite all the advances which have been made in the numerical methodology and the rapid increase of the computational resources, the high complexity of most configurations precludes the - from a numerical point of view certainly most generic - concept of resolving directly all relevant effects in space and time. To date, the application of this concept termed Direct Numerical Simulation (DNS) has been largely restricted to incompressible, non-reacting, single-phase flow at low Reynolds numbers. The application of this concept is not only very limited due to exceedingly high computational costs, which arise from the need to resolve all relevant small-scale effects, such as the convective and diffusive transport in chemical reaction zones or at interfaces in multi-phase flows. In many cases, there exists no rigorous mathematical formulation describing in detail all the physical/chemical phenomena involved, and one would have to use phenomenological correlations instead. Being generally based on global parameters, such correlations mostly provide a very global description of the individual effects rather than a detailed and highly accurate knowledge of the local quantities. This precludes any attempt to resolve directly all relevant small-scale characteristics. The specification of reliable boundary conditions often represents a further open issue. The difficulty to derive a sufficiently accurate mathematical formulation for the governing equations, together with the tremendous computational costs to solve them numerically, makes evident that the computation of complex technical flows will keep relying on appropriate models to capture all physically relevant, but numerically unresolved effects. In most cases there exist numerous model approaches, and there is no “best model”. An adequate approach can be found by appraising the available models on various attributes which may be highly relevant to the considered problem, or demanded by the user. Pope (2000) suggested a catalogue of important criteria which may be used to assess different approaches, namely

- accuracy of the predictions,
- level of description,
- completeness,
- computational costs,
- ease of use, and
- the range of applicability.

The method of DNS would match here the first three of these criteria best. Due to its high resolution DNS by definition provides a very accurate and detailed description of the flow, and it represents a very complete method, as it requires no case-dependent modifications of the formulation, such as empirical model coefficients to be adjusted from

case to case. On the other hand, it is the two last criteria, the computational costs and the range of applicability, which preclude DNS from a use in typical engineering flow as already outlined above. An appraisal of models based on empirical correlations would give a very different picture. While empirical models tend to be computationally cheap, they are mostly incomplete and in general provide a very low level of description. Their accuracy is strongly related to the criterion of completeness, which means that the accuracy of the predictions depends on the appropriate setting of the adjustable model parameters. Since most large size simulations are run on multi-processor architectures today, the criterion of a good scalability should not be overlooked as well. Basically, this criterion favours explicit formulations to keep the amount of node-to-node communication low, as well as numerical procedures which allow for a most evenly distributed work load among the individual processors.

The present work surveys the computation of two very complex phenomena, which are both highly relevant in numerous engineering devices involving the conversion and transmission of energy. The first is associated with the numerical simulation of non-premixed turbulent combustion, the second with the computation of subcooled boiling flow. From an application point of view, the internal combustion engine may serve as a very illustrative example, as its working cycle involves both processes considered here. Inside the engine's combustion chamber, chemical energy is converted into heat via an exothermic chemical reaction of fuel with oxidizer. The underlying turbulent flow of the reactants can have a significant effect on the chemistry and vice versa. Acceptably accurate predictions for the heat release as well as for the composition of the exhaust-gas combustion products require a reliable modeling of the turbulent flames. The increasing demand on predictive accuracy as the emission limits have been getting tighter, together with the expanding computational capabilities have set the ground to replace the formerly used zero-dimensional flame models by three-dimensional simulations including appropriate combustion submodels. Thereby, the reactive turbulent flow field is commonly simulated using the statistical approach of the Reynolds Averaged Navier-Stokes calculation (RANS), or using the increasingly popular approach of Large-Eddy Simulation (LES).

The intense release of heat within a confined space naturally leads to high thermal loads on the walls of the combustion chamber. The increasing output of power aimed at by the design of modern internal combustion engines is ever more challenging the cooling system. Inside the water-cooled jackets, the onset of nucleate boiling in high temperature wall regions is a long known phenomenon. Contrary to the traditional design generally attempting to avoid the two-phase regime, modern cooling concepts often deliberately provide for a transition to nucleate boiling. Following such a strategy, the onset of nucleate boiling is even desired to enhance the local heat transfer rates leading to more uniform wall temperatures and, hence, lower thermal stresses, which may finally result in longer material life times. Aside from this automotive application the concept to enhance the heat transfer rates by nucleate boiling is also seen in many other highly efficient compact cooling systems, such as those of microelectronic devices. The ongoing miniaturization and increasing power of the individual processing units inevitably requires a highest possible cooling of their surface to prevent them from overheating and thermal failure.

The method of Large-Eddy Simulation (LES) can be basically regarded as a computationally affordable extension of the DNS to high Reynolds number turbulent flow, as it resolves the motion only on the larger scales, while it models the contribution from the small, unresolved scales. An appraisal of the method on the five criteria mentioned above would assign to LES a much wider range of applicability than DNS, however, at the sacrifice of a lower level of description. Compared to the statistical approach of RANS, LES provides basically a higher level of completeness, in that the small-scale motion tends to be more universal than the resolved large-scale motion, which allows for a more general modeling with no need for various case-dependent adjustable parameters. Contrary to the RANS method, LES has not become the method of choice in the simulation of engineering applications, because its computational costs are still comparatively high and the posture of appropriate, unsteady boundary conditions is more difficult as well. However, in the scientific research of non-premixed turbulent combustion, LES has already become highly appreciated as a very powerful tool to simulate the underlying flow of the reactants. Most of the combustion models proposed to date have been originally developed in the context of RANS, from where they have been adopted and further modified for use in LES. Resolving the instantaneous large scale mixing characteristics, LES is capable to supply valuable input parameters to the combustion models. As such LES basically pathed the way to a realistic coupling of the chemistry with the unsteady turbulent flow field, which is particularly beneficial for swirling flames or bluff-body flames, where large-scale motion plays a dominant role. Until recently, due to its substantial computational requirements, LES was mostly used with rather simple combustion submodels, such as one-parametric approaches assuming fast, purely mixing controlled chemistry. More comprehensive submodels, which parameterize the flame in terms of two or more parameters, are being introduced. Using these multi-parametric combustion submodels, encouraging results could be achieved in the LES of non-premixed single-phase combustion, involving gaseous fuel and oxidizer feeds. On the other hand, comparatively small advances have been made in the case of multi-phase combustion, where a liquid fuel feed is injected into a gaseous oxidizer. The presence of a second phase introduces a great deal of additional complexity associated with the dynamics of the gas/liquid interfaces such as liquid break-up, or evaporation. Especially, the region of the primary break-up of the liquid feed stream is still not fully understood. The state-of-the-art models for the primary break-up are essentially based on empirical parameters rather than on a physically rigorous description. In the case of premixed combustion, where the turbulent flame is propagated through a gaseous premixture of fuel and oxidizer, the progress lags behind that of the non-premixed case as well. This is mainly due to the stronger coupling between the chemistry and the turbulence, as well as the ongoing controversy on the validity of the assumption of certain regimes, such as the thin flame sheet regime or the thickened flame regime, and on the appropriate parameterization of those regimes. The scope of the present work is restricted to the non-premixed single-phase case, although the combustion of a liquid fuel sprays in ambient gaseous oxidizer is certainly of high practical importance. Various types of non-premixed combustion submodels which have been proposed for use in LES will be discussed in section 2. Thereby, the focus will lie on those concepts, which parameterize the flame essentially dependent on the mixing related conditions of the reactants.

While the modeling of turbulent combustion during the last twenty years was strongly directed toward an application of the proposed approaches to CFD of reacting flow, the modeling of nucleate boiling flow followed very different guidelines. The conditions in nucleate boiling flow are determined by a variety of vapor-liquid-heated surface interactions, where many of the involved sub-processes cannot be parameterized adequately, or are not even fully understood yet. This high level of complexity made an appropriate numerical treatment an almost impossible task. The application to CFD was therefore generally not a primary issue, and the focus was rather laid on a reliable prediction of the total heat flux from the superheated surface. In most approaches the underlying flow is considered in a strongly simplified way via empirical correlations for the convective single-phase heat transfer based on bulk flow conditions. The boiling contribution to the total heat flux is mostly computed from correlations developed for pool boiling, i.e., boiling with the bulk liquid at rest, and it is incorporated as multiplicative or additive enhancement of the single-phase base convection. Beginning from the early fifties of the last century with the fundamental work by Rohsenow (1952), numerous models for nucleate boiling have been proposed. All these approaches involve a lot of empiricism, and especially for boiling on technical surfaces a well calibrated set of parameters is a pre-requisite to obtain acceptably accurate predictions.

Much effort to model nucleate boiling flow was motivated by the design and development of steam generators for thermal power plants as well as the design of evaporators used in refrigeration machinery. As such, the investigation of the boiling heat transfer was essentially carried out within the framework of the heat exchanger research. During the last years the need for most compact and efficient cooling systems has become an important stimulus to advance the state-of-the-art models not only with respect to their accuracy, but also to their applicability in CFD, as CFD has been established as an important tool in the modern design of cooling systems as well. Much attention was paid here to the regime of subcooled boiling flow, which emerges from the contact between highly superheated wall regions and a bulk liquid being well below the saturation temperature. In this regime, the onset of nucleate boiling enhances the local total heat transfer rates significantly as compared to pure single-phase convection, and there is practically no undesired net production of vapor, as the bubbles condense immediately after their departure from the superheated wall layer. Several different modeling concepts, which have been proposed to predict the total wall heat flux and are today widely used in technical applications, will be presented in section 3. The survey will comprise the basic model assumptions, the mathematical formulations, as well as the required parameters. There will be also outlined the limitations in accuracy which are basically faced by any of the state-of-the-art models, when applied to typical engineering applications.

## 2 Large-Eddy Simulation of non-premixed flames

### 2.1 Introduction

The worldwide growing demand on energy accompanied by an increasing environmental pollution makes high efficiency as well as low emissions to be important objectives in the research and development of modern combustion devices. The discussion on the Greenhouse effect has particularly emphasized the issue how to reduce the output of CO<sub>2</sub>, which represents the main part of the exhaust gas in the combustion of fossil fuels. The development and design of machinery which meets all the economical and ecological demands requires detailed knowledge of the chemical kinetics, especially when focussing on pollutant formation. Experimental research has provided a large amount of reliable kinetic data and the complete, mostly multi-step, reaction mechanisms can be described in much detail now. At the same time, in pace with the rapid gain in computational capacity, the numerical simulation techniques have been advanced to a level such that they can be seen as a well-established powerful tool in combustion research. Since many combustion devices like turbo-engine combustors, directly injected diesel engines, furnaces fired with swirl burners, etc., involve highly turbulent flows, the simulation of turbulent flames is of particular interest. The quality of the numerical predictions for such turbulent reactive flows crucially depends on a realistic modeling of the interactions between the chemistry and the turbulent fluctuations. However, many combustion models would get computationally too expensive when using the full kinetic mechanisms for the considered chemistry. In this case an appropriate reduction to a simplified, but still realistic mechanism is an important issue as well.

Various turbulent combustion models have been proposed, and, alike in the modeling of non-reacting turbulent flows, it cannot be said which modeling strategy is superior to all the others. From the viewpoint of the technical application, two different regimes of turbulent combustion are commonly distinguished: premixed and non-premixed combustion. In premixed combustion the turbulent flame is propagated through an already well mixed region of fuel and oxidizer. Thereby, the turbulent flame brush separates the region of unburned fuel-oxidizer mixture lying ahead of the flame from the region of burned reactants lying behind the flame. The main challenge to numerical simulations of premixed flames is to track the turbulent flame front correctly. This requires an appropriate modeling of the turbulent flame speed, at which the strongly wrinkled front is propagated in the turbulent flow field. Premixed flame regimes are typically found in Bunsen burners, or in spark ignition engines. In non-premixed combustion the fuel and the oxidizer are fed into the combustion chamber separately. There, they have to get mixed before they can react, and the reactive process is essentially controlled by the turbulent mixing. Hence, it is a basic requirement for any numerical simulation of non-premixed flames to capture the turbulent mixing process accurately. The turbulent reacting flow in a combustor of a gas turbine represents a typical non-premixed configuration.

Since its first introduction into the computation of meteorological flows in the late 1960s, the method of Large-Eddy Simulation (LES) has been receiving rising attention in the

simulation of turbulent flows. The use of LES in non-premixed combustion is particularly reasonable, because this technique has the very attractive feature that it captures the unsteady turbulent large scale motion. Thus, LES it is capable to track the local instantaneous mixing state providing valuable information for the prediction of highly unsteady local effects like flame quenching, auto-ignition or acoustic combustion instabilities.

## 2.2 Formulation in LES

The basic idea of LES is that it resolves directly only the large scale motion, while it models the effect of the unresolved small scale motion. It represents an attractive compromise between the Direct Numerical Simulation (DNS) and the Reynolds-Averaged Navier-Stokes (RANS) calculation for mainly two reasons. Since LES requires a significantly coarser resolution than DNS, it does not exceed any available computational capacities also in high Reynolds number flows, while it still captures most part of the instantaneous turbulent motion. On the other hand, the unresolved turbulent small scale motion tends to be more universal which facilitates the modeling of these small scale, or subgrid-scale, structures. From this point of view LES can be regarded as conceptually superior to RANS-type simulations, which have to capture the full turbulent spectrum from the smallest to the largest scales. For that reason RANS models tend to be rather inaccurate in flows governed by non-universal, geometry dependent, unsteady turbulent large scale motion, e.g., in separating, or vortex shedding flows. Nevertheless, it is noted that in industrial engineering applications the computational fluid dynamics (CFD) mainly relies on RANS calculations. The mostly very complex geometries and the high resolution necessary near the walls require big computational meshes for LES which makes this technique in many cases prohibitively expensive compared to RANS. However, the increasing computational power strongly favours the application of LES also in engineering flows in the near future. Mathematically, LES sifts out the large scale structures by applying a low-pass filtering operation to all flow variables. Since the density can strongly vary in combustion flows due to the reactive heat release, a mass-weighted, or Favre, filter, is mostly used. For an arbitrary turbulent fluctuating quantity  $F(\mathbf{x}, t)$  the Favre filter operation reads

$$\tilde{F}(\mathbf{x}, t) = \frac{\overline{\rho F}}{\bar{\rho}} = \frac{1}{\bar{\rho}} \int_{-\infty}^{\infty} \rho(\boldsymbol{\xi}, t) F(\boldsymbol{\xi}, t) G(\boldsymbol{\xi} - \mathbf{x}) d\boldsymbol{\xi}, \quad (2.1)$$

with  $\mathbf{x}$ ,  $\boldsymbol{\xi}$  and  $t$  being independent space and time variables, respectively. The filter function  $G$  depends on the the filter width  $\Delta$ , which is proportional to the computational grid spacing  $\Delta\mathbf{x}$  such that the resulting filtered quantities  $\tilde{F}$  can be well resolved on the computational mesh. Ideally, the filter width  $\Delta$  should be smaller than  $l_{EI}$ , which is the length scale of the smallest energy containing eddies and represents the upper limit of the inertial range of the turbulent energy spectrum in wave number space. Since about 80% of the total turbulent energy is made up by eddies of a size larger than  $l_{EI}$ , the condition  $\Delta < l_{EI}$  ensures that most part of the energy is captured and the effect of the modeling of the small scale structures on the LES results is of minor importance. However, in regions which are dominated by small scale structures like near-wall regions this condition would allow only for a very small filter width which is associated with a computationally

expensive fine grid resolution. Using in this case a coarser grid implies a significantly higher portion of unresolved motion which requires a higher modeling effort to predict accurately the contribution of the unresolved, subgrid-scale, transport (Pope, 2000).

Analogously to the Reynolds decomposition used in the RANS-type modeling, which splits any instantaneous quantity into a statistical mean (ensemble average) and a fluctuating component, any local instantaneous quantity can be decomposed into a (resolved) Favre filtered mean and a (unresolved) subgrid-scale component

$$F = \tilde{F} + F'', \quad (2.2)$$

where the filtered mass-weighted subgrid-scale fluctuation is zero,  $\overline{\rho F''} = 0$ , by definition. Applying the mass-weighted filtering (2.1) to the differential conservation equations of mass, momentum, reactive species and energy yields the LES transport equations for the corresponding filtered quantities:

**mass:**

$$\frac{\partial \bar{\rho}}{\partial t} + \frac{\partial \bar{\rho} \tilde{u}_l}{\partial x_l} = 0 \quad (2.3)$$

**momentum:**

$$\begin{aligned} \frac{\partial \bar{\rho} \tilde{u}_k}{\partial t} + \frac{\partial \bar{\rho} \tilde{u}_k \tilde{u}_l}{\partial x_l} = & -\frac{\partial \bar{p}}{\partial x_k} + \frac{\partial}{\partial x_l} \left[ \tilde{\mu}_{mol} \left( \frac{\partial \tilde{u}_k}{\partial x_l} + \frac{\partial \tilde{u}_l}{\partial x_k} \right) - \frac{2}{3} \tilde{\mu}_{mol} \frac{\partial \tilde{u}_i}{\partial x_i} \delta_{kl} \right] \\ & - \frac{\partial}{\partial x_l} \underbrace{[\bar{\rho} (\tilde{u}_k \tilde{u}_l - \tilde{u}_k \tilde{u}_l)]}_{\tau_{kl}} \end{aligned} \quad (2.4)$$

**species:**

$$\begin{aligned} \frac{\partial \bar{\rho} \tilde{Y}_J}{\partial t} + \frac{\partial \bar{\rho} \tilde{u}_l \tilde{Y}_J}{\partial x_l} = & \frac{\partial}{\partial x_l} \left( \bar{\rho} \tilde{D}_{mol,J} \frac{\partial \tilde{Y}_J}{\partial x_l} \right) + \overline{\rho \dot{\Omega}_J} \\ & - \frac{\partial}{\partial x_l} \underbrace{[\bar{\rho} (\tilde{u}_l \tilde{Y}_J - \tilde{u}_l \tilde{Y}_J)]}_{\sigma_{J,l}} \end{aligned} \quad (2.5)$$

**energy:**

$$\begin{aligned} \frac{\partial \bar{\rho} \tilde{T}}{\partial t} + \frac{\partial \bar{\rho} \tilde{u}_l \tilde{T}}{\partial x_l} = & \frac{1}{c_p} \frac{\partial}{\partial x_l} \left( \tilde{\kappa}_{mol} \frac{\partial \tilde{T}}{\partial x_l} \right) + \overline{\left( \sum_{J=1}^{n_J} \rho D_{mol,J} \frac{\partial \tilde{Y}_J}{\partial x_l} \right) \frac{\partial \tilde{T}}{\partial x_l}} - \frac{1}{c_p} \sum_{J=1}^{n_J} \left( \overline{\rho \dot{\Omega}_J} h_{0,J} \right) \\ & - \frac{\partial}{\partial x_l} \underbrace{[\bar{\rho} (\tilde{u}_l \tilde{T} - \tilde{u}_l \tilde{T})]}_{\sigma_{T,l}} \end{aligned} \quad (2.6)$$

Here,  $\bar{\rho}$ ,  $\bar{p}$ ,  $\tilde{\mathbf{u}}$ , and  $\tilde{T}$  are the filtered density, pressure, velocity vector and temperature, respectively.  $\tilde{Y}_J$  is the filtered mass fraction of species  $J$ ,  $h_{0,J}$  is the enthalpy of formation

of species  $J$ . The specific heat capacities were assumed equal and constant for all  $n_J$  species,  $c_{p,J} = c_p$ . The diffusive transport terms involve the molecular viscosity,  $\mu_{mol}$ , the molecular diffusivity of the species  $J$ ,  $D_{mol,J}$ , and the thermal conductivity  $\kappa_{mol}$ . Since the total diffusive fluxes are generally very small in comparison to the corresponding turbulent convective fluxes especially in high Reynolds number flows, the corresponding subgrid diffusive transport terms were ignored in the derivation of the Eqs. (2.3)-(2.6), and, hence, the filtered diffusive flux terms were assumed here as

$$\overline{\mu_{mol} \frac{\partial u_k}{\partial x_l}} \approx \tilde{\mu}_{mol} \frac{\partial \tilde{u}_k}{\partial x_l}, \quad \overline{\rho D_{mol,J} \frac{\partial Y_J}{\partial x_l}} \approx \bar{\rho} \tilde{D}_{mol,J} \frac{\partial \tilde{Y}_J}{\partial x_l}, \quad \overline{\kappa_{mol} \frac{\partial T}{\partial x_l}} \approx \tilde{\kappa}_{mol} \frac{\partial \tilde{T}}{\partial x_l}.$$

If, for simplicity, equal molecular diffusivities are assumed for all species,  $D_{mol,J} = D_{mol}$ , the second term on the RHS of the energy equation (2.6) becomes zero, as

$$\sum_{J=1}^{n_J} \rho D_{mol,J} \frac{\partial \tilde{Y}_J}{\partial x_l} = \rho D_{mol} \sum_{J=1}^{n_J} \frac{\partial \tilde{Y}_J}{\partial x_l} = 0.$$

Rather than applying the filtering operation (2.1) to the differential conservation equations to obtain an explicitly filtered set of equations it has become common praxis to use the concept of implicit filtering. This concept is based on the fact that the numerical discretization of the differential equations represents already implicitly a filtering operation. It was analytically shown for the one-dimensional case that a second-order central difference approximation of a first-order derivative is equivalent to an explicit filtering of the derivative using a top-hat filter (Rogallo & Moin, 1984). The implicit filtering is determined by the accuracy of the numerical discretization scheme and the mesh size, and, as no explicit filtering is required, the mathematical formulation is simpler. On the other hand, employing mostly three dimensional higher-order discretization schemes makes it practically impossible to determine analytically the corresponding equivalent explicit filter function  $G$ . The mathematical formulation of the actually applied filter function  $G$  and, hence, the exact filter width  $\Delta$  are basically unknown. Being implicitly dependent on the mesh size, the filter width  $\Delta$  will also become space-dependent in the case of local grid refinement which conflicts with a basic requirement for the filter's commutation with spatial derivation, i.e.,

$$\overline{\left( \frac{\partial F}{\partial x_k} \right)} = \frac{\partial \bar{F}}{\partial x_k}.$$

The resulting commutation errors would have to be accounted for by additional correction terms in the discretized formulation. However, since the magnitude of these commutation errors does in general not exceed the magnitude of the discretization errors of the applied numerical schemes, they are mostly neglected (Ghosal & Moin, 1995; Vasilyev *et al.*, 1998). The closure for the convective subgrid momentum transport is commonly based on the eddy-viscosity concept

$$\tau_{kl} - \frac{1}{3} \tau_{ii} \delta_{kl} = -\bar{\rho} \nu_t \left[ \left( \frac{\partial \tilde{u}_k}{\partial x_l} + \frac{\partial \tilde{u}_l}{\partial x_k} \right) - \frac{2}{3} \left( \frac{\partial \tilde{u}_i}{\partial x_i} \right) \delta_{kl} \right], \quad (2.7)$$

where the eddy-viscosity is mostly computed with the Smagorinsky model as base model (Smagorinsky, 1963)

$$\nu_t = C\Delta^2|\tilde{S}|, \quad \tilde{S}_{kl} = \frac{\partial\tilde{u}_k}{\partial x_l} + \frac{\partial\tilde{u}_l}{\partial x_k}, \quad |\tilde{S}| = \left(2\tilde{S}_{kl}\tilde{S}_{kl}\right)^{\frac{1}{2}},$$

whose model coefficient  $C$  is calculated using a dynamic procedure due to Germano *et al.* (1991). The dynamic procedure relies on the idea of a scale similarity between the turbulent motion on the unresolved scales (represented by  $\tau_{kl}$ ) and the motion on the smallest resolved scales. The latter comprises the motion of those eddies which are a little bit larger than the length scale associated with the filter width ( $\Delta$ ). The dynamic concept was later extended to variable density flows and to the subgrid scalar transports,  $\sigma_{J,l}$  and  $\sigma_{T,l}$  in Eqs. (2.5)-(2.6) by Moin *et al.* (1991) in order to obtain the eddy-diffusivities  $D_{t,J}$  and  $\kappa_t$  occurring in the gradient transport formulations for the unclosed convective scalar fluxes

$$\sigma_{J,l} = -\bar{\rho}D_{t,J}\frac{\partial\tilde{Y}_J}{\partial x_l} \quad \text{and} \quad \sigma_{T,l} = -\kappa_t\frac{\partial\tilde{T}}{\partial x_l}. \quad (2.8)$$

Thereby, the transport coefficients are rewritten in terms of turbulent Schmidt numbers  $Sc_{t,J}$  and the turbulent Prandtl number  $Pr_t$

$$D_{t,J} = \frac{\nu_t}{Sc_{t,J}}, \quad \kappa_t = \bar{\rho}c_p\frac{\nu_t}{Pr_t},$$

respectively, which are provided by the dynamic model. To date, the dynamic procedure has been extensively used and tested in many turbulent flow configurations, see, e.g., Zang *et al.* (1993), Yang & Ferziger (1993), Zhao & Voke (1996), Wu & Squires (1997), Wu & Squires (1998), where it generally performed very well. LES of non-reacting flow with special emphasis on the modeling of the turbulent subgrid-scale transport has been subject of numerous reviews in the LES literature (Lesieur & Métais, 1996; Moin, 1997; Meneveau & Katz, 2000; Sagaut, 2001; Breuer, 2002).

## 2.3 Subgrid-scale modeling of non-premixed combustion

Besides the realistic modeling of the convective subgrid-scale fluxes, the closure of the filtered chemical source terms occurring in Eqs. (2.5) and (2.6) is still the crucial point in the simulation of turbulent combustion. These unclosed chemical source terms

$$\overline{\rho\dot{\Omega}_J} = W_J \sum_{K=1}^{n_K} (\nu''_{JK} - \nu'_{JK}) \bar{\omega}_K \quad (2.9)$$

involve phenomenological expressions of chemical kinetics

$$\dot{\omega}_K = A_K T^{\alpha_K} \exp\left(-\frac{E_K}{RT}\right) \prod_{I=1}^{n_J} \left(\frac{\rho Y_I}{W_I}\right)^{\nu'_{IK}}, \quad (2.10)$$

which are highly nonlinear functions of the temperature  $T$ , density  $\rho$  and the participating reactive species mass fractions  $Y_I$ .  $W_I$  is the molecular weight of species  $I$ , the exponents

$\nu'_{IK}$  and  $\nu''_{IK}$  are the stoichiometric coefficients of species  $I$  in reaction  $K$  in forward and backward direction, respectively.  $A_K$  is the frequency factor,  $\alpha_K$  is the pre-exponential temperature exponent, and  $E_K$  is the activation energy of reaction  $K$ .  $n_K$  is the total number of elementary reactions, and  $R$  is the universal gas constant. Due to the strong nonlinearity of Eq. (2.10), a simple first-order moment closure, which approximates the filtered reaction rates  $\bar{\omega}_K$  by evaluating Eq. (2.10) with the spatially filtered quantities  $\bar{\rho}$ ,  $\tilde{Y}_J$  and  $\tilde{T}$  as inputs

$$\bar{\omega}_K \approx \dot{\omega}_K(\bar{\rho}, \tilde{Y}_J, \tilde{T}) + \varepsilon_{\omega_K} \quad (2.11)$$

will generally lead to unacceptably large errors  $\varepsilon_{\omega_K}$ . Borghi (1974) demonstrated analytically the inaccuracy of the approximation (2.11) for a Reynolds-averaged first-order moment closure applied to irreversible one-step chemistry ( $n_K = 1$ ) involving two reactive species, fuel ( $Y_F$ ) and oxidizer ( $Y_O$ ). Assuming unity stoichiometric coefficients,  $\nu'_F = \nu'_O = 1$ , the non-averaged representation of Eqs. (2.9)-(2.10) for the reactive source term of the fuel mass fraction can then be simply written as

$$\varrho \dot{\Omega}_F = -A \varrho^2 Y_F Y_O T^\alpha \exp\left(-\frac{E}{RT}\right). \quad (2.12)$$

Splitting the instantaneous input quantities into a statistical mean (Reynolds-average) and a fluctuating component

$$Y_F = \tilde{Y}_F + Y_F'', \quad Y_O = \tilde{Y}_O + Y_O'', \quad T = \tilde{T} + T''$$

and expanding the nonlinear expressions in (2.12) into Taylor series of the relative fluctuations  $\frac{T''}{\tilde{T}}$ ,  $\frac{Y_F''}{\tilde{Y}_F}$  and  $\frac{Y_O''}{\tilde{Y}_O}$ , finally yields after averaging

$$\begin{aligned} \overline{\varrho \dot{\Omega}_F} = & -A \bar{\varrho}^2 \tilde{Y}_F \tilde{Y}_O \tilde{T}^\alpha \exp\left(-\frac{E}{R\tilde{T}}\right) \left[ 1 + \frac{\widetilde{Y_F'' Y_O''}}{\tilde{Y}_F \tilde{Y}_O} \right. \\ & \left. + (P_1 + Q_1) \left( \frac{\widetilde{Y_F'' T''}}{\tilde{Y}_F \tilde{T}} + \frac{\widetilde{Y_O'' T''}}{\tilde{Y}_O \tilde{T}} \right) + (P_1 Q_1 + P_2 + Q_2) \frac{\widetilde{T''^2}}{\tilde{T}^2} + \dots \right]. \end{aligned} \quad (2.13)$$

The coefficients of this series which is shown here up to the second-order terms emerge from the expansion of the temperature  $T = \tilde{T}(1 + \frac{T''}{\tilde{T}})$  occurring in the pre-exponential term and in the argument of the exponential function itself. They are written as

$$\begin{aligned} P_1 = \alpha, \quad P_2 = \frac{\alpha(\alpha-1)}{2}, \quad \dots \quad P_n = \frac{\alpha(\alpha-1)\cdots(\alpha-n+1)}{n!}, \\ Q_1 = \frac{T_A}{\tilde{T}}, \quad Q_2 = -\frac{T_A}{\tilde{T}} + \frac{1}{2} \left( \frac{T_A}{\tilde{T}} \right)^2, \quad \dots \quad Q_n = \sum_{k=1}^n \frac{(-1)^{n-k} (n-1)!}{(n-k)! [(n-k)!]^2 k} \left( \frac{T_A}{\tilde{T}} \right)^k \end{aligned}$$

with  $T_A = \frac{E}{R}$ . In real flames the activation energies are generally that high, that the magnitude of the ratio  $\frac{T_A}{\tilde{T}}$  is of the order of 10 or more, and, hence, the related coefficients  $Q_1, Q_2, \dots, Q_n$  are large (e.g.,  $Q_1 = 10, Q_2 = 40$  for  $\frac{T_A}{\tilde{T}} = 10$ ). As a consequence

the Taylor series (2.13) converges very slowly, and the truncation error of the first-order approximation, which is obtained upon omission of all nonlinear fluctuation terms, is significant. It becomes very evident that an appropriate model must be provided for the closure of the (statistically or spatially) averaged chemical source terms  $\overline{\rho\dot{\omega}_j}$ .

A model based on a Taylor series expansion as shown in (2.13) does not represent a feasible closure method. Due to the very slow convergence of the series one would have to include third-order or even fourth-order terms to obtain fairly accurate predictions, which requires additional modeling for various nonlinear higher-order moments  $\widetilde{Y_j''T''^m}$  and  $\widetilde{T''^m}$ . A dynamic modeling strategy based on the similarity between the resolved and unresolved structures which is successfully used for the modeling of the subgrid-scale momentum and scalar transports in non-reacting LES, is hardly applicable to chemical closure as well. Chemical reactions are typically determined by very small scale transport processes, e.g., thermal diffusion, and, it has to be doubted, if these small scale phenomena can be simply extrapolated from the resolved large scale fields to give accurate results. Therefore, the dynamic procedure proposed by Jaberri & James (1998), which computes the filtered reactive source terms based on a scale similarity assumption, is scarcely used in LES of combustion.

To date, several different closure strategies, which are for the most part applicable to RANS calculations (most approaches were originally derived in a RANS context) as well as to LES have been proposed and further developed. They are well documented in the turbulent combustion literature - see, e.g., Borghi (1988), Libby & Williams (1994), Peters (2000), Veynante & Vervisch (2002).

The Probability Density Function (PDF) transport approach proposed by Pope (1985) solves for the evolution of the joint pdf of all the dependent fluctuating flow quantities as random variables. In the pdf transport equation the chemical source terms occur in closed form and no closure model is needed for them. This very attractive feature is however somehow counterpoised by the need for a model of the unclosed diffusion term commonly known as micromixing term. In addition, the high dimensionality of the formulation - each velocity component and reactive scalar represents a further dimension in random variable space - basically restricts the method to strongly reduced chemistry for computational economy. The mathematical formulation combining the PDF method with LES was first introduced by Gao & O'Brien (1993). Colucci *et al.* (1998) incorporated the LES inherent concept of spatial filtering into the PDF approach by defining a "filtered density function" (fdf) and assessed their model in a LES of a spatially developing planar jet for the reacting as well as for non-reacting case. A dynamic procedure for the micromixing term was proposed by Réveillon & Vervisch (1998).

Kerstein (1988) developed the concept of the Linear-Eddy Model (LEM) to capture the subgrid-scale mixing at first and extended later his approach to reacting flow (Kerstein, 1992*a,b*). Calhoon & Menon (1996) and Desjardin & Frankel (1996) investigated the LEM approach for use in LES of reacting mixing layers. The basic idea of LEM is to couple the

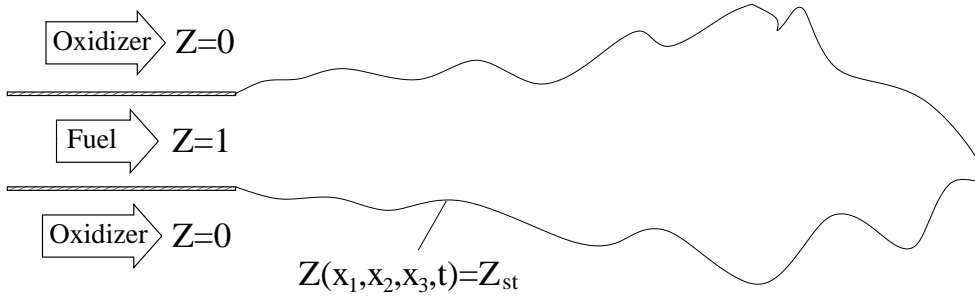


Figure 2.1: Non-premixed reacting jet flow configuration.

LES with a spatially one-dimensional direct numerical simulation (1D-DNS) of a reactive diffusion equation. The 1D-DNS solution is simultaneously computed to provide the required subgrid-scale contributions to the three-dimensional LES field. The advantage of LEM is that the transport equations for the reactive scalars involving the reactive source terms and probably strongly differing diffusivities can be fully, one-dimensionally though, resolved. The difficulties of LEM lie mainly in mimicking realistically the subgrid-scale intercellular turbulent stirring, which is generally done via stochastic rearrangement events, and in the appropriate coupling of the one-dimensional DNS with the LES. In addition, applying a more detailed multi-step chemistry may still lead to prohibitively high computational costs of the DNS part.

In the case of non-premixed combustion, where the fuel feed and the oxidizer feed enter separately the combustor, the reactive process is essentially controlled by mixing. Figure 2.1 shows a typical non-premixed jet flow configuration. The local mixedness can be described appropriately by the so-called mixture fraction  $Z$ . The mixture fraction can be defined as the local mass fraction of an inert tracer introduced with the fuel, which is in the case of insignificant differential diffusion equal to the local ratio between the mass flux originating from the fuel feed and the total mass flux,  $Z = \dot{m}_F / \dot{m}_{tot}$ . By definition,  $Z = 1$  in the fuel feed,  $Z = 0$  in the oxidizer feed, and  $0 < Z < 1$  in the mixing layer. The flame is located at the surface of stoichiometric mixture,  $Z(x_1, x_2, x_3) = Z_{st}$ , where the fuel-to-oxidizer ratio is such that there remains neither redundant fuel nor oxidizer after their complete combustion to products. The importance of the mixture fraction  $Z$  as a key parameter of non-premixed combustion was also confirmed by Bilger's observations making evident that the fluctuations in the temperature and the reactive scalars are strongly coupled with the fluctuations in mixture fraction (Bilger, 1993*b*). Therefore, several of the proposed non-premixed combustion models are based on the mixture fraction as key parameter. The Laminar Flamelet Model (LFM) and the Conditional Moment Closure (CMC) are the two most prominent representatives of this type of models.

## 2.4 Mixture fraction based models

The fundamental idea of all mixture fraction based models is that they solve for the chemistry in mixture fraction space ( $Z$ -space) and map the results to the resolved physical space. Figure 2.2 shows exemplarily the non-premixed flame structure in mixture fraction

space for a simple one-step chemistry, where only two reactants, fuel [F] and oxidizer [O], are reacted to the product [P]:



In each graph displaying the mass fractions,  $Y_F$ ,  $Y_O$  and  $Y_P$ , versus  $Z$ , respectively, the grey shaded regions denote all possible states accessible to the reactants and product in the  $Z$ -space. The straight solid bounding lines denoted by (a) represent chemically inert mixing, where no reaction occurs. The other boundary of the accessible region which is denoted by the dashed straight lines, labeled by (b), represents the case of infinitely fast irreversible chemistry, known as the Burke-Schumann solution. The typical structure of a real flame, exemplarily shown here as curved lines denoted by (c) may lie somewhere between these limits. Most of the by now well-established mixture fraction models differ mainly in their assumptions on the interactions between reaction kinetics and the underlying turbulent flow field, in particular, how the flame responds to instantaneous changes in the local scalar composition due to convective and diffusive transports. Several widely used approaches shall be outlined in the following.

### 2.4.1 Chemical equilibrium models

The chemical equilibrium models assume infinitely fast reaction rates, which implies that at any given mixing condition the flame reaches immediately the corresponding chemical equilibrium state. Since the resulting chemical composition does not depend on any specific time scale associated with the reaction mechanism, the structure of the flame is determined completely by the mixing state described in terms of mixture fraction. Basically, two types of chemical equilibrium models can be distinguished, one with infinitely fast *irreversible* chemistry and the other with infinitely fast *reversible* chemistry.

*Infinitely fast irreversible chemistry:*

This approach assumes that the chemical equilibrium is reached immediately only via irreversible reactions. It is commonly termed “mixed = burned”-regime and also known as the Burke-Schumann solution, where the flame evolves as an infinitely thin sheet repre-

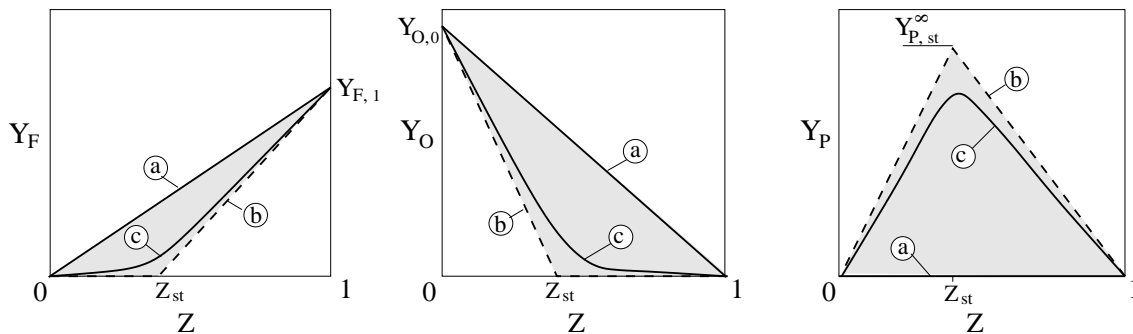
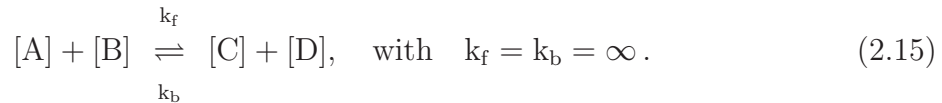


Figure 2.2: Accessible domains for fuel, oxidizer and product in mixing space ( $Z$ -space).

sented by the surface of stoichiometric mixture  $Z = Z_{st}$ . Considering only infinitely fast forward and no backward reactions, fuel and oxidizer cannot coexist. As shown in Figure 2.2 by the dashed lines denoted by  $\textcircled{D}$ , the chemical compositions, and consequently the temperature being equivalent to the product species ( $T \sim Y_P$ ), are fully determined as piecewise linear functions of  $Z$ . The assumption of infinitely fast irreversible chemistry is certainly one of the simplest approaches in describing the flame structure in mixing space ( $Z$ -space). Nonetheless, it has been proven to give acceptably accurate results in cases, where the chemistry acts on time scales which are significantly smaller than the relevant flow time scales (Cook & Riley, 1994; Jiménez *et al.*, 1997).

*Infinitely fast reversible chemistry:*

The assumption “mixed = burned” inherent in the concept of infinitely fast irreversible chemistry rules out the possibility to capture the formation of any intermediate species. To avoid this shortcoming one can assume chemical equilibrium including reversible reactions. Under this assumption the reactions are still considered as infinitely fast, but, unlike in the irreversible Burke-Schumann limit, the chemical mechanism involves both forward as well as backward reactions,  $k_f$  and  $k_b$ , balancing each other:



Due to the underlying equilibrium assumption the temperature as well as the total chemical composition are still entirely determined by the mixture fraction  $Z$ . However, in contrast to the Burke-Schumann solutions, the reversibility of the chemistry allows for a co-existence of fuel and oxidizer, as well as intermediate species, being all in an equilibrium state of steady formation and consumption.

Concerning the accuracy of this model, basically the same restrictions apply as in the case with irreversible chemistry. If the considered chemical mechanisms are very fast compared to the relevant flow time scales, the equilibrium assumption with reversible chemistry was proven to give fairly accurate results, as it was demonstrated in a LES of a hydrogen-air flame by Branley & Jones (2001). On the other hand, in the case of comparatively slow chemical kinetics, real turbulent flames are generally not in equilibrium. In methane-air diffusion flames it is, for example, a known deficiency of the equilibrium assumption that it excessively overpredicts the formation of CO on the fuel-rich side of the reaction zone.

*Mapping of the flame structures to the physical space:*

Since in the chemical equilibrium models, either with irreversible or with reversible reactions, the chemical composition is only dependent on the mixing state, the structure of the flame in  $Z$ -space can be primarily determined independently from the underlying reactive flow field. As such, the flow-independent solutions for the flame structure in  $Z$ -space, they shall be generally denoted here by  $\phi(Z)$ , are incorporated into the LES by

convolving them with the local filtered density function (fdf),  $\tilde{\mathcal{P}}(Z; \mathbf{x}, t)$ , to finally obtain the corresponding filtered counterparts in the resolved physical space  $\tilde{\phi}$ . The convolution generally reads

$$\tilde{\phi}(\mathbf{x}, t) = \int_0^1 \phi(Z) \tilde{\mathcal{P}}(Z; \mathbf{x}, t) dZ, \quad \text{where} \quad \phi(Z) = Y_J(Z), T(Z). \quad (2.16)$$

The filtered density function  $\tilde{\mathcal{P}}$ , which is defined as the spatially filtered representation of Dirac's delta, or fine-grain, function  $\delta(Z - \zeta(\mathbf{x}, \mathbf{t}))$

$$\tilde{\mathcal{P}}(Z; \mathbf{x}, t) = \frac{1}{\bar{\rho}} \int_{-\infty}^{\infty} \rho(\boldsymbol{\xi}, t) \delta(Z - \zeta(\boldsymbol{\xi}, t)) G(\boldsymbol{\xi} - \mathbf{x}) d\boldsymbol{\xi}, \quad (2.17)$$

accounts for the unresolved subgrid-scale fluctuations of the mixture fraction  $\zeta(\boldsymbol{\xi}, t)$  with respect to its resolved filtered mean  $\tilde{\zeta}$  in the physical space. Being dependent on the resolved Favre mean and variance,  $\tilde{\zeta}$  and  $\widetilde{\zeta'^2}$ , respectively, the fdf  $\tilde{\mathcal{P}}$  describes the state of mixedness within each computational cell of the LES, as schematically shown in Figure 2.3. It has become common practice to use a  $\beta$ -function

$$\begin{aligned} \tilde{\mathcal{P}}(Z; \tilde{\zeta}, \widetilde{\zeta'^2}) &= \frac{Z^{a-1} (1-Z)^{b-1}}{\int_0^1 x^{a-1} (1-x)^{b-1} dx} \\ \text{with} \quad a &= \tilde{\zeta} \left[ \frac{\tilde{\zeta}(1-\tilde{\zeta})}{\widetilde{\zeta'^2}} - 1 \right], \quad b = a \left( \frac{1}{\tilde{\zeta}} - 1 \right), \end{aligned} \quad (2.18)$$

for the shape of the local fdf. The required moments  $\tilde{\zeta}(\mathbf{x}, \mathbf{t})$  and  $\widetilde{\zeta'^2}(\mathbf{x}, \mathbf{t})$  to determine the fdf according to (2.18) can be obtained from the corresponding filtered transport equations

$$\frac{\partial \bar{\rho} \tilde{\zeta}}{\partial t} + \frac{\partial \bar{\rho} \tilde{u}_l \tilde{\zeta}}{\partial x_l} = \frac{\partial}{\partial x_l} \left( \bar{\rho} \tilde{D}_{mol, \zeta} \frac{\partial \tilde{\zeta}}{\partial x_l} \right) - \frac{\partial}{\partial x_l} \left( \bar{\rho} \widetilde{u_l' \zeta''} \right) \quad (2.19)$$

and

$$\frac{\partial \bar{\rho} \widetilde{\zeta'^2}}{\partial t} + \frac{\partial \bar{\rho} \tilde{u}_l \widetilde{\zeta'^2}}{\partial x_l} = - \frac{\partial}{\partial x_l} \left( \bar{\rho} \widetilde{u_l' \zeta''^2} \right) - 2 \bar{\rho} \widetilde{u_l' \zeta''} \frac{\partial \tilde{\zeta}}{\partial x_l} - 2 \bar{\rho} \tilde{D}_{mol, \zeta} \frac{\partial \zeta''}{\partial x_l} \frac{\partial \zeta''}{\partial x_l}. \quad (2.20)$$

In most LES the Eq. (2.19) is solved for  $\tilde{\zeta}$  using a gradient transport assumption for the unclosed subgrid-scale flux analogously to (2.8)

$$\bar{\rho} \widetilde{u_l' \zeta''} = - \bar{\rho} D_{t, \zeta} \frac{\partial \tilde{\zeta}}{\partial x_l},$$

with the eddy-diffusivity  $D_{t, \zeta}$  obtained from a Smagorinsky-type dynamic subgrid-scale model in terms of a dynamically computed turbulent Schmidt number  $Sc_{t, \zeta} = \nu_t / D_{t, \zeta}$ . Rather than solving a transport equation for  $\widetilde{\zeta'^2}$ , Eq. (2.20), which requires closure for

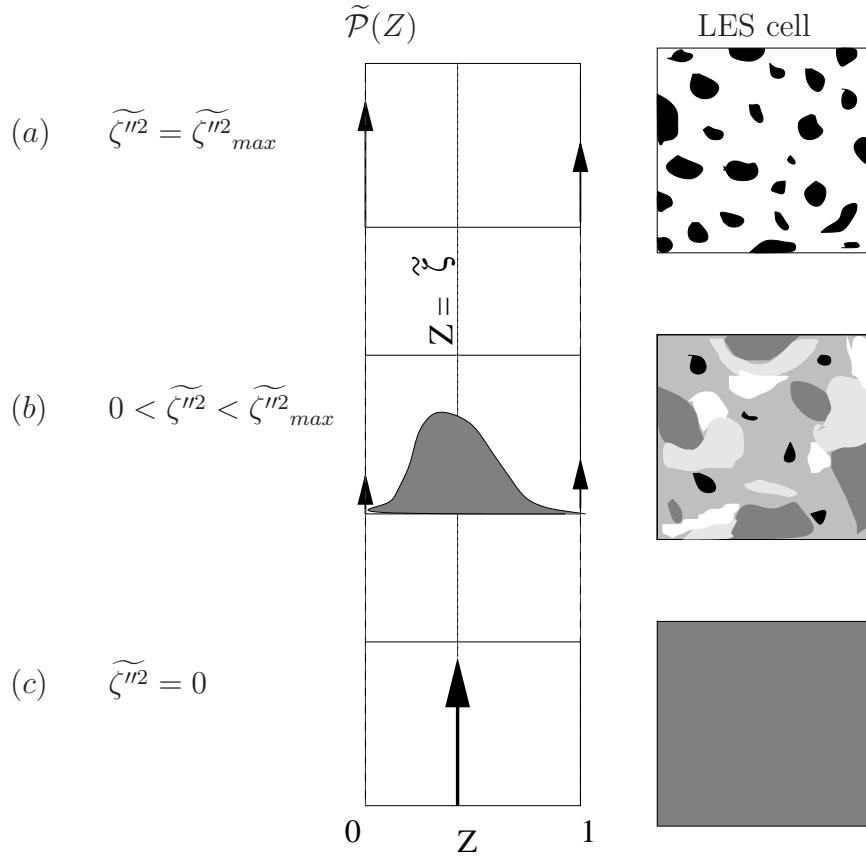


Figure 2.3: Three different states of subgrid-scale mixedness within a LES-cell, where the filtered mean mixture fraction  $\tilde{\zeta}$  has always the same value: (a) unmixed, (b) partially mixed, (c) totally mixed. The black areas denote pure fuel, the white areas denote pure oxidizer, the grey areas represent mixed regions. The maximum variance is given by  $\tilde{\zeta}^{m2}_{max} = \tilde{\zeta}(1 - \tilde{\zeta})$ .

two further unresolved subgrid-scale terms on its rhs, the variance is frequently modeled directly as

$$\bar{\rho} \tilde{\zeta}^{m2} = \bar{\rho} C_{\zeta} \frac{\partial \tilde{\zeta}}{\partial x_i} \frac{\partial \tilde{\zeta}}{\partial x_i}$$

using again a dynamic procedure for the coefficient  $C_{\zeta}$  (Pierce & Moin, 1998).

The chemical equilibrium models certainly greatly benefit from the capability of LES to capture the unsteady turbulent mixing motion very accurately providing them with reliable inputs needed to specify the local fdfs  $\tilde{\mathcal{P}}$ . It is, however, conceivable that the chemical equilibrium models will hit their limits, as soon as the underlying unsteady turbulent mixing motion acts on a time scale of comparable size to that of the principal chemical reactions. The then possible interactions between turbulent motion and chemistry may prevent the flame from reaching a chemical equilibrium. In such cases, at least one further parameter is needed to determine the real non-equilibrium flame structure

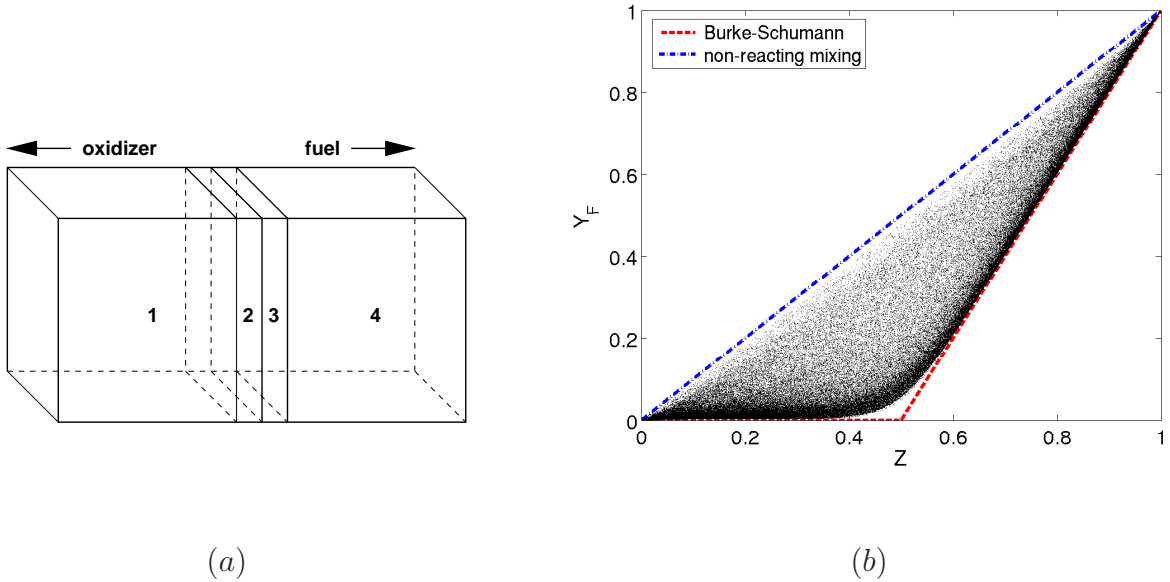


Figure 2.4: Non-premixed planar flame: (a) configuration, the turbulent flame is located inside the zones 2 and 3; (b) scatter plot of the instantaneous fuel mass fractions  $Y_F$  vs the instantaneous mixture fractions  $Z$ .

in the mixing space. The deviations of a turbulent diffusion flame located in a planar mixing layer from the equilibrium state are exemplarily demonstrated in Figure 2.4. The presented data are obtained from a DNS data base computed for a planar turbulent flame in the middle of a periodic box as shown on the left hand side. The DNS was carried out by Vervisch (1992) applying a simple one-step irreversible model mechanism for the chemistry as given by Eq. (2.14) with the stoichiometric point at  $Z_{st} = 0.5$ . The instantaneous values of the fuel mass fraction plotted over the corresponding instantaneous values of mixture fraction considerably scatter away from the Burke-Schumann limit towards the non-reacting mixing diagonal line. This indicates that there is a lot of extinction present in this particular flame. The considerable scatter especially in the region around the stoichiometric point,  $Z_{st} = 0.5$ , underlines again that the mixture fraction only may be not sufficient to describe the real structure of the flame.

### 2.4.2 Laminar Flamelet Model

The Laminar Flamelet Model (LFM) allows for an extension from equilibrium to non-equilibrium chemistry including also very detailed kinetic mechanisms. It considers the flame as an ensemble of laminar flamelets strained by the turbulent flow field, as it is schematically sketched in Figure 2.5. The chemical reaction rates are assumed as finite but sufficiently fast to ensure that the reactive layer is thinner than the smallest turbulent length scale, the Kolmogorov scale  $\eta$ , such that  $l_R \ll \eta$ . Within the reaction layer, the flow field can therefore be considered as quasi-laminar, where the smallest turbulent eddies do not penetrate into. The laminar flamelet equations can be derived by a coordinate

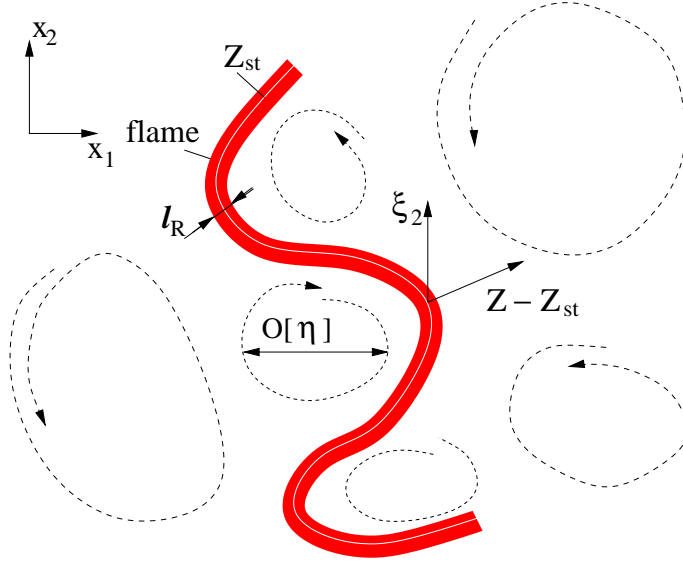


Figure 2.5: Thin flamelet stretched by turbulent eddies (two-dimensional illustration in the coordinates  $x_1$  and  $x_2$  for simplicity).

transformation into a coordinate system attached to the surface of stoichiometric mixture,  $Z(x_1, x_2, x_3) = Z_{st}$  (Peters, 1984). The transformation written as

$$\left( t, x_1, x_2, x_3 \right) \rightarrow \left( \tau, Z(x_1, x_2, x_3), \xi_2, \xi_3 \right), \quad (2.21)$$

where  $\tau = t$ ,  $\xi_2 = x_2$  and  $\xi_3 = x_3$ , basically consists in a simple replacement of the coordinate  $x_1$  by the new coordinate  $Z$  defining thereby the original coordinate system such that the direction  $x_1$  does not lie within the surface  $Z = Z_{st}$  to ensure uniqueness. As seen from Figure 2.5, the new principal direction  $Z$  is by definition locally orthogonal to the surface of stoichiometry  $Z = Z_{st}$ . Neglecting all the transports into the directions other than  $Z$ , such that

$$\frac{\partial}{\partial \xi_2}, \frac{\partial}{\partial \xi_3} \ll \frac{\partial}{\partial Z} \quad \text{and} \quad \frac{\partial^2}{\partial \xi_2 \partial \xi_3}, \frac{\partial^2}{\partial \xi_2^2}, \frac{\partial^2}{\partial \xi_3^2} \ll \frac{\partial^2}{\partial Z^2},$$

and assuming the molecular diffusivities of all species  $J$  as equal to the thermal diffusivity (unity Lewis numbers assumption), such that

$$Le_J = \frac{\kappa_{mol}}{\rho c_p D_{mol,J}} = \frac{D_T}{D_{mol,J}} = 1,$$

leads to the so-called laminar flamelet equations

$$\frac{\partial Y_J}{\partial \tau} - \frac{\chi_{st}}{2} \frac{\partial^2 Y_J}{\partial Z^2} = \dot{\Omega}_J, \quad (2.22)$$

$$\frac{\partial T}{\partial \tau} - \frac{\chi_{st}}{2} \frac{\partial^2 T}{\partial Z^2} = -\frac{1}{c_p} \sum_J \dot{\Omega}_J h_{0,J}, \quad (2.23)$$

which are basically valid in the vicinity of stoichiometric mixture  $Z = Z_{st}$ . The coefficient in front of the diffusion terms involves the scalar dissipation rate, here occurring as a statistical (ensemble) average conditioned on  $Z = Z_{st}$

$$\chi_{st} = \left\langle 2 D_T \frac{\partial Z}{\partial x_l} \frac{\partial Z}{\partial x_l} \middle| Z = Z_{st} \right\rangle. \quad (2.24)$$

$\chi_{st}$  represents the diffusive and convective transports normal to the surface of stoichiometric mixture,  $Z = Z_{st}$ , and it can be regarded as an external parameter which is imposed on the structure of the flamelet by the underlying strained flow field. As such, it incorporates the flow-induced deviation of the flame from the equilibrium state, and is therefore generally used as the second quantity to parameterize the flame structure in addition to  $Z$ . Being a turbulent fluctuating unresolved quantity, the determination of the average scalar dissipation rate, be it conditional or unconditional, needs appropriate closure models (Girimaji & Zhou, 1996; Pierce & Moin, 1998; Pitsch & Steiner, 2000b).

Omitting the transient terms in (2.22)-(2.23) finally gives the constitutive equations for the Stationary Laminar Flamelet Model (SLFM), which has become a very popular approach in the numerical computation of turbulent combustion in the context of RANS as well as of LES. Cook *et al.* (1997), Cook & Riley (1998) and De Bruyn Kops *et al.* (1998) investigated the SLFM approach for use in LES carrying out early *a priori* tests, where the LES results obtained with the assessed subgrid-scale model are compared against filtered DNS results. From a computational point of view, the SLFM concept offers the very attractive feature that the complete chemistry can be computed off-line in advance and stored in a so-called flamelet library. The separate solution of the chemistry independently from the considered flow field allows for the use of a very detailed kinetic mechanism. The flamelet library comprises a set of stationary flamelet solutions obtained for varying the parameter  $\chi_{st}$  up to a certain “quenching” limit  $\chi_q$ , beyond which no steady state burning solutions of (2.22)-(2.23) exist for the given chemistry. Be these steady laminar flamelet solutions generally written here as  $\phi(Z, \chi_{st})$ , they are mapped to the physical flow domain analogously to Eq. (2.16) by a convolution with the local joint pdf  $\tilde{\mathcal{P}}$  accounting for the subgrid-scale fluctuations of  $Z$  and  $\chi_{st}$ . This convolution can be generally written as

$$\tilde{\phi}(\mathbf{x}, t) = \int_0^1 \phi(Z, \chi_{st}) \tilde{\mathcal{P}}(Z, \chi_{st}; \mathbf{x}, t) dZ, \quad \text{with } \phi = Y_J, T. \quad (2.25)$$

The omission of the transient terms in the SLFM inherently assumes that the scalar dissipation rate changes on a time scale which is much longer than the time scales of the reactive processes, such that  $\chi_{st}$  can be assumed to be in a quasi-steady state relative to the rate determining chemical reactions. The SLFM comprises, therefore, only steadily burning solutions associated each with a certain constant value for the scalar dissipation rate lying always below the upper (quenching) limit,  $\chi_{st} < \chi_q$ . It follows that the SLFM is basically not capable to capture typical burning/nonburning transition phenomena like extinction, or reignition, which are both strongly related to unsteady fluctuations in  $\chi_{st}$ . Sripakagorn *et al.* (2004) investigated extinction and reignition viewed as the most fundamental deviations from the steady laminar flamelet burning solutions by carrying out

an *a priori* test of DNS data of a non-premixed combustion in homogeneous turbulence with a simple one-step fuel-oxidizer mechanism. Their study gave evidence that, while the scalar dissipation rate was on average always below the quenching limit,  $\langle \chi_{st} \rangle < \chi_q$ , it is essentially the instantaneous unsteady fluctuations beyond this limit,  $\chi_{st} > \chi_q$ , which cause local extinction.

Besides missing the unsteady transitions between the burning and nonburning state, the predictions of the SLFM tend to become inaccurate, if the considered chemistry involves elementary reactions, which are slow in comparison with the transient changes in  $\chi_{st}$ , as it is, for instance, the case in the formation of  $\text{NO}_x$ . This shortcoming motivated the development of the so-called Lagrangian Laminar Flamelet Model (LLFM), which was first tested for use in LES of a reacting jet by Pitsch & Steiner (2000*a*). The LLFM represents an unsteady laminar flamelet concept which is capable to account, to some extent, for transient effects on the flame structure in mixture fraction space ( $Z$ -space). In this approach the flame structure in  $Z$ -space is assumed as dependent of the axial distance downstream from the nozzle of the jet. The downstream distance,  $x$ , is thereby related to a Lagrangian type flamelet time  $\tau$  by the integral

$$\tau(x) = \int_0^x \frac{dx'}{\langle u|Z = Z_{st} \rangle}, \quad (2.26)$$

where  $\langle u|Z = Z_{st} \rangle$  is the mean downstream velocity component conditionally averaged on  $Z = Z_{st}$ . According to its definition (2.26),  $\tau(x)$  represents the average time needed by a flamelet to get convected from the nozzle downstream to the axial distance  $x$ . Along this path the laminar flamelet is subject to the downstream-varying conditionally averaged scalar dissipation rate  $\chi_{st} = \chi_{st}(\tau(x))$ , which has to be extracted from the resolved mixture fraction field by an appropriate model. The unsteadiness is thus incorporated by mapping the spatial evolution of the conditionally averaged scalar dissipation rate to a temporal evolution in a Lagrangian-type time frame as defined by Eq. (2.26). The integration of the unsteady laminar flamelet equations (2.22)-(2.23) imposing the Lagrangian time-dependent  $\chi_{st}(\tau(x))$  gives for each Lagrangian time  $\tau$ , and, hence, each downstream position  $x$ , an individual flamelet solution  $\phi(Z, x) = \phi(Z, \tau(x))$ . Analogously to Eq. (2.16), the convolution of these Lagrangian time-dependent, i.e., downstream distance  $x$ -dependent flamelet solutions  $\phi(Z, \tau(x))$  with the local pdf  $\tilde{\mathcal{P}}(Z; \mathbf{x}, t)$  yields the corresponding filtered chemical composition vector and temperature in physical space. The Lagrangian laminar flamelet model evidently accounts for the history of the flamelets in a statistical sense, i.e., in terms of their mean residence time in the flow field. Therefore, it does not capture any local unsteadiness impacting the flamelet structure, e.g., imposed by an instantaneous change of the local strain in the flow field. However, as it was shown in the study of Pitsch & Steiner (2000*a*), it gives considerably more accurate predictions for the formation of  $\text{NO}_x$  and OH compared to the stationary laminar flamelet model. It should be noted at this point that LES accompanied by a simultaneous integration of the complete set of the unsteady laminar flamelet equations (2.22)-(2.23) would theoretically make it possible to capture all transient effects, but is computationally unfeasible. Since the Lagrangian flamelet model relates the Lagrangian time to the motion downstream, it is restricted to parabolic flow configurations. It is therefore not applicable in cases with significant re-

versed flow like swirling jets. The Eulerian Particle Flamelet Model introduced by Barths *et al.* (1998) was devised to consider non-parabolic cases as well. This approach solves for the concentration fields of several classes of marker particles representing an individual unsteady flamelet each. It was applied by Coelho & Peters (2001) to a RANS-type calculation of a combustor with strong recirculation flow, where it gave good predictions for NO emissions. A rigorous application of the model in a predictive LES has not been done so far.

As an alternative to the commonly used parameterization based on the scalar dissipation rate  $\chi_{st}$ , the flamelet/progress variable approach parameterizes the steady laminar flamelet solutions in terms of a progress variable (Pierce & Moin, 2004). The progress variable, be it denoted here by  $C$ , can be defined as the sum of several product and intermediate species mass fractions, such as,  $\text{CO}_2$ ,  $\text{H}_2\text{O}$ ,  $\text{CO}$ ,  $\text{H}_2$ . The main advantage of such an alternative parameterization, using  $\phi(Z, C)$  instead of  $\phi(Z, \chi_{st})$ , is that all possible values of the progress variable can be uniquely related to a steady-state laminar flamelet solution including the nonburning, completely extinguished, states associated with  $\chi_{st} < \chi_q$ , as well. This regime of mixing without reaction, which may arise after extinction or before re-ignition, cannot be captured by a parameterization with the scalar dissipation rate, which covers only the burning solution for  $\chi_{st} < \chi_q$  for uniqueness reason. While being still a steady laminar flamelet model, the progress/variable approach was proven to capture to some extent the basically unsteady phenomenon of local extinction.

### 2.4.3 Conditional Moment Closure

The Conditional Moment Closure (CMC) approach was independently developed by Klimenko (1990) and Bilger (1993*a,b*). In the CMC method the transport equations are conditionally averaged with the mixture fraction  $Z$  being the conditioning variable. For some arbitrary scalar  $\phi_J$  the conditional averaging procedure may be generally written as

$$Q_J(\mathbf{x}, t; Z) = \langle \phi_J(\mathbf{x}, t) | \zeta(\mathbf{x}, t) = Z \rangle = \frac{\sum_{n=1}^N \phi_J(\mathbf{x}, t; n) \delta(\zeta(\mathbf{x}, t; n) - Z)}{\sum_{n=1}^N \delta(\zeta(\mathbf{x}, t; n) - Z)}, \quad (2.27)$$

where  $N$  denotes the total number of realizations within the considered sample space.  $\delta$  represents Dirac's delta function. Applying the conditional averaging procedure to the transport equation for an arbitrary scalar  $\phi_J$  yields then

$$\frac{\partial Q_J}{\partial t} + \langle u_k | \zeta = Z \rangle \frac{\partial Q_J}{\partial x_k} = \langle \dot{\Omega}_J | \zeta = Z \rangle + \frac{\partial^2 Q_J}{\partial Z^2} \left\langle D_{mol,J} \frac{\partial Z}{\partial x_k} \frac{\partial Z}{\partial x_k} \Big| \zeta = Z \right\rangle. \quad (2.28)$$

Therein, as suggested by Bilger (1993*a*), all terms of the order of the inverse of the turbulent Reynolds number  $1/Re_t = \nu_{mol}/u'l_0$  with  $u'$  and  $l_0$  representing the rms velocity fluctuation and the integral length scale of the underlying turbulent flow field, respectively, have been neglected. It is noted that the laminar flamelet solutions obtained from

Eqs. (2.22)-(2.23) are basically equivalent to the conditional averages defined by Eq. (2.27). Accordingly, the CMC-transport equations given by (2.28) essentially resemble the laminar flamelet equations (2.22)-(2.23), involving also the average scalar dissipation rate conditional on  $Z$  in front of the diffusion term. Here it appears in the second term on the rhs of (2.28) again as an unclosed coefficient, which has to be modeled. The basic assumption of the CMC method is that the fluctuations with respect to the conditional averages are small. This assumption implies that the conditionally averaged chemical source terms  $\langle \dot{\Omega}_J | \zeta = Z \rangle$  may be accurately obtained by evaluating the constitutive expressions for the elementary reactions with conditionally averaged input quantities, such that

$$\langle \dot{\omega}_K | \zeta = Z \rangle \approx \dot{\omega}_K (\langle \rho | \zeta = Z \rangle, \langle Y_J | \zeta = Z \rangle, \langle T | \zeta = Z \rangle). \quad (2.29)$$

As such this closure approach represents the conditional formulation of the unconditional first-order closure Eq. (2.11), which would be in general unacceptably inaccurate. For flames being away from extinction and involving reactions with not too high activation energies it was shown that the conditional first-order moment closure yields very accurate results (Kim & Huh, 2002; Cleary *et al.*, 2002). The conditionally averaged scalars can be related to their unconditional filtered counterparts in physical space by a convolution with the mixture fraction pdf analogously to Eq. (2.16) here rewritten as

$$\tilde{\phi}_J(\mathbf{x}, t) = \int_0^1 Q_J(\mathbf{x}, t; Z) \tilde{\mathcal{P}}(Z; \mathbf{x}, t) dZ. \quad (2.30)$$

In flames with significant local extinction and local re-ignition, the conditional first-order closure is not sufficiently accurate, as it was shown by Roomina & Bilger (2001) for the case of a methane-air jet flame. In such a case the effect of the fluctuations with respect to the conditional average defined as

$$\phi_J''(\mathbf{x}, t) = \phi_J(\mathbf{x}, t) - Q_J(\mathbf{x}, t; Z) \quad (2.31)$$

is not negligible any more. A second-order closure incorporates the influence of these conditional fluctuations by including higher-order terms, namely the conditional variances and covariances,  $\langle \phi_J''^2 | Z = \zeta \rangle$  and  $\langle \phi_I'' \phi_J'' | Z = \zeta \rangle$ , respectively, into the closure equation for the conditional reaction terms (2.29) (Klimenko & Bilger, 1999). The conditional second-order moments needed here are obtained by solving corresponding transport equations. This suggests to use strongly simplified chemical reaction mechanism to keep the number of such transport equations small, as it was done by Kronenburg *et al.* (1998) for a hydrogen-air diffusion flame. Alternatively to second-order closure, the accuracy of the conditional closure (2.29) can be improved using double conditioning. A conditioning on the mixture fraction as well as on a further appropriate parameter, which could be the scalar dissipation rate (Cha *et al.*, 2001), or the sensible enthalpy (Kronenburg, 2004), was proven to yield very accurate predictions for the conditional reaction rates also in flames with strong local extinction and re-ignition. Despite these very promising results, the wider application of double conditioning CMC is greatly challenged by the unclosed doubly-conditional scalar dissipation rate occurring in the double conditioned counterpart of the CMC transport equation (2.28). In addition, an appropriate model is also needed

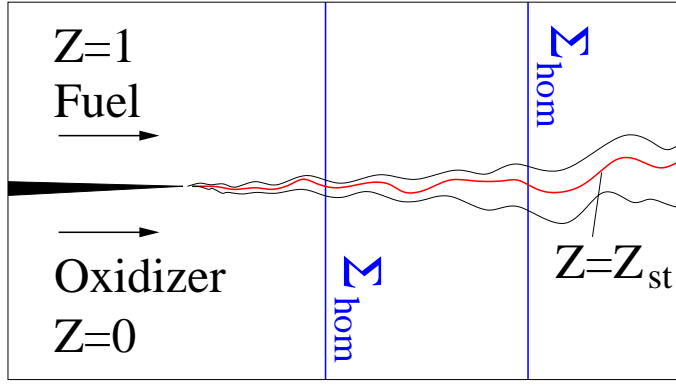


Figure 2.6: Planar reactive mixing layer: Fuel and oxidizer feeds are separated by a splitter plate,  $\Sigma_{hom}$  denote surfaces, where homogeneity can be assumed,  $Z = Z_{st}$  denotes an instantaneous position of the flame.

for the two-parametric joint pdf occurring in the convolution (2.30) when recast into a double conditioned formulation. To overcome this problem Klimenko & Pope (2003) proposed the multiple mapping conditioning (MMC) approach, which brings together the CMC and PDF approaches. The method introduces a set of “reference variables” as conditioning variables, and it solves for a consistent set of modelled transport equations for the averages conditional on these reference variables. The required multiple-variable joint-pdf is constructed based on the assumption that the reference variables are stochastically independent having all Gaussian distributions. The first test of this concept considering a three-stream mixing problem gave promising results. A key issue for its future application to turbulent flames will be the development of accurate and efficient numerical algorithms to ensure a computationally feasible solution procedure, especially when extending to a higher dimensionality of the reference variable space.

Since the CMC method adds at least one further dimension (in the single conditioning case it is normally the mixture fraction  $Z$ ) to the time and the three spatial dimensions, its use as a combustion model for LES of inhomogeneous reacting flows would lead to excessively high computational costs. This problem could be circumvented by the Conditional Source-term Estimation (CSE) method proposed by Bushe & Steiner (1999). The CSE approach still utilizes the CMC first-order hypothesis (2.29) to obtain closure for the spatially filtered reaction terms. However, it does not need to solve for the evolution equations of the conditional averages, Eq. (2.28), as it is required in the original CMC method. The basic assumption of the CSE approach is that inside the physical flow domain, there can be identified statistically homogeneous surfaces  $\Sigma_{hom}$ , on which the conditional averages can be assumed to be invariant. As exemplarily shown in Figure 2.6 for the case of a planar reacting mixing layer, planes perpendicular to the surface, where the flame is on average located, can be assumed as statistically homogeneous. For each surface of homogeneity the conditional averages  $\langle \phi_J | \zeta = Z \rangle$  can then be approximated by

inverting the convolution

$$\tilde{\phi}_J(\mathbf{x}_n, t) = \int_0^1 \langle \phi_J | \zeta = Z \rangle \tilde{\mathcal{P}}(Z; \mathbf{x}_n, t) dZ \quad \text{with } \mathbf{x}_n \in \Sigma_{hom} \quad (2.32)$$

for an ensemble of  $n = 1, \dots, N$  unconditional filtered scalars  $\tilde{\phi}_J(\mathbf{x}_n, t)$ , which are sampled on the considered homogenous surface  $\Sigma_{hom}$  at the points  $\mathbf{x}_n$ . As such the inversion of the integral equation (2.32) serves to map the flame conditions from the physical space ( $\tilde{\phi}_J$ ) to the parameter space ( $\langle \phi_J | \zeta = Z \rangle$ ). Bushe & Steiner (1999) validated the CSE method first in an *a priori* test based on DNS results of a reactive mixing layer, where a simple one-step model mechanism had been applied (Chen *et al.*, 1992). This *a priori* test made also evident that a second conditioning variable is needed to capture local extinction which was significant in the considered model flame. Accordingly, applying the CMC closure Eq. (2.29) with averages conditioned on two variables, the mixture fraction  $Z$  and the scalar dissipation rate  $\chi$ , considerably improved the predictions of the model. In a successive work, Steiner & Bushe (2001) investigated the predictive capability of CSE for use in a real flame. They considered a piloted methane-air jet flame which had been investigated in experiments by Barlow & Frank (1998). A reduced two-step kinetic mechanism introduced by Williams (1991) was used for the methane-air chemistry. The LES results obtained with the CSE method showed very good agreement with the measurements. The instantaneous contours of the temperature as well as the instantaneous position of the stoichiometric surface,  $Z = Z_{st}$ , can be seen from Figure 2.7. For this jet flame configuration, planes normal to the axis of the jet were assumed as surfaces of homogeneity for the conditional averages,  $\Sigma_{hom}$ .

The attractive features of the CSE approach are that it basically does not need to assume very fast, i.e., close-to-equilibrium chemistry, or a steady-state flame structure like SLFM. In addition, since CSE relates the conditional averages to the instantaneous resolved flow field provided by the LES equations, it is capable to capture unsteady effects of the turbulent motion on the chemical reactions. The CSE method has, however, still some limitations. First, the method requires the assumption of the existence of homogeneous surfaces, where the conditional averages practically do not change. Especially in strongly non-parabolic configurations, e.g., in cases with significant reversed flow, it may become very difficult to identify such statistically homogenous surfaces, on which the conditional averages do not vary markedly. This issue will certainly have to be addressed in the further development of the model. Second, the conditional averages are obtained as solutions of an integral equation as given by Eq. (2.32). Thereby, a linear regularization is applied to suppress the occurrence of unphysical maxima and minima in the resulting curves for  $\langle \phi_J | \zeta = Z \rangle$ , which, on the other hand, may lead to overly diffusive solutions. Third, in case of extinction or re-ignition a second conditioning variable, most suitably the scalar dissipation rate  $\chi$ , has to be introduced, which requires some additional assumptions on the fdf of  $\chi$ . Moreover, having to solve for doubly conditioned averages increases the computational costs for the solution of the integral equation (2.32) considerably. The latter two constraints motivated to develop the CSE method further to the CSE-Laminar Flamelet Decomposition method (CSEFD) as proposed by Bushe & Steiner (2003). It

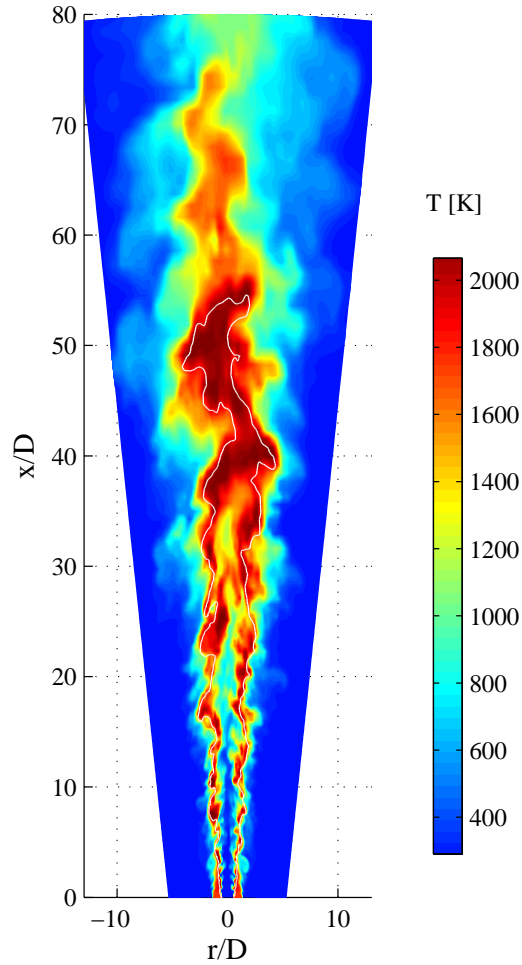


Figure 2.7: LES of a non-premixed reacting piloted jet flow: instantaneous temperature contours. The white line denotes the instantaneous position of the stoichiometric surface,  $Z = Z_{st}$ . (Reprinted from Steiner & Bushe (2001)).

can be regarded as a hybrid between the Laminar Flamelet method (LFM) and CSE. In the CSEFD method the conditional averages are estimated as a superposition of a set of unsteady laminar flamelet solutions  $\phi_m(Z)$

$$\langle \phi | \zeta = Z \rangle \approx \sum_{m=1}^M a_m \phi_m(Z). \quad (2.33)$$

The weighting coefficients  $a_m$  are obtained analogously to the original CSE approach upon the inversion of an integral equation

$$\tilde{\phi}(\mathbf{x}_n, t) = \int_0^1 \sum_{m=1}^M a_m \phi_m(Z) \tilde{\mathcal{P}}(Z; \mathbf{x}_n, t) dZ \quad (2.34)$$

for  $n = 1, \dots, N$  sample points on a homogeneous surface. The unsteady laminar flamelet solutions  $\phi_m(Z)$  can represent a typical spectrum of physically realizable conditions for

the flame including solutions which arise from re-ignition or extinction and, hence, no additional conditioning variable might be needed to capture these effects. Alike in the Steady Laminar Flamelet Model (SLFM) highly complex multi-step kinetic mechanism can be used to predict the formation of intermediate species and pollutants. Bushe & Steiner (2003) carried out an *a priori* test using a DNS data base. It turned out that the most accurate results could be achieved with the computationally least expensive procedure which solves the integral equation (2.34) only for the temperature, such that  $\tilde{\phi} = \tilde{T}$ . The thereby obtained coefficient vector  $a_m$  is then used to compute the conditionally averaged reaction rates directly as a linear combination of the reaction rates from the unsteady flamelet library for the elementary reaction rates  $\omega_{K,m}(Z)$

$$\langle \dot{\omega}_K | \zeta = Z \rangle \approx \sum_{m=1}^M a_m \dot{\omega}_{K,m}(Z). \quad (2.35)$$

Although the CSEFD method does not require a regularization technique to obtain smooth solutions alike the original CSE, it has to cut-off negativ coefficients of  $a_m$ , which might eventually occur but are physically meaningless and therefore discarded. In a sense the weighting coefficient vector  $a_m$  plays the role of the fdf of the scalar dissipation rate  $\chi$  getting involved in the case of double-condition CSE with conditioning on  $Z$  and  $\chi$ . From this viewpoint the method can be practically regarded as a promising candidate for unsteady flamelet modeling with the great benefit of having not to model a fdf of  $\chi$ . It is noted, however, that alike in the original CSE approach the assumption of surfaces of statistical homogeneity is still a basic requirement of the model. With this respect, as it was already pointed out above, there is scope for a further developments of the model especially when dealing with very complex flow configurations inside the combustor.

## 2.5 Concluding remarks

During the last decade LES has become increasingly acknowledged as a powerful simulation tool for its potential of providing valuable instantaneous information especially needed as input for a reliable modeling of turbulent combustion. The typically applied approaches mostly still resemble equilibrium or close-to-equilibrium chemistry concepts, which were originally derived for use in RANS-type simulations. When applying more comprehensive combustion models to LES, the major part of the considered configurations were of academic type, such as jet flows, or plane mixing layer flows, rather than real engineering problems. Nonetheless, important advancements have been made towards a realistic modeling of non-equilibrium flames, where the turbulent fluctuating, instantaneous local strain may strongly affect the reactions. In the case of non-premixed combustion, the Conditional Moment Closure, the unsteady laminar flamelet models, and the transported filtered density function method were proven as most promising approaches. The incorporation of these approaches into predictive LES still raises many open issues, though, such as a most efficient computation of the flame structure in parameter space, the appropriate mapping of the flame structure from the parameter space to the physical space, the substantial computational costs added by the models, or the closure for the unresolved micromixing terms. Even the basic resolution requirements for LES, which are

generally determined by the criterion that the energy contained in the unresolved subgrid scales is small compared to the resolved part, may need revision. In contrast to the non-reacting case, combustion brings in an important part of energy especially on the small, unresolved, subgrid scales. The significant contribution from these unresolved scales puts the same fundamental problem of insufficient resolution to LES as it does to RANS. In summary, there are evidently many practical as well as very fundamental aspects, which need further investigation to pave the way for a use of LES as a standard tool in technical combustion.

## 3 Modeling of subcooled boiling flow

### 3.1 Introduction

In the modern design and layout of highly efficient cooling systems, investigations on subcooled boiling flow have been gaining much attention. Especially in thermally highly loaded wall regions, where highest possible heat transfer rates are required to keep the local surface temperatures on an acceptable level regarding material lifetime, the cooling power which can be achieved with pure single-phase forced convection is often limited and insufficient. The limitations of the convective single-phase cooling may be due to a very compact space- and weight-saving design of the individual cooling system components, which often leads to small cooling surface areas as well as unfavorable flow conditions for the convective transport of heat. There may be also restrictions on the available magnitude of the coolant feed into the cooling system. In all such cases the concept of utilizing the strongly enhanced heat transfer associated with nucleate boiling represents an attractive approach. It offers a great potential for application in many energy conversion and heat exchange systems, ranging from the cooling of electronic components to the thermal management of modern internal combustion engines. The application of this novel concept in today's design of cooling systems requires, however, reliable mathematical models which predict the convective boiling heat transfer with acceptable accuracy. Furthermore, these models should be well suited for use in CFD of coolant flows.

Nucleate boiling flow is a highly complex phenomenon, which involves numerous types of interactions between the liquid, the vapor phase, and the solid heater, as schematically shown in Figure 3.1. The interaction between the liquid bulk flow and the non-boiling part of the heated surface, denoted by *1*, represents basically the convective single-phase heat transfer, generally termed macroconvection. The interaction between the bulk flow and the vapor bubbles, denoted by *2*, comprises the hydrodynamic forces of the flow acting on the bubbles and vice versa. These flow induced forces can strongly influence the bubble growth, the bubble detachment from the nucleation sites, as well as the paths of the rising bubbles. Moreover, a densely populated heated surface may change the near-wall flow conditions significantly. The bubble-liquid phase interaction, denoted by *3*, is often subsumed as the so-called microconvection. It includes the entrainment of liquid into the wake of a rising bubble immediately after detachment, which mixes portions of cool liquid from the - mostly subcooled - outer flow region into the superheated wall layer. This bubble lift-off induced transport of cool bulk liquid towards the heated surface increases instantaneously the local convective heat transfer. At the same time, it cools down the area around the nucleation sites below the critical temperature for nucleation. This cooling down of the nucleation sites immediately after bubble lift-off is generally termed "surface quenching". A quenched nucleation site needs some period of time to be re-heated beyond a critical temperature, where bubble nucleation is initiated again. The required heat is supplied by the solid heater via conductive heat transfer, denoted by *4*. Aside from the hydrodynamical effect of the bubble motion on the liquid, the bubble-liquid interaction also includes the thermal effect of condensation at the vapor-liquid interface. This process occurs at the top of the bubbles, once the interface reaches a zone where

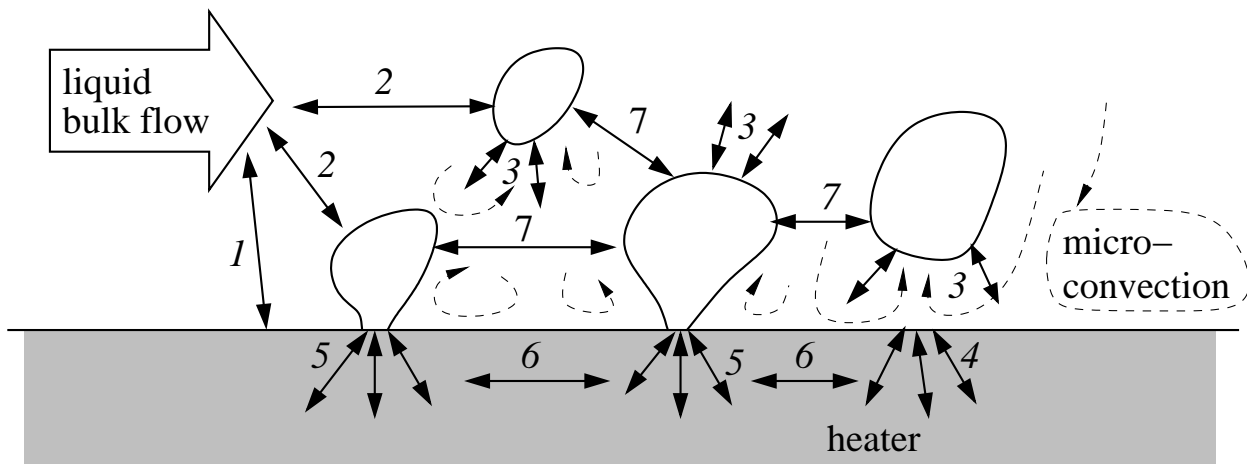


Figure 3.1: Interactions between liquid phase, the vapor bubbles and the solid heater.

the local temperature is below the saturation level. The evaporative counterpart of this mechanism of latent heat transport is realized by the interaction between the bubble foot and heated surface, denoted by 5. While the bubble is growing on its nucleation site, the latent heat needed for evaporation is continuously removed from the solid heater material, which causes a local drop of the temperature on the heated surface structure. The local cooling due to the removal of heat of evaporation during bubble growth, as well as the local cooling associated with the surface quenching after bubble detachment, are the main reasons why the surface temperature is highly non-uniform in time and space. This non-uniformity of the surface temperature also leads to considerable thermal interactions (conductive heat exchange) between the individual nucleation sites inside the solid heater, denoted by 6. It is noted that most of the boiling models used today do not account for these spatial and temporal fluctuations in the surface temperature assuming in general a stationary and uniform wall temperature. For denser bubble populations occurring at higher wall superheats the bubble-bubble interactions, denoted by 7, such as coalescence or formation of columns, can play an important role. It is conceivable that this type of interaction makes simple single bubble considerations, on which many boiling models are based, highly questionable. The complexity shown in Figure 3.1 still does not give the complete picture. Contact surface related aspects associated with surface tension, wettability, surface roughness, and porosity are known to have an important influence on the number of active nucleation sites needed for the formation of vapor bubbles. The so-called surface aging, which can be caused by chemical depositions on the heater surface leading to a long term deactivation of nucleation sites, also falls into this group. It is especially these surface related properties which impair a rigorous parameterization, such that the theoretical boiling models proposed to date involve many empirical constants, which have to be adjusted from case to case.

Despite the numerous and physically complex effects which can be relevant in nucleate boiling, it is generally agreed that the marked increase in the heat transfer rate relative to the single-phase convection essentially results from two basic mechanisms:

- the microconvection induced by the motion of the bubbles and
- the latent heat transport to and from the bubbles.

However, in many cases no consensus has been reached on the quantitative contribution of each mechanism to the total heat flux.

### 3.2 Basic model considerations

Boiling is a very complex and elusive process, whose underlying physics is still not fully understood. No rigorous theoretical model has yet been developed to predict the heat transfer rate as a function of the wall superheat. The difficulty to develop a mathematical formalism to capture all the relevant mechanisms is not only due to the highly complex interactions between the numerous sub-processes involved in nucleate boiling. The modeling also faces the arduous problem of measuring all the properties which are essential for the physics of the interfacial contact between the vapor, liquid, and the solid (heater) phases. In view of the fact that for technical surfaces it is practically impossible to measure rigorously contact physics related properties, such as roughness, wettability or aging conditions, it is even doubted if deterministic modeling is an appropriate approach at all to describe the nucleate boiling process. Following such an argument, boiling should be considered rather as a chaotic process subject to strongly nonlinear interactions. The non-deterministic approach to model the so-called “boiling chaos”, whose basic ideas and critical issues were discussed in much detail in a review by Shoji (2004), particularly focuses on the nucleation site problem as the most relevant sub-process. The current research in this field primarily aims at a better understanding of the non-linear physics of boiling rather than yielding most accurate quantitative predictions in particular configurations. It is expected that a better understanding of the real phenomena will finally lead to more reliable theoretical models also in a quantitative sense. Mosdorf & Shoji (2004) presented a simple nonlinear model which mimicks the temporal chaotic changes in the surface temperature at a given active nucleation site. The authors attribute the chaotic fluctuations in the surface temperature, which are also observed in experiments, to the temporal changes in the heat flux absorbed by the bubbles. The approach based on the nonlinear analysis will certainly give more insight into the real physical phenomena governing the nucleate boiling process, however, much theoretical as well as experimental work has still to be done to finally yield predictive boiling models for an application in technical flows.

In pace with the steady increase of computer power, the use of Computational Fluid Dynamics (CFD) has become state-of-the-art in the modern design of energy conversion and transmission devices. The model-free CFD method, which solves directly all relevant transport processes, as it is done in the Direct Numerical Simulation (DNS) of turbulent flow at low Reynolds numbers, has to be ruled out for real-life boiling configurations on technical surfaces due to its prohibitively high computational costs. At the most, direct numerical simulations can be carried out in strongly simplified configurations, such as boiling from a predefined small number of nucleation sites on an otherwise perfectly smooth surface (Mei *et al.*, 1995*a,b*; Shin *et al.*, 2005). This limitation will apply at least

in the foreseeable future, despite the ongoing increase of the available computational resources. CFD of boiling flow will therefore keep relying heavily on the modeling of the interfacial heat and mass transfer.

Today’s commonly used approaches involve a lot of empiricism built into the various model correlations, which limits their general applicability considerably. The generation of a vapor phase at the incipience of nucleate boiling basically suggests a two-fluids simulation, where the discretized Eulerian transport equations are numerically solved both for the liquid and the vapor phase (Končar *et al.*, 2004; Xu *et al.*, 2005). Since technical flows are mostly turbulent, one in general solves the Reynolds averaged formulations of the transport equations, which requires appropriate turbulence models for the unclosed averages of the nonlinear transport terms, as it is already the case in turbulent single-phase flow. The complex nature of the liquid/vapor interactions as well as the difficulty in defining adequate wall boundary conditions for the void fraction makes the two-fluids simulations reliant on many - partly questionable - modeling assumptions, which again introduce much empiricism and may finally lead to a loss of general applicability and accuracy. It has therefore become a frequently adopted praxis to use only a single-phase formulation neglecting completely the dynamics associated with the motion of the vapor phase. In the case of subcooled boiling flow the simplification to simulate only the motion of the liquid carrier phase can certainly be reasoned by the zero net production of vapor, because the bubbles condense immediately, once they escape from the very confined superheated wall layer with the temperature within being  $T > T_s$ . It can then be argued that the vapor phase exists only inside a very thin layer next to the superheated wall, while the other, much larger part of the flow domain is occupied by liquid phase only, such that the dynamical effect of vapor phase can be neglected. Concerning the total wall heat flux, the single-fluid modeling does account for the presence of the vapor phase near the wall by imposing thermal wall boundary conditions, which include nucleate boiling heat transfer through corresponding boiling models. As such, the single-fluid modeling, which includes the boiling wall heat transfer, certainly represents a very simple way to capture the strongly enhanced heat transfer associated with nucleate boiling. However, in the presence of a significant void fraction at the heated wall, the single-fluid concept inherently misses several important features typically found in the bubble-laden near-wall flow, such as retarded mean velocities, or an enhanced turbulence in the liquid phase. The effects of the vapor bubbles on the flow of the liquid were investigated in a number of experimental studies (Maurus, 2003; Ramstorfer *et al.*, 2005). It is expected that the results of these experimental studies will help to improve the modeling of the fluid/vapor interactions in the two-fluids simulations. To some extent these studies may also be very useful in the single-fluid modeling to account for the presence of the vapor bubbles by modifying the wall boundary conditions for the velocity as well.

Figure 3.2a shows a typical subcooled boiling flow configuration. Basically, the subcooled boiling flow regime is characterized by a superheated wall with  $T_w > T_s$ , and a bulk temperature, which is lower than the saturation temperature,  $T_b < T_s$ . The formation of vapor bubbles starts once the heated wall has reached the onset of nucleate boiling (ONB) temperature,  $T_w = T_{ONB}$  at point *B*. Figure 3.2b shows three boiling curves de-

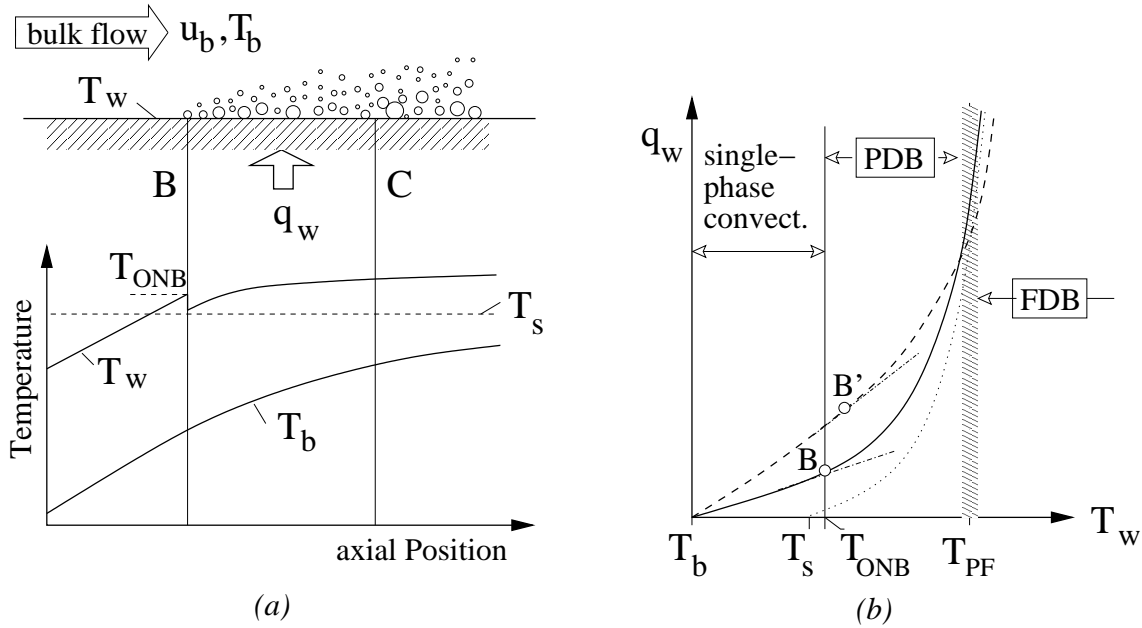


Figure 3.2: Subcooled boiling flow: (a) variation of bulk and wall temperatures into the streamwise direction; (b) boiling curves for different velocities of the bulk liquid; the dashed line,  $--$ , denotes the highest velocity case, the dotted line,  $\cdots$ , denotes the zero velocity, i.e. the pool boiling case.

predicting the wall heat fluxes  $q_w$  versus the wall temperatures  $T_w$  for three different bulk velocities with zero velocity - representing the pool boiling case - being the lowest. Two subranges can be distinguished in the subcooled boiling region: in the partially developed boiling (PDB) regime at lower wall superheats, the bulk flow rate affects the heat transfer significantly. So the onset of nucleate boiling is shifted to higher wall superheats for higher flow rates ( $B \rightarrow B'$ ), as shown in Figure 3.2b. In the fully developed boiling (FDB) regime at higher wall superheats, the boiling curves converge towards the pool boiling curve, which indicates that the flow rate becomes insignificant once the wall superheat is sufficiently high.

### 3.2.1 Onset of nucleate boiling (ONB)

The determination of the point of the incipience of boiling, ONB-point, was the subject of many studies, as it provides a criterion for the minimum wall superheat

$$T_w - T_s = T_{ONB} - T_s,$$

which is required for the formation of vapor bubbles. As such, it specifies the lower limit above which the nucleate boiling heat transfer has to be accounted for through corresponding boiling models. Hsu (1962) was the first to develop an analytical condition for the onset of nucleate boiling at a given cavity. Hsu's analysis starts from a vapor bubble of radius  $r_b$  in equilibrium with its surrounding liquid of temperature  $T_l$  and pressure  $p_l$ .

The pressure inside the bubble  $p_g$  is given by the Young-Laplace equation as

$$p_g = p_l + \frac{2\sigma}{r_b} \quad (3.1)$$

with  $\sigma$  being the surface tension at the interface. Assuming the vapor phase as perfect gas and a small vapor/liquid-phase density ratio,  $\rho_v/\rho_l \ll 1$ , the overpressure  $p_g - p_l$  can be related to the corresponding superheat using the Clausius-Clapeyron equation written as

$$\frac{dp}{dT} = \frac{h_{lg}}{T \left( \frac{1}{\rho_v} + \frac{1}{\rho_l} \right)} \approx \frac{h_{lg}\rho_v}{T} = \frac{h_{lg}p}{RT^2}, \quad (3.2)$$

where  $h_{lg}$  represents the latent heat of evaporation and  $R$  is the specific gas constant. The integration of (3.2) from  $p_l$  to  $p_g$  yields the saturation temperature of the vapor inside the bubble written as

$$T_g = T_s + \frac{RT_s T_g}{h_{lg}} \ln \left( 1 + \frac{2\sigma}{r_b p_l} \right), \quad (3.3)$$

where  $T_s = T_s(p_l)$  refers to the saturation temperature of the liquid outside the bubble having the pressure  $p_l$ .

Eq. (3.3) can be further simplified assuming  $\frac{2\sigma}{r_b p_l} \ll 1$  and  $\frac{p_l}{RT_g} \approx \frac{p_g}{RT_g} = \rho_v$ . Thereafter, applied to a truncated spherical bubble, as shown in Figure 3.3a, the saturation temperature  $T_g$  can be rewritten as a function of the wall normal distance at the tip of the bubble,  $y = y_b = r_b(1 + \cos\beta)$ ,

$$T_g(y_b) = T_s + \frac{T_s}{\rho_v h_{lg}} \left( \frac{2\sigma}{\frac{y_b}{1 + \cos\beta}} \right). \quad (3.4)$$

Hsu postulated for the ONB condition that the temperature at the tip of the bubble is at least equal to the saturation temperature inside the bubble given by Eq.(3.4), such that

$$T_g(y_b) = T_l(y_b), \quad (3.5)$$

where the temperature of the liquid phase is assumed as a linear function of the wall distance as

$$T_l(y_b) = T_w - \frac{q_w}{\lambda_l} y_b, \quad (3.6)$$

whose gradient is determined by the wall heat flux  $q_w$  and the thermal conductivity of the liquid phase  $\lambda_l$ . As shown in Figure 3.3b, the solution of Eq. (3.5) corresponds to the intersection points between the curved line for  $T_g$  and the straight line for the liquid temperature  $T_l$ , given by Eqs. (3.4) and (3.6), respectively, where the height of the bubble,  $y_b$ , has been rewritten in terms of the cavity mouth radius

$$r_c = \frac{y_b \sin\beta}{1 + \cos\beta}.$$

Both lengths are equal,  $r_c = y_b$ , in the case of a hemispherical bubble, which is associated with a contact angle  $\beta = 90^\circ$ . The two intersection points at

$$r_{c_{min, max}} = \frac{T_w - T_s}{2} \frac{\lambda_l}{q_w} \frac{\sin\beta}{1 + \cos\beta} \left[ 1 \pm \sqrt{1 - \frac{8q_w T_s \sigma (1 + \cos\beta)}{\lambda_l \rho_v h_{lg} (T_w - T_s)^2}} \right] \quad (3.7)$$

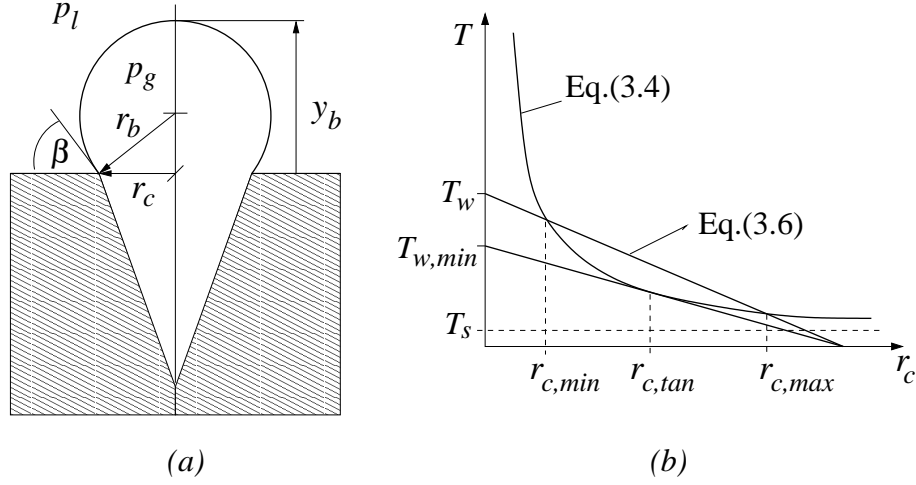


Figure 3.3: Onset of nucleate boiling: (a) bubble nucleus at the incipience of boiling (ONB); (b) superheat criterion for the ONB, tangency condition  $r_c = r_{c,tan}$ .

represent the limits of the range of effective cavity radii for a given wall superheat  $T_w - T_s$ , because only cavities inside the interval  $r_{c,min} \leq r_c \leq r_{c,max}$  satisfy the condition  $T_l(y_b) \geq T_g$  for the incipience of boiling. It can be further concluded from Eq. (3.7) that effective cavities only exist for a non-negative discriminant. The limit of a zero discriminant provides a minimum superheat criterion for the incipience of boiling generally termed “tangency condition for the ONB”, which relates the wall heat flux at the ONB to the minimum wall superheat as

$$q_{ONB} = \frac{\lambda_l \rho_v h_{lg} (T_{w,min} - T_s)^2}{8 T_s \sigma (1 + \cos \beta)}. \quad (3.8)$$

Furthermore, invoking the tangency condition for a given cavity size  $r_c$ , such that

$$r_c = r_{c,tan} = \frac{T_{w,min} - T_s}{2} \frac{\lambda_l}{q_{ONB}} \frac{\sin \beta}{1 + \cos \beta},$$

yields an expression for the minimum wall superheat

$$T_{w,min} - T_s = \frac{4 T_s \sigma \sin \beta}{\rho_v h_{lg} r_c}. \quad (3.9)$$

Bergles & Rohsenow (1964) applied Hsu’s analysis to a hemispherical bubble ( $\beta = 90^\circ$ ). However, they considered the full equation (3.3) and not the approximation (3.4), which finally leads to no explicit formulation for the incipient heat flux alike Eq. (3.8) when invoking the tangency condition. Based on experimental data they provided a graphical solution

$$q_{ONB} = 1082 p^{1.156} [1.8(T_w - T_s)]^{\frac{2.16}{p^{0.0234}}} \quad (3.10)$$

instead, where  $p$  is the pressure of the liquid measured in atmospheres.

It is known that for well wetting fluids, the flooding of cavities reduces markedly the probability of finding an unflooded cavity of the size  $r_{c,tan}$  corresponding to the minimum

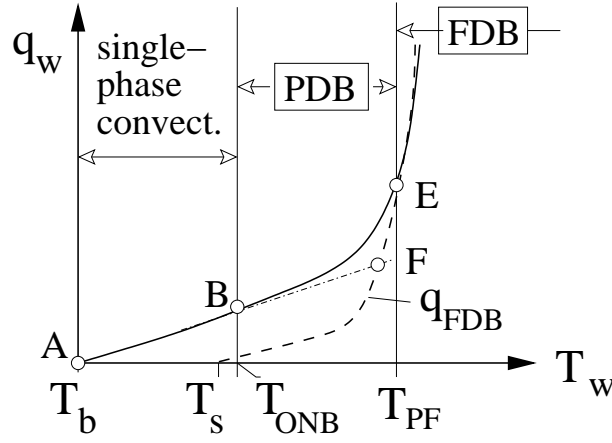


Figure 3.4: Location of the transition from partially developed boiling (PDB) to fully developed boiling (FDB).

superheat criterion, as shown in Figure 3.3b. As a consequence, the minimum superheat criterion (3.9) based on the tangency condition proposed by Hsu in general underpredicts the minimum superheat, which is required for the inception of boiling. In order to account for the wettability of the surface, Basu *et al.* (2002) introduced a correlation for an *effectively* available cavity size, which reads

$$r_{c,eff} = r_{c,tan} \mathcal{F}. \quad (3.11)$$

The correction factor  $\mathcal{F}$  introduced here varies between zero and unity, and is computed as an empirical function of the contact angle  $\beta$ . For increasing wettability associated with  $\beta \rightarrow 0$ , more and more cavities are flooded, and hence  $\mathcal{F} \rightarrow 0$ . The resulting decrease in the effective cavity size consequently leads to higher minimum wall superheats, as seen from the criterion (3.9) when using  $r_{c,eff}$  for the cavity size in the nominator.

Newly developed three-dimensional techniques to measure surface topologies have made it possible to obtain more detailed information on the shape and the distribution of the available cavities. Based on such high-resolution scanning techniques Luke (2004) determined the spatial distribution of cavities on different technical heated surfaces using the so-called envelope method. In this method an envelope area is created by a roller ball of a certain diameter, which is virtually rolled over the measured surface topography. The three nearest contact points of the envelope area and the heated surface beneath always form a cavity, which represents a potential nucleation site. Repeating this method with varying diameters of the virtual roller makes it possible to measure the whole spectrum of cavity sizes on the considered technical surface.

### 3.2.2 Transition from partially developed (PDB) to fully developed boiling (FDB)

For the specification of the condition, where fully developed boiling begins, the model proposed by Bowring (1962) is widely used. As seen from Figure 3.4, this model locates

the beginning of the FDB regime by intersecting the extension of the straight single-phase line (A-B) with the fully developed boiling curve (dashed curve  $q_{FDB}$ ), which majorily depends on the wall superheat  $T_w - T_s$  and only little on the mass flow rate. Multiplying the heat flux at the intersection point “F” by a factor of 1.4 gives then the heat flux at the transition to the FDB region

$$q_{PF} = q_E = 1.4 q_F. \quad (3.12)$$

Shah (1977) assumed the demarcation between PDB and FDB essentially dependent on the subcooling and proposed

$$T_{PF} = T_s + \frac{1}{2} \underbrace{(T_s - T_b)}_{\Delta T_{sub}} \quad (3.13)$$

There is evidently much of arbitrariness involved in (3.12) and (3.13), which has not much impact though. Most of the models proposed for the wall heat flux do not explicitly distinguish between the PDB and the FDB region, as they are in general devised to span both regions.

### 3.3 Models for the wall heat flux

A great variety of wall heat flux models has been developed for a use in engineering applications, and basically all of them adhere to the deterministic approach. The proposed models can be broadly grouped into two categories:

- *General empirical correlations*, which describe the wall heat transfer rates mostly as general power functions of non-dimensional groups.
- *Mechanistic models*, which attempt to capture the basic relevant mechanisms for the total heat flux, i.e., the hydrodynamic convective transport and the thermal heat transport associated with evaporation.

While the first concept relies completely on experimental data in deriving the non-dimensional model correlations, the latter is more analytical in that it accounts explicitly for the different physical mechanisms contributing to the total heat flux. Therefore, the mechanistic models in general perform better in transition regimes, where the relative contribution of the individual mechanisms may change substantially. Despite their more physical basis, the mechanistic models still involve a good deal of empiricism in the modeling of the individual mechanisms.

#### 3.3.1 General empirical correlations

In the FDB region, most empirical correlations model the total heat flux as a power function of the wall superheat

$$q_w = K(T_w - T_s)^m = K\Delta T_{sat}^m \quad (3.14)$$

with  $K$  being some empirically determined model parameter. The correlation proposed by McAdams *et al.* (1949) for water

$$q_w = 4.77 \Delta T_{sat}^{3.86} \quad (3.15)$$

shall be quoted here as a typical representative. Some authors additionally consider the influence of the pressure  $p$ , as it is the case in the correlations due to Thom *et al.* (1965)

$$\Delta T_{sat} = 22.65 q_w^{0.5} \exp\left(\frac{p}{87}\right) \quad (3.16)$$

and Labuntzov (1972)

$$\Delta T_{sat} = \frac{1 - 0.0045 p}{3.4 p^{0.18}} q_w^{2/3} \quad (3.17)$$

with the pressure  $p$  always measured in bars. Another group of models assumes the total wall heat flux in the FDB region as an enhanced convective transfer by multiplying the heat transfer coefficient for forced single-phase convection,  $\alpha_{fc}$ , with some enhancement factor. In the correlation proposed by Shah (1977)

$$q_w = \alpha_{fc} 230 Bo^{0.5} \Delta T_{sat} \quad (3.18)$$

this enhancement factor involves the boiling number

$$Bo = \frac{(q_w / \rho_l h_{lg})}{u_b} \quad (3.19)$$

which relates the contribution of nucleate boiling, represented by the “boiling velocity”  $q_w / \rho_l h_{lg}$ , to the contribution of forced convection, represented by the velocity of the bulk liquid  $u_b$ . In Shah’s approach the forced convection heat transfer coefficient  $\alpha_{fc}$  is computed from the Dittus-Boelter equation

$$Nu_{fc} = \frac{\alpha_{fc} D_h}{\lambda_l} = 0.023 Re_l^{0.8} Pr^{0.4}, \quad (3.20)$$

which represents a well-established correlation for hydraulically and thermally fully developed channel flow. It writes the Nusselt number  $Nu_{fc}$  as a simple power function of the liquid phase Reynolds number  $Re_l = \rho_l u_b D_h / \mu_l$  and Prandtl number  $Pr_l = \mu_l c_{p,l} / \lambda_l$  with  $\mu_l$ ,  $c_{p,l}$ , and  $\lambda_l$  being the dynamic viscosity, the specific heat at constant pressure, and the thermal conductivity of the liquid phase, respectively. The characteristic length scale  $D_h = 4A/U$ , generally termed hydraulic diameter, depends on the cross-sectional area  $A$  and the perimeter  $U$  of the channel.

The approach proposed by Kandlikar (1998*b*) for the FDB region is written as

$$q_w = \alpha_{fc} 1058 F_{fl} Bo^{0.7} \Delta T_{sat}. \quad (3.21)$$

In extension to Shah’s model this correlation introduces a fluid-surface parameter  $F_{fl}$  representing the surface fraction covered by the liquid phase.

Only a few attempts have been made to provide specific correlations for the PDB regime.

This is mainly due to the considerable uncertainty in estimating the upper limit of the PDB regime, beyond which the influence of the bulk flow convection becomes insignificant. The proposed models are mostly devised to assure a smooth transition from the single-phase region to the PDB region, and then to the FDB region. Among these, the correlation suggested by Bergles & Rohsenow (1964) reads

$$q_w = q_{fc} \left\{ 1 + \left[ \frac{q_{FDB}}{q_{fc}} \left( 1 - \frac{q_{ONB}}{q_{FDB}} \right) \right]^2 \right\}^{\frac{1}{2}}. \quad (3.22)$$

Therein, as seen from Figure 3.4,  $q_{fc}$  represents the single-phase convection line A-B-F,  $q_{FDB}$  the fully developed boiling curve F – E, and  $q_{ONB}$  the total wall heat flux at the incipience of boiling located at B. Later Kandlikar (1998b) suggested for the PDB region the equation

$$q_w = a + b(T_w - T_s)^m \quad (3.23)$$

with the model parameters  $a, b$  and  $m$  being defined as functions of  $q_w$  and  $T_w - T_s$  evaluated at the points B, F and E, as shown in Figure 3.4. Aside from these interpolation models, Shah (1977) presented a correlation which fitted best the empirical data base underlying his analysis

$$\Delta T_{sat} = \frac{q_w}{\alpha_{fc} \left( \Psi_0 + \frac{\Delta T_{sub}}{\Delta T_{sat}} \right)} \quad (3.24)$$

with  $\Psi_0$  being a function of the boiling number  $Bo$  defined in (3.19).

Among the empirical correlations which have been developed to cover both the PDB and the FDB region, the approach due to Moles & Shaw (1972) correlates the - relative to the single-phase coefficient  $\alpha_{fc}$  - enhanced two-phase heat transfer coefficient  $\alpha_{tp}$  as

$$\frac{\alpha_{tp}}{\alpha_{fc}} = 78.5 Bo^{0.67} Ja_{sub}^{-0.5} \left( \frac{\rho_v}{\rho_l} \right)^{0.03} Pr^{0.45}. \quad (3.25)$$

This correlation is based on experimental data from 10 different sources including both organic and inorganic liquids. It introduces a modified Jakob number  $Ja_{sub} = c_{p,l} \Delta T_{sub} / h_{lg}$ , where the wall superheat  $\Delta T_{sat}$  has been replaced by  $\Delta T_{sub}$ , to capture effect of subcooling, which is typically very strong in the PDB region. In a later study the model constants in Moles' approach (3.25) were modified by Prodanovic *et al.* (2002) to improve the overall agreement of the model predictions with the data base used in their study.

### 3.3.2 Mechanistic models

The basic strategy of mechanistic models is to identify and to model the essential physical mechanisms which contribute to the total wall heat flux. They mostly assume the heat flux to be composed of three components, namely, the single-phase convection  $q_{fc}$ , the evaporation heat flux needed directly for the phase change  $q_{ev}$ , and the sensible heating of the portion of liquid which fills the volume vacated by a departing or collapsing bubble  $q_{qu}$ . The total wall heat flux can then be written as

$$q_w = q_{fc} + q_{ev} + q_{qu}. \quad (3.26)$$

The forced convection component is commonly obtained as

$$q_{fc} = \alpha_{fc} A_{sp} (T_w - T_b), \quad (3.27)$$

where the heat transfer coefficient  $\alpha_{fc}$  is frequently computed from correlations proposed by Petukhov (1970) and Gnielinski (1976), or simply from the classical textbook correlation by Dittus-Boelter (3.20). The explicit distinction between the area fraction only influenced by single-phase convection,  $A_{sp}$ , and the fraction only influenced by the nucleate bubbles  $A_{nb} = 1 - A_{sp}$  is frequently omitted.

The evaporation heat flux can be basically obtained as

$$q_{ev} = N_a f \frac{d_D^3 \pi}{6} \rho_v h_{lg}, \quad (3.28)$$

where  $N_a$  is the number of the active nucleation sites per unit wall area,  $f$  is the bubble frequency, and  $d_D$  the average bubble diameter at the departure from the heated surface. The frequency  $f$  is mostly computed based on the empirically observed relationship with diameter  $d_D$  raised to the power  $\gamma$  (the empirical exponent  $\gamma$  is of the order of unity)

$$f d_D^\gamma = const. \quad (3.29)$$

leading to correlations such as

$$f = \sqrt{\frac{4}{3} \frac{g(\rho_l - \rho_v)}{d_D \rho_l}}, \quad (3.30)$$

as suggested by Ivey (1967). To date, there is no theoretically based formulation available for the specification of the nucleation site density on technical surfaces. It is generally assumed as a power function of the wall superheat

$$N_a = [m (T_w - T_s)]^n \quad (3.31)$$

involving two empirical constants,  $m$  and  $n$  (Lemmert & Chawla, 1977). Their values are frequently set to  $m = 185$  and  $n = 1.805$  following a proposal by Kurul & Podowski (1990).

It is noted that the explicit modeling of the evaporation heat flux also plays an important role in the two-fluids simulations. They require the specification of source terms for the vapor phase at the superheated walls which is practically equivalent to the modeling of the evaporative heat flux. This is also the reason why the general empirical correlations discussed in the former section are a priori not applicable in two-fluids simulations, as they do not involve any separate modeling of the evaporative heat flux.

The quenching heat flux can be computed based on the transient conduction problem of the heat-up of a semi-infinite liquid adjacent to the heated wall. As shown by Victor *et al.* (1985), the solution of this transient problem finally provides for the quenching heat flux, which is written as

$$q_{qu} = \alpha_{qu} A_{nb} (T_w - T_s), \quad (3.32)$$

the required transfer coefficient

$$\alpha_{qu} = 2 \sqrt{\frac{\lambda_l \rho_l c_{p,l}}{\pi \tau_{qu}}} \tau_{qu} f. \quad (3.33)$$

Therein, the bubble influenced area fraction is computed from

$$A_{nb} = \min(1, KN_a \pi d_D^2 / 4) \quad \text{with} \quad K = 4, \quad (3.34)$$

and the quenching period is assumed as proportional to the inverse of the bubble frequency

$$\tau_{qu} = \frac{C_{qu}}{f} \quad (3.35)$$

with the parameter  $C_{qu}$  ranging from 0.5 to 1. As an alternative to the direct modeling, as given by Eqs.(3.32)-(3.35), Bowring (1962) proposed to compute  $q_{qu}$  from the ratio  $\varepsilon_{qu} = q_{qu}/q_{ev}$  by rewriting Eq.(3.26) as

$$q_w = q_{fc} + q_{ev}(1 + \varepsilon_{qu}). \quad (3.36)$$

Bowring assumed the ratio  $\varepsilon_{qu}$  in dependence of the considered pressure range as

$$\varepsilon_{qu} = \frac{q_{qu}}{q_{ev}} = \begin{cases} 3.2 \frac{\rho_l c_{p,l} \Delta T_{sub}}{\rho_v h_{lg}}, & 1 \leq p \leq 9.5 \\ 2.3, & 9.5 \leq p \leq 50 \\ 2.6, & p > 50 \quad [bars]. \end{cases} \quad (3.37)$$

For low-pressure subcooled flow boiling Hainoun *et al.* (1996) proposed to correlate the ratio  $\varepsilon_{qu}$  as

$$\varepsilon_{qu} = \frac{1}{2 C_{qu}} \left( 1 + \frac{\Delta T_{sub}}{\Delta T_{sat}} \right)^2 - 1 \quad (3.38)$$

with the parameter  $C_{qu}$  being about 0.5.

Most mechanistic models do not account for the quenching heat flux separately. They rather combine the quenching contribution with the evaporation component to one single “pool boiling”, or “nucleate boiling” term,  $q_{nb}$ , such that Eq.(3.26) is rewritten as

$$q_w = q_{fc} + q_{nb}. \quad (3.39)$$

There have been proposed a large number of models falling into this category. In contrast to the boiling number based methods discussed above (Shah, 1977; Kandlikar, 1998b), the distinction between a convective and a nucleate boiling contribution brings about much freedom in selecting an appropriate model for each component. It also provides by definition the right asymptotical behavior when approaching the limits of single-phase convection, where the nucleate boiling composition becomes zero,  $q_{nb} \rightarrow 0$ , as well as the

limit of pool boiling, where the forced convection contribution goes to zero,  $q_{fc} \rightarrow 0$ . The latter limit is particularly troublesome for the boiling number based empirical correlations, because, as seen from its definition in (3.19), the boiling number goes to infinity for vanishing bulk velocity  $u_b \rightarrow 0$ , which makes this type of models incapable to provide a smooth transition from the flow boiling to the pool boiling regime and vice versa. The superposition concept includes further the possibility of a non-linear combination, as suggested first by Kutateladze (1963), who superimposed the individual contributions squared

$$q_w = (q_{fc}^2 + q_{nb}^2)^{\frac{1}{2}}. \quad (3.40)$$

The introduction of this quadratic addition was mainly motivated by the fact, that such a power-additive formulation intrinsically captures the vanishing influence of the forced convection term  $q_{fc}$  in the limit of the fully developed boiling (FDB), as it is indicated by the convergence of the boiling curves in the FDB region in Figure 3.2b. Kutateladze’s quadratic concept was later generalized by Steiner & Taborek (1992). Their approach will be described in more detail later in this section.

One of the simplest methods to compute the nucleate boiling component was proposed by Maroti (1977). Assuming a linear temperature profile in the liquid and the boiling contribution as proportional to the superheated part of the thermal wall layer, he obtained

$$q_{nb} = q_w \left( \frac{\Delta T_{sat}}{\Delta T_{sat} + \Delta T_{sub}} \right)^2. \quad (3.41)$$

Other more sophisticated approaches mostly model  $q_{nb}$  based on correlations (empirical and semi-empirical), which were originally developed for typical pool boiling configurations. Among these, rather than combining the heat fluxes themselves, most approaches superimpose the corresponding heat transfer coefficients to obtain a coefficient for the total wall heat flux. A pioneering superposition model, whose underlying concept is still widely used, was proposed by Chen (1963). Chen defined the total heat flux coefficient as composed of a “macroconvection” coefficient of the two-phase flow and a “microconvection” coefficient associated with nucleate boiling written as

$$\alpha = \alpha_{mac} + \alpha_{mic} = \alpha_l F + \alpha_{nb} S. \quad (3.42)$$

The macroconvection coefficient is obtained from the Dittus-Boelter Eq.(3.20) as

$$\alpha_{mac} = F \alpha_l = \frac{\lambda_l}{D_h} 0.023 \underbrace{F Re_l^{0.8}}_{Re_{tp}^{0.8}} Pr^{0.4} \quad (3.43)$$

involving a two-phase Reynolds number  $Re_{tp}$ . As such, Eq. (3.43) basically represents an extension of the Dittus-Boelter equation from pure liquid-phase to two-phase convective flow, where the factor  $F = (Re_{tp}/Re_l)^{0.8}$  is introduced to account for the enhanced convective heat transport caused by the vapor bubble agitation in terms of a higher, two-phase

Reynolds number. Chen correlated the factor  $F$  as a function of the Martinelli parameter,  $F = \text{fct}(X_{tt})$ , which by its definition

$$X_{tt} = \left( \frac{1-x}{x} \right)^{0.9} \left( \frac{\rho_v}{\rho_l} \right)^{0.5} \left( \frac{\mu_l}{\mu_v} \right)^{0.1} \quad (3.44)$$

strongly varies with the vapor mass fraction  $x$ . The microconvection coefficient is obtained from the Forster and Zuber correlation (Forster & Zuber, 1955)

$$\alpha_{nb} = 0.00122 \frac{\lambda_l^{0.79} c_{p,l}^{0.45} \rho_l^{0.49}}{\sigma^{0.5} \mu_l^{0.29} h_{lg}^{0.24} \rho_v^{0.24}} \Delta T_{sat}^{0.25} \Delta p_{sat}^{0.75}, \quad (3.45)$$

where  $\Delta p_{sat}$  denotes the saturation pressure difference corresponding to the wall superheat

$$\Delta p_s = p_s(T_w) - p_s(T_s).$$

The introduction of the suppression factor  $S$  is needed in (3.42) to reflect the observed decrease in the nucleate boiling with increasing flow rates. Chen correlated  $S$  as an empirical function of the two-phase flow Reynolds number  $Re_{tp}$ . In later work Butterworth (1979) provided the following best-fit functions for both factors  $F(X_{tt})$  and  $S(Re_{tp})$ :

$$x > 0.1 : F = 2.35 \left( \frac{1}{X_{tt}} + 0.213 \right)^{0.736}, \quad (3.46)$$

$$x \leq 0.1 : F = 1,$$

$$S = \frac{1}{1 + 2.53 \cdot 10^{-6} Re_{tp}^{1.17}}. \quad (3.47)$$

Gungor & Winterton (1986) modified Chen's approach including also the boiling number in the enhancement factor, which reads

$$F = 1 + 24000 Bo^{1.16} + 1.37 X_{tt}^{-0.86}, \quad (3.48)$$

and rewriting  $S$  as

$$S = \frac{1}{1 + 1.15 \cdot 10^{-6} F^2 Re_l^{1.17}}. \quad (3.49)$$

For the computation of the nucleate boiling coefficient they suggested Cooper's method (Cooper, 1984)

$$\alpha_{nb} = 55 q_{nb}^{0.67} p_r^{(0.12 - 0.2 \log_{10} R_a)} (-\log_{10} p_r)^{-0.55} M^{-0.5} \quad (3.50)$$

involving the reduced pressure  $p_r = p/p_{crit}$  with the critical pressure  $p_{crit}$ .  $R_a$  is the average roughness height in  $\mu m$  (DIN 4762), and  $M$  is the molecular weight in  $g/mol$ .

Especially at higher heat fluxes and moderate mass flow rates, it was generally observed that the Chen-type simple additive composition using a function for  $S$  in the form (3.47) or (3.49) does not suppress sufficiently the nucleate boiling component. The resulting

overpredictions for the total heat flux motivated Liu & Winterton (1991) to adopt Kutateladze's power-additive concept (Kutateladze, 1963) instead of a simple linear addition. They proposed a quadratic superposition for the total heat flux coefficient written as

$$\alpha = [(\alpha_l F)^2 + (\alpha_{nb} S)^2]^{\frac{1}{2}}, \quad (3.51)$$

which provides - relative to a simple linear addition - further suppression once the convective component  $\alpha_l F$  is appreciably larger than  $\alpha_{nb} S$ . The nucleate pool boiling heat transfer coefficient  $\alpha_{nb}$  is again obtained with Cooper's method (Cooper, 1984), which is modified by the suppression factor written as

$$S = \frac{1}{1 + 0.055 \cdot F^{0.1} Re_l^{0.16}}. \quad (3.52)$$

The convection enhancement factor correlated as

$$F = \left[ 1 + x Pr_l \left( \frac{\rho_l}{\rho_v} - 1 \right) \right]^{0.35} \quad (3.53)$$

depends on the vapor mass fraction, the density ratio, as well as the liquid phase Prandtl number. While Liu and Winterton proposed the addition of the squares of the two heat transfer coefficients, Steiner & Taborek (1992) introduced a more general power-additive formulation concerning the choice of the exponent. They proposed

$$\alpha = [(\alpha_l F)^n + (\alpha_{nb} F_{nb})^n]^{\frac{1}{n}}, \quad (3.54)$$

where a regression analysis of the data base available to the authors gave the best agreement for the exponent  $n \approx 3$ .  $F$  represents again a convection enhancement factor associated with two-phase flow. The factor  $F_{nb}$  compensates for the differences between pool and flow boiling. However, contrarily to the Chen-type models as well as to the quadratic approach by Liu and Winterton shown above in Eq. (3.51), the factor  $F_{nb}$  in (3.54) does not account for any flow-induced suppression of nucleate boiling. Questioning the relevance of a suppression of nucleate boiling with increasing flow rate, Steiner and Taborek correlate the factor  $F_{nb}$  including only the parameters pressure, heat flux, tube diameter, surface roughness, and molecular weight. As such,  $F_{nb}$  does not depend on the flow rate. The nucleate pool boiling coefficient  $\alpha_{nb}$  is modeled using Gorenflo's method (Gorenflo, 1988):

$$\alpha_{nb} = \alpha_{nb,0} F_{pn} \left( \frac{q_{nb}}{q_{nb,0}} \right)^m \left( \frac{R_a}{R_{a,0}} \right)^{0.133}. \quad (3.55)$$

Herein,  $\alpha_{nb,0}$  denotes a reference pool boiling heat transfer coefficient obtained for a certain reference heat flux  $q_{nb,0}$  and wall roughness  $R_{a,0}$ . Gorenflo recommended to estimate the reference value  $\alpha_{nb,0}$  with the method proposed by Stephan & Abdelsalam (1980). The parameters  $F_{pn}$  and  $m$  are modeled as empirical functions of the reduced pressure  $p_r$ . As for the choice of the exponent  $n$ , which determines the power-addition in Eq.(3.54), it should be noted that for increasing values of  $n > 1$  the power-additive formulation inherently gives more weight to the convective heat transfer at low superheats, where

$\alpha_l \gg \alpha_{nb}$ , while it gives more weight to the nucleate boiling at high superheats, where  $\alpha_{nb} \gg \alpha_l$ . This asymptotic weighting, which becomes more and more pronounced as the value of the exponent  $n$  is chosen higher, is attractive especially in the FDB region. Since it intrinsically produces converging flow boiling curves with increasing superheat, it nicely reflects the vanishing influence of the mass flow rate on the total heat flux, as it is observed in the FDB region.

Both concepts, the Chen-type simple linear addition as well as the power-additive combination have become well-established mechanistic approaches for the modeling of subcooled boiling flow. Their application in the CFD of coolant flows in engineering devices is rather limited though. This is largely due to modeling of the suppression factor, which is generally written in the form

$$S = (1 + a \cdot F^m Re_l^n)^{-1}, \quad (3.56)$$

as it has been shown above by the correlations (3.47) and (3.52). In addition to the drawback that this formulation tends to give insufficient suppression at moderate flow rates combined with higher heat fluxes, the dependence on the bulk flow Reynolds number is troublesome to CFD for mainly two reasons. First, especially in CFD of geometrically complex flow configurations it is practically not possible to define a Reynolds number based on bulk flow conditions in a meaningful way. Second, the suppression is basically a local effect, it should therefore be modeled dependent of local flow quantities, which may be readily provided by the CFD solution. A modeling solely based on bulk flow quantities is certainly not appropriate. These obvious deficiencies motivated Kobor (2003) to develop a Chen-type model using an alternative correlation for the flow-induced suppression. He proposed a model, termed Boiling Departure Lift-off (BDL) model, which considers the dynamic effect of the near-wall flow field on the bubble detachment from the heated surface. The BDL model utilizes a bubble departure model proposed first by Zeng *et al.* (1993), who distinguish three stages of detachment, as shown in Figure 3.5. A balance of the flow forces acting on the bubble at the instant of departure (stage I), including the drag force  $F_d$ , the shear-lift force  $F_{sl}$ , the buoyancy  $F_{bcy}$ , and the bubble-growth force  $F_{du}$ , as shown in Figure 3.6, is solved for the corresponding bubble departure diameter  $d_D$ . Solving analogously the force balance for the sliding bubble immediately before lift-off (stage III) provides the corresponding bubble lift-off diameter  $d_L$ . The ratio of these two characteristic diameters is then used to measure the suppression factor

$$S_{flow} = (d_D/d_L)^\Phi \quad (3.57)$$

with the exponent  $\Phi$  being a model constant of the order of unity. The BDL model was originally calibrated and validated for the boiling of liquid coolants used in internal combustion engines. Steiner *et al.* (2005) extended the BDL model to the boiling of pure water. They introduced an additional suppression factor for the nucleate pool boiling component to capture explicitly the influence of subcooling. This further modification is based on the concept of the so-called extrapolated thermal wall-layer thickness, which was suggested in an experimental study on subcooled pool boiling by Wiebe & Judd (1971), and is schematically shown in Figure 3.7. The ratio of the effective superheated wall layer

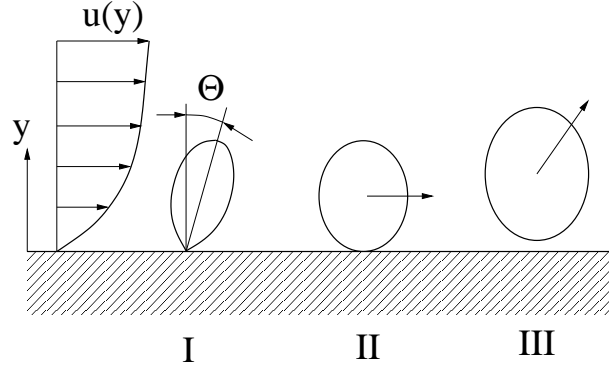


Figure 3.5: Three stages of a vapor bubble departing from the heated surface: I, inclined bubble at the instant of departure from the nucleation site; II, sliding bubble; III, instant of lift-off.

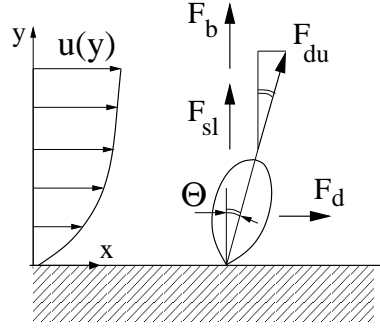


Figure 3.6: Forces acting on a vapor bubble at the instant of departure from its nucleation site.

thickness  $\delta_{th}^e$  to the extrapolated thickness  $\delta_{th}$  is used to measure the effect of subcooling, and the corresponding correction factor is written as

$$S_{sub} = \frac{T_w - T_s}{T_w - T_b}. \quad (3.58)$$

Modeling the total suppression

$$S = S_{flow} S_{sub} \quad (3.59)$$

dependent of the degree of subcooling and the dynamic flow forces acting on the bubbles, the BDL approach can be certainly regarded as physically better grounded than the solely bulk flow quantities dependent correlations of the type (3.56). The model, however, clearly reaches its limits in the FDB regime at high superheats, where the underlying single-bubble concept shown in Figure 3.5 becomes more questionable the more bubble-bubble interaction comes into play. Since the model requires only local input quantities, which are generally known in conventional CFD of convective flows, it is also well applicable in numerical simulations of geometrically complex coolant flows. The BDL approach has already been implemented in commercial software, where it exhibited a good predictive capability as well as high robustness in various simulations of liquid coolant jackets in automotive applications.

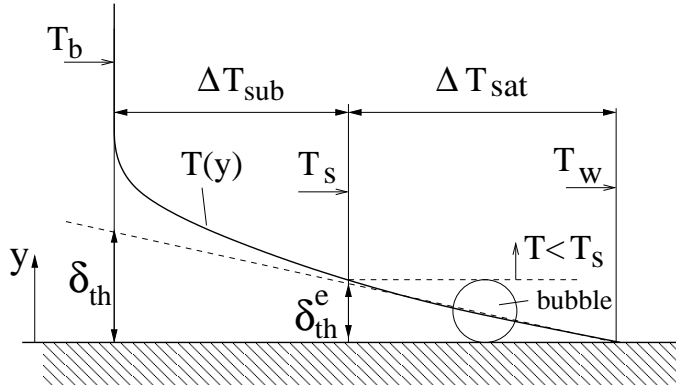


Figure 3.7: Superheated thermal boundary layer in subcooled boiling.

The BDL model was basically devised for subcooled boiling flow conditions, where the vapor bubbles typically collapse immediately after their lift-off from the heated surface. The vapor phase practically resides only inside a very thin superheated layer next to the heated wall, while the remaining part of the flow region is occupied by the liquid phase only. Due to the absence of the vapor phase in the most part of the domain, the flow is considered as single-phase flow, and all dynamical effects of the bubbles on the liquid carrier phase are neglected by the model. As such, the BDL approach clearly falls into the category of flow boiling models for use in single-fluid simulations omitting the influence of the bubbles on the near-wall motion of the liquid phase, which was observed in experiments (Maurus, 2003; Ramstorfer *et al.*, 2005). In order to account for the dynamical effects of the bubbles, thereby still remaining within the framework of a single-fluid formulation, the BDL model was further developed by introducing a bubble-equivalent wall roughness (Ramstorfer *et al.*, 2005). Substituting this “artificial” roughness, which is modeled as dependent of the bubble departure diameter and the nucleate boiling activity, into standard near-wall functions for turbulent flows, the modified model is capable to reflect the experimentally observed main effects associated with the presence of the vapor bubbles at the wall, such as a retarded flow into the streamwise direction, as well as an enhanced level of turbulence. It is certainly the most attractive feature of the modified BDL model that it captures to a certain extent the near-wall characteristics of a bubble-laden flow, while the simplifying assumption of single-phase flow can still be upheld. Besides the more realistic prediction for the near-wall flow field, the predicted increase in the near-wall turbulence associated with the bubble-equivalent roughness also enhances the convective turbulent heat transfer from the wall to the core flow region. The so enhanced transmission of convective heat through the superheated wall layer avoids the unphysical heat-up of the first wall cells, which may otherwise arise in the single-fluid simulation, as the total heat flux from the solid wall boundary becomes very high. As a result, no unrealistically high temperatures inside the first wall cells are obtained. The predicted temperature field is not only more realistic, the more uniform temperature distribution near the superheated wall is also favorable for the stability of numerical solution.

### 3.3.3 Accuracy limiting effects in technical flows

In general, the models proposed for the wall heat flux in nucleate boiling flow are calibrated and validated for very specific conditions concerning working fluid, material and surface quality of the heater, as well as flow configuration. As such, the models, be they empirical or mechanistic, involve correlations and parameter settings, which are typically based on laboratory experiments using purified, degassed liquids, clean homogeneous surfaces with a specified finish and a defined, uniformly heated area. The employed experimental set-ups mostly embody closed-loop channel flow configurations with the test sections being square ducts heated from beneath, or co-annular, in general vertically oriented pipes, where the inner pipe is heated from inside. Conducting the boiling flow experiments on such particular set-ups gives a rather limited scope to the measured data, and hence to the nucleate boiling models based on these data, as well. Moreover, despite the higher effort generally made in the design of the test facilities and the experimental procedure compared to single-phase flow investigations to ensure reproducible results, there remain various highly complex phenomena, which are mostly not considered, but can bias the experimental results markedly. Some of these effects, particularly those related to surface characteristics such as wettability or surface microstructure, cannot be quantified or may not even be fully understood yet. It is therefore often very hard if not impossible to control these effects during the measurements, and the obtained data may vary considerably under otherwise the same imposed conditions.

Both issues, the uncertainty associated with unconsidered but eventually very relevant effects, as well as the limited scope of the model coefficients obtained from the underlying laboratory experiments, may severely constrain the applicability of the models, especially, when considering real-life conditions in engineering problems. It has become best practice to extend the available well-established standard approaches to these engineering problems using specially adapted model coefficients and/or introducing additional parameters to capture effects of particular importance for the actually considered case. Several of these effects shall be briefly discussed in the following.

#### *Multi-component composition of the working fluid*

The boiling of multi-component mixtures can be strongly affected by binary diffusion as well as differing volatilities of the individual components. The latter leads to an enrichment of the vapor/liquid interface with the less volatile component such that the local mixture at the interface has a higher saturation temperature,  $T_{s,int} > T_s$ , and the evaporation rate decreases. This effect is typically accounted for by incorporating a diffusion-induced suppression factor  $F_D$  into model correlations which were originally derived for pure liquids. For mixtures of acetone, isopropanol and water, Wenzel & Müller-Steinhagen (1994) proposed

$$F_D = \frac{\alpha_{nb}}{\alpha_{nb,mix}} = \frac{1}{1 + \frac{\alpha_{nb,mix}}{q_{nb}} (T_{s,int} - T_s)}, \quad (3.60)$$

where the heat transfer coefficient of the mixture is computed from the sum of the inverse of the heat transfer coefficients of the individual components,  $i = 1, \dots, n$ , weighted with their molar fractions  $X_i$

$$\alpha_{nb,mix} = \left( \sum_{i=1}^n \frac{X_i}{\alpha_{nb,i}} \right)^{-1}.$$

Wenzel & Müller-Steinhagen substituted  $F_D$  obtained from (3.60) as an additional suppression factor of the nucleate boiling contribution into Chen's superposition approach (3.42), which they adopted as base model. In an analogous way, Kandlikar (1998a) extended his boiling number based single-component correlation (3.21) by a diffusion-induced suppression factor to cover binary mixtures as well.

### *Microgeometry of the heated surface*

The microgeometry of technical surfaces is generally described in terms of surface roughness, which is mostly expressed as an average roughness height  $R_a$  given in  $\mu m$ . Being a rather crude measure,  $R_a$  certainly does not represent the effectively boiling relevant microgeometry, which may be constituted by many different types of geometry elements such as plateaus, peaks, valleys, cavities, etc.. It is generally accepted that only those surface elements can act as stable bubble generating centers (active nucleation sites), which are not completely filled with liquid after bubble departure. Therefore, an increase in the average surface roughness may lead to an increase in the boiling heat transfer, only if the higher roughness is associated with additional active and stable nucleation sites. Numerous - mostly pool boiling - experiments have investigated this effect. They turned out that the heat transfer rate in general rises as the surface roughness is increased. The quantitative extent, however, strongly depends on the considered surface quality. The variation of surface roughness affects the nucleate boiling heat transfer most pronouncedly when considering high quality finished surfaces, where the average roughness is of the order of  $R_a \approx 1 \mu m$  and lower (Corty & Foust, 1955; Kurihara & Myers, 1960; Berenson, 1962). For surfaces without a special high quality finish (polishing, lapping), where  $R_a > 1 \mu m$ , the increase of the boiling heat transfer rates with increasing surface roughness is less pronounced.

The microstructure of the superficial layer of the heater plays an important role in the case of the so-called enhanced surfaces. Depending on their fabrication, these specially designed surfaces may be structured (Memory *et al.*, 1995; Kim & Choi, 2001), e.g. with microfins, with pores connected by subsurface gaps, or unstructured such as porous coatings (Afgan *et al.*, 1985; Rainey *et al.*, 2001; Kim *et al.*, 2002; Rainey *et al.*, 2003). Using enhanced surfaces in general provides a higher number of active nucleation sites which leads to lower minimum wall superheats required for the onset of nucleate boiling (ONB). Beyond the ONB, mostly higher boiling heat transfer rates are observed as compared to the unmodified smooth surfaces. The intensified boiling activity is commonly explained by the hypothesis that on enhanced surfaces the bubble nucleation occurs predominantly in subsurface, hence higher superheated, microchannel-like dendritic cavities, which are also

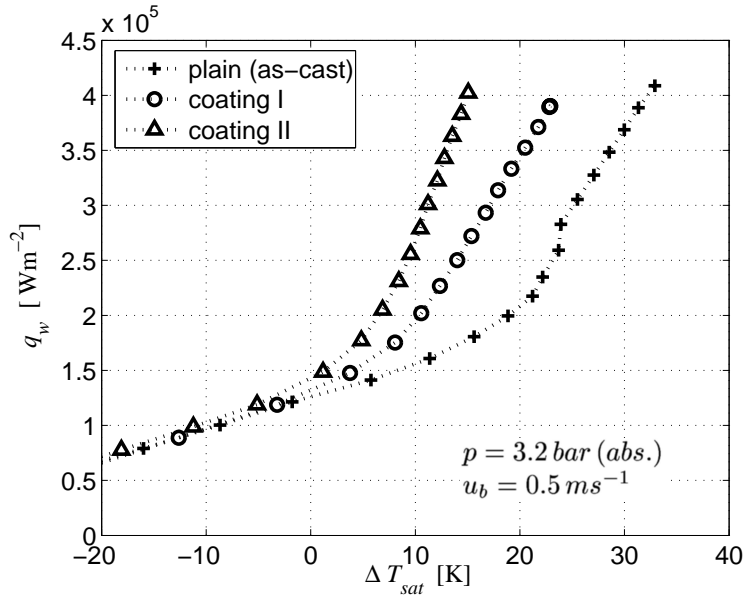


Figure 3.8: Flow boiling curves of a 60/40Vol% mixture of water and ethylene-glycol from a plain cast iron surface and two coated surfaces. The subcooling and the velocity of the bulk liquid are always  $\Delta T_{sub} = T_s - T_b = 43\text{ K}$  and  $u_b = 0.5\text{ m s}^{-1}$ , respectively (from Ramstorfer *et al.* (2006)).

more likely to entrap a gaseous rest after bubble departure than the superficial cavities on the unmodified surfaces. The potential of this concept to enhance the boiling activity is exemplarily shown in Figure 3.8, where the flow boiling heat flux from a plain as-cast iron surface is compared against those from two porously coated surfaces. The first type of coating (“coating I”) is fabricated by sintering a highly porous layer of iron particles on the cast-iron ground body. The second type of coating (“coating II”) is produced by spraying melted mild steel on the ground surface. The shown flow boiling curves are taken from the experiments carried out by Ramstorfer *et al.* (2006) using a 60/40Vol% mixture of water and ethylene-glycol as working fluid. The comparison of the individual flow boiling curves turns out significantly higher boiling heat transfer rates for the coated surfaces, which can be clearly observed from the markedly reduced wall superheats ranging up to 15K. It is interesting to note that coating I performs best although its porosity is much lower than that of coating II. This can be attributed to the particular microstructure of the coating I. The coating I is not a typical granular-porous nor a channel-porous layer, as it consists for the most part of a solid metallic base matrix, which is penetrated by a few, but comparatively deep cavities. These deep cavities are evidently most capable to entrap vapor, hence, to act as bubble nucleation centers, as it was also observed by Qi *et al.* (2004).

#### *Thermophysical properties of the heated surface*

Due to the spatial discreteness of the active nucleation sites being the centers of bubble

generation, the local heat transfer rates as well as the local temperatures may strongly vary on the heated surface. As this spatial non-uniformity leads to a redistribution of heat between the active boiling centers and the free non-boiling surface, the thermal conductivity of the surface may affect the heat transfer rates considerably. A low thermal conductivity impedes the conductive redistribution of local heat fluxes between the free surface and the surface covered by active centers, and the temperature of the free surface will rise as the heat flux increases, which implies a decreasing heat transfer coefficient (HTC). However, this reduction in the HTC with increasing heat flux has only to be expected, if the low-conductive surface is very smooth providing only a small number of potential nucleation sites. If sufficient potential nucleation sites are available, e.g. on rough or enhanced surfaces, the increase in the temperature of the free surface due to the low conductive redistribution of heat tends to activate further nucleation sites, which finally leads to a decrease in the surface temperature, such that the HTC increases as the heat flux increases. For a thermally high-conductive surface the redistributive transport supplies more heat to the active bubble generating centers lowering at the same time the temperature of the free surface as the heat flux increases, such that the HTC becomes higher. The decrease/increase in the HTC with increasing heat flux was illustrated by Piro *et al.* (2004) comparing experimental data obtained for nucleate boiling on smooth plastic and on smooth copper.

### *Interfacial properties*

The strong influence of the interfacial properties such as surface tension and contact angle can be demonstrated very clearly on the basis of the effect of surfactants. Since surface active substances by definition determine the interfacial physical properties between the liquid, the vapor, and the solid heater phase, they strongly influence the activation/deactivation of the nucleation sites on the heated surface. Their high potential to alter significantly the boiling behavior was highlighted by Hetsroni *et al.* (2001) for pool boiling of water with additions of the surfactant Habon G. As it is seen from Figure 3.9, for increasing Habon G concentrations the boiling heat transfer is enhanced to such an extent that the resulting wall superheats  $\Delta T_{sat}$  are reduced by more than 10 K. Within a certain range of the wall heat fluxes the superheat  $\Delta T_{sat}$  becomes even non-monotonous with respect to  $q_w$ . Sher & Hetsroni (2002) successfully modeled this non-monotonous (S-shaped) trend in the boiling curves by deriving analytical expressions for the liquid-vapor and the liquid-solid surface tensions,  $\sigma_{lg}$  and  $\sigma_{ls}$ , respectively, and for the contact angle  $\beta$  as functions of the wall heat flux. They incorporated those analytical expressions for  $\sigma_{lg}$  and  $\beta$  into the classical nucleate boiling correlation of Rohsenow (1952)

$$\frac{c_{p,l}(T_w - T_s)}{h_{lg}} = \beta C_{sf} \left[ \frac{q_w}{\mu_l h_{lg}} \sqrt{\sigma_{lg} g(\rho_l - \rho_g)} \right]^{0.33} \left( \frac{c_{p,l} \mu_l}{\lambda_l} \right)^n, \quad (3.61)$$

which predicts then fairly accurate the non-monotonous curves observed in the experiments (see Figure 3.9). The modeling strategy is here evidently again to adopt a well-established standard approach, to introduce an additional parameter (here being  $\beta$ ) accounting for a problem-specific effect, and to determine a best-fitting set of model coeffi-

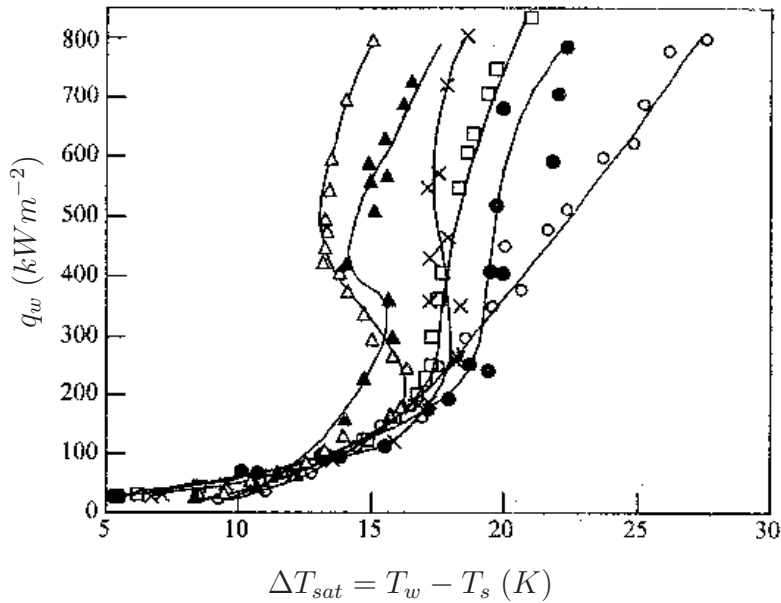


Figure 3.9: Boiling curves of water and water with Habon G addition in different concentrations:  $\circ$  - water,  $\bullet$  - 65 ppm,  $\square$  - 130 ppm,  $\times$  - 260 ppm,  $\blacktriangle$  - 530 ppm,  $\triangle$  - 1060 ppm, (from Hetsroni *et al.* (2001)).

cients from a validation against experimental data.

### *Aging*

Aging is a phenomenon which may strongly affect the long-term activity of the nucleation sites on the heated surface. It therefore represents a great challenge and persistent source of inaccuracy for all boiling models. Due to its potential influence on the liquid-vapor-solid interfacial interactions at the nucleation sites, it may be highly relevant for the entire boiling process starting from the onset of nucleate boiling (ONB). Aging assumes the gradual, mostly slow changes of the working fluid, as well as those of the heated surface, which in general lead to less favorable conditions for the incipience of nucleate boiling. As such, aging is a process acting over long time scales, which is manifested in a steady decrease in the boiling heat transfer rate observed during long periods of operation time (weeks or months). Especially under technical flow conditions, it is often impossible to clearly identify and eventually eliminate all the relevant causes for aging. It can have many - single or multiple - causes, such as a continuous flooding of cavities, depositions on the surface, corrosion and/or mechanical erosion of the surface material, chemical reactions in the liquid phase, etc.. The quantitative impact of aging can be exemplarily seen from Figure 3.10 showing the case of nucleate boiling of an automotive coolant liquid. The series of boiling curves presented herein is taken from measurements by Kobor (2003), who investigated nucleate boiling flow of a mixture of ethylene-glycol and water on an as-cast aluminium surface, which resembles the conditions commonly met in cooling jackets of modern internal combustion engines. The shown curves were

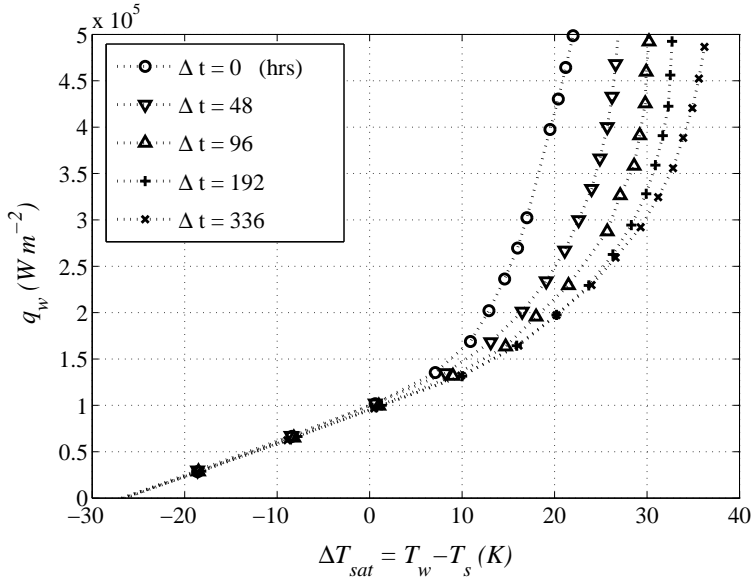


Figure 3.10: Boiling curves of a 50/50Vol% mixture water and ethylene-glycol. The subcooling and the velocity of the bulk liquid are always  $\Delta T_{sub} = T_s - T_b = 25 K$  and  $u_b = 1 ms^{-1}$ , respectively (from Kobor (2003)).

measured over a period of two weeks. The temperature, pressure and velocity of the bulk liquid were always kept the same. Within the considered range of wall heat fluxes, the first and the last curve differ up to  $15K$  in wall superheat  $\Delta T_{sat}$ . It could be shown that the aging effect observed here is partly caused by a continuous flooding of the cavities on the surface, which reduces the number of active nucleation sites. The other part could be attributed to depositions on the heated surface originating from the employed coolant liquid. The significant shift in the boiling curves exemplarily shown here strongly suggests that the aging conditions of the heated surface and the working fluid should not be overlooked in the interpretation of boiling flow measurements and in the specification of the model parameters based on such data.

### *Orientation of the heated surface*

Since nucleate boiling by nature involves the motion of a low-density vapor phase in a high-density liquid carrier phase, the dynamics in the thermal boundary layer may be strongly influenced by the buoyancy forces, especially at low flow rates of the bulk liquid. In such a case the orientation of the superheated surface relative to the gravitational direction is of major importance. This aspect is mostly ignored by the nucleate boiling models though. Klausner *et al.* (2003) investigated the influence of buoyancy in much detail experimentally as well as computationally. They operated their experimental facility with the perfluorocarbon liquid FC-87 varying the streamwise inclination angle of the heated surface from  $0^\circ$  to  $360^\circ$ . Their subcooled boiling flow experiments were specially focussed on the effect of the orientation on the bubble lift-off diameters, which they found out to be mainly dependent on two non-dimensional groups, the Jakob number and a flow

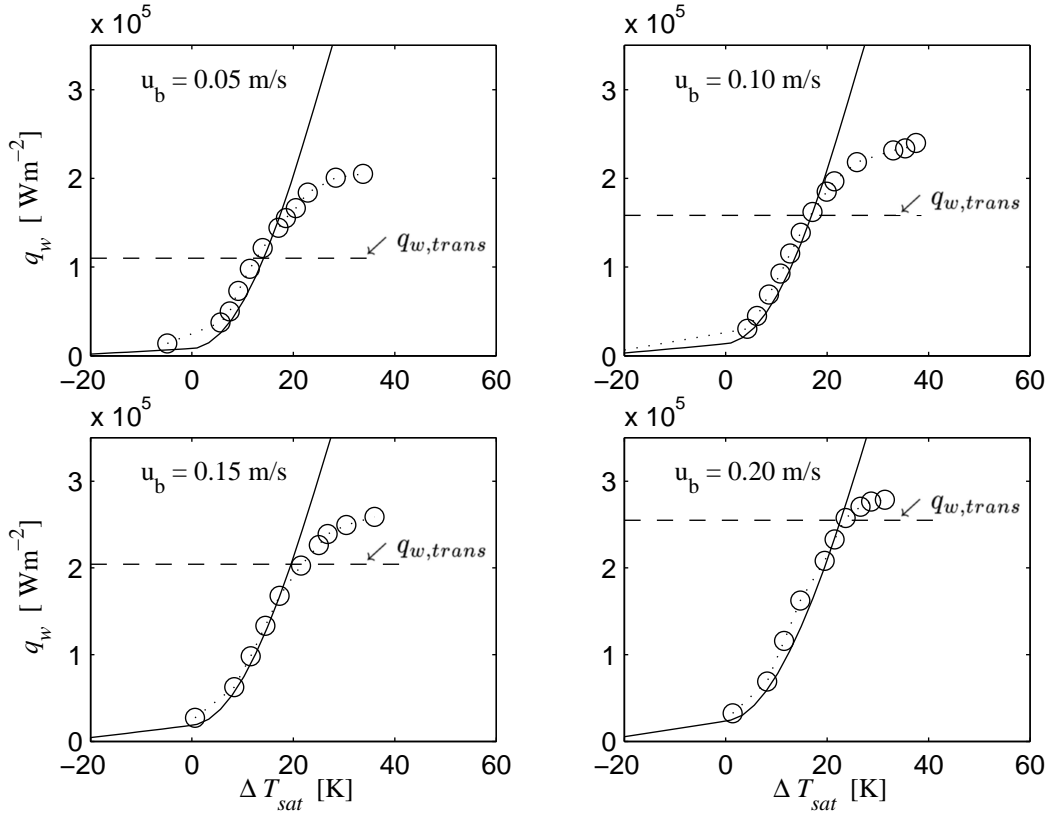


Figure 3.11: Flow boiling curves of a 50/50Vol% mixture of water and ethylene-glycol on a downward facing heated surface at different velocities of the bulk flow  $u_b$ . The open rings, 'o', denote the experiments, the solid lines, '—', denote the predictions of the BDL model, the dashed lines, '- -', denote the wall heat flux, where the formation of vapor films sets in. The subcooling is always  $\Delta T_{sub} = T_s - T_b = 25 \text{ K}$ ; (from Breitschädel & Steiner (2006)).

rate parameter,

$$Ja = \frac{\rho_l c_{p,l} (T_w - T_{sat})}{\rho_v h_{lg}} \quad \text{and} \quad \Psi = \frac{u_b \mu_l}{\sigma} \frac{\rho_l}{\rho_l - \rho_v},$$

respectively. The non-dimensionalized representation of all their experimental data points in the  $(Ja, \Psi)$ -plane finally yielded a two-parametric demarcation correlation  $\mathcal{F}(\Psi, Ja) = 0$  separating the orientation dependent/independent flow regime. Furthermore, they observed in their experiments that the critical heat flux, where film boiling sets in, was reduced by almost an order of magnitude for a certain inclination at low flow rates. Roughly the same extent of reduction in the critical heat flux was measured by Kim *et al.* (2005) for saturated pool boiling with water at atmospheric pressure, when they compared an upward against downward facing heated surface. While Klausner *et al.* (2003) were mainly interested in the influence of the surface orientation on the dynamics of the bubble departure, Breitschädel & Steiner (2006) investigated the impact on the boiling curves. Figure 3.11 shows experimental results measured with a downward facing heated surface, where a transition from nucleate boiling to partial film boiling was observed by

the authors. Exceeding a certain value of the wall heat flux, denoted here by  $q_{w,trans}$ , the wall superheats  $\Delta T_{sat} = T_w - T_s$  turn to increase much faster than below this limit, which indicates the formation of vapor films on the heated surface. The predictions of the BDL model also shown in the figure strongly deviate from the measurements in this region. At the onset of partial film boiling the BDL approach clearly reaches its limit, as it has to be expected for any wall heat flux model which has been developed for the nucleate boiling regime. The strong flow rate dependence of the critical limit can be seen from Figure 3.11, as well. At the lower bulk velocities presented herein, the transitional limits  $q_{w,trans}$  drop down to a level which is an order of magnitude lower than the critical heat flux in the corresponding pool boiling case on an upward facing surface. The quantitative extent of this reduction is well in line with the findings of Klausner *et al.* (2003) and Kim *et al.* (2005) mentioned above. As one might expect, once the buoyancy force acts rather to keep the vapor bubbles near the superheated wall than to drive them away from it, bubble agglomeration and finally the formation of continuous vapor films occur already at comparatively low wall heat fluxes. The agglomeration of the vapor phase is no local phenomenon, because it is strongly influenced by the conditions upstream. It is therefore hardly possible to model this effect only dependent of local input parameters. Since there are no approaches or model extensions available to capture this orientation-dependent transition to partial film boiling accurately, it basically represents a critical upper limit to the state-of-the-art nucleate boiling models. Wherever the buoyancy forces are directed towards the superheated wall, the relevance of this limit should be examined. A demarcation correlation similar to that introduced by Klausner *et al.* (2003),  $\mathcal{F}(\Psi, Ja) = 0$ , may serve here as an useful criterion.

### 3.4 Concluding remarks

Since boiling flow represents an important mechanism of heat transfer in many technical devices, a large number of different approaches have been proposed to model this phenomenon, and they are still being further developed. The present survey can clearly not cover all of them, but it intends to outline some basic modeling concepts, which have become well-established methods in the design and development of heating and cooling systems.

In summary, one can say that given all the progress which has been made in the past and will expectedly be made in the future, the modeling of boiling flow will keep relying on a great deal of empiricism. This is specially true in boiling flow on technical surfaces, which mostly involves a number of effects, whose determining parameters are difficult to obtain and therefore remain unknown. The situation can even be worse if no parameters can be specified to measure a certain effect appropriately. The so-called aging of the heated surface and of the liquid falls into this category, because there exists no reliable measure for this typical long-term phenomenon. Since the knowledge about the basic mechanisms and the relevant parameters determining the aging process is vague and very limited, this issue is mostly spared in the conventional modeling. Basically the same applies to effects associated with the microstructure of the surface, such as the topology, or the porosity of the surface, which have not been accessed by a rigorous modeling yet.

There is evidently much room for the further development of nucleate boiling models, be

it improvements in defining relevant - accessible - parameters, or be it - for an application in the farther future - the development of novel, more general concepts such as the nonlinear chaotic approach.

As it was pointed out in a comprehensive assessment of available nucleate boiling models by Piro *et al.* (2004), the state-of-the-art modeling of the wall heat flux basically offers two choices. The first is to use a very general approach involving only a few model coefficients, which do not vary from case to case. The second is to forgo a most complete parameterization to capture all the relevant effects, but rather to introduce a set of tunable model coefficients, which have to be adapted in dependence of the actually considered surface/liquid combination. While the first concept provides models which are applicable to a wide range of different conditions, the latter yields more accurate predictions. This higher accuracy is, however, only achievable within a very limited range of conditions, for which the model coefficients have been specially adapted. The user has evidently to choose between a good general applicability and a highest possible accuracy.

## 4 Conclusions

The present review is intended to survey the present status and to comment on crucial aspects in the computation and modeling of two groups of highly complex flows found in many technical devices involving conversion and/or transmission of energy. Both problems, the simulation of turbulent non-premixed combustion as well as the computation of subcooled boiling flow, represent typical cases, where a full numerical resolution of all relevant effects exceeds by far the available computational capacities. In technical flow, this limitation will apply also in the foreseeable future, even if Moore's law (Moore, 1965), saying that the computer power increases exponentially with time, is expected to continue. The steady increase of computer power makes it certainly possible to tackle problems with higher complexity and larger physical size, such as complete jet flames using multi-step chemistry. This was impressively demonstrated in large DNS of diffusion flames (Mizobuchi *et al.*, 2002; Pantano, 2004). In addition to the outstandingly high computational costs of such direct simulations, the large mesh-size with hundreds of millions of grid points also raises the issue of handling the huge amount of data, especially concerning their storage and postprocessing. From a scientific point of view these big computations are certainly very important and insightful, as they extend our understanding of the basic mechanisms acting on the smallest scales, from which greatly benefits the modeling as well. Nonetheless, the largest and most complex problems which have been computed with DNS thus far, are still strongly simplified as compared the real-life applications. In the case of technical combustion almost always liquid fuel is used such as gasoline, diesel and jet fuel, which are injected into combustors with fairly complex geometry, while the simulations mostly consider gaseous fuels to circumvent the additional complexity of liquid break-up and evaporation associated with liquid fuels. The current state-of-the-art of the direct numerical simulations of subcooled boiling flow is certainly less advanced than in the case of combustion. Aside from the simulation of the nucleate boiling from one single or a few discrete nucleation sites, no DNS has been carried out for nucleate boiling flow from a real technical surface. Hence, Moore's law will not spare us from modeling also in the foreseeable future.

As for the simulation of non-premixed combustion, the computers as well as the models have become mature, powerful tools in the modern design of combustion devices. The further development of the proposed models is today strongly challenged by the tighter emission limits which require the use of more detailed chemical kinetics as well as an accurate prediction of local extinction and re-ignition phenomena to describe realistically the formation of intermediate and product species. The upcoming of the method of LES made here certainly important advancements possible, as it captures the instantaneous mixing of the reactants providing invaluable input into the combustion models. A wider use of comprehensive, multi-parametric flame models in LES is however still limited due to the method's substantial computational costs and its higher difficulty of use in CFD of technical flows. Aside from that it is not generally agreed how many and which parameters are needed to describe a real turbulent non-equilibrium flame. An important aspect on this question is that the multi-parametric flames models may be basically more accurate as compared to simpler, e.g., one-parametric, approaches, but they always in-

involve additional unclosed expressions whose closure introduces further assumptions and uncertainty. The computational feasibility of the coupling between the multi-parametric combustion models with the solution procedure for the underlying turbulent flow field is another important issue which must not be overlooked as well.

The considerable accuracy of the phenomenological expressions for the elementary chemical reaction rates assures a high level of description for the chemical kinetics, which is a prerequisite for a reliable modeling of combustion. The level of description of the mechanisms behind subcooled boiling is much lower. Many effects are not fully understood, vaguely described by empirical parameters, or even not amenable to a stringent parameterization. This uncertainty introduces much empiricism into the model correlations, and accurate predictions in general require a well adapted set of empirical parameters. The lack of detailed knowledge about the mechanisms associated with the bubble nucleation on a heated surface, together with the difficulty to model strong dynamic interactions between the vapor and the liquid phase in a two-fluids simulation, represent certainly the major stumbling blocks for further advancements in the simulation of subcooled boiling flows.

Given the considerable progress which has certainly been made in our capacity to compute the highly complex phenomena of turbulent non-premixed combustion and nucleate boiling flow, our understanding of the basic mechanisms behind these phenomena is still far from complete though. Detailed experimental as well as numerical investigations are needed to bring light to the small-scale characteristics related to the local instantaneous flame structure or the process of micro-bubble nucleation. Among the well-established methods to compute turbulent flow, LES will certainly profit most from Moore's law, as with increasing computational power a higher numerical resolution becomes possible, such that a more complete and accurate information from the resolved scales is available for use as input to the modeling of unresolved subgrid-scale effects.

## References

- AFGAN, N. H., JOVIC, L. A., KOVALEV, S. A. & LENYKOV, V. A. 1985 Boiling heat transfer from surfaces with porous layers. *Int. J. Heat Mass Transfer* **28**, 415–422.
- BARLOW, R. S. & FRANK, J. H. 1998 Effect of turbulence on species mass fractions in methane/air flames. In *Twenty-Seventh Symposium (Int.) on Combustion (Proc.)*, pp. 1087–1095. The Combustion Institute, Pittsburgh, PA.
- BARTHS, H., PETERS, N., BREHM, N., MACK, A., PFITZNER, M. & SMILJANOSVSKI, V. 1998 Simulation of pollutant formation in a gas turbine combustor using unsteady flamelets. In *Twenty-Seventh Symposium (Int.) on Combustion (Proc.)*, pp. 1841–1847. The Combustion Institute, Pittsburgh, PA.
- BASU, N., WARRIER, G. R. & DHIR, V. K. 2002 Onset of nucleate boiling and active nucleation site density during subcooled boiling flow. *ASME J. Heat Transfer* **124**, 717–728.
- BERENSON, P. J. 1962 Experiments on pool boiling heat transfer. *Int. J. Heat Mass Transfer* **5**, 985–999.
- BERGLES, A. E. & ROHSENOW, W. M. 1964 The determination of forced convective surface boiling heat transfer. *ASME J. Heat Transfer* **86**, 365–372.
- BILGER, R. W. 1993a Conditional moment closure for turbulent reacting flows. *Phys. Fluids* **A5**, 436–444.
- BILGER, R. W. 1993b Conditional moment closure modelling and advanced laser measurements. In *Turbulence and Molecular Processes in Combustion* (ed. T. Takeno). Elsevier Science Publishers.
- BORGHI, R. 1974 Chemical reactions calculations in turbulent flows: application to a CO-containing turbojet plume. *Advances in Geophysics* **18B**, 349–365.
- BORGHI, R. 1988 Turbulent combustion modeling. *Prog. Energy Combust. Sci.* **14**, 245–292.
- BOWRING, W. R. 1962 Physical model of bubble detachment and void volume in subcooled boiling. OECD Halden Reactor Project Report No. HPR-10.
- BRANLEY, N. & JONES, W. P. 2001 Large eddy simulation of a turbulent non-premixed flame. *Combust. Flame* **127**, 1914–1934.
- BREITSCHÄDEL, B. & STEINER, H. 2006 Analyse der Wärmeübergangs beim unterkühlten Strömungssieden an metallischen Oberflächen. Report vif-AB-026/2006, The "Virtual Vehicle" Competence Center, Graz.
- BREUER, M. 2002 Direkte Numerische Simulation und Large-Eddy Simulation turbulenter Strömungen auf Hochleistungsrechnern. Habilitation, Universität Erlangen-Nürnberg.

- BUSHE, W. K. & STEINER, H. 1999 Conditional moment closure for large eddy simulation of non-premixed turbulent reacting flows. *Phys. Fluids* **11**, 1896–1906.
- BUSHE, W. K. & STEINER, H. 2003 Laminar flamelet decomposition for conditional source-term estimation. *Phys. Fluids* **15**, 1564–1575.
- BUTTERWORTH, D. 1979 The correlation of cross flow pressure drop data by means of a permeability concept. UKAEA Report AERE-R9435.
- CALHOON, W. H. & MENON, S. 1996 Subgrid modeling for reacting large eddy simulations. AIAA Paper 96-0516.
- CHA, C. M., KOSÁLY, G. & PITSCH, H. 2001 Modeling of extinction and reignition in turbulent nonpremixed combustion using a double-conditional moment closure approach. *Phys. Fluids* **13**, 3824–3834.
- CHEN, J. C. 1963 A correlation for boiling heat transfer to saturated fluid in convective flow. ASME Paper 63-HT-34.
- CHEN, J. H., MAHALINGAM, S., PURI, I. K. & VERVISCH, L. 1992 Effect of finite rate chemistry and unequal Schmidt on turbulent nonpremixed flames modeled with single-step chemistry. In *Proceedings of 1992 Summer Programm*, pp. 367–387. Center for Turbulence Research, NASA Ames/Stanford University.
- CLEARY, M. J., KENT, J. H. & BILGER, B. W. 2002 Prediction of carbon monoxide in fires by conditional moment closure. In *Twenty-Ninth Symposium (Int.) on Combustion (Proc.)*, pp. 273–279. The Combustion Institute, Pittsburgh, PA.
- COELHO, P. J. & PETERS, N. 2001 Numerical simulation of a mild combustion burner. *Combust. Flame* **124**, 503–518.
- COLUCCI, P. J., JABERI, F. A., GIVI, P. & POPE, S. B. 1998 Filtered density function for large eddy simulation of turbulent reacting flows. *Phys. Fluids* **10**, 499–515.
- COOK, A. W. & RILEY, J. J. 1994 A subgrid model for equilibrium chemistry in turbulent flows. *Phys. Fluids* **6**, 2868–2870.
- COOK, A. W. & RILEY, J. J. 1998 Subgrid-scale modeling for turbulent reacting flows. *Combust. Flame* **112**, 593–606.
- COOK, A. W., RILEY, J. J. & KOSÁLY, G. 1997 A laminar flamelet approach to subgrid-scale chemistry in turbulent flows. *Combust. Flame* **109**, 332–341.
- COOPER, M. G. 1984 Heat flow rates in saturated nucleate pool boiling - a wide ranging examination using reduced properties. *Advances in Heat Transfer* **16**, 157–239.
- CORTY, C. & FOUST, A. S. 1955 Surface variables in nucleate boiling. *Chem. Eng. Progress Symp. Ser.* **51**, 1–12.

- DE BRUYN KOPS, S., RILEY, J., KOSÁLY, G. & COOK, A. 1998 Investigation of modeling for non-premixed turbulent combustion. *Flow Turbulence Comb.* **60**, 105–122.
- DESJARDIN, P. E. & FRANKEL, S. H. 1996 Assessment of turbulent combustion sub-models using the linear eddy model. *Combust. Flame* **104**, 343–357.
- FORSTER, H. K. & ZUBER, N. 1955 Dynamics of vapor bubbles and boiling heat transfer. *AIChE J.* **1**, 531–535.
- GAO, F. & O'BRIEN, E. E. 1993 A large-eddy simulation scheme for turbulent reacting flows. *Phys. Fluids* **5**, 1282–1284.
- GERMANO, M., PIOMELLI, U., MOIN, P. & CABOT, W. H. 1991 A dynamic subgrid-scale eddy viscosity model. *Phys. Fluids A* **3**, 1760–1765.
- GHOSAL, S. & MOIN, P. 1995 The basic equations of large eddy simulation of turbulent flows in complex geometry. *J. Comp. Phys.* **118**, 22–37.
- GIRIMAJI, S. & ZHOU, Y. 1996 Analysis and modeling of subgrid scalar mixing using numerical data. *Phys. Fluids* **8**, 1224–1236.
- GNIELINSKI, V. 1976 New equations for heat and mass transfer in turbulent pipe and channel flow. *Int. Chem. Eng.* **16**, 359–368.
- GORENFLO, D. 1988 *Behältersieden*, in: VDI Wärmeatlas, Sec. *Ha*. VDI Verlag, Düsseldorf.
- GUNGOR, K. E. & WINTERTON, R. H. S. 1986 A general correlation for flow boiling in tubes and annuli. *Int. J. Heat Mass Transfer* **29**, 351–358.
- HAINOUN, A., HICKEN, E. & WOLTERS, J. 1996 Modeling of void formation in the subcooled boiling regime in the ATHLET code to simulate flow instability for research reactors. *Nucl. Eng. Design* **167**, 175–191.
- HETSRONI, G., ZAKIN, J. L., LIN, Z., MOSYAK, A., PANCALLO, E. A. & ROZENBLIT, R. 2001 The effect of surfactants on bubble growth, wall thermal patterns and heat transfer in pool boiling. *Int. J. Heat Mass Transfer* **44**, 485–497.
- HSU, Y. Y. 1962 On the size range of active nucleation cavities on a heating surface. *ASME J. Heat Transfer* **84**, 207–216.
- IVEY, H. J. 1967 Relationships between bubble frequency, departure diameter, and rise velocity in nucleate boiling. *Int. J. Heat Mass Transfer* **10**, 1023–1040.
- JABERI, F. A. & JAMES, S. 1998 A dynamic similarity model for large eddy simulation of turbulent combustion. *Phys. Fluids* **10**, 1775–1777.

- JIMÉNEZ, J., LINÁN, A., ROGERS, M. M. & HIGUERA, F. J. 1997 A priori testing of subgrid models for chemically reacting non-premixed turbulent shear flow. *J. Fluid Mech.* **349**, 149–171.
- KANDLIKAR, S. G. 1998a Boiling heat transfer with binary mixtures: Part II - Flow boiling in plain tubes. *ASME J. Heat Transfer* **120**, 388–394.
- KANDLIKAR, S. G. 1998b Heat transfer characteristics in partial boiling, fully developed boiling, and significant void flow regions of subcooled flow boiling. *ASME J. Heat Transfer* **120**, 395–401.
- KERSTEIN, A. R. 1988 A linear-eddy model of turbulent scalar transport and mixing. *Combust. Sci. and Techn.* **60**, 391–421.
- KERSTEIN, A. R. 1992a Linear-eddy modelling of turbulent transport. Part 4. Structure of diffusion flames. *Combust. Sci. and Techn.* **81**, 75–96.
- KERSTEIN, A. R. 1992b Linear-eddy modelling of turbulent transport. Part 7. Finite-rate chemistry and multi-stream mixing. *J. Fluid Mech.* **240**, 289–313.
- KIM, J. H., RAINEY, K. N., YOU, S. M. & PAK, J. Y. 2002 Mechanism of nucleate boiling heat transfer from microporous surfaces in saturated FC-72. *ASME J. Heat Transfer* **124**, 500–506.
- KIM, N.-H. & CHOI, K.-K. 2001 Nucleate pool boiling on structured enhanced tubes having pores with connecting gaps. *Int. J. Heat Mass Transfer* **44**, 17–28.
- KIM, W. T. & HUH, K. Y. 2002 Use of the conditional moment closure model to predict NO formation in a turbulent CH<sub>4</sub>/H<sub>2</sub> flame over a bluff-body. *Combust. Flame* **130**, 94–111.
- KIM, Y. H., KIM, S. J., KIM, J. J., NOH, S. W., SUH, K. Y., REMPE, J. L., CHEUNG, F. B. & KIM, S. B. 2005 Visualization of boiling phenomena in inclined rectangular gap. *Int. J. Multiphase Flow* **31**, 618–642.
- KLAUSNER, J. F., BOWER, J. S. & SATHYANARAYAN, S. 2003 Development of advanced gravity-independent high heat flux phase-change heat exchanger technology and design. Final Report Grant No. NAG3-2593.
- KLIMENKO, A. Y. 1990 Multicomponent diffusion of various admixtures in turbulent flow. *Fluid Dynamics* **25**, 327–334.
- KLIMENKO, A. Y. & BILGER, R. W. 1999 Conditional moment closure for turbulent combustion. *Prog. Energy Combust. Sci.* **25**, 595–687.
- KLIMENKO, A. Y. & POPE, S. B. 2003 The modeling of turbulent reactive flows based on multiple mapping conditioning. *Phys. Fluids* **15**, 1907–1925.

- KOBOR, A. 2003 Entwicklung eines Siedemodells für die Simulation des kühlmittelseitigen Wärmeübergangs bei Verbrennungskraftmaschinen. Doctoral thesis, Technische Universität Graz.
- KONČAR, B., KLJENAK, I. & MAVKO, B. 2004 Modelling of local two-phase flow parameters in upward subcooled flow boiling at low pressure. *Int. J. Heat Mass Transfer* **47**, 1499–1513.
- KRONENBURG, A. 2004 Double conditioning of reactive scalar transport equations in turbulent nonpremixed flames. *Phys. Fluids* **16**, 2640–2648.
- KRONENBURG, A., BILGER, R. W. & KENT, J. H. 1998 Second-order conditional moment closure for turbulent jet diffusion flames. In *Twenty-Seventh Symposium (Int.) on Combustion (Proc.)*, pp. 1097–1104. The Combustion Institute, Pittsburgh, PA.
- KURIHARA, H. M. & MYERS, J. E. 1960 The effect of superheat and surface roughness on boiling coefficients. *J. AIChE* **6**, 83–86.
- KURUL, N. & PODOWSKI, M. Z. 1990 Multidimensional effects in forced convection subcooled boiling. In *Ninth International Heat Transfer Conference (Proc.)*, pp. 21–26. Jerusalem, Israel.
- KUTATELADZE, S. S. 1963 *Fundamentals of heat transfer*. Edward Arnold, London.
- LABUNTZOV, D. 1972 Heat transfer problems with nucleate boiling in liquids. *Thermal Eng.* **9**, 21–28.
- LEMMERT, M. & CHAWLA, J. M. 1977 *Influence of flow velocity on surface boiling heat transfer coefficient*, in: E. Hahne, U. Grigull (eds.), *Heat Transfer in Boiling*. Academic Press.
- LESIEUR, M. & MÉTAIS, O. 1996 New trends in large-eddy simulations of turbulence. *Ann. Rev. Fluid Mech.* **28**, 45–82.
- LIBBY, P. A. & WILLIAMS, F. A. 1994 *Turbulent Reacting Flows*. Academic Press.
- LIU, Z. & WINTERTON, R. H. S. 1991 A general correlation for saturated and subcooled flow boiling in tubes and annuli based on a nucleate boiling equation. *Int. J. Heat Mass Transfer* **34**, 2759–2766.
- LUKE, A. 2004 Active and potential bubble nucleation sites on different structured heated surfaces. *Chem. Eng. Res. Design* **82**, 462–470.
- MAROTI, L. 1977 Axial distribution of void fraction in subcooled boiling. *Nuclear Technology* **34**, 8–17.
- MAURUS, R. 2003 Bestimmung des Blasenverhaltens beim unterkühlten Strömungssieden mit der digitalen Bildfolgenanalyse. Doctoral thesis, Technische Universität München.

- MCADAMS, W., KENNEL, W., MINDEN, C., CARL, R., PICORNELL, P. & DEW, J. 1949 Heat transfer at high rates to water with surface boiling. *Ind. Eng. Chem.* **41**, 1945–1953.
- MEI, R., CHEN, W. & KLAUSNER, J. 1995a Vapour bubble growth in heterogeneous boiling. I. Formulation. *Int. J. Heat Mass Transfer* **38**, 909–919.
- MEI, R., CHEN, W. & KLAUSNER, J. 1995b Vapour bubble growth in heterogeneous boiling. II. Growth rate and thermal fields. *Int. J. Heat Mass Transfer* **38**, 921–934.
- MEMORY, S. B., SUGIYAMA, D. C. & MARTO, P. J. 1995 Nucleate pool boiling of R-114 and R-114-oil mixtures from smooth and enhanced surfaces - I. Single tubes. *Int. J. Heat Mass Transfer* **38**, 1347–1361.
- MENEVEAU, C. & KATZ, J. 2000 Scale-invariance and turbulence models for large-eddy simulations. *Ann. Rev. Fluid Mech.* **32**, 1–32.
- MIZOBUCHI, Y., TACHIBANA, S., SHINJO, J., OGAWA, S. & TAKENO, T. 2002 A numerical analysis of the structure of a turbulent hydrogen jet lifted flame. In *Twenty-Ninth Symposium (Int.) on Combustion (Proc.)*, pp. 2009–2015. The Combustion Institute, Pittsburgh, PA.
- MOIN, P. 1997 Progress in large eddy simulation of turbulent flows. AIAA Paper 97-0749.
- MOIN, P., SQUIRES, K. D., CABOT, W. & LEE, S. 1991 A dynamic subgrid-scale model for compressible turbulence and scalar transport. *Phys. Fluids A* **3**, 2746–2757.
- MOLES, F. & SHAW, J. 1972 Boiling heat transfer in subcooled liquids under condition of forced convection. *Trans. Int. Chem. Eng.* **50**, 76–84.
- MOORE, G. E. 1965 Cramming more components onto integrated circuits. *Electronics* **38**.
- MOSDORF, R. & SHOJI, M. 2004 Chaos in nucleate boiling - nonlinear analysis and modelling. *Int. J. Heat Mass Transfer* **47**, 1515–1524.
- PANTANO, C. 2004 Direct simulation of non-premixed flame extinction in a methane-air jet with reduced chemistry. *J. Fluid Mech.* **514**, 231–270.
- PETERS, N. 1984 Laminar diffusion flamelet models. *Prog. Energy Combust. Sci.* **10**, 319–339.
- PETERS, N. 2000 *Turbulent Combustion*. Cambridge University Press.
- PETUKHOV, S. B. 1970 *Advances in Heat Transfer*, pp. 503–564. Academic Press.
- PIERCE, C. D. & MOIN, P. 1998 A dynamic model for the subgrid-scale variance and dissipation rate of a conserved scalar. *Phys. Fluids* **10**, 3041–3044.

- PIERCE, C. D. & MOIN, P. 2004 Progress-variable approach for large-eddy simulation of non-premixed combustion. *J. Fluid Mech.* **504**, 73–97.
- PIORO, I. L., ROHSENOW, W. & DOERFFER, S. S. 2004 Nucleate pool-boiling heat transfer: II. assessment of prediction methods. *Int. J. Heat Mass Transfer* **47**, 5045–5057.
- PITSCH, H. & STEINER, H. 2000a Large-eddy simulation of a turbulent methane/air diffusion flame. *Phys. Fluids* **12**, 2541–2554.
- PITSCH, H. & STEINER, H. 2000b Scalar mixing and dissipation rate in large-eddy simulations of non-premixed turbulent combustion. In *Twenty-Eighth Symposium (Int.) on Combustion (Proc.)*, pp. 41–49. The Combustion Institute, Pittsburgh, PA.
- POPE, S. B. 1985 Pdf methods for turbulent reactive flows. *Prog. Energy Combust. Sci.* **11**, 119–192.
- POPE, S. B. 2000 *Turbulent Flows*. Cambridge University Press.
- PRODANOVIC, V., FRASER, D. & SALCUDEAN, M. 2002 On the transition from partial to fully developed subcooled boiling flow. *Int. J. Heat Mass Transfer* **45**, 4727–4738.
- QI, Y., KLAUSNER, J. F. & MEI, R. 2004 Role of surface structure in heterogeneous nucleation. *Int. J. Heat Mass Transfer* **47**, 3097–3107.
- RAINEY, K. N., LI, G. & YOU, S. M. 2001 Flow boiling heat transfer from plain and microporous coated surfaces in subcooled fc-72. *ASME J. Heat Transfer* **123**, 918–925.
- RAINEY, K. N., YOU, S. M. & LI, G. 2003 Effect of pressure, subcooling and dissolved gas on pool boiling heat transfer from microporous surfaces in FC-72. *ASME J. Heat Transfer* **125**, 75–83.
- RAMSTORFER, F., BREITSCHÄDEL, B., STEINER, H. & BRENN, G. 2005 Modeling of the near-wall velocity field of the liquid in subcooled boiling flow. In *ASME International Heat Transfer Conference (Proc.) July 17<sup>th</sup> – 22<sup>th</sup>*, 2005. San Francisco, USA.
- RAMSTORFER, F., STEINER, H., BRENN, G., KORMANN, C. & RAMMER, F. 2006 Subcooled boiling flow heat transfer from plain and enhanced surfaces in automotive applications. *submitted to ASME J. Heat Transfer* .
- RÉVEILLON, J. & VERVISCH, L. 1998 Subgrid-scale turbulent micromixing: dynamic approach. *AIAA J.* **36**, 336–341.
- ROGALLO, R. S. & MOIN, P. 1984 Numerical simulation of turbulent flows. *Ann. Rev. Fluid Mech.* **16**, 99–137.
- ROHSENOW, W. M. 1952 A method of correlating heat transfer data for surface boiling of liquids. *ASME Trans.* **74**, 969–976.
- ROOMINA, M. R. & BILGER, B. W. 2001 Conditional moment closure (CMC) predictions for a turbulent methane-air jet flame. *Combust. Flame* **125**, 1176–1195.

- SAGAUT, P. 2001 *Large Eddy Simulation for Incompressible Flows*. Springer.
- SHAH, M. M. 1977 A general correlation for heat transfer during subcooled boiling in pipes and annuli. *ASHRAE Trans.* **83**, Part I, 205–217.
- SHER, I. & HETSRONI, G. 2002 An analytical model for nucleate pool boiling with surfactant additives. *Int. J. Multiphase Flow* **28**, 699–706.
- SHIN, S., ABDEL-KHALIK, S. & JURIC, D. 2005 Direct three-dimensional numerical simulation of nucleate boiling using the level contour reconstruction method. *Int. J. Multiphase Flow* **31**, 1231–1242.
- SHOJI, M. 2004 Studies of boiling chaos: a review. *Int. J. Heat Mass Transfer* **47**, 1105–1128.
- SMAGORINSKY, J. 1963 General circulation experiments with the primitive equations. I. The basic experiment. *Mon. Weather Rev.* **91**, 99–165.
- SRIPAKAGORN, P., MITARAI, S., KOSÁLY, G. & PITSCH, H. 2004 Extinction and reignition in a diffusion flame: a direct numerical simulation study. *J. Fluid Mech.* **518**, 231–259.
- STEINER, D. & TABOREK, J. 1992 Flow boiling heat transfer in vertical tubes correlated by an asymptotic model. *Heat Transfer Eng.* **13**, 43–69.
- STEINER, H. & BUSHE, K. W. 2001 Large eddy simulation of a turbulent reacting jet with conditional source-term estimation. *Phys. Fluids* **13**, 754–769.
- STEINER, H., KOBOR, A. & GEBHARD, L. 2005 A wall heat transfer model for subcooled boiling flow. *Int. J. Heat Mass Transfer* **48**, 4161–4173.
- STEPHAN, K. & ABDELSALAM, M. 1980 Heat transfer correlations for natural convection boiling. *Int. J. Heat Mass Transfer* **23**, 73–80.
- THOM, J., WALKER, W., FALLON, T. & REISING, G. 1965 Boiling in subcooled water during flow up heated tubes or annuli. Proc. Inst. Mech. Eng., Manchester, UK.
- VASILYEV, O. V., LUND, T. S. & MOIN, P. 1998 A general class of commutative filters for LES in complex geometries. *J. Comp. Phys.* **146**, 82–104.
- VERVISCH, L. 1992 Study and modeling of finite rate chemistry effects in turbulent nonpremixed flames. Annual Research Briefs, Center for Turbulence Research, NASA Ames/Stanford University.
- VEYNANTE, D. & VERVISCH, L. 2002 Turbulent combustion modeling. *Prog. Energy Combust. Sci.* **28**, 193–266.
- VICTOR, H., DELVALLE, M. & KENNING, D. B. R. 1985 Subcooled flow boiling at high heat flux. *Int. J. Heat Mass Transfer* **28**, 1907–1920.

- WENZEL, U. & MÜLLER-STEINHAGEN, H. 1994 Heat transfer to mixtures of acetone, isopropanol and water under subcooled flow boiling conditions - II. Prediction of heat transfer coefficients. *Int. J. Heat Mass Transfer* **33**, 185–194.
- WIEBE, J. R. & JUDD, R. L. 1971 Superheat layer thickness measurements in saturated and subcooled nucleate boiling. *ASME J. Heat Transfer* **93**, 455–461.
- WILLIAMS, F. A. 1991 in: *Reduced kinetic mechanisms and asymptotic approximations in methane-air flames*. Chapter 4. Overview of asymptotics for methane flames. Smooke M. D. (Ed.) , pp. 68–85. Springer, New York.
- WU, X. & SQUIRES, K. D. 1997 Large eddy simulation of an equilibrium three-dimensional boundary layer. *AIAA J.* **35**, 67–74.
- WU, X. & SQUIRES, K. D. 1998 Prediction of the three-dimensional turbulent boundary layer over a swept bump. *AIAA J.* **36**, 505–514.
- XU, J. L., WONG, T. N. & HUANG, X. Y. 2005 Two-fluid modeling for low pressure subcooled flow boiling. *Int. J. Heat Mass Transfer* **49**, 377–386.
- YANG, K. S. & FERZIGER, J. H. 1993 Large-eddy simulation of turbulent obstacle flow using a dynamic subgrid-scale model. *AIAA J.* **31**, 1406–1413.
- ZANG, Y., STREET, R. L. & KOSEFF, J. R. 1993 A dynamic mixed subgrid-scale model and its application to turbulent recirculating flows. *Phys. Fluids A* **5**, 3186–3196.
- ZENG, L. Z., KLAUSNER, J. F., BERNHARD, D. M. & MEI, R. 1993 A unified model for the prediction of bubble detachment diameters in boiling systems - II. Flow boiling. *Int. J. Heat Mass Transfer* **36**, 2271–2279.
- ZHAO, H. & VOKE, P. R. 1996 A dynamic subgrid-scale model for low-Reynolds-number channel flow. *Int. J. Numer. Meth. Fluids* **23**, 19–27.

## Appendix-Papers

- P 1 W. K. BUSHE & H. STEINER 1999 Conditional Moment Closure for Large Eddy Simulation of non-premixed turbulent reacting flows. *Phys. Fluids* **11**, 1896–1906.
- P 2 H. PITSCH & H. STEINER 2000 Large-eddy simulation of a turbulent methane/air diffusion flame. *Phys. Fluids* **12**, 2541–2554.
- P 3 H. PITSCH & H. STEINER 2000 Scalar mixing and dissipation rate in large-eddy simulations of non-premixed turbulent combustion. In *Twenty-Eighth Symposium (Int.) on Combustion (Proc.)*, pp. 41–49, The Combustion Institute, Pittsburgh, PA.
- P 4 H. STEINER & W. K. BUSHE 2001 Large eddy simulation of a turbulent reacting jet with conditional source-term estimation. *Phys. Fluids* **13**, 754–769.
- P 5 W. K. BUSHE & H. STEINER 2003 Laminar flamelet decomposition for conditional source-term estimation *Phys. Fluids* **15**, 1564–1575.
- P 6 H. STEINER, A. KOBOR & L. GEBHARD 2005 A wall heat transfer model for subcooled boiling flow. *Int. J. Heat Mass Transfer* **48**, 4161–4173.
- P 7 F. RAMSTORFER, B. BREITSCHÄDEL, H. STEINER & G. BRENN 2005 Modeling of the near-wall velocity field of the liquid in subcooled boiling flow. In *ASME International Heat Transfer Conference (Proc.)*, July 17<sup>th</sup> – 22<sup>th</sup>, 2005, San Francisco, USA.

P 1

W. K. BUSHE & H. STEINER

Conditional Moment Closure for Large Eddy Simulation of  
non-premixed turbulent reacting flows

*Phys. Fluids* **11** (1999), 1896–1906

# Conditional moment closure for large eddy simulation of nonpremixed turbulent reacting flows

W. Kendal Bushe<sup>a)</sup> and Helfried Steiner

Center for Turbulence Research, Stanford University, Stanford, California 94305-3030

(Received 31 August 1998; accepted 10 March 1999)

A method for closing the chemical source terms in the filtered governing equations of motion is proposed. Conditional filtered means of quantities appearing in the chemical reaction rate expressions are approximated by assuming that these conditional filtered means are constant for some ensemble of points in the resolved flow field; for such an ensemble, integral equations can be solved for the conditional filtered means. These conditional filtered means are then used to approximate the conditional filtered mean of the chemical source term by invoking the Conditional Moment Closure hypothesis. The filtered means of the chemical source terms are obtained by integrating their conditional filtered means over the filtered density function of the conditioning variable(s). The method is applied to direct numerical simulation results to directly compare the prediction of the reaction rates with the actual filtered reaction rates. The results of this *a priori* test appear to show that the method is capable of predicting the filtered reaction rates with adequate accuracy—even in the presence of heat release, and local extinction phenomena. This is especially true for predictions obtained using two conditioning variables. © 1999 American Institute of Physics. [S1070-6631(99)00607-8]

## I. INTRODUCTION

The potential application of large-eddy simulation (LES) concepts to turbulent reacting flows is currently receiving considerable attention. Many turbulent reacting flows of interest involve significant transient effects which cannot be modeled using conventional Reynolds averaging approaches. Indeed, the transient behavior is frequently the behavior of the greatest interest. The LES approach is one which promises to shed light on such processes.

In LES, the governing equations are spatially filtered such that the unsteady flow at scales greater than the filtering length scale is resolved, but the transport and dissipation at scales smaller than this scale is modeled. For a detailed discussion of LES, the reader is directed to the reviews of Lesieur and Métais<sup>1</sup> and Moin.<sup>2</sup>

Applying a filter to the energy and scalar transport equations results in several unclosed terms which must be modeled. Closure for terms involving mixing and transport at small scales have been proposed and tested;<sup>3-9</sup> these typically derive from assumptions similar in form to those made in closing the viscous terms in the momentum equation. Closure for the filtered chemical source term has proven to be more difficult. Several approaches have been proposed, largely based on models which were originally proposed for Reynolds averaged modeling. This paper will address methods applicable to the nonpremixed regime of combustion, in which the fuel and oxidizer streams are initially separated and must mix together before they can react.

There are several different closure approaches currently

receiving attention. In fast chemistry,<sup>10</sup> the closure problem is circumvented by assuming that the chemical reaction rates are infinitely fast; the thermodynamic state and chemical composition can then be completely determined as functions of one conserved scalar, the “mixture fraction.” While this approximation is valid for many flames of interest, it cannot be used to predict such fundamentally important phenomena as pollutant formation, extinction, and ignition.

In laminar flamelet approaches,<sup>11,12</sup> the typical length scale of the region in which chemical reaction takes place (the thickness of the “reaction zone”) is assumed to be smaller than the smallest length scale of turbulence. In this regime, the flame can be treated as an ensemble of strained laminar flames. The laminar flamelet approach should only be used for flames which lie in the “flamelet regime.” There is considerable argument as to just how limiting this restriction will be, and it is not known just how inaccurate the approach would be if used for flames not in the “flamelet regime.”

In PDF methods,<sup>7,13</sup> rather than solving transport equations for the filtered mass fractions, energy, etc., one solves a transport equation for filtered joint probability density function of these quantities; the chemical source term in that equation is closed. As the chemical kinetic mechanism becomes more complicated—involving more species—the number of dimensions in which the transport equation must be solved increases, making solution increasingly expensive. Solution of the equation generally requires the use of Monte Carlo type methods. Furthermore, while the need for closure of the chemical source term is eliminated by solving in the hyperdimensional probability space, the closure problem has effectively been commuted to the molecular mixing term, which is unclosed in the PDF transport equation. This draw-

<sup>a)</sup> Author to whom correspondence should be addressed. Electronic mail: wkb@leland.stanford.edu; Tel: 650-725-6635; Fax: 650-723-9617.

back is somewhat offset by the fact that conventional flow solvers also must provide models for scalar transport in LES.

Another approach to circumventing the closure problem is the Linear Eddy method,<sup>5</sup> where the Linear Eddy model of Kerstein<sup>14</sup> is used to model transport and chemistry at small scales. The Linear Eddy model is an ad hoc model for turbulence in one dimension where the turnover of turbulent eddies is represented by a simple remapping operation. Because the Linear Eddy model is one-dimensional, it is possible to provide sufficient points in the one dimension to completely resolve the subgrid-scale dissipation, mixing and reaction. Unfortunately, adding a one-dimensional Linear Eddy at every grid point effectively adds another dimension to the flow field, making the method computationally expensive for three-dimensional LES problems. Furthermore, if complex chemistry is to be included, resolution constraints could conceivably require many thousands of points in each Linear Eddy, making the solution of the resulting system unfeasible.

Recently, Bilger<sup>15,16</sup> and Klimenko<sup>17</sup> independently proposed a new approach for modeling turbulent reacting flows, called conditional moment closure (CMC). This technique was originally developed for Reynolds averaged modeling approaches. This paper will describe a means of making use of the CMC chemical closure hypothesis for closing the chemical source term in the filtered transport equations for use in LES.

## II. FORMULATION

In the nonpremixed regime, the state of mixedness of the system can be described by the mixture fraction—a property which is often used to obtain closure for the chemical source terms. This is a conserved scalar obeying the transport equation

$$\frac{\partial \rho Z}{\partial t} + \frac{\partial \rho u_i Z}{\partial x_i} = \frac{\partial}{\partial x_i} \left( \rho \mathcal{D}_Z \frac{\partial Z}{\partial x_i} \right),$$

and initialized so as to have a value of zero in pure oxidizer and unity in pure fuel. If the diffusivities of all species are the equal, then the mixture fraction can be expressed as a linear combination of the constituent species' mass fractions, although the assumption of equal species' diffusivities is not necessary for the discussion that follows.

The transport equation for the mass fraction  $Y_I$  of some species  $I$  is

$$\frac{\partial \rho Y_I}{\partial t} + \frac{\partial \rho u_i Y_I}{\partial x_i} = \frac{\partial}{\partial x_i} \left( \rho \mathcal{D}_I \frac{\partial Y_I}{\partial x_i} \right) + \dot{\omega}_I, \quad (1)$$

where  $\mathcal{D}_I$  is the diffusivity of species  $I$  and  $\dot{\omega}_I$  is the mass rate of change of this species due to chemical reaction. A spatial filter is defined,

$$\bar{f}(x_k, t) = \int_V f(x'_k, t) g(x_k, x'_k) dx'_k, \quad (2)$$

where the function  $g(x_k, x'_k)$  is some filter function, such as a Gaussian or tophat filter. If this filter is applied to Eq. (1), one obtains Eq. (3):

$$\frac{\partial \bar{\rho} \bar{Y}_I}{\partial t} + \frac{\partial \bar{\rho} \bar{u}_i \bar{Y}_I}{\partial x_i} = \frac{\partial}{\partial x_i} \left( \bar{\rho} \bar{\mathcal{D}}_I \frac{\partial \bar{Y}_I}{\partial x_i} \right) + s g s_{\text{conv.}} + s g s_{\text{diff.}} + \bar{\dot{\omega}}_I, \quad (3)$$

where  $\bar{\rho}$  is the spatially filtered  $\rho$  and

$$\bar{Y}_I = \frac{\rho Y_I}{\rho}$$

is the density weighted (or Favre) filtered  $Y_I$ .

Of the terms on the right hand side of Eq. (3), only the first term, representing resolved diffusion, is closed. The other terms must be modeled. The two subgrid scale terms,

$$s g s_{\text{conv.}} = \frac{\partial}{\partial x_i} [\bar{\rho} (\bar{u}_i \bar{Y}_I - \widetilde{u_i Y_I})]$$

and

$$s g s_{\text{diff.}} = \frac{\partial}{\partial x_i} \left[ \bar{\rho} \left( \bar{\mathcal{D}}_I \frac{\partial \bar{Y}_I}{\partial x_i} - \widetilde{\mathcal{D}_I Y_I} \right) \right]$$

represent transport and diffusion at the unresolved scales. As was mentioned above, several different models are available for these terms. The last term in Eq. (3), the mean rate of change due to chemical reaction, must also be modeled. A similar source term for energy appears in the filtered transport equation for energy.

The main challenge faced in modeling combustion is that chemical reaction rates are usually highly nonlinear functions of temperature, density, and species mass fractions. For a system with  $N$  possible species, the  $K$ th chemical reaction can be written as

$$\sum_{J=1}^N \eta'_{JK} A_J \rightleftharpoons \sum_{J=1}^N \eta''_{JK} A_J,$$

where  $A_J$  is the chemical symbol for species  $J$  and  $\eta'_{JK}$  and  $\eta''_{JK}$  are the stoichiometric coefficients for species  $J$  in reaction  $K$ . If  $M$  chemical reactions are to be considered, then the chemical source term for species  $I$  becomes<sup>18</sup>

$$\dot{\omega}_I = W_I \sum_{K=1}^M (\eta''_{IK} - \eta'_{IK}) B_K T^{\gamma_K} \times \exp(-E_k/RT) \prod_{J=1}^N \left( \frac{\rho Y_J}{W_J} \right)^{\eta'_{JK}}, \quad (4)$$

where  $W_I$  is the molecular mass of species  $I$ ,  $T$  is the temperature, and  $R$  is the universal ideal gas constant. The activation energy  $E_K$  is a function of how much energy a collision of reactant molecules must supply for reaction  $K$  to proceed. The frequency factor  $B_K$  is a function of the frequency at which collisions between reactant molecules for reaction  $K$  can be expected to supply more than the activation energy. The power of the pre-exponential term  $\gamma_K$  for reaction  $K$ , accounts for nonexponential temperature dependence of the reaction rate.<sup>19</sup>

In LES, transport equations for spatially filtered temperatures, densities and mass fractions are to be solved. The chemical source terms in these equations represent linear

combinations of the chemical reaction rates. Clearly, the filtered reaction rates cannot be modeled satisfactorily by substituting the filtered temperature, density, and mass fractions into Eq. (4). This is also a problem for Reynolds averaging approaches; it is what is known as the “chemical closure problem,” and is what combustion modeling attempts to circumvent.

A method for closing the chemical source term (in a Reynolds averaging context) was recently proposed by Klimenko<sup>17</sup> and Bilger,<sup>15,16</sup> known as conditional moment closure (CMC). In the CMC method, the transport equations are conditionally averaged, with the condition being some variable on which the chemical reaction rates are known to depend. For nonpremixed combustion, the mixture fraction is clearly the most appropriate conditioning variable.

The average of the mass fraction  $Y_I$  of a particular species  $I$ , conditional on the mixture fraction  $Z$  having some value  $\zeta$ , is

$$Q_I(x_k, t; \zeta) \equiv \langle Y_I(x_k, t) | Z(x_k, t) = \zeta \rangle, \quad (5)$$

where the  $\langle a \rangle$  denotes an ensemble average of  $a$  for many realizations of the flow field being investigated. The “spatially degenerate” form (in which both the velocity and mixture fraction fields are isotropic and homogeneous) of the conditionally averaged transport equation for  $Y_I$ , assuming constant density, is<sup>20</sup>

$$\rho \frac{\partial Q_I}{\partial t}(\zeta) = \langle \dot{\omega}_I | Z = \zeta \rangle + \rho \frac{\partial^2 Q_I}{\partial \zeta^2} \left\langle \mathcal{D} \frac{\partial Z}{\partial x_i} \frac{\partial Z}{\partial x_i} \middle| Z = \zeta \right\rangle. \quad (6)$$

The right-hand side of Eq. (6) has two unclosed terms: the conditionally averaged reaction rate and a mixing term in which appears the conditionally averaged scalar dissipation,  $\langle \mathcal{D}(\partial Z / \partial x_i)(\partial Z / \partial x_i) | Z = \zeta \rangle$ .

The chemical source term is closed with the first order CMC hypothesis: the conditional average of the chemical source term of some species  $I$  can be modeled by evaluating the chemical reaction rates using the conditional averages of the composition vector  $Q_J$ , temperature  $\langle T | Z = \zeta \rangle$ , and density  $\langle \rho | Z = \zeta \rangle$ . Thus,

$$\langle \dot{\omega}_I(Y_J, T, \rho) | Z = \zeta \rangle \approx \dot{\omega}_I(Q_J, \langle T | Z = \zeta \rangle, \langle \rho | Z = \zeta \rangle). \quad (7)$$

Some refinements to the closure hypothesis for the chemical source term have been proposed, using either a second conditioning variable<sup>21,22</sup> or a second moment.<sup>20,23</sup> These refinements are intended to extend the validity of the closure hypothesis so as to account for ignition and extinction phenomena and to improve the performance of the model for chemical reactions where the activation energies are high.

### III. MODEL DERIVATION

The proposed method for incorporating the CMC hypothesis into LES will now be described. The description is broken into two parts. In the first part, the basic first moment CMC hypothesis will be used, which will allow for prediction of mean reaction rates in flames far from extinction. In the second part, a second conditioning variable will be added

to the method which will allow for prediction of mean reaction rates even in the presence of local extinction and ignition phenomena.

#### A. Singly conditional moment closure

It has been established that the CMC hypothesis, based on a single conditioning variable as described in the previous section, provides adequate predictions of reaction rates for flames far from extinction.<sup>15,24</sup> In this section, a method for incorporating the single conditioning variable CMC model into LES will be described.

To incorporate CMC into LES, one would want to make use of conditional filtered means of quantities such as the temperature; these conditional filtered means are defined using the filtered density function (FDF),<sup>7</sup>

$$P_Z(x_k, t; \zeta) = \int_V \delta[\zeta - Z(x'_k, t)] g(x_k, x'_k) dx'_k, \quad (8)$$

where  $\delta$  is the delta function. The conditional filtered mean of some random variable  $\theta$  is

$$\overline{\theta(x_k, t)} | \zeta \equiv \frac{\int_V \theta(x'_k, t) \delta[\zeta - Z(x'_k, t)] g(x_k, x'_k) dx'_k}{P_Z(x_k, t; \zeta)}. \quad (9)$$

Closure for the chemical source terms would be achieved by using conditional filtered means; that is  $\dot{\omega}_I(Y_K, T, \rho) | \zeta$  would be approximated by Eq. (10),

$$\overline{\dot{\omega}_I(Y_K, T, \rho)} | \zeta \approx \dot{\omega}_I(\overline{Y_K} | \zeta, \overline{T} | \zeta, \overline{\rho} | \zeta), \quad (10)$$

where the spatial and time dependence of the random variables  $Y_K(x_k, t)$ ,  $T(x_k, t)$ ,  $\rho(x_k, t)$  and their conditional filtered means is omitted for brevity. One way to obtain the conditional filtered mean mass fractions, temperature, and density might be to explicitly solve transport equations for these conditional filtered mean quantities. Unfortunately, this would involve adding a new independent variable  $\zeta$  to the system of equations being solved, which would likely lead to a prohibitively high computational cost.

An alternative might be to take advantage of some spatial homogeneity of the conditional means. For example, in the case of a mixing layer, conditional mean properties of a flame along the interface between the fuel and oxidizer streams would surely vary in the direction of the mean flow, but they would have a very weak sensitivity in the direction normal to the interface. Furthermore, they should have no dependency on the transverse direction, this being a direction of statistical homogeneity in both the flow and scalar fields. If a simulation were to be performed solving filtered transport equations in three dimensions, it might be possible to estimate the conditional averages of the mass fractions, density, and temperature on planes of constant distance downstream of the splitter plate by assuming the conditional averages on those planes are statistically homogeneous. A more justifiable, but somewhat less practical suggestion might be to assume statistical homogeneity of the conditional averages on a surface of constant convective residence time in the system.

The filtered temperature  $\overline{T}(x_k, t)$  can be expressed as

$$\bar{T}(x_k, t) = \int_{-\infty}^{\infty} P_Z(x_k, t; \zeta) \overline{T(x_k, t) | \zeta} d\zeta. \tag{11}$$

In Eq. (11), the filtered temperature is known and one might find a reasonable approximation for the FDF of the mixture fraction based on known properties of the mixture fraction field; unfortunately, this equation clearly cannot be solved for a unique conditional filtered mean of the temperature.

In LES, Eq. (3) would be integrated in time for discrete points on a computational grid in space. Equation (11) would be valid at each discrete point on that computational grid. We can define the ensemble average of the conditional filtered mean for some ensemble  $A$  of  $N$  points in the flow as

$$\langle \overline{T | \zeta} \rangle_{A,t} = \frac{1}{N} \sum_{n=1}^N \overline{T(x_k^{(n)}, t) | \zeta}. \tag{12}$$

This is not a random function of space; it is a function of time and of which discrete points in space are included in the ensemble  $A$ . If the conditional filtered mean for this ensemble of points is homogeneous, then for any point  $x_k^{(n)}$  in that ensemble,

$$\overline{T(x_k^{(n)}, t) | \zeta} = \langle \overline{T | \zeta} \rangle_{A,t}, \tag{13}$$

and Eq. (11) can be rewritten for that point as

$$\bar{T}(x_k^{(n)}, t) = \int_{-\infty}^{\infty} P_Z(x_k^{(n)}, t; \zeta) \langle \overline{T | \zeta} \rangle_{A,t} d\zeta, \tag{14}$$

which is the  $n$ th integral in an ensemble of  $N$  integrals. If these integrals are approximated by a numerical quadrature with  $M < N$  quadrature points in  $\zeta$ , each of these integrals becomes a linear equation for  $\langle \overline{T | \zeta} \rangle_{A,t}$  and this set of  $N$  linear equations can be solved in the least-squares sense for  $\langle \overline{T | \zeta} \rangle_{A,t}$  at the  $M$  quadrature points. Put another way, Eq. (14) is an integral equation—a Fredholm equation of the first kind—which can be solved for discrete intervals in  $\zeta$  to yield  $\langle \overline{T | \zeta} \rangle_{A,t}$ . Similar equations can be written for the density and the mass fractions.

The conditional filtered mean of the chemical source terms can now be estimated by invoking the CMC hypothesis and evaluating the reaction rates with the ensemble average of the conditional filtered means (or the approximations to these) of the temperature, the density and the mass fractions,

$$\langle \overline{\dot{\omega}_I | \zeta} \rangle_{A,t} \approx \dot{\omega}_I(\langle \overline{Y_K | \zeta} \rangle_{A,t}, \langle \overline{T | \zeta} \rangle_{A,t}, \langle \overline{\rho | \zeta} \rangle_{A,t}). \tag{15}$$

The filtered mean of the chemical source term at each point in the ensemble is then

$$\overline{\dot{\omega}_I}(x_k^{(n)}, t) = \int_{-\infty}^{\infty} P_Z(x_k^{(n)}, t; \zeta) \langle \overline{\dot{\omega}_I | \zeta} \rangle_{A,t} d\zeta. \tag{16}$$

In this manner, it is possible to obtain closure for the filtered mean reaction rate for any chemical kinetic mechanism. No assumptions have been made regarding the thickness of the regions in which chemical reactions are significant relative to the turbulent length scales. Only the assumption of statistical homogeneity of the conditional fil-

tered means of temperature, density, and pressure for an ensemble of LES points—perhaps on some surface in the flow—must be made.

If the conditional filtered mean for the ensemble is *not* homogeneous, then Eq. (14) would only be an approximation. Nevertheless, the solution would still yield an estimate for the ensemble average of the conditional filtered mean for the ensemble. This estimate might not be an adequate representation of the conditional filtered mean for certain points in the ensemble; the resulting estimate of the conditional filtered mean of the reaction rates might be a poor approximation to the local conditional filtered mean at such points. This would be an especially important consideration in a wall-bounded flow, for example, where the conditional filtered mean of the temperature at points near the wall would be very different from that at points far away from the wall. Thus, some care—and certain global, *a priori* information about the flow—must be used in selecting discrete points to include in the ensemble  $A$ . Also, it is clear that, for flows with inhomogeneities in the conditional filtered means, it would likely be necessary to have several different ensembles to which the process described above would be applied.

It is necessary to provide some assumed form for the FDF of the mixture fraction. One approach that has received considerable attention<sup>10,16</sup> is to approximate  $P_Z(x_k^{(n)}, t; \zeta)$  with a  $\beta$ -PDF with the same mean and variance, as in

$$P_Z(x_k^{(n)}, t; \zeta) \approx \zeta^{a_n-1} (1-\zeta)^{b_n-1} \frac{\Gamma(a_n+b_n)}{\Gamma(a_n)\Gamma(b_n)}, \tag{17}$$

with

$$a_n = \bar{Z}(x_k^{(n)}, t) \left( \frac{\overline{Z(x_k^{(n)}, t) \cdot [1 - \bar{Z}(x_k^{(n)}, t)]}}{\overline{Z'^2(x_k^{(n)}, t)}} - 1 \right), \tag{18}$$

and

$$b_n = \frac{a_n}{\bar{Z}(x_k^{(n)}, t)} - a_n, \tag{19}$$

where

$$\overline{Z'^2}(x_k^{(n)}, t) = \overline{[Z(x_k^{(n)}, t) - \bar{Z}(x_k^{(n)}, t)]^2} \tag{20}$$

is the filtered variance of the mixture fraction.

In the absence of differential diffusion, the filtered mean mixture fraction could be expressed as a linear combination of the filtered means of the species mass fractions. The filtered variance of the mixture fraction could be approximated using the similarity approach proposed by Jiménez *et al.*<sup>4</sup> Thus, it would only strictly be necessary to solve filtered transport equations for the filtered mass fractions, density, and temperature in order to use this approximation for the reaction rates.

Alternatively, if a separate transport equation for the filtered mean of the mixture fraction were solved, then, so long as the diffusivity of the mixture fraction were chosen to be greater than those of all species (and temperature), it would not be necessary to make any assumption regarding different species' diffusivities. Also, if yet another transport equation

for the filtered mixture fraction variance were solved, the need to make the similarity approximation could be circumvented—unfortunately, this would necessitate obtaining closure for additional terms in the transport equation for the filtered mixture fraction variance.

**B. Doubly conditional moment closure**

As was mentioned in the previous section, the CMC hypothesis with one conditioning variable has been found to give very good predictions for flames that are far from extinction. Thus, the closure proposed above would be expected to provide a good prediction of the reaction rates for such flames. However, when extinction is present, it is known that the single condition is inadequate. Furthermore, ignition processes cannot be adequately predicted with only a single conditioning variable unless a second moment closure is used.<sup>25</sup>

As was mentioned earlier, one proposed way to improve prediction in the presence of extinction is to introduce a second conditioning variable.<sup>21,22</sup> Since reaction rates are known to depend strongly on the scalar dissipation, it seems sensible that scalar dissipation—or some quantity on which scalar dissipation is known to depend—be added as the additional conditioning variable.<sup>26</sup> In the traditional CMC approach, this has the drawback of adding *two* independent variables to the system of equations. However, as was shown above, the need to add independent variables may be circumvented by taking advantage of some spatial homogeneity in the conditional filtered means.

Ideally, the second conditioning variable should be statistically independent of the mixture fraction; unfortunately, the local scalar dissipation

$$\chi(x_k, t) = 2\rho D \frac{\partial Z}{\partial x_i} \frac{\partial Z}{\partial x_i} \tag{21}$$

is a function of the local mixture fraction. Thus, closure for the joint filtered density function

$$P_{Z,\chi}(x_k, t; \zeta, c) = \int_V \delta[\zeta - Z(x'_k, t)] \times \delta[c - \chi(x'_k, t)] g(x_k, x'_k) dx'_k, \tag{22}$$

is difficult to obtain.

A functional form of the dependence of scalar dissipation on mixture fraction will be assumed—that of a laminar counterflow solution<sup>27</sup>—and the scalar dissipation will be written as

$$\chi = \chi_0 \cdot \exp(-2[\text{erf}^{-1}(Z)]^2), \tag{23}$$

where  $\chi$ ,  $\chi_0$ , and  $Z$  are random variables of space and time. The new random variable  $\chi_0$  is not a strong function of the mixture fraction and is sufficiently independent of  $Z$  for the purposes of the model. One drawback to using  $\chi_0$  as a conditioning variable is that it is undefined in the fuel and oxidizer streams, however, since the mass fractions, temperatures, and densities are already known in these streams, this does not present a difficulty.

Assuming that the filtered mean of the scalar dissipation,  $\overline{\chi}(x_k, t)$ , can be modeled (if a transport equation for the filtered variance of mixture fraction is to be solved explicitly then  $\overline{\chi}(x_k, t)$  must be modeled), then the filtered mean,  $\overline{\chi_0}(x_k, t)$ , can be obtained by assuming that  $\chi_0$  is statistically independent of  $Z$ . Writing the unconditional mean scalar dissipation as a function of its conditional mean, and substituting Eq. (23),

$$\begin{aligned} \overline{\chi}(x_k, t) &= \int_{-\infty}^{\infty} P_Z(x_k, t; \zeta) \overline{\chi(x_k, t) | \zeta} d\zeta \\ &= \overline{\chi_0}(x_k, t) \int_{-\infty}^{\infty} P_Z(x_k, t; \zeta) \cdot \exp(-2[\text{erf}^{-1}(\zeta)]^2) d\zeta \end{aligned} \tag{24}$$

the estimate for the filtered mean of  $\chi_0$  becomes

$$\overline{\chi_0}(x_k, t) = \overline{\chi}(x_k, t) / Y,$$

with

$$Y = \int_{-\infty}^{\infty} P_Z(x_k, t; \zeta) \cdot \exp(-2[\text{erf}^{-1}(\zeta)]^2) d\zeta.$$

The FDF of the scalar dissipation is often taken to be approximately log-normal.<sup>28–30</sup> The FDF of  $\chi_0$  will be assumed to *also* be log-normal, and the standard deviation of the logarithm of  $\chi_0$  will be taken to be unity. Thus, it is being assumed that the FDF of  $\chi_0$  is

$$P_{\chi_0}(x_k, t; c) \approx \frac{1}{\sqrt{2\pi c}} \exp\left[-\frac{(\ln c - \mu)^2}{2}\right],$$

with

$$\mu \approx \ln \overline{\chi_0} - \frac{1}{2}.$$

Where the mixture fraction is a scalar that is used to describe the state of mixedness of a flow,  $\chi_0$  can be thought of as a measure of the cumulative effects of the straining in the flow field on that state of mixedness. Regions where  $\chi_0$  is low are well mixed, whereas regions where  $\chi_0$  is high are likely to be regions in which a high strain in the flow field is aligned with the gradient of mixture fraction, drawing the fuel and oxidizer streams close to one another. At high values of  $\chi_0$ , reaction rates would be expected to be lower than at lower values of  $\chi_0$ . Regions of local extinction are likely to occur when  $\chi_0$  becomes large. Autoignition is most likely to occur where  $\chi_0$  is smallest. Using  $\chi_0$  as a conditioning variable cannot capture the entire accumulated effects of the scalar dissipation on the local flame, for example, high scalar dissipation could arise and locally extinguish a flame, then that scalar dissipation could drop, while the flame might remain extinguished. Nevertheless, insofar as the statistical approach underlying conditional moment closure can only predict mean reaction rates, adding  $\chi_0$  as a conditioning variable helps to reduce the conditional variance of temperatures, mass fractions, and density, and make the chemical closure hypothesis valid even in the presence of local extinctions or autoignition.

For some ensemble  $A$  of  $N$  discrete points in a LES domain (which, again, might lie on a surface in the flow such as those suggested in the previous section), the filtered temperature at each point  $x_n$  in the ensemble can be expressed as

$$\bar{T}(x_k^{(n)}, t) = \int_{-\infty}^{\infty} \int_{-\infty}^{\infty} P_{Z, \chi_0}(x_k^{(n)}, t; \zeta, c) \overline{T(x_k^{(n)}, t) | \zeta, c} d\zeta dc, \tag{25}$$

where

$$P_{Z, \chi_0}(x_k^{(n)}, t; \zeta, c) \approx P_Z(x_k^{(n)}, t; \zeta) P_{\chi_0}(x_k^{(n)}, t; c)$$

is the joint FDF of  $Z$  and  $\chi_0$  at the point  $x_k^{(n)}$ , and

$$\overline{T(x_k^{(n)}, t) | \zeta, c} \equiv \frac{\int_V T(x'_k, t) \delta[\zeta - Z(x'_k, t)] \delta[c - \chi_0(x'_k, t)] g(x_k^{(n)}, x'_k) dx'_k}{P_{Z, \chi_0}(x_k^{(n)}, t; \zeta, c)} \tag{26}$$

is the two-condition conditional filtered mean of the temperature at  $x_k^{(n)}$ . If this conditional filtered mean of the temperature for the ensemble of points is homogeneous, then

$$\overline{T(x_k^{(n)}, t) | \zeta, c} = \langle \overline{T | \zeta, c} \rangle_{A, t},$$

and Eq. (25) can be rewritten as

$$\bar{T}(x_k^{(n)}, t) = \int_{-\infty}^{\infty} \int_{-\infty}^{\infty} P(x_k^{(n)}, t; \zeta, c) \langle \overline{T | \zeta, c} \rangle_{A, t} d\zeta dc. \tag{27}$$

This is a two-dimensional integral equation which, for discrete intervals in  $\zeta$  and  $c$ , can be solved to yield  $\langle \overline{T | \zeta, c} \rangle_{A, t}$ . Similar equations can be written for the density and the mass fractions. As before, if that conditional filtered mean of the temperature for the ensemble of points is *not* homogeneous, then Eq. (27) would only be an approximation; nevertheless, the solution would still yield an estimate for ensemble average of the conditional filtered mean of the temperature in the ensemble.

Invoking the CMC hypothesis to predict the chemical source term,

$$\langle \overline{\dot{\omega}_I | \zeta, c} \rangle_{A, t} \approx \dot{\omega}_I(\langle \overline{Y_K | \zeta, c} \rangle_{A, t}, \langle \overline{T | \zeta, c} \rangle_{A, t}, \langle \overline{\rho | \zeta, c} \rangle_{A, t}), \tag{28}$$

the mean chemical source term becomes

$$\overline{\dot{\omega}_I}(x_k^{(n)}, t) = \int_{-\infty}^{\infty} \int_{-\infty}^{\infty} P(x_k^{(n)}, t; \zeta, c) \langle \overline{\dot{\omega}_I | \zeta, c} \rangle_{A, t} d\zeta dc. \tag{29}$$

In a numerical implementation of the method, it would not be necessary to integrate these integrals to infinity. The mixture fraction is typically defined such that it is bounded by zero and unity and  $\chi_0$  must always be greater than or equal to zero. Furthermore, it should be possible to truncate the upper bound of the outer integral at some very large value of  $\chi_0$  beyond which the FDF would be negligible small.

By adding the second condition to the model, it should be possible to predict autoignition, extinction and reignition phenomena. As was described above, it is not necessary to make assumptions regarding the thickness of the flame relative to turbulent length scales, nor the relative diffusivities of

different species, or temperature. An explicit chemical source term can be estimated and incorporated into LES, for any arbitrarily complex chemical kinetic mechanism. Unfortunately, the same caveats mentioned with respect to the selection of discrete points to include in an ensemble in the previous discussion of the single conditioning variable technique apply as well to the two conditioning variable method.

### C. Effects of density weighted filtering

Ultimately, the filtered transport equation of the mass fraction, Eq. (3), will be solved for the Favre filtered means of mass fraction and energy, since using the Favre filtered means eliminates the need to close terms involving fluctuations in density. When the method described herein is implemented into a simulation where the density is allowed to vary, it must be rewritten in terms of these density weighted filtered means. This does not present any problem to the closure hypothesis, nor to the process described above.

Equation (14) is rewritten as

$$\bar{T}(x_k^{(n)}, t) = \int_{-\infty}^{\infty} \bar{P}_Z(x_k^{(n)}, t; \zeta) \langle \overline{T | \zeta} \rangle_{A, t} d\zeta, \tag{30}$$

where

$$\bar{P}_Z(x_k, t; \zeta) = \frac{1}{\bar{\rho}(x_k, t)} \int_V \rho(x'_k, t) \times \delta[\zeta - Z(x'_k, t)] g(x_k, x'_k) dx'_k \tag{31}$$

is the Favre filtered density function of the mixture fraction, which will be approximated using the  $\beta$ -PDF evaluated with the Favre filtered mean and variance of the mixture fraction. Equation (30) is solved for the ensemble average of the conditional filtered mean of the temperature; a similar integral equation is solved for that of the species mass fractions. The conditional filtered mean of the density can be estimated from the state equation by neglecting the effects of pressure fluctuations within the ensemble of points being averaged together. In high Mach-number flows, this would imply a further restriction on which discrete points can be included in

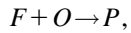
the ensemble  $A$ . The conditional reaction rates are approximated using Eq. (10), and the filtered reaction rate is estimated with

$$\bar{\dot{\omega}}(x_k, t) = \bar{\rho}(x_k, t) \int_{-\infty}^{\infty} \bar{P}_Z(x_k, t; \zeta) \langle \dot{\omega} | \zeta \rangle_{A,t} (\langle \rho | \zeta \rangle_{A,t})^{-1} d\zeta. \quad (32)$$

The two-condition method can be extended to Favre filtering in a similar fashion.

**IV. RESULTS**

In order to test the method described above, the output from several different time steps in the direct numerical simulation (DNS) database of Vervisch *et al.*<sup>31,32</sup> was filtered. The simulation was of a shear-free, temporal mixing layer, with fuel and oxidizer mixing in the presence of turbulence. The domain was rectangular, with 128 points across the layer and 64 points in each direction tangential to the layer. The chemical kinetic mechanism used in creating the database was a single step,



with  $F$ ,  $O$ , and  $P$  being fuel, oxidizer, and product, respectively. The reaction rate was

$$\dot{\omega} = B \exp\left(-\frac{\beta}{\alpha}\right) \rho^2 Y_F Y_O \exp\left(\frac{-\beta(1-\theta)}{1-\alpha(1-\theta)}\right), \quad (33)$$

with  $\alpha = (T_{ad} - T_0)/T_{ad} = 0.8$ ,  $\beta = 8$ , and the reduced temperature  $\theta = (T - T_0)/(T_{ad} - T_0)$ ; all temperatures—including  $T_0$  (the initial temperature) and  $T_{ad}$  (the adiabatic flame temperature at stoichiometric conditions)—were non-dimensionalized with the reference temperature  $T_{ref} = (\gamma$

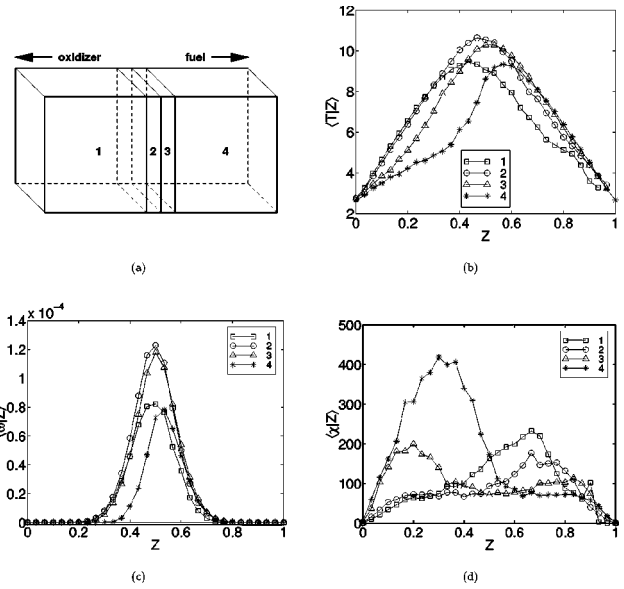


FIG. 1. Variations in conditional filtered means across the mixing layer; (b) temperature, (c) reaction rate, and (d) scalar dissipation. The four lines in (b), (c), and (d) are the conditional filtered means taken from the volumes depicted in (a).

$-1)T_0$  and  $\gamma$ , the ratio of specific heats, was taken to be 1.4. The quantity  $B$  was chosen such that the Damköhler number was unity.

**A. Test of assumptions**

The validity of the various assumptions made in obtaining closure for the filtered chemical source term were examined by comparing them directly to the DNS data. Results will only be shown for one time in the database—a fairly late

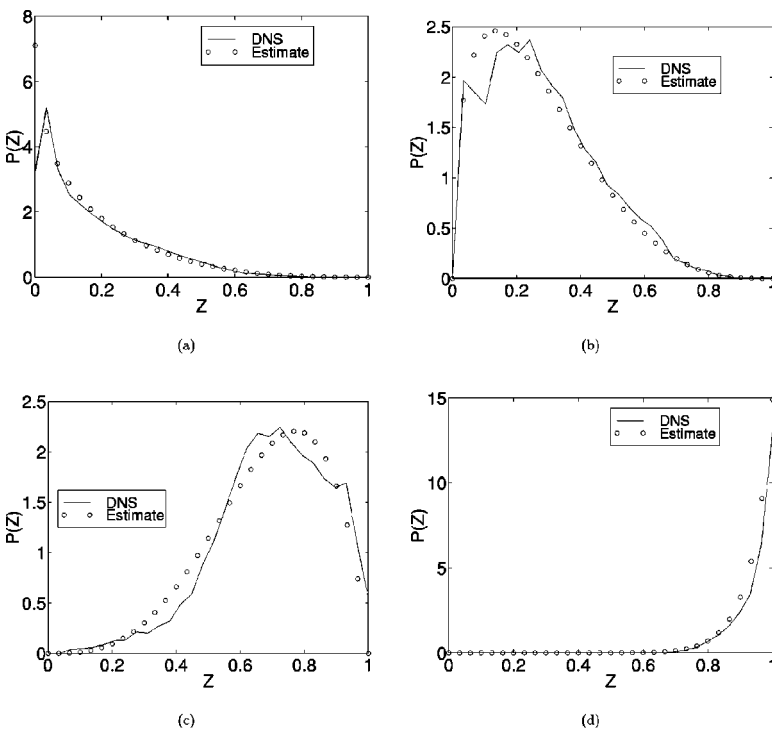


FIG. 2. Comparison of the actual FDF of mixture fraction within four different subgrid cells to the  $\beta$ -PDF evaluated with the same mean and variance.

time, approximately 1.6 eddy turnover times into the simulation—however, these results were found to be representative of those obtained at all available times.

In Fig. 1, the variation in the conditional filtered mean of the temperature, reaction rate and scalar dissipation across the mixing layer are compared. Figure 1(a) depicts the volumes in which conditional filtered means were obtained using a tophat filter; volumes 1 and 2 are on the lean side of the flame and volumes 3 and 4 are on the rich side. While volumes 2 and 3 are narrow—only  $16 \times 64 \times 64$  points each—they both contain a considerable fraction of the flow in which  $Z$  is not zero or unity. Figure 1(b) seems to indicate that there is a significant variation in the temperature across the mixing layer, and this causes a significant variation in the conditional filtered mean of the reaction rate, shown in Fig. 1(c); however these variations appear to be correlated with high scalar dissipation, shown in Fig. 1(d). Unfortunately, the DNS database does not provide sufficient data to obtain statistically converged conditional filtered means when two conditions are used, thus it proved impossible to demonstrate a lack of variation in two-condition conditional filtered quantities across the mixing layer.

Next, the filtered means and variances of the mixture fraction were extracted from the database. The filter used was a tophat filter with the filter width set to  $16 \times 8 \times 8$ , so that 128 filtered means would be available. In Fig. 2, the FDF of the mixture fraction extracted from four different filtered discrete points is compared to the  $\beta$ -PDF evaluated with the same mean and variance. Clearly, the  $\beta$ -PDF provides a good approximation to the actual FDF of the mixture fraction over a wide range of conditions—similar results were found at all points in space.

Figure 3 shows scatter plots of the scalar dissipation  $\chi$  and  $\chi_0$  against mixture fraction. The dependence of  $\chi$  on the mixture fraction is evident at the extremes of mixture fraction, where  $\chi$  tends to zero. While  $\chi_0$  does have a weak dependence on the mixture fraction, this is much less significant than the dependence of  $\chi$ .

In Fig. 4, the FDF of  $\chi_0$  for the entire DNS domain is compared to a log-normal PDF evaluated with the same mean and variance. The log-normal PDF fails to capture the peak of the FDF of  $\chi_0$ , however it does predict the tail of the FDF very well. It was found that the exact shape of the FDF of  $\chi_0$  has a very small effect on the prediction of the model. This is because the FDF of  $\chi_0$  is used only to establish the effect of scalar dissipation on the mass fractions, density, and temperature, and therefore on the reaction rates. The integral equation, Eq. (27), effectively transforms resolved grid filtered values into a space described by mixture fraction and scalar dissipation; Eq. (29) transforms the chemical reaction rates back onto the resolved grid.

## B. One condition

The filtered mean mass fractions, temperatures, densities, and reaction rates were extracted from the database, as were the filtered means of the mixture fraction and scalar dissipation and the filtered variance of the mixture fraction. The filter used was again a tophat filter with the filter width

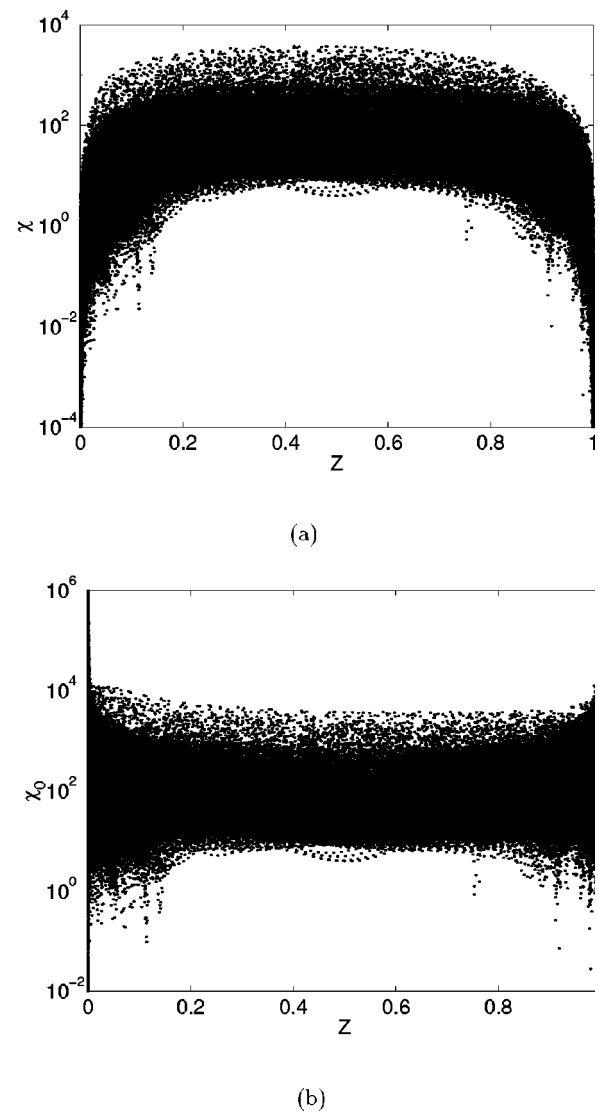


FIG. 3. Scatter plots of (a)  $\chi$  and (b)  $\chi_0$  against the mixture fraction.

set to  $16 \times 8 \times 8$ , so that 128 filtered means would be available. When the filter width was narrowed to provide a larger sample set for the integral inversion process, the subgrid sample size was found to be too small to give sufficiently converged statistics.

The first test of the method itself is to try to use the quantities  $\bar{Z}(x_k^{(n)}, t)$  and  $\overline{Z'^2}(x_k^{(n)}, t)$  at each point  $n$  to predict  $P(x_k^{(n)}, t; \zeta)$  using the  $\beta$ -PDF, as described above, and then substitute  $\bar{\rho}(x_k^{(n)}, t)$ ,  $\overline{Y_F}(x_k^{(n)}, t)$ ,  $\overline{Y_O}(x_k^{(n)}, t)$ ,  $\bar{T}(x_k^{(n)}, t)$ , and  $P(x_k^{(n)}, t; \zeta)$  into Eq. (14) to predict the conditional filtered means. The results of this *a priori* test for the same time in the simulation are shown in Fig. 5, where the results of the solution of the integral equation using a simple linear regularization method<sup>33</sup> is compared to the actual conditional mean from the entire flow field. With the exception of a slight under-prediction of the maximum temperature, the prediction of the conditional means is very good. Similar results have been found for all other times at which data are available.

The next test is to invoke the CMC hypothesis, and use

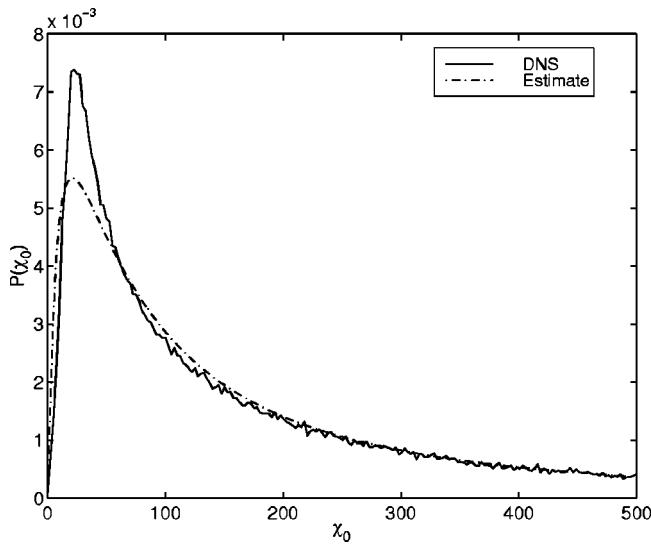


FIG. 4. Comparison of the actual FDF of  $\chi_0$  in the entire DNS domain to the log-normal PDF with the same mean and variance.

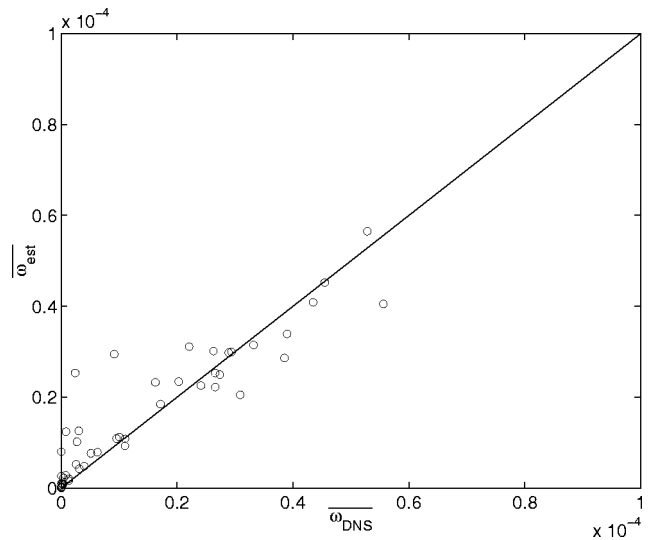


FIG. 6. Comparison of reaction rate estimated using integral equation solution and CMC closure hypothesis with one conditioning variable to filtered reaction rate from DNS data.

these conditional filtered means to predict the conditional mean reaction rate by substituting the conditional filtered means of the mass fractions, density, and temperature into Eq. (33). Then, the filtered reaction rate is predicted from the conditional filtered mean reaction rate using Eq. (16). The estimate obtained by this process is compared to the actual filtered reaction rate for every point in Fig. 6. The standard error in the prediction of those points where  $\dot{\omega}_{DNS}$  is significant (greater than  $1 \times 10^{-5}$ ) is about 15%. It should be noted that there is some extinction in the DNS database, which cannot be predicted by the single condition version of this method. This is made evident by the presence of several points where  $\dot{\omega}_{DNS}$  is very small, but  $\dot{\omega}_{est}$  is still significant.

These are points where the tophat filter encompasses a local extinction event. Nevertheless, that the method is capable of predicting the reaction rates with such accuracy, even in the presence of heat release and extinction, is encouraging.

**C. Two conditions**

As was discussed above, adding a second condition to the method is expected to make it capable of modeling extinction and ignition phenomena. This was tested by simply adding the second condition and solving the two-dimensional problem described by Eq. (27), using the ensemble averaged conditional filtered means to estimate that of the reaction rate

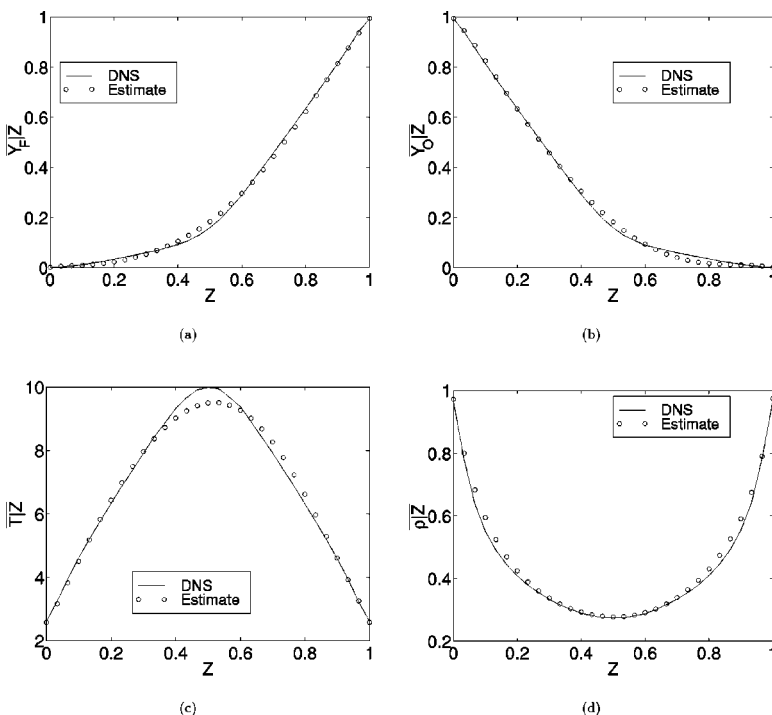


FIG. 5. Result of *a priori* test of integral equation solution for (a) mass fraction of fuel, (b) mass fraction of oxidizer, (c) nondimensional temperature, (d) nondimensional density. Solid line is the DNS value, symbol is a result of the integral equation solution.

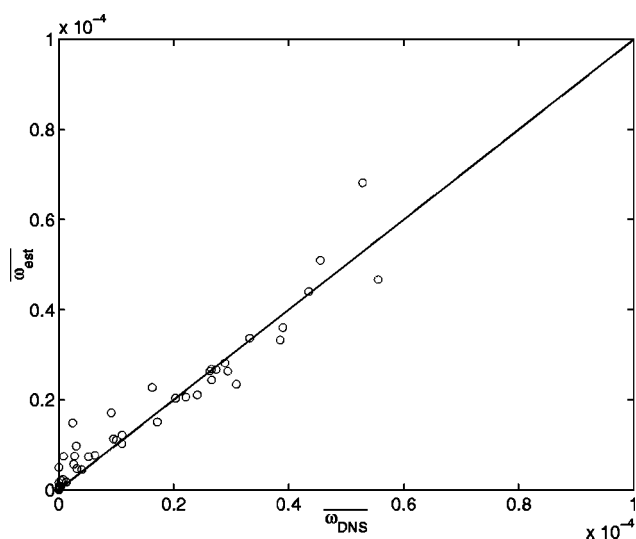


FIG. 7. Comparison of reaction rate estimated using integral equation solution and CMC closure hypothesis with two conditioning variables to the filtered reaction rate from DNS data.

with Eq. (28), and integrating Eq. (29). The result of this process is shown in Fig. 7. The standard error in the prediction of the points where  $\dot{\omega}_{\text{DNS}}$  is significant (again, greater than  $1 \times 10^{-5}$ ) is about 10%. Not only is the error in the prediction somewhat smaller than was found with only one condition, the evidence of overprediction of the reaction rate for points where the tophat filter encompassed extinction events is no longer apparent. The extinction phenomenon is captured, at least to some extent, by the inclusion of the second conditioning variable.

## V. DISCUSSION

The method described herein has several significant advantages over other closure approaches. No assumption has been made about the relative thickness of the flame to the turbulent length scales. The method can be used for arbitrarily complex chemical kinetic mechanisms. No steady state assumption has been made. The chemical source terms are calculated in “mixing space,” rather than in real space, therefore the chemical reactions need only be resolved in mixture fraction, which significantly eases the resolution constraints that are typically associated with simulations of reacting flows.<sup>26</sup>

Perhaps the most significant advantage is the potential to predict ignition and local extinction/reignition phenomena. The effect of scalar dissipation on the rate of diffusion of the mass fractions and temperature is resolved in real space. Regions where the filtered scalar dissipation is large will see greater rates of diffusion of the temperature and mass fractions, and the method will detect this effect. If the temperature in a region of high scalar dissipation dips below some threshold then the chemical reactions will drop. Regions where the filtered scalar dissipation is low will see much slower rates of diffusion of mass fractions and temperature, and these conditions will likely be more favorable for ignition.

The method also has shortcomings. First and foremost among these is the need to assume homogeneity of the conditional filtered means of mass fractions, density, and temperature for ensembles of points in the flow. While this may be justifiable in simple flows, such as mixing layers or free jets, it would be more difficult to assemble such an ensemble in flows past solid objects, where heat transfer and flame quenching would have to be accounted for.

A second potential shortcoming is that the method requires the solution of many integral equations, which could be computationally expensive. Currently, the method is being implemented into a LES code, and it appears that using the method results in a lower computational cost than simply evaluating the reaction rates with resolved grid quantities (performing the simulation without any subgrid scale model for the source terms). This is because the chemical source terms are evaluated in mixing space, which can have many fewer points than are needed in real space, and chemical source terms—which involve costly exponential evaluations—tend to be more computationally expensive than the solution of the integral equations.

A similar model is currently being developed for use in premixed reacting flows. It has also been suggested that the method be used in Reynolds Averaged models. Finally, the potential for using second moment statistics—particularly the second moment of the temperature—to incorporate Li and Bilger’s<sup>23</sup> second moment closure hypothesis for the reaction rates is being investigated. This could improve the prediction of the reaction rates, although it might prove to be too computationally expensive to be justifiable in a LES context, given that it would require the solution of additional transport equations for the temperature and mass fraction variances.

## VI. CONCLUSIONS

A new subgrid scale model for large-eddy simulation of combustion has been proposed and tested. The new model makes use of the chemical closure hypothesis in conditional moment closure to estimate the chemical source term in the filtered equations for scalar and energy transport. It is assumed that, for some ensemble of resolved grid points in a LES calculation, the conditional filtered means of the mass fractions, density, and temperature will be homogeneous, and an integral equation is solved for those conditional filtered means. The method has been tested against DNS data, and found to predict the filtered reaction rate within 15%. Using a second conditioning variable, the prediction is improved somewhat; more importantly, it becomes possible to predict extinction and ignition phenomena.

## ACKNOWLEDGMENTS

The authors wish to thank G. Košaly, A. Kerstein, N. Peters, R. W. Bilger, and the staff at the Center for Turbulence Research for useful suggestions and discussions. H. S. gratefully acknowledges the financial support of the FWF of Austria.

- <sup>1</sup>M. Lesieur and O. Métais, "New trends in large-eddy simulations of turbulence," *Annu. Rev. Fluid Mech.* **28**, 45 (1996).
- <sup>2</sup>P. Moin, "Progress in large eddy simulation of turbulent flows," AIAA Paper No. 97-0749.
- <sup>3</sup>P. Moin, K. Squires, W. Cabot, and S. Lee, "A dynamic subgrid-scale model for compressible turbulence and scalar transport," *Phys. Fluids A* **3**, 2746 (1991).
- <sup>4</sup>J. Jiménez, A. Liñán, M. M. Rogers, and F. J. Higuera, "A priori testing of subgrid models for chemically reacting nonpremixed turbulent shear flows," in *Proceedings of the 1996 Summer Program*, Center for Turbulence Research, NASA Ames/Stanford University, 1996 (unpublished).
- <sup>5</sup>P. A. McMurtry, S. Menon, and A. R. Kerstein, "A linear eddy subgrid model for turbulent reacting flows: Application to hydrogen-air combustion" in *Proceedings of the 24th Symposium (International) on Combustion* (The Combustion Institute, Pittsburgh, 1992), p. 271.
- <sup>6</sup>S. Menon, P. A. McMurtry, and A. R. Kerstein, "A linear eddy subgrid model of turbulent combustion, in *Large Eddy Simulations of Complex Engineering and Geophysical Flows*, edited by B. Galperin and S. A. Orszag (Cambridge University Press, Cambridge, 1993), p. 287.
- <sup>7</sup>P. J. Colucci, F. A. Jaber, P. Givi, and S. B. Pope, "Filtered density function for large eddy simulation of turbulent reacting flows," *Phys. Fluids* **10**, 499 (1998).
- <sup>8</sup>F. Gao and E. E. O'Brien, "A large-eddy simulation scheme for turbulent reacting flows," *Phys. Fluids A* **5**, 1282 (1993).
- <sup>9</sup>S. B. Pope, "Computations of turbulent combustion: Progress and challenges," in *Proceedings of the 23rd Symposium (International) on Combustion* (The Combustion Institute, Pittsburgh, 1990), p. 591.
- <sup>10</sup>A. W. Cook and J. J. Riley, "A subgrid model for equilibrium chemistry in turbulent flows," *Phys. Fluids* **6**, 2868 (1994).
- <sup>11</sup>A. W. Cook, J. J. Riley, and G. Kosály, "A laminar flamelet approach to subgrid-scale chemistry in turbulent flows," *Combust. Flame* **109**, 332 (1997).
- <sup>12</sup>N. Peters, "Four lectures on turbulent combustion," ERCOFTAC Summer School, Institute für Technische Mechanik, RWTH Aachen, Germany, 1997.
- <sup>13</sup>P. Givi, "Model free simulations of turbulent reacting flows," *Prog. Energy Combust. Sci.* **15**, 1 (1989).
- <sup>14</sup>A. R. Kerstein, "Linear-eddy modeling of turbulent transport. Part 7. Finite-rate chemistry and multistream mixing," *J. Fluid Mech.* **240**, 289 (1992).
- <sup>15</sup>R. W. Bilger, "Conditional moment closure for turbulent reacting flow," *Phys. Fluids A* **5**, 436 (1993).
- <sup>16</sup>R. W. Bilger, "Conditional moment closure modeling and advanced laser measurements," in *Turbulence and Molecular Processes in Combustion*, edited by T. Tekeno (Elsevier Science, New York, 1993).
- <sup>17</sup>A. Yu. Klimenko, "Multicomponent diffusion of various admixtures in turbulent flow," *Fluid Dyn. (USSR)* **25**, 327 (1990).
- <sup>18</sup>F. A. Williams, *Combustion Theory* (Benjamin Cummings, Menlo Park, 1985).
- <sup>19</sup>I. Glassman, *Combustion* (Academic, Orlando, 1987).
- <sup>20</sup>N. A. S. Smith, Conditional moment closure of mixing and reaction in turbulent nonpremixed combustion, Annual Research Briefs, Center for Turbulence Research, NASA Ames/Stanford University, 1996.
- <sup>21</sup>R. W. Bilger, "Conditional moment methods for turbulent reacting flow using Crocco variable conditions," Charles Kolling Laboratory Report, Department of Mechanical Engineering, The University of Sydney, TN F-99, 1991.
- <sup>22</sup>W. K. Bushe, "Conditional Moment Closure Methods for Autoignition Problems," Ph.D. thesis, Cambridge University, Cambridge, December, 1995.
- <sup>23</sup>J. D. Li and R. W. Bilger, "Measurement and prediction of the conditional variance in a turbulent reactive-scalar mixing layer," *Phys. Fluids A* **5**, 3255 (1993).
- <sup>24</sup>N. S. A. Smith, "Development of the Conditional Moment Closure Method for Modeling Turbulent Combustion," Ph.D. thesis, Department of Mechanical and Mechatronic Engineering, University of Sydney, Sydney, Australia, October, 1994.
- <sup>25</sup>E. Mastorakos and R. W. Bilger, "Second-order conditional moment closure for the autoignition of turbulent flows," *Phys. Fluids* **10**, 1246 (1998).
- <sup>26</sup>W. K. Bushe, R. W. Bilger, and G. R. Ruetsch, "Incorporating realistic chemistry into direct numerical simulations of turbulent nonpremixed combustion," Annual Research Briefs, Center for Turbulence Research, NASA Ames/Stanford University, 195, 1997.
- <sup>27</sup>N. Peters, "Laminar diffusion flamelet models," *Prog. Energy Combust. Sci.* **10**, 319 (1984).
- <sup>28</sup>A. S. Monin and A. M. Yaglom, *Statistical Fluid Mechanics* (MIT Press, Cambridge, 1975).
- <sup>29</sup>V. Eswaran and S. B. Pope, "Direct numerical simulations of the turbulent mixing of a passive scalar," *Phys. Fluids* **31**, 506 (1988).
- <sup>30</sup>P. K. Yeung and S. B. Pope, "Lagrangian statistics from direct numerical simulations of isotropic turbulence," *J. Fluid Mech.* **207**, 531 (1989).
- <sup>31</sup>L. Vervisch, "Study and modeling of finite rate chemistry effects in turbulent nonpremixed flames," Annual Research Briefs, Center for Turbulence Research, NASA Ames/Stanford University, 1992.
- <sup>32</sup>J. H. Chen, S. Mahalingam, I. K. Puri, and L. Vervisch, "Effect of finite-rate chemistry and unequal Schmidt numbers on turbulent nonpremixed flames modeled with single-step chemistry," in *Proceedings of the 1992 Summer Program* (Center for Turbulence Research, NASA Ames/Stanford University, 1992).
- <sup>33</sup>W. H. Press, S. A. Teukolsky, W. T. Vetterling, and B. P. Flannery, *Numerical Recipes in Fortran* (Cambridge University Press, Cambridge, 1992).

P 2

H. PITSCH & H. STEINER

Large-eddy simulation of a turbulent methane/air diffusion  
flame

*Phys. Fluids* **12** (2000), 2541–2554

# Large-eddy simulation of a turbulent piloted methane/air diffusion flame (Sandia flame D)

H. Pitsch<sup>a)</sup>

*Flow Physics and Computation Division, Department of Mechanical Engineering, Stanford University, Stanford, California 94040-3030*

H. Steiner

*Center for Turbulence Research, Department of Mechanical Engineering, Stanford University, Stanford, California 94040-3030*

(Received 2 March 2000; accepted 16 June 2000)

The Lagrangian Flamelet Model is formulated as a combustion model for large-eddy simulations of turbulent jet diffusion flames. The model is applied in a large-eddy simulation of a piloted partially premixed methane/air diffusion flame (Sandia flame D). The results of the simulation are compared to experimental data of the mean and RMS of the axial velocity and the mixture fraction and the unconditional and conditional averages of temperature and various species mass fractions, including CO and NO. All quantities are in good agreement with the experiments. The results indicate in accordance with experimental findings that regions of high strain appear in layer like structures, which are directed inwards and tend to align with the reaction zone, where the turbulence is fully developed. The analysis of the conditional temperature and mass fractions reveals a strong influence of the partial premixing of the fuel. © 2000 American Institute of Physics.

[S1070-6631(00)50910-6]

## I. INTRODUCTION

While numerical simulations of turbulent flows applying Reynolds averaging techniques solve equations for ensemble or time averaged mean quantities, Large-Eddy Simulations (LES) have the capability of resolving the major part of the turbulent kinetic energy of turbulent flows. Hence, only the influence of the small turbulent scales on the resolved field has to be modeled. Since, in addition, the small turbulent scales fulfill the common modeling assumption of isotropy much better than the large scales, a very high accuracy in predictions of the turbulent flow field can be achieved by using LES. This is particularly interesting for simulations of chemically reacting flows, where an accurate description of mixing is essential and very complex phenomena like turbulent transition and instabilities might be of great importance.

The success of LES in predictions of turbulent flows is due to the fact that the kinetic energy content of the turbulent motion decreases with increasing wave number. Thereby, the major part of the Reynolds stresses is resolved. In the modeling of the unresolved part it is still most important to represent the larger scales by a sub-grid scale model. However, since chemical reactions in nonpremixed combustion occur only by molecular mixing of fuel and oxidizer, which in practical applications occurs only on the dissipative turbulent scales, the combustion process occurs essentially at the smallest scales of the sub-filter level, and has to be modeled entirely. This also explains why sub-grid modeling techniques, which have successfully been used in predictions of

sub-grid scale stresses and variances, might not necessarily be applicable in the modeling of the chemical source terms.

In recent years many studies have been devoted to *a priori* testing of the applicability of combustion models in LES.<sup>1-7</sup> Most of the proposed models have previously been used, or could very similarly be applied, in RANS calculations. Essentially, the proposed models can be divided into four categories: the direct method, the Linear-Eddy Model, the transported probability density function (pdf) method, and the conserved scalar method.

Similarly, as in RANS combustion models, the direct modeling of the spatially filtered chemical source terms is a very challenging problem. Different direct closure models have been proposed by DesJardin and Frankel.<sup>1</sup> They first show that modeling the reaction term by only using the resolved scales without a sub-grid model gives very poor agreement compared with DNS results. This has also been shown in many other studies, for instance by Colucci *et al.*<sup>7</sup> In addition they propose two different direct closure models based on the scale similarity assumption, which considerably improve the predictions, but are still not in good agreement with DNS data. The reason for this is obvious. The scale similarity assumption actually implies that the smallest resolved scales are statistically similar to the largest unresolved scales. This assumption seems to be very reasonable, but still, it does not assist in the modeling of the chemical source term. As mentioned earlier, in turbulent nonpremixed combustion, chemical reactions occur on the dissipative rather than the larger unresolved scales. This problem is inherent for all models, which estimate the reaction rates by only using the resolved scales and it explains why the com-

<sup>a)</sup> Author to whom correspondence should be addressed; Phone: (650) 725-6635; fax: (650) 725-7834; electronic mail: H.Pitsch@stanford.edu

bustion models applied in LES do not differ significantly from RANS combustion models.

The Linear-Eddy Model (LEM) has been proposed by Kerstein.<sup>8</sup> In this method scalar mixing is described in lines, the linear eddies, which are convectively transported with the mean flow. The governing one-dimensional equations include molecular transport as well as turbulent convection modeled by random flow field rearrangement events. This model has been formulated in the frame of LES by McMurtry *et al.*<sup>9</sup> In this implementation one or more linear eddies are solved for each computational control volume. The convective transport of the linear eddies is modeled by so called splicing events, which randomly exchange adjacent cell linear eddies based on the LES-resolved velocity field.

The transported compositional pdf method has been applied to turbulent reactive flows using RANS methods in many studies<sup>10–12</sup> and has also been extended to LES by using so called filtered density functions (FDF),<sup>7,10,13</sup> which are pdfs of the sub-grid scale scalar quantities.

The concept of sub-grid scale pdfs has also been adopted in the application of conserved scalar methods, which assume that the chemical state and thereby the species mass fractions, can be related to a conserved scalar, typically the mixture fraction in the case of nonpremixed combustion. Then, by presuming the sub-grid scale pdf of the mixture fraction  $\tilde{P}(Z)$ , the filtered species mass fractions  $\tilde{Y}_i$  in each computational cell can be evaluated by

$$\tilde{Y}_i = \int_{Z=0}^1 Y_i(Z) \tilde{P}(Z) dZ, \quad (1)$$

provided the functional dependence  $Y_i(Z)$  is known. Here and in the following the tilde denotes density-weighted spatial filtering.

$\tilde{P}(Z)$  is commonly assumed to follow a  $\beta$ -function distribution, parametrized by the first two moments of the mixture fraction. The filtered mixture fraction is determined by the solution of a transport equation; its sub-grid scale variance is typically given by a sub-grid scale model. The validity of the  $\beta$ -function representation of the pdf of the mixture fraction has been investigated by several authors using DNS data of nonpremixed reacting flows for constant and variable density.<sup>1,3–5,14–16</sup> The two main conclusions are that the  $\beta$ -function pdf provides an excellent estimate for the sub-grid scale mixture fraction distribution and that this estimate is even much better for LES than for RANS models. This is shown to be particularly true if the mixture fraction variance is taken from the DNS data, suggesting that the  $\beta$ -function as a model for the statistical distribution of the mixture fraction performs much better than the commonly used sub-grid scale models for the mixture fraction variance.

The mixture fraction variance can be determined by standard sub-grid scale modeling methods like the scale similarity model as proposed by Cook and Riley,<sup>3</sup> or by using a small scale equilibrium assumption and determining the remaining coefficient by the Dynamic Procedure following Pierce and Moin.<sup>17</sup> However, DesJardin and Frankel,<sup>1</sup> for instance, have shown that their modeling results do not differ if they use a  $\delta$ -function instead of the  $\beta$ -function as sub-grid

mixture fraction pdf in a conserved scalar approach. This conclusion depends certainly on the spatial resolution of the calculation and the turbulence intensity.

Different approaches have been used to specify the function  $Y_i(Z)$  appearing in Eq. (1). Among these are the infinitely fast irreversible chemistry assumption,<sup>17</sup> the equilibrium assumption,<sup>3</sup> the conditional moment closure method,<sup>6,18</sup> and the steady laminar flamelet model.<sup>4,5</sup>

In the present study the Lagrangian Flamelet Model<sup>19,20</sup> is applied in a large-eddy simulation for a turbulent, piloted methane/air diffusion flame. The results are discussed and compared with experimental data by Refs. 21–23.

## II. MATHEMATICAL MODEL

### A. Large-eddy simulation

The set of equations solved in the current modeling study can be derived by applying a spatial, density-weighted filter to the continuity equation, the momentum equations, and the mixture fraction transport equation resulting in

$$\frac{\partial \bar{\rho}}{\partial t} + \nabla \cdot (\bar{\rho} \tilde{\mathbf{v}}) = 0, \quad (2)$$

$$\frac{\partial \bar{\rho} \tilde{\mathbf{v}}}{\partial t} + \nabla \cdot (\bar{\rho} \tilde{\mathbf{v}} \tilde{\mathbf{v}}) = -\nabla \bar{p} + \nabla \cdot \tilde{\boldsymbol{\sigma}} - \nabla \cdot (\bar{\rho} (\tilde{\mathbf{v}} \tilde{\mathbf{v}} - \tilde{\mathbf{v}} \tilde{\mathbf{v}})), \quad (3)$$

$$\frac{\partial \bar{\rho} \tilde{Z}}{\partial t} + \nabla \cdot (\bar{\rho} \tilde{\mathbf{v}} \tilde{Z}) = \nabla \cdot (\bar{\rho} \tilde{D}_Z \nabla Z) - \nabla \cdot (\bar{\rho} (\tilde{\mathbf{v}} \tilde{Z} - \tilde{\mathbf{v}} \tilde{Z})), \quad (4)$$

with

$$\tilde{\boldsymbol{\sigma}} = \bar{\mu} ((\nabla \tilde{\mathbf{v}}) + (\nabla \tilde{\mathbf{v}})^T) - \frac{2}{3} \bar{\mu} \nabla \cdot \tilde{\mathbf{v}} \boldsymbol{\delta}. \quad (5)$$

Here,  $\rho$  is the density,  $t$  the time,  $\mathbf{v}$  the velocity vector,  $p$  the pressure,  $Z$  the mixture fraction,  $D_Z$  the molecular diffusion coefficient of the mixture fraction,  $\boldsymbol{\delta}$  the unity tensor, and  $\mu$  the dynamic viscosity.

The spatially filtered value  $\bar{\phi}$  of a quantity  $\phi$  is defined as

$$\bar{\phi} = \int_{\mathcal{D}} G(\mathbf{x} - \mathbf{x}') \phi(\mathbf{x}') d\mathbf{x}', \quad (6)$$

where  $\mathcal{D}$  denotes the integration domain,  $\mathbf{x}$  is the coordinate vector, and given the filter size  $\Delta$ , the spatial filter function is defined as

$$G(\mathbf{x} - \mathbf{x}') = \begin{cases} 1, & \text{if } |\mathbf{x} - \mathbf{x}'| \leq \frac{\Delta}{2}, \\ 0, & \text{otherwise.} \end{cases} \quad (7)$$

As mentioned earlier the tilde denotes the Favre filtered value, for any quantity  $\phi$  given by  $\tilde{\phi} = \bar{\rho} \phi / \bar{\rho}$ .

The unclosed terms in Eqs. (3) and (4) are expressed by using eddy viscosity type models, such that the sub-grid scale fluxes in the momentum equations and the mixture fraction transport equation are given by

$$\bar{\rho} (\tilde{\mathbf{v}} \tilde{\mathbf{v}} - \tilde{\mathbf{v}} \tilde{\mathbf{v}}) = -2 \bar{\rho} \nu_t \tilde{\mathbf{S}}, \quad \tilde{\mathbf{S}} = \frac{1}{2} ((\nabla \tilde{\mathbf{v}}) + (\nabla \tilde{\mathbf{v}})^T) \quad (8)$$

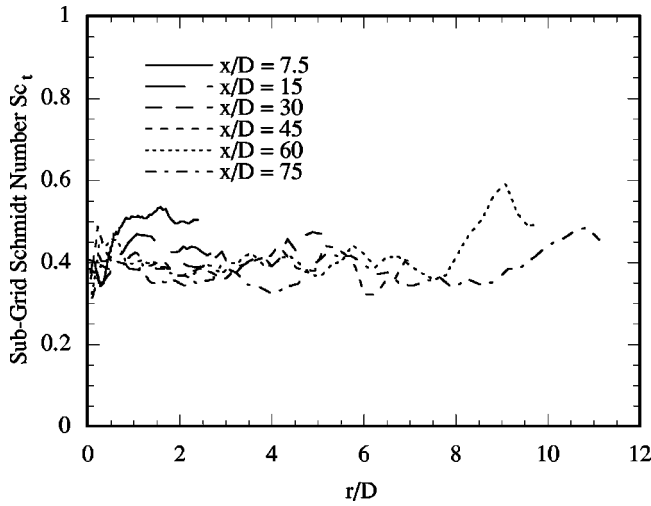


FIG. 1. Sub-grid scale Schmidt number of methane/air jet diffusion flame (Flame D) at different downstream positions.

and

$$\bar{\rho}(\widetilde{\mathbf{v}Z} - \widetilde{\mathbf{v}}\widetilde{Z}) = -\bar{\rho}D_t\nabla\widetilde{Z}, \tag{9}$$

where  $\nu_t$  and  $D_t$  are the sub-grid kinematic eddy viscosity and eddy diffusivity, respectively.

The eddy viscosity  $\nu_t$  is given by the Smagorinsky model as

$$\nu_t = C\Delta^2|S|, \tag{10}$$

where following Moin *et al.*<sup>24</sup> the Smagorinsky constant  $C$  is determined by the Dynamic Model as a function of time and space. This procedure needs no model constants and assures that the turbulent fluxes vanish in the limit of a laminar flow.

The sub-grid diffusivity  $D_t$  is determined from

$$D_t = \nu_t/Sc_t, \tag{11}$$

assuming a constant turbulent Schmidt number. In Reynolds averaged simulations the turbulent Schmidt number is commonly assumed to be equal to 0.7. However, in LES this value is different. An approximation for a constant sub-grid scale Schmidt number has been obtained by evaluating the sub-grid eddy viscosity  $\nu_t$  and the sub-grid diffusivity  $D_t$  by applying the Dynamic Model. The sub-grid Schmidt number can then be determined from Eq. (11). The resulting time averaged sub-grid Schmidt number distribution for the flow configuration described below is shown in Fig. 1 at different downstream positions. The data clearly indicate that a constant value of  $Sc_t=0.4$  is a good approximation throughout the whole domain.

The sub-grid scale diffusivity  $D_t$  is computed as  $D_t = \nu_t/Sc_t$  assuming a constant turbulent Schmidt number  $Sc_t=0.4$ . This value has been found to be appropriate from calculations, where  $D_t$  has also been determined by the Dynamic Model.

### B. The Lagrangian Flamelet Model

The Lagrangian Flamelet Model (LFM) is used in this study to describe the turbulence–chemistry interactions. This approach has successfully been applied in RANS calcula-

tions of turbulent jet diffusion flames.<sup>19,20</sup> The model follows the conserved scalar approach, which has briefly been described in the Introduction, and uses the flamelet ideas.<sup>25,26</sup> Here however, the function  $Y_i(Z)$  is determined by the solution of the unsteady rather than the steady flamelets equations.

The unsteady flamelet equations for the species mass fractions  $Y_i$  and the temperature  $T$  can be written as

$$\rho \frac{\partial Y_i}{\partial \tau} - \rho \frac{\chi}{2} \frac{\partial^2 Y_i}{\partial Z^2} - \dot{m}_i = 0, \tag{12}$$

$$\rho \frac{\partial T}{\partial \tau} - \rho \frac{\chi}{2} \left( \frac{\partial^2 T}{\partial Z^2} + \frac{1}{c_p} \frac{\partial c_p}{\partial Z} \frac{\partial T}{\partial Z} \right) + \frac{1}{c_p} \left( \sum_{k=1}^N h_k \dot{m}_k + \dot{q}_R''' - \mathcal{H} \right) = 0. \tag{13}$$

Here  $\tau$  is a Lagrangian type flamelet time,  $h_i$  and  $\dot{m}_i$  are the specific enthalpy and the chemical production rate per unit volume of species  $i$ , respectively,  $c_p$  is the constant pressure specific heat capacity, and the scalar dissipation rate  $\chi$  has been introduced as

$$\chi = 2D_Z\nabla Z \cdot \nabla Z. \tag{14}$$

$D_Z$  is the diffusion coefficient of the mixture fraction and  $\mathcal{H}$  accounts for the enthalpy flux by mass diffusion. The exact form for this term depends on the particular diffusion model and is given in Ref. 27 for the present work. In Eqs. (12) and (13) the Lewis numbers of all chemical species have been assumed to be unity. This assumption is discussed in great detail in Ref. 20, where it has been argued that in turbulent combustion only a thin region around the reaction zone is governed by molecular transport, whereas turbulent transport is predominant in the outer inert mixing region, which implies unity Lewis numbers. Numerical simulations have been performed for the present configuration assuming nonunity Lewis numbers. The results show that Lewis number effects indeed cannot explain the remaining discrepancies to the experimental data discussed below. These simulations show that the temperature is only influenced in the lean part of the flame. Of the major species only molecular hydrogen reveals changes on the rich side, which lead to an even stronger overprediction than the unity Lewis number results.

The radiation heat loss term  $\dot{q}_R'''$  is represented by using an optically thin gray gas approximation as given by Smith *et al.*<sup>28</sup> This model provides some basic features of the radiation process, for example, that the heat loss essentially occurs at the highest temperature and that the radiation process is slow compared to other physical time scales of the problem, which has been discussed in detail in Ref. 19. The validity of the model has been assessed by comparing the predicted with the measured conditionally averaged temperatures at  $x/D=60$  and  $x/D=75$ , which are in very good agreement. In contrast, calculations which neglect the influence of radiation overestimate the temperature at  $x/D=75$  by approximately 100 K.

The consideration of the time dependence certainly adds some complexity to the problem, but it has been shown that

it is essential to consider the unsteadiness, if for instance radiation cannot be neglected or NO formation is considered.<sup>19</sup>

Equations (12) and (13) can readily be solved and the solution used to provide the remaining unknown quantities such as the density and the temperature if the scalar dissipation is known as a function of the mixture fraction, and the flamelet time  $\tau$  can be related to the physical space coordinates. These relations will be derived next.

The basic idea of the model is that flamelets are introduced at the inflow boundary. These flamelets then move downstream, essentially by convective transport. In the following, for all instantaneous scalar quantities  $\phi$ , where  $\phi$  stands for the temperature or the species mass fractions, only averages over planes of equal nozzle distance  $x$ , conditioned on the mixture fraction, will be considered. This implies that these conditional averages, here denoted as  $\langle \phi | Z \rangle(x, t)$  depend only on one spatial coordinate, the axial nozzle distance  $x$ , and the time  $t$ . Hence, the flamelet solution needed in Eq. (1) can be parametrized as a function of  $x$  and  $t$  as  $Y_i(Z, x, t)$ , where  $x$  will be expressed by the flamelet time  $\tau$ .

Since flamelets are actually associated with the reaction zone, which is located in the vicinity of the stoichiometric mixture, the instantaneous local velocity of a flamelet particle has to be associated with the velocity of a point on the surface of a stoichiometric mixture fraction. Following Gibson<sup>29</sup> the velocity of iso-surfaces of a conserved scalar has contributions from the mean velocity and from the diffusion of that scalar. Thereby, the velocity of the resolved mixture fraction iso-surfaces can be expressed as

$$\tilde{v}_{\tilde{z}}(\mathbf{x}, t) = \tilde{\mathbf{v}}(\mathbf{x}, t) - \frac{\nabla \cdot (\bar{\rho}(D_z + D_t)\nabla \tilde{Z})}{\bar{\rho}|\nabla \tilde{Z}|} \mathbf{i}_z, \quad (15)$$

where  $\mathbf{i}_z = \nabla \tilde{Z} / |\nabla \tilde{Z}|$  is the unit vector in the direction of the gradient of the resolved mixture fraction.

If Eq. (15) is multiplied by the unit direction vector  $\mathbf{e}_x$ , then conditionally averaged over planes of equal nozzle distance  $x$ , and written for  $\tilde{Z} = Z_{st}$ , one obtains for the resolved axial velocity  $u$  of the stoichiometric mixture fraction surface,

$$\begin{aligned} \langle \tilde{u}_{\tilde{z}} | \tilde{Z} = Z_{st} \rangle(x, t) &= \langle \tilde{u} | \tilde{Z} = Z_{st} \rangle(x, t) \\ &- \left\langle \left( \frac{\nabla \cdot (\bar{\rho}(D_z + D_t)\nabla \tilde{Z})}{\bar{\rho}|\nabla \tilde{Z}|^2} \frac{\partial \tilde{Z}}{\partial x} \right) \Big|_{\tilde{Z} = Z_{st}} \right\rangle, \end{aligned} \quad (16)$$

which will be written as  $\langle \tilde{u}_{\tilde{z}} | \tilde{Z}_{st} \rangle$  in the following. Equation (16) can now be used to relate the Lagrangian type flamelet time  $\tau$  to the flamelet location in physical space as

$$\tau = \int_0^x \frac{1}{\langle \tilde{u}_{\tilde{z}} | \tilde{Z}_{st} \rangle(x', t)} dx'. \quad (17)$$

The second term on the right hand side of Eq. (16) represents the axial component of the velocity of the stoichiometric surface caused by diffusion normal to this surface. Hence, this term is identical to zero, if the mixture fraction

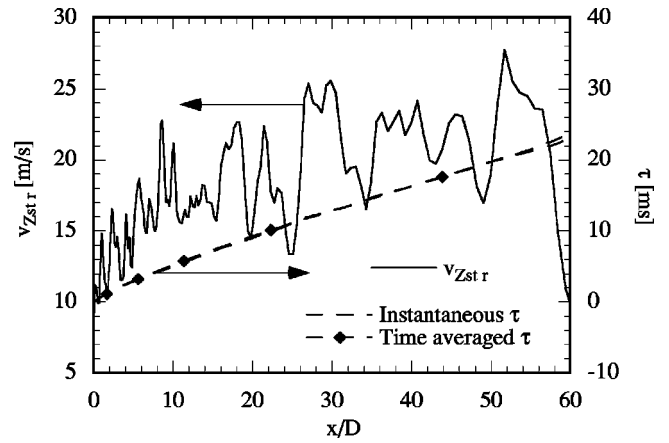


FIG. 2. Instantaneous velocity of the stoichiometric surface and instantaneous and time averaged Lagrangian type flamelet time as a function of the nozzle distance.

gradient vector  $\mathbf{i}_z$  is normal to the nozzle axis. This indeed is a good approximation for the time averaged mixture fraction field in turbulent jet diffusion flames. Since in the present formulation both the conditional averaging in Eq. (16) and also the integration in Eq. (17) introduce an average, the net effect of this term on the Lagrangian type flamelet time  $\tau$  is also assumed to be small and is therefore neglected.

As an example, Fig. 2 shows one instantaneous realization of  $\langle \tilde{u}_{\tilde{z}} | \tilde{Z}_{st} \rangle$  and the corresponding development of the Lagrangian type flamelet time  $\tau$  as a function of the dimensionless nozzle distance  $x/D$ . It is very obvious that the velocity  $\langle \tilde{u}_{\tilde{z}} | \tilde{Z}_{st} \rangle$  reveals strong turbulent fluctuations, whereas these do not appear in  $\tau$ . The reason for this can be explained as follows. It is also obtained in Fig. 2 that after a transitional region at approximately  $x/D=10$ , when the jet becomes self-similar, the mean value of  $\langle \tilde{u}_{\tilde{z}} | \tilde{Z}_{st} \rangle$  hardly changes and seems to be around 20 m/s, independent of  $x/D$ . This independence of the axial nozzle distance can be shown analytically<sup>30</sup> and has also been found in experiments.<sup>31</sup> The integration in Eq. (17) can hence be interpreted as a time integration, which would, after normalization, yield the time averaged mean velocity at stoichiometric mixture. This in turn implies that the time average of  $\tau$  should not be different from any instantaneous representation. Indeed, comparing the instantaneous representation of  $\tau$  with the time averaged value, which is also given in Fig. 2, shows that these are almost identical.

Using Eqs. (12) and (17) the resolved mass fractions of chemical species  $\tilde{Y}_i$  are given by

$$\tilde{Y}_i(\mathbf{x}, t) = \int_{Z=0}^1 Y_i(Z, x, t) \tilde{P}(Z, x, t) dZ. \quad (18)$$

$\tilde{P}(Z, x, t)$  is presumed to follow a  $\beta$ -function, whose shape is determined by the mean and the sub-grid scale variance of the mixture fraction. Since no transport equation for the mixture fraction variance is solved, this value has to be modeled. Following Pierce and Moin<sup>17</sup> the sub-grid scale mixture fraction variance can be expressed as

$$\overline{\rho} \widetilde{Z}^{\prime 2} = C_Z \Delta^2 \overline{\rho} |\nabla \widetilde{Z}|^2, \quad (19)$$

where the coefficient  $C_Z$  is determined using the Dynamic Procedure.

Similarly, the spatially filtered scalar dissipation rate, which will be needed in the following, is expressed in terms of the eddy diffusivity and the gradient of the resolved mixture fraction following Girimaji and Zhou<sup>32</sup> as

$$\widetilde{\chi} = 2(D_Z + D_t) \nabla \widetilde{Z} \cdot \nabla \widetilde{Z}, \quad (20)$$

where following Smooke<sup>33</sup>  $D_Z \sim T^{1.7}$ , which is evaluated with the mean temperature.

In Eqs. (12) and (13), the temporal development of the scalar dissipation rate is unknown and has to be related to the unconditional mean given by Eq. (20). A common approach is to presume the functional dependence of the scalar dissipation rate on the mixture fraction as  $\langle \chi | Z \rangle(x, t) = \langle \chi_{st} \rangle \times(x, t) f(Z)$ , where different analytic expressions for the function  $f(Z)$  have been suggested.<sup>19,25,34</sup> Then, it is sufficient to determine the value conditioned on stoichiometric mixture. This can be achieved by using this expression in the equation for the filtered scalar dissipation rate  $\widetilde{\chi}$ , which can be written as

$$\widetilde{\chi}(\mathbf{x}, t) = \int_{Z=0}^1 \langle \chi | Z \rangle(x, t) \overline{P}(Z, \mathbf{x}, t) dZ. \quad (21)$$

However, since in the present study a piloted flame is considered, the function  $f(Z)$  cannot be represented by the commonly applied expressions, which will be demonstrated below.

In the present model, the conditional average of the scalar dissipation rate as a function of the axial distance from the nozzle  $\langle \chi | Z \rangle(x, t)$  is computed by the inversion of the integral in Eq. (21), similar to the approach used by Bushe and Steiner<sup>6</sup> for the estimation of chemical source terms. The details of this model are described in Ref. 35, where also predictions for  $\langle \chi | Z \rangle(x, t)$  close to the nozzle are presented and discussed. There, it is shown that the influence of the pilot flame on flame stabilization can be explained only by its influence on the conditional scalar dissipation rate.

It should be noted that this model also ensures that the actual flamelet does not necessarily extend over the whole mixture fraction space. This can be observed from the conditional mean scalar dissipation rate distributions at  $x/D = 15, 30,$  and  $45$ , which are given in Fig. 3. At  $x/D = 15$  the scalar dissipation rate still extends over the complete mixture fraction space. This has already changed at  $x/D = 30$ , where the maximum mixture fraction value with non-zero scalar dissipation rate has become smaller than unity. This continues in the downstream direction, such that at  $x/D = 45$  the scalar dissipation rate is zero for  $Z > 0.65$ . In the calculations of the flamelets this region is still included. However, it can easily be seen from Eqs. (12) and (13) that for zero scalar dissipation rate, diffusive transport in mixture fraction space vanishes, resulting in localized homogeneous reactors at each value of  $Z$ , which are independent from each other.

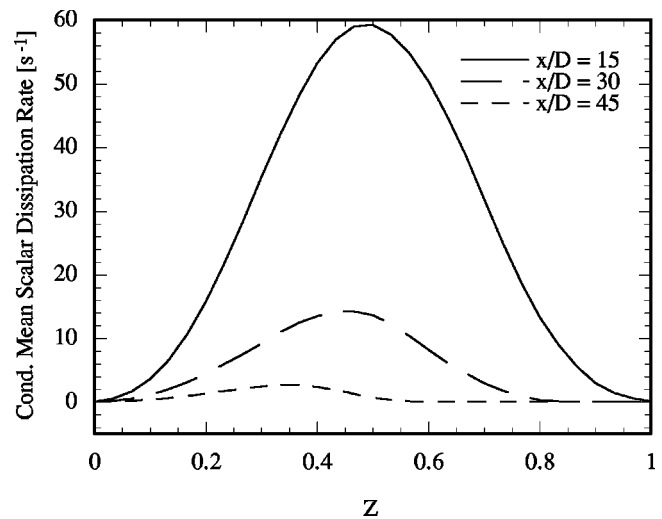


FIG. 3. Conditional mean scalar dissipation rate at different downstream locations.

In order to solve the unsteady flamelet equations, the scalar dissipation rate  $\chi(Z, \tau, t)$  appearing in Eqs. (12) and (13), which can be written as  $\chi(Z, x, t)$ , has to be expressed in terms of the conditional mean scalar dissipation rate  $\langle \chi | Z \rangle(x, t)$  determined from Eq. (21). The closure assumption here is that  $\chi(Z, x, t)$  is given by the conditional mean scalar dissipation rate,

$$\chi(Z, x, t) = \langle \chi | Z \rangle(x, t), \quad (22)$$

which in turn implies that also the results obtained by solving the flamelet equations are conditional mean values.

In this model the solution of the flamelet equations  $Y_i(Z, x, t)$  is still a function of the time  $t$ , because the Lagrangian type flamelet time  $\tau(x, t)$  given by Eq. (17) and also the model for the scalar dissipation rate given by Eq. (22) have an implicit time dependence. However, as demonstrated in Fig. 2, the comparison of an arbitrary instantaneous representation of  $\tau$  with its time averaged mean indicates that the time dependence of  $\tau$  is very weak and will therefore be neglected. In order to simplify the model, the time dependence of the scalar dissipation rate is also neglected, which means that in the calculations presented below time averaged values are used for the scalar dissipation rate.

Note that this assumption still allows for turbulent fluctuations of the resolved mass fractions and temperature, because it only neglects the influence of fluctuations of the scalar dissipation rate on the chemistry. This assumption can be justified for nonpremixed combustion far from extinction as discussed by Kuznetsov and Sabel'nikov.<sup>36</sup> The reason for this is that for lower values of the scalar dissipation rate its influence on the mass fractions of the chemical species and the temperature is weak, as for instance shown in Ref. 27. The validity of this assumption is demonstrated in Ref. 35 by a comparison with calculations using the time dependent instantaneous conditional scalar dissipation rate.

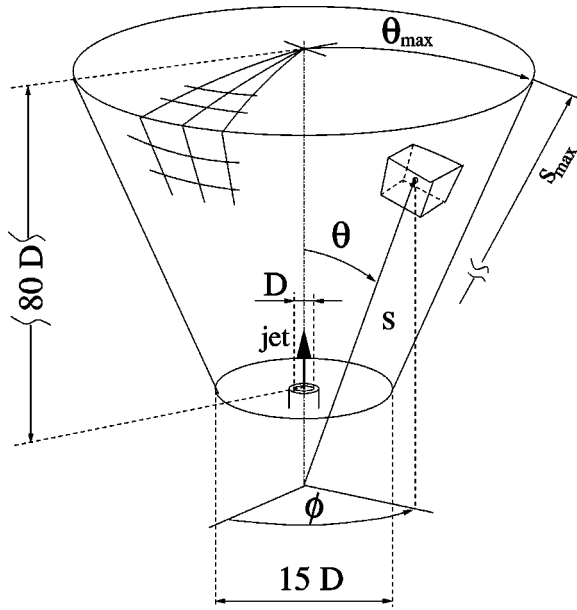


FIG. 4. Schematic representation of the coordinate system used in the simulation.

### III. NUMERICAL PROCEDURE

#### A. Algorithm

The numerical computation of the flow was carried out with a second-order finite volume code, which has originally been developed for the DNS of nonreacting, low Mach number turbulent jets by Boersma *et al.*<sup>37</sup> The computational mesh is in spherical coordinates as shown in Fig. 4. It has 192 cells in the radial coordinates  $s$ , 110 points in the tangential direction  $\Theta$ , and 48 points in the azimuthal direction  $\phi$ .

The LES transport equations for momentum and the scalar  $Z$  as given by Eqs. (3) and (4) are advanced in time using a predictor–corrector–projection scheme following Najm *et al.*<sup>38</sup> The advancement of the numerical solution from time-level  $t^n$  to  $t^{n+1} = t^n + \Delta t^n$  involves the following steps.

- (1) The Adams–Bashford predictor-step:

$$\begin{aligned} (\widehat{\rho \tilde{u}_i})^* &= (\rho \tilde{u}_i)^n - \frac{\Delta t^n}{2} \left[ \left( 2 + \frac{\Delta t^n}{\Delta t^{n-1}} \right) (\text{adv.} + \text{diff.})_{u_i}^n \right. \\ &\quad \left. - \frac{\Delta t^n}{\Delta t^{n-1}} (\text{adv.} + \text{diff.})_{u_i}^{n-1} \right], \end{aligned} \quad (23)$$

$$\begin{aligned} (\widehat{\rho \tilde{Z}})^* &= (\rho \tilde{Z})^n - \frac{\Delta t^n}{2} \left[ \left( 2 + \frac{\Delta t^n}{\Delta t^{n-1}} \right) (\text{adv.} + \text{diff.})_Z^n \right. \\ &\quad \left. - \frac{\Delta t^n}{\Delta t^{n-1}} (\text{adv.} + \text{diff.})_Z^{n-1} \right], \end{aligned} \quad (24)$$

yields the predictions denoted with the asterisk resulting from the advective and diffusive fluxes, here abbreviated as (adv. + diff.), which are given at the time-levels  $t^n$  and  $t^{n-1}$ . Even though for the sake of a simple notation it is not indicated in Eqs. (23) and (24) all diffusive terms, which involve derivatives with respect to  $\phi$ , are treated implicitly. A TVD scheme is applied for the advection of

the scalar  $Z$  to avoid spurious oscillations in the vicinity of strong gradients which occur particularly in the shear layer of the jet close to the nozzle exit, where large amounts of unmixed fuel meet the oxidizer from the co-flow.

- (2) The predicted density  $\bar{\rho}^*$  is obtained by

$$\tilde{Z}^* = \frac{(\rho \tilde{Z})^*}{\bar{\rho}^n}, \quad (25)$$

$$\frac{1}{\bar{\rho}^*} = \int_0^1 \frac{1}{\rho(Z, s)} \tilde{P}^*(Z, \mathbf{x}, t) dZ, \quad (26)$$

integrating the pdf of the mixture fraction given as  $\tilde{P}^*(Z, \mathbf{x}, t) = P(Z, \tilde{Z}^*, \tilde{Z}^{n2*})$ . The density  $\rho(Z, s)$  is given by the solution of the flamelet equations as described in the previous section. The sub-grid scale variance of the mixture fraction  $\tilde{Z}^{n2*}$  is evaluated using  $\tilde{Z}^*$  in Eq. (19).

- (3) Pressure correction: The corrected velocity field at the predictor level is computed as

$$(\tilde{\rho \tilde{u}_i})^* = (\widehat{\rho \tilde{u}_i})^* - \Delta t^n \frac{\partial p^*}{\partial x_i}, \quad (27)$$

where the pressure gradient is obtained from the solution of the Poisson equation,

$$\left[ \frac{\partial (\tilde{\rho \tilde{u}_i})^*}{\partial x_i} + \frac{\partial \bar{\rho}^*}{\partial t} \right] = \frac{1}{\Delta t^n} \frac{\partial^2 p^*}{\partial x_i \partial x_i}, \quad (28)$$

with the time derivative of the density being approximated by

$$\frac{\partial \bar{\rho}^*}{\partial t} \approx \frac{\left[ \left( 1 + \frac{\Delta t^n}{\Delta t^{n-1}} \right)^2 - 1 \right] \bar{\rho}^* - \left( 1 + \frac{\Delta t^n}{\Delta t^{n-1}} \right)^2 \bar{\rho}^n + \bar{\rho}^{n-1}}{\Delta t^n \Delta t^{n-1} \left( 1 + \frac{\Delta t^n}{\Delta t^{n-1}} \right)}. \quad (29)$$

- (4) The Adams–Molton corrector-step:

$$(\widehat{\rho \tilde{u}_i})^{n+1} = (\tilde{\rho \tilde{u}_i})^* - \frac{\Delta t^n}{2} [(\text{adv.} + \text{diff.})_{u_i}^n + (\text{adv.} + \text{diff.})_{u_i}^*], \quad (30)$$

$$(\bar{\rho \tilde{Z}})^{n+1} = (\bar{\rho \tilde{Z}})^* - \frac{\Delta t^n}{2} [(\text{adv.} + \text{diff.})_Z^n + (\text{adv.} + \text{diff.})_Z^*], \quad (31)$$

involves the advective and diffusive fluxes, (adv. + diff.)<sup>\*</sup>, obtained with the predictor-step solution  $\bar{\rho}^*$ ,  $\tilde{u}_i^*$ ,  $\tilde{Z}^*$ .

- (5)  $\bar{\rho}^{n+1}$  is computed by

$$\tilde{Z}^{n+1} = \frac{(\bar{\rho \tilde{Z}})^{n+1}}{\bar{\rho}^*}, \quad (32)$$

$$\frac{1}{\bar{\rho}^{n+1}} = \int_0^1 \frac{1}{\rho(Z, r)} \tilde{P}(Z, \mathbf{x}, t)^{n+1} dZ. \quad (33)$$

- (6) Pressure correction:

$$(\tilde{\rho \tilde{u}_i})^{n+1} = (\widehat{\rho \tilde{u}_i})^{n+1} - \Delta t^n \frac{\partial p^{n+1}}{\partial x_i}, \quad (34)$$

with the pressure gradient obtained from the Poisson equation:

$$\left[ \frac{\partial(\widehat{\rho u_i})^{n+1}}{\partial x_i} + \frac{\partial(\widehat{\rho})^{n+1}}{\partial t} \right] = \frac{1}{\Delta t^n} \frac{\partial^2 p^{n+1}}{\partial x_i \partial x_i}. \quad (35)$$

## B. Boundary conditions

At the inflow boundary all the required mean quantities are specified according to the experimental data given in Ref. 22 for the fuel jet, pilot, and co-flowing air stream. Velocity fluctuations are added to the measured mean profiles  $u_{in,m}$  to mimic turbulent inflow conditions. The perturbed axial inflow velocity  $\tilde{u}_{in}$  is obtained by superimposing rotating helical and oscillating axisymmetric perturbations<sup>39</sup> on the mean profile as

$$\begin{aligned} \tilde{u}_{in}(\Theta, t) = & u_{in,m} + \sum_{i=1}^6 [A_i \sin(\alpha_i + i\phi + \Psi_i t)] \\ & + \sum_{i=7}^8 [A_i \sin(\Psi_i t)]. \end{aligned} \quad (36)$$

The numerical values for  $\alpha_i$ , which determine the phase shift of each helical mode in the azimuthal direction relative to  $i\phi$ , as well as the frequencies  $\Psi_i$  are randomly chosen. The coefficients  $A_i$  are specified to match the time averaged inflow velocity RMS  $u'_{in,m}$  observed in the experiments. With the present velocity perturbation this is achieved by setting  $A_i = 0.5 \cdot u'_{in,m}$  for all modes  $i = 1, \dots, 8$ . Calculations have also been performed without the random velocity fluctuations resulting in only very slight changes in the flow field predictions.

Following Akselvoll and Moin<sup>40</sup> a convective boundary condition is used for the outflow boundary at  $s = s_{\max}$  as

$$\frac{\partial \tilde{u}_i}{\partial t} + U_{\text{con}} \frac{\partial \tilde{u}_i}{\partial s} = 0. \quad (37)$$

Therein, the convection velocity  $U_{\text{con}}$  is the mean outflow velocity averaged over the azimuthal direction  $\phi$ . The convective boundary condition convects vortical structures, which eventually approach the outflow boundary, out of the computational domain, thereby stabilizing the simulation. Although this approach introduces an error in elliptic problems, it can still be applied to flows of convective nature like free jets without disturbing the upstream solution.<sup>37</sup> However, the region very close to the outflow boundary has to be disregarded in the analysis of the numerical results.

A traction-free condition is used for the lateral boundary at  $\Theta = \Theta_{\max}$ .<sup>41</sup> This condition is given by

$$\boldsymbol{\sigma} \cdot \mathbf{n} = \mathbf{0}, \quad (38)$$

where  $\mathbf{n}$  is the unit vector normal to the boundary. Unlike the no-slip or free-slip conditions it allows for a flux of ambient fluid across the lateral boundary. Thus, it is well-suited to capture the entrainment in a spreading jet.

## C. Flamelet calculations

The unsteady flamelet calculations have been performed using the FLAMEMASTER code.<sup>42</sup> The chemical mechanism used for the results presented in the following is the GRI 2.11 mechanism,<sup>43</sup> which includes reactions among 48 chemical species. In order to reduce the computational time a reduced version of the mechanism has been developed, which consists of 29 global reactions. The reduced chemical scheme has been kept rather large in order to avoid numerical difficulties in the formulation of the steady state concentrations and to yield exactly the same results as the original mechanism. As an example, the maximum difference in the NO mass fraction calculated using the detailed and the reduced mechanism is approximately 0.4%.

It will be discussed below that the main differences in the comparison of predictions and experiments is in the onset of chemical reactions in the very rich premixed part of the configuration, which in the current predictions occurs too early. In order to investigate the influence of the chemical scheme on the computational results, unsteady flamelet calculations have been performed with different chemical mechanisms, including GRI 3.0<sup>44</sup> and recent mechanisms from other authors.<sup>45-48</sup> The predictions using the mechanism by Warnatz show large differences and a strong overprediction of the temperature in the rich part of the flame, because the mechanism predicts the onset of chemical reactions in that region even earlier. The results obtained by the remaining mechanisms show some differences in the mass fractions of individual species. But only for the NO mass fractions a stronger sensitivity to the individual chemical scheme is observed. The GRI 3.0 mechanism, for instance, leads to substantially higher NO mass fraction than GRI 2.11. However, the qualitative performance of all these chemical schemes is very similar.

## IV. RESULTS AND DISCUSSION

The configuration used for the validation of the proposed models is a piloted methane/air jet diffusion flame (Sandia Flame D). The fuel is a 25/75% methane/air mixture. The fuel has been premixed with air in order to minimize the formation of polycyclic aromatic hydrocarbons and soot. The fuel nozzle has a diameter of  $D = 7.2$  mm and is enclosed by a broad pilot nozzle with a diameter of  $D_p = 2.62D$  and an air-co-flow. In the experiments the pilot composition and temperature have been adjusted such that the pilot stream has the same equilibrium composition as a mixture of the main fuel and oxidizer with a mixture fraction of  $Z = 0.27$ , which is slightly lean compared with a stoichiometric mixture fraction of  $Z = 0.35$ . In the LES the pilot can thereby be represented by specifying the appropriate inlet mixture fraction. The fuel bulk velocity is 49.6 m/s, which leads to a fuel stream based Reynolds number of  $Re = 22400$ .

The flame has been experimentally investigated by Hasel *et al.*,<sup>23</sup> who provided data for the velocity field obtained by LDV measurements and by Barlow and Frank,<sup>21,22</sup> who performed Rayleigh measurements for the temperature, and Raman and LIF measurements to obtain mass fractions of chemical species and the mixture fraction.

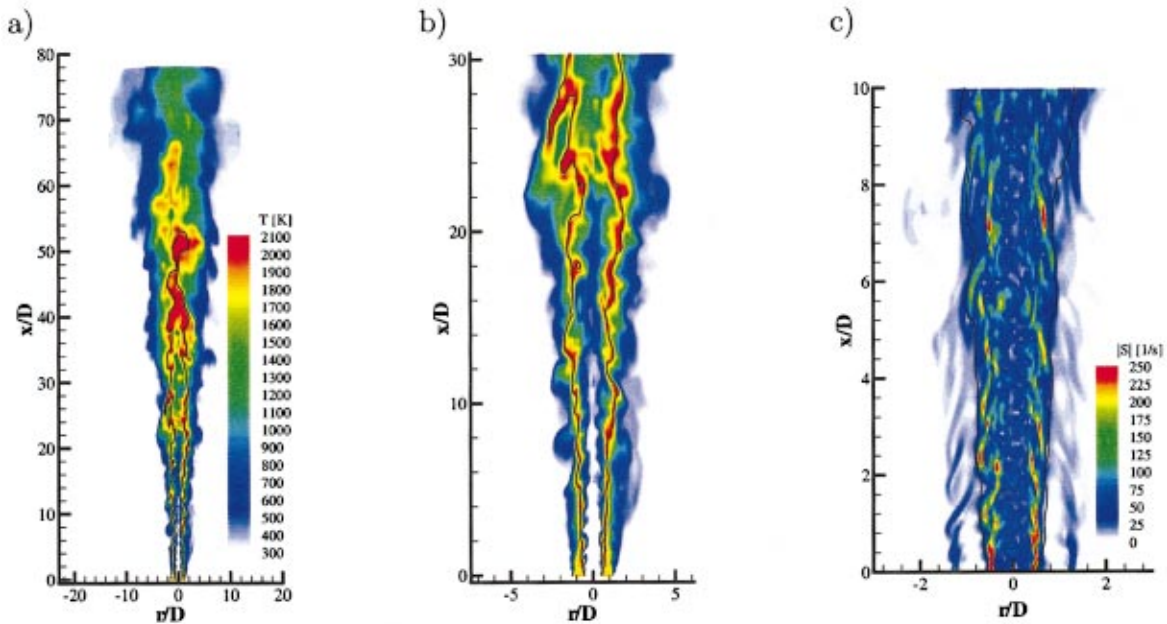


FIG. 5. (Color) Instantaneous temperature and strain rate distribution. The black line represents the contour of the stoichiometric mixture fraction.

In the remaining part of the paper, time averaged results from the simulation are discussed and compared with the experimental data. The averages have been obtained from the computational results by sampling over two flow-through times, where the flow-through time is defined as the time a particle traveling along the centerline would reside within the flow field. After a general discussion of the flame, the predictions of the flow field calculation, including velocity and mixture fraction field will be discussed. These results essentially serve as input quantities for the combustion model. Then, the predicted temperature and species mass

fractions will be shown and compared with unconditionally and conditionally averaged experimental data.

#### A. General observations

Figure 5(a) shows an instantaneous temperature field of the computed jet and Fig. 5(b) gives an enlarged view of the near field region at the same instance. Also shown in these figures is the surface of the stoichiometric mixture, which indicates the location of the reaction zone. Figure 5(b) clearly shows the broad pilot flame. It is also interesting to

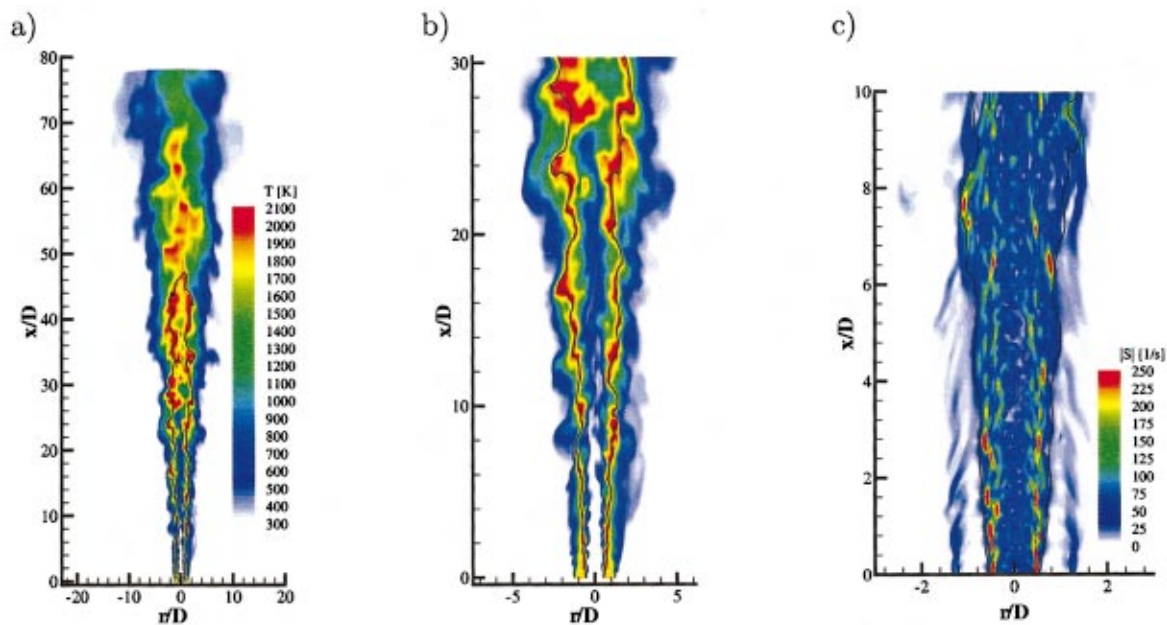


FIG. 6. (Color) Instantaneous temperature and strain rate distribution at a time 3.2 ms later than Fig. 5. The black line represents the contour of a stoichiometric mixture fraction.

note in this figure that close to the nozzle the region around the reaction zone hardly shows turbulent motion and might be regarded as being laminar. This has been found in many experiments and might be of great importance, since for fuels with Lewis numbers different from unity it can be the source of strong differential diffusion effects, which can survive even far downstream of the transition to turbulence as has been discussed in Ref. 20. In order to give an impression of the dynamics of the flame, Figs. 6(a) and 6(b) show the instantaneous temperature distribution at a time approximately 3.2 ms later than in Fig. 5. The comparison with Fig. 5 reveals that the jet core shows a completely different structure, indicating that turbulent structures have been transported far downstream, while in the outer part hardly any motion can be observed. It can also be seen that the location of the flame tip, indicated by the stoichiometric contour can strongly vary with time. For the current calculation the flame tip location moves between approximately  $x/D=48$  to  $x/D=62$ . In order to provide a better picture of the dynamics of the flame, animations of the computational results corresponding to Figs. 5(a) and 5(b) are provided on the world wide web.<sup>49</sup>

The temperature distribution given in Figs. 5 and 6 also allows some qualitative comparison with fundamental observations from experiments in jet diffusion flames. It can be observed, for instance in Fig. 6(b), that regions of very broad high temperature zones around the stoichiometric contour are alternating with regions of very narrow high temperature distribution. It can also be seen that the broad temperature regions always coincide with reaction zones, which are directed outwards, whereas the narrow temperature regions can be associated with reaction zone structures, which are inwardly directed. The analysis shows that these changes are essentially caused by fluctuations in the mixture fraction gradients which also cause fluctuations of the scalar dissipation rate. Since the scalar dissipation rate is also related to the rate of strain, it can be concluded from the calculations that regions of high strain rate are aligned with regions of a narrow temperature maximum. This is in accordance with the experimental findings of Rehm and Clemens.<sup>50</sup> The strain rate field in the region very close to the nozzle is shown in Figs. 5(c) and 6(c). The alignment of the reaction zone and the strain rate field starts to become obvious in the downstream regions of these figures. However, it is interesting to note that closer to the nozzle the reaction zone embraces the region of high rate of strain rather than to follow the high strain layers. This lack of alignment is, as pointed out by Rehm and Clemens,<sup>50</sup> because of the laminar nature of the region around the reaction zone, where the high viscosity does not allow the fluid to freely adjust to the applied strain. Similar structures have been found by Donbar *et al.*<sup>31</sup> in the analysis of two-dimensional CH measurements and PIV measurements in jet diffusion flames. It is generally observed in experiments that these structures occur in an angle with the jet axis of approximately  $45^\circ$ . A similar discussion on the scalar dissipation rate is provided in Ref. 35.

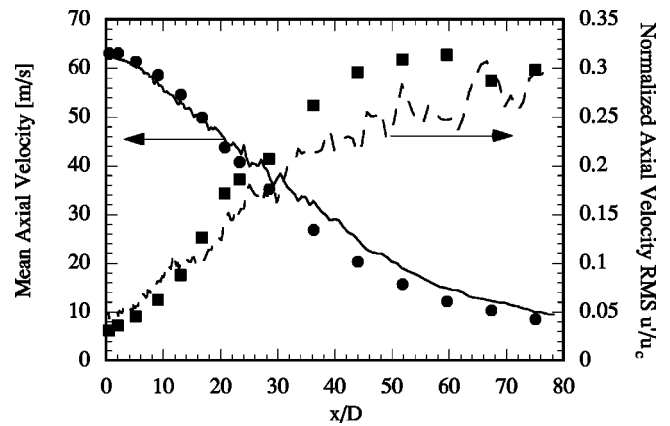


FIG. 7. Mean and RMS of axial velocity along the centerline (lines: calculation; symbols: experiments).

## B. Prediction of the flow field

The mean axial velocity and its normalized root mean square (RMS) along the centerline are given in Fig. 7. Both quantities are in reasonable agreement with the experimental data, although the mean values seem to be overpredicted in the far field region of the jet.

Figure 8 shows that the mean mixture fraction is well predicted by the current simulation along the centerline until  $x/D=60$ . Thereafter, the experimental data is slightly overpredicted. The mixture fraction RMS, including resolved and sub-grid contributions, is also given in Fig. 8. The experiment is slightly underpredicted in the far field of the jet. The underprediction for  $x/D < 10$  might be attributed to experimental uncertainties, since the RMS has to go to zero close to the nozzle. This conclusion is supported by the comparison of the temperature variance, which will be given in the following. In addition, Fig. 8 shows the sub-grid scale RMS of the mixture fraction, which is shown to be much smaller than the RMS based on the resolved and the sub-grid fluctuations, indicating that the major part of the turbulent mixture fraction fluctuations is resolved by the LES.

Radial mixture fraction profiles are given in Fig. 9 at  $x/D = 15, 30,$  and  $45$ . The comparison with the experimental data shows that the general agreement for both the mean and

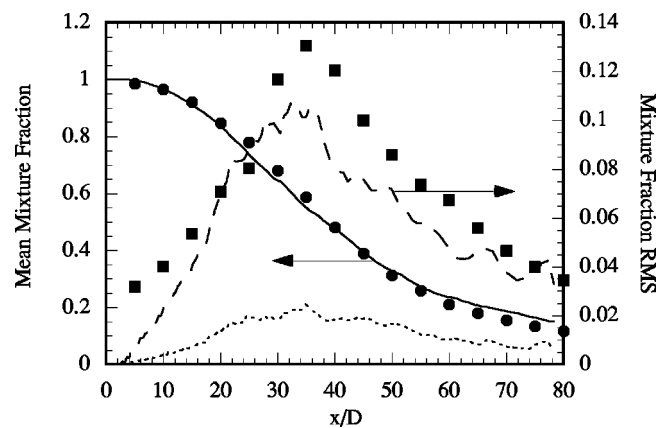


FIG. 8. Mean and RMS of mixture fraction along the centerline (lines: calculation; symbols: experiments).

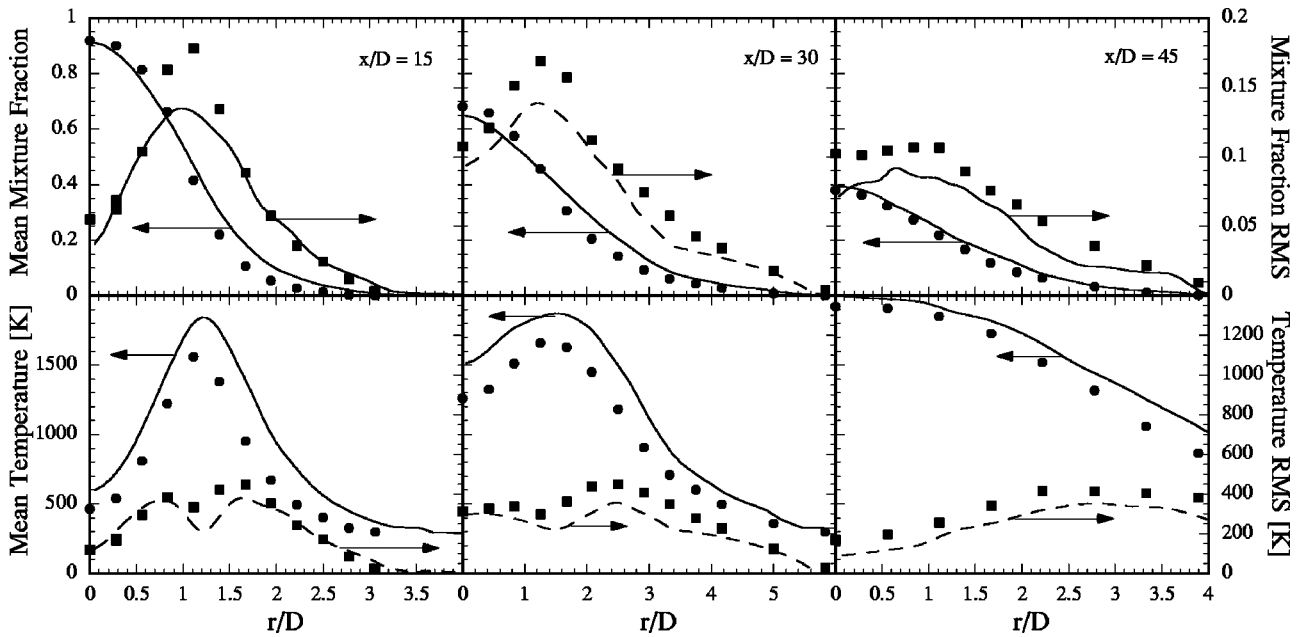


FIG. 9. Radial distribution of mean and the RMS of the mixture fraction and temperature at different downstream positions (lines: calculation; symbols: experiments).

the RMS of the mixture fraction, is reasonable at all these positions, although the maximum values of the mixture fraction RMS seem to be consistently underpredicted.

**C. Predictions by the chemistry model**

The calculated mean temperature and the temperature RMS along the centerline are shown in Fig. 10. Radial profiles of these quantities are provided in Fig. 9. Both the mean and the RMS agree well with the experimental data. Even the decrease in the temperature RMS around the maximum mean temperature, which can be observed very clearly in the axial profile in Fig. 10, is well represented by the simulation. It is interesting to note that this is not caused by heat release, but is simply because of the vanishing temperature gradient with respect to the mixture fraction. The mean temperature is slightly overpredicted up to  $x/D=40$ , which will be discussed below.

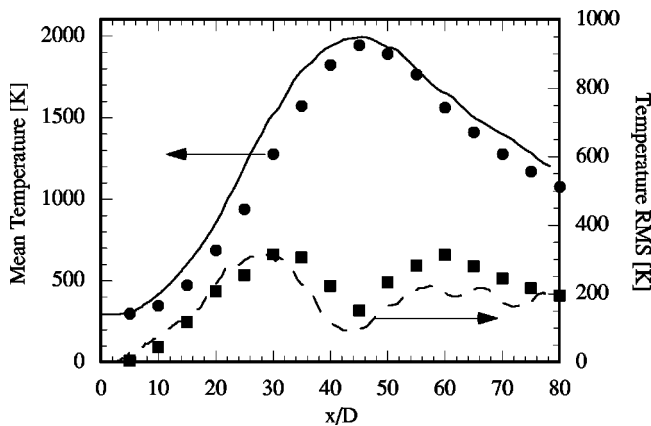


FIG. 10. Mean and RMS of temperature along the centerline (lines: calculation; symbols: experiments).

The following figures show centerline profiles for species mass fractions of  $CH_4$  and  $O_2$  (Fig. 11),  $H_2O$  and  $H_2$  (Fig. 12),  $CO_2$  and  $CO$  (Fig. 13), and  $NO$  and  $OH$  (Fig. 14). In general all profiles agree well with the experimental data. Small discrepancies at  $x/D > 60$  can mainly be attributed to the overprediction of the mixture fraction. In the rich part of the flame at  $x/D < 40$ ,  $H_2O$  and  $CO_2$  are also slightly overpredicted, while  $CH_4$  and  $O_2$  are underpredicted. Also very obvious is the overprediction of the intermediates  $H_2$  and  $CO$  on the rich side. The reason for this is the partial premixing of the fuel with air. As will be shown below, this causes substantial chemical reactions to occur in the rich premixed part of the jet farther downstream. The onset of this partially premixed burning occurs in the current simulation earlier than can be estimated from the experiments. The  $OH$  radical

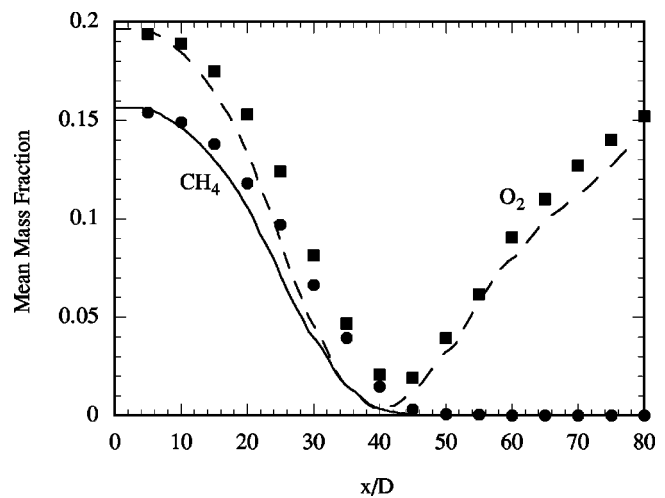


FIG. 11. Mean  $CH_4$  and  $O_2$  mass fractions along the centerline (lines: calculation; symbols: experiments).

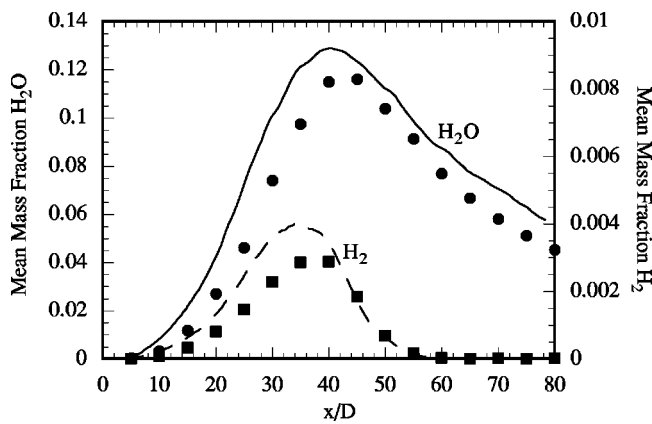


FIG. 12. Mean H<sub>2</sub>O and H<sub>2</sub> mass fractions along the centerline (lines: calculation; symbols: experiments).

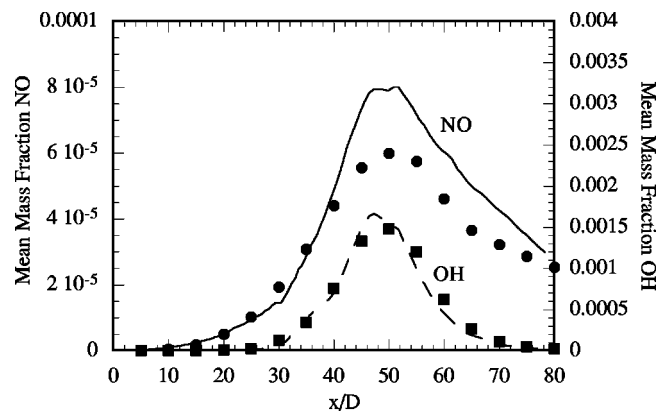


FIG. 14. Mean NO and OH mass fractions along the centerline (lines: calculation; symbols: experiments).

mass fraction shown in Fig. 14 is predicted very accurately. Also the agreement of predicted and measured NO mass fractions can be considered to be very good. The analysis of the formation of nitric oxide shows that only approximately one third of the total NO is formed by the thermal path and that the N<sub>2</sub>O path contributes to approximately 10%. The formation of NO is thereby dominated by the prompt path.

The comparison of the radial profiles of the chemical species with the experimental data shows reasonable agreement and does not differ substantially from the centerline profiles. The presentation is therefore being omitted.

Although the results discussed so far are quite encouraging, the conclusions about the chemical structure of the turbulent flame, which can be drawn from these, are quite limited, because only time averaged quantities have been discussed. It is therefore important to compare the time averages of the temperature and mass fractions of the chemical species conditioned on the mixture fraction, because conditioned data provide substantially more insight in turbulence/chemistry interactions.

The conditional averages at the axial locations  $x/D = 15, 30,$  and  $45$  for the temperature and the mass fractions

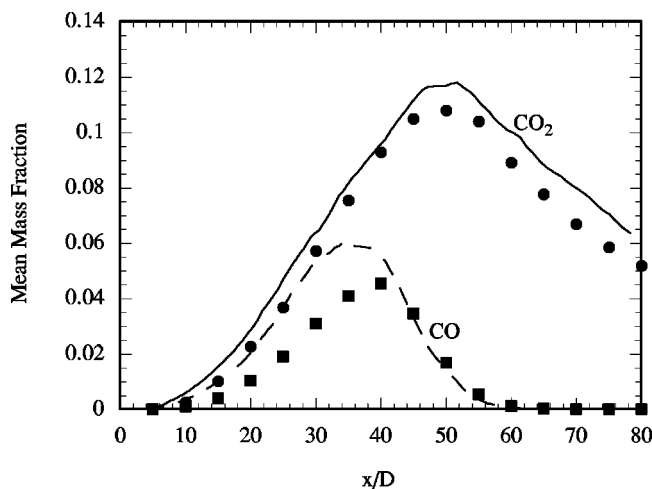


FIG. 13. Mean CO<sub>2</sub> and CO mass fractions along the centerline (lines: calculation; symbols: experiments).

of the chemical species CH<sub>4</sub>, O<sub>2</sub>, H<sub>2</sub>O, H<sub>2</sub>, CO<sub>2</sub>, CO, NO, and OH are shown in Fig. 15. At  $x/D = 15$  the temperature as well as all the species mass fraction profiles agree quite well with the experimental data on the lean side, but tend to overpredict fuel to product conversion on the rich side. In addition to the reasons given above, this can be attributed to the fact that the current model does not allow for local flame extinction. By comparing the simulation with the single point experimental data, it becomes evident that, at least up to a mixture fraction of  $Z = 0.5$ , the temperature, as an example, agrees very well with the burning branch of the data. The lower values of the conditional mean temperature in the experimental data in Fig. 15 are caused by comparably few extinguished data points. This is shown in Fig. 15 for the temperature at  $x/D = 15$ , which includes the single point data from the experiments used to determine the conditional averages. However, this seems to demonstrate the need for an extension of the model.

As discussed earlier, the consumption of fuel and molecular oxygen in the fuel consumption layer is slightly overpredicted, which also leads to an overprediction of the water and carbon dioxide values.

Farther downstream at  $x/D = 30$  the profiles still agree reasonably well with the experimental data. For mixture fraction values of  $Z > 0.4$  the consumption of CH<sub>4</sub> and O<sub>2</sub> on the rich premixed side is already visible in both the computational results and the experiments. Also, in the predicted and the measured H<sub>2</sub>O profile a formation region is observed at approximately  $Z = 0.6$ . However, the partially premixed burning is stronger in the predicted results, which is very obvious in the temperature, and leads to overpredicted intermediate mass fractions. NO is well predicted on the stoichiometric to lean side. However, the predicted profile reveals a NO consumption region at the location of the rich premixed flame, which cannot be observed in the experimental data.

At  $x/D = 45$  the effect of the partially premixed reaction zone becomes very strong and chemical reactions start at even richer mixtures. This is observed in the temperature profile, which indicates heat release at approximately  $Z = 0.65$ . The partially premixed burning leads to a plateau region in the H<sub>2</sub>O profile of the numerical simulation, which is also very obvious in the experiment. Also the CO<sub>2</sub> profile,

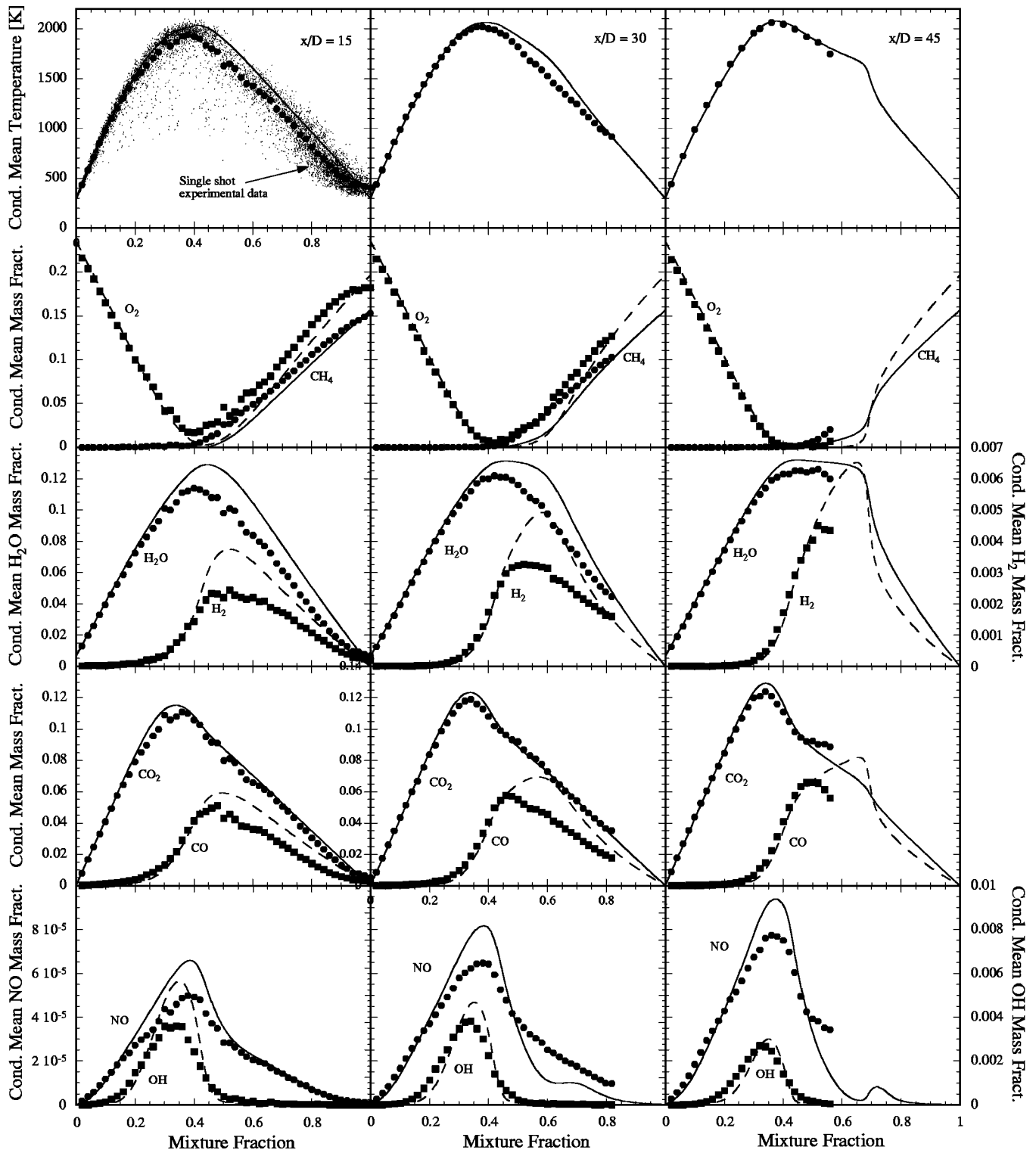


FIG. 15. Conditional averages at different downstream positions (lines: calculation; symbols: experiments).

which is much less influenced by the chemical reactions on the rich side, is in good agreement with the experimental data. The discrepancies discussed for CO and NO on the rich side seem to remain at this location, but are limited to the very rich region. On the lean side the agreement can still be considered to be quite good.

### V. CONCLUSIONS

The Lagrangian Flamelet Model, which has been successfully used in RANS calculations of turbulent diffusion flames has been formulated as a combustion model for large-eddy simulations of turbulent jet diffusion flames. The model has been applied in a large-eddy simulation of a turbulent

methane/air flame (Sandia flame D), which has a partially premixed fuel stream. In the LES, sub-grid scale quantities have generally been determined using the Dynamic Procedure. The eddy-diffusivity has been computed from the assumption of a constant sub-grid turbulent Schmidt number. From calculations employing the Dynamic Procedure to compute the eddy diffusivity it has been found that a constant value of  $Sc_t=0.4$  is a very good approximation.

The results are compared with experimental data for the velocity and the mixture fraction field, and for unconditional and conditional averages of temperature and various chemical species, including CO and NO. The agreement is very reasonable for all quantities. The remaining differences have been discussed. In the analysis of the computational results it has been found in accordance with experimental data that regions of high strain appear in layers, which are generally directed inwards. In regions with developed turbulence these layers tend to align with the reaction zone. It has also been found in the analysis of the conditional mean temperature and mass fraction profiles that downstream of  $x/D=30$  chemical reactions lead to substantial fuel consumption in the rich partially part of the flame. In the present calculations the onset of the partially premixed burning occurs to early leading to a slight overprediction in the consumption of the reactants and the formation of water and the intermediates molecular hydrogen and carbon monoxide.

## ACKNOWLEDGMENTS

This work was funded in part by the U.S. Department of Energy in the frame of the ASCI program. This support is gratefully acknowledged. The authors are indebted to Robert Barlow for his help in providing the experimental data. We also thank George Kosály for many helpful discussions.

- <sup>1</sup>P. E. DesJardin and S. H. Frankel, "Large eddy simulation of a nonpremixed reacting jet: Application and assessment of subgrid-scale combustion models," *Phys. Fluids* **10**, 2298 (1998).
- <sup>2</sup>S. M. De Bruyn Kops, J. J. Riley, G. Kolaly, and A. W. Cook, "Investigation of modeling for non-premixed turbulent combustion," *Flow, Turbul. Combust.* **60**, 105 (1998).
- <sup>3</sup>A. W. Cook and J. J. Riley, "A subgrid model for equilibrium chemistry in turbulent flows," *Phys. Fluids* **6**, 2868 (1994).
- <sup>4</sup>A. W. Cook, J. J. Riley, and G. Kosaly, "A laminar flamelet approach to subgrid-scale chemistry in turbulent flows," *Combust. Flame* **109**, 332 (1997).
- <sup>5</sup>A. W. Cook and J. J. Riley, "Subgrid-scale modeling for turbulent reactive flows," *Combust. Flame* **112**, 593 (1998).
- <sup>6</sup>W. K. Bushe and H. Steiner, "Conditional moment closure for large eddy simulation of nonpremixed turbulent reacting flows," *Phys. Fluids* **11**, 1896 (1999).
- <sup>7</sup>P. J. Colucci, F. A. Jaber, P. Givi, and S. B. Pope, "Filtered density function for large eddy simulation of turbulent reacting flows," *Phys. Fluids* **10**, 499 (1998).
- <sup>8</sup>A. R. Kerstein, "A linear-eddy model of turbulent scalar transport and mixing," *Combust. Sci. Technol.* **60**, 391 (1988).
- <sup>9</sup>P. A. McMurtry, S. Menon, and A. R. Kerstein, "A linear eddy sub-grid model for turbulent reacting flows: Application to hydrogen-air combustion," *Proc. Combust. Inst.* **24**, 271 (1992).
- <sup>10</sup>S. B. Pope, "Pdf methods for turbulent reactive flows," *Prog. Energy Combust. Sci.* **11**, 119 (1985).
- <sup>11</sup>J. Y. Chen, W. Kollman, and R. W. Dibble, "Pdf modeling of turbulent methane-air nonpremixed jet flames," *Combust. Sci. Technol.* **64**, 315 (1989).
- <sup>12</sup>V. Saxena and S. B. Pope, "Pdf calculations of major and minor species in a turbulent piloted jet flame," *Proc. Combust. Inst.* **27**, 1081 (1998).
- <sup>13</sup>F. Gao and E. E. O'Brien, "A large-eddy simulation scheme for turbulent reacting flows," *Phys. Fluids A* **5**, 1282 (1993).
- <sup>14</sup>J. Jimenez, A. Linan, M. M. Rogers, and F. J. Higuera, "A priori testing of subgrid models for chemically reacting non-premixed turbulent shear flows," *J. Fluid Mech.* **349**, 149 (1997).
- <sup>15</sup>C. K. Madnia and P. Givi, "Direct numerical simulation and large eddy simulation of reacting homogeneous turbulence," in *Large Eddy Simulation of Complex Engineering and Geophysical Flows*, edited by B. Galperin and S. A. Orszag (Cambridge University Press, Cambridge, 1993).
- <sup>16</sup>C. Wall, B. Boersma, and P. Moin, "An evaluation of the assumed beta probability density function subgrid-scale model for large eddy simulation of nonpremixed, turbulent combustion with heat release," *Phys. Fluids* **7**, 2522 (2000).
- <sup>17</sup>C. D. Pierce and P. Moin, "A dynamic model for subgrid-scale variance and dissipation rate of a conserved scalar," *Phys. Fluids* **10**, 3041 (1998).
- <sup>18</sup>H. Steiner and W. K. Bushe, "Large eddy simulation of a turbulent diffusion flame with conditional source-term estimation," *Phys. Fluids* (submitted).
- <sup>19</sup>H. Pitsch, M. Chen, and N. Peters, "Unsteady flamelet modeling of turbulent hydrogen/air diffusion flames," *Proc. Combust. Inst.* **27**, 1057 (1998).
- <sup>20</sup>H. Pitsch, "Unsteady flamelet modeling of differential diffusion in turbulent jet diffusion flames," *Combust. Flame* (accepted).
- <sup>21</sup>R. S. Barlow and J. H. Frank, "Effect of turbulence on species mass fractions in methane/air jet flames," *Proc. Combust. Inst.* **27**, 1087 (1998).
- <sup>22</sup>R. S. Barlow and J. Frank, [www.ca.sandia.gov/tdf/Workshop.html](http://www.ca.sandia.gov/tdf/Workshop.html), 1998.
- <sup>23</sup>E. Hassel, [www.ca.sandia.gov/tdf/Workshop.html](http://www.ca.sandia.gov/tdf/Workshop.html), 1998.
- <sup>24</sup>P. Moin, K. Squires, W. Cabot, and S. Lee, "A dynamic subgrid-scale model for compressible turbulence and scalar transport," *Phys. Fluids A* **3**, 2746 (1991).
- <sup>25</sup>N. Peters, "Laminar diffusion flamelet models in non-premixed turbulent combustion," *Prog. Energy Combust. Sci.* **10**, 319 (1984).
- <sup>26</sup>N. Peters, "Laminar flamelet concepts in turbulent combustion," *Proc. Combust. Inst.* **21**, 1231 (1987).
- <sup>27</sup>H. Pitsch and N. Peters, "A consistent flamelet formulation for nonpremixed combustion considering differential diffusion effects," *Combust. Flame* **114**, 26 (1998).
- <sup>28</sup>N. Smith, J. Gore, and J. Kim, <http://www.ca.sandia.gov/tdf/Workshop/Submodels.html>, 1998.
- <sup>29</sup>C. H. Gibson, "Fine structure of scalar fields mixed by turbulence. I. Zero-gradient points and minimal gradient surfaces," *Phys. Fluids* **11**, 2305 (1968).
- <sup>30</sup>N. Peters, *Turbulent Combustion* (Cambridge University Press, Cambridge, 2000).
- <sup>31</sup>J. M. Donbar, J. F. Driscoll, and D. C. Carter, "Strain rates measured along the wrinkled flame contour within turbulent nonpremixed jet flames," presented at the Joint Meeting of the U.S. Sections of the Combustion Institute, Washington, DC, 1999.
- <sup>32</sup>S. S. Girimaji and Y. Zhou, "Analysis and modeling of subgrid scalar mixing using numerical data," *Phys. Fluids* **8**, 1224 (1996).
- <sup>33</sup>M. D. Smooke and V. Giovangigli, "Formulation of the premixed and nonpremixed test problems," in *Reduced Kinetic Mechanisms and Asymptotic Approximations for Methane-Air Flames*, edited by M. D. Smooke (Springer Verlag, Berlin, 1991).
- <sup>34</sup>J. S. Kim and F. A. Williams, "Structures of flow and mixture-fraction fields for counter-flow diffusion flames with small stoichiometric mixture fractions," *SIAM (Soc. Ind. Appl. Math.) J. Appl. Math.* **53**, 1551 (1993).
- <sup>35</sup>H. Pitsch and H. Steiner, "Scalar mixing and dissipation rate in large-eddy simulations of non-premixed turbulent combustion," *Proc. Combust. Inst.* (accepted).
- <sup>36</sup>V. R. Kuznetsov and V. A. Sabel'nikov, *Turbulence and Combustion* (Hemisphere, New York, 1990).
- <sup>37</sup>B. J. Boersma, G. Brethouwer, and F. T. M. Nieuwstadt, "A numerical investigation on the effect of the inflow conditions on the self-similar region of a round jet," *Phys. Fluids* **10**, 899 (1998).
- <sup>38</sup>H. N. Najm, P. S. Wyckoff, and O. M. Knio, "A semi-implicit numerical scheme for reacting flow," *J. Comput. Phys.* **143**, 381 (1998).
- <sup>39</sup>I. Danaïla and B. J. Boersma, "DNS of forced jet at low Reynolds numbers, in *Proceedings of the 1998 Summer Program*, Center for Turbulence Research, NASA Ames/Stanford University, 1998, p. 141.
- <sup>40</sup>K. Akselvoll and P. Moin, "Large-eddy simulation of turbulent confined coannular jets," *J. Fluid Mech.* **315**, 387 (1996).

- <sup>41</sup>P. M. Gresho, "Incompressible fluid dynamics: Some fundamental formulations issues," *Annu. Rev. Fluid Mech.* **23**, 413 (1991).
- <sup>42</sup>H. Pitsch, "A C++ computer program for 0-D combustion and 1-D laminar flame calculations," RWTH Aachen, 1998.
- <sup>43</sup>C. T. Bowman, R. K. Hanson, D. F. Davidson *et al.*, Gri-mech 2.11, [http://www.me.berkeley.edu/gri\\_mech/](http://www.me.berkeley.edu/gri_mech/).
- <sup>44</sup>G. P. Smith, D. M. Golden, M. Frenklach, N. W. Moriarty, B. Eiteneer, M. Goldenberg, C. T. Bowman, R. Hanson, S. Song, W. C. Gardiner, Jr., V. Lissianski, and Z. Qin, Gri-mech 3.0, [http://www.me.berkeley.edu/gri\\_mech/](http://www.me.berkeley.edu/gri_mech/).
- <sup>45</sup>N. Peters, "Flame calculations with reduced mechanisms—an outline," in *Reduced Kinetic Mechanisms for Applications in Combustion Systems*, edited by N. Peters and B. Rogg (Springer-Verlag, Berlin, 1993).
- <sup>46</sup>S. C. Li and F. A. Williams (private communication, 1999).
- <sup>47</sup>J. Warnatz, U. Maas, and R. W. Dibble, *Combustion, Physical and Chemical Fundamentals, Modeling and Simulation, Experiments, Pollutant Formation* (Springer-Verlag, New York, 1996).
- <sup>48</sup>H. Wang, A. Laskin, Z. M. Djuricic, C. K. Law, S. G. Davis, and D. Zhu, "A comprehensive mechanism of C<sub>2</sub>H<sub>x</sub> and C<sub>3</sub>H<sub>x</sub> fuel combustion," presented at the Fall Technical Meeting of the Eastern States Section of the Combustion Institute, Raleigh, 1999.
- <sup>49</sup>H. Pitsch, [www.stanford.edu/~hpitsch](http://www.stanford.edu/~hpitsch).
- <sup>50</sup>J. E. Rehm and N. T. Clemens, "The relationship between vorticity/strain and reaction zone structure in turbulent non-premixed jet flames," *Proc. Combust. Inst.* **27**, 1113 (1998).

H. PITSCH & H. STEINER

Scalar mixing and dissipation rate in large-eddy simulations of  
non-premixed turbulent combustion.

*Twenty-Eighth Symposium (Int.) on Combustion (Proc.)* **28** (2000),  
The Combustion Institute, Pittsburgh, PA., 41–49

## SCALAR MIXING AND DISSIPATION RATE IN LARGE-EDDY SIMULATIONS OF NON-PREMIXED TURBULENT COMBUSTION

HEINZ PITTSCH AND HELFRIED STEINER

*Center for Turbulence Research  
Flow Physics and Computation Division  
Stanford University  
Stanford, CA 94305-3030, USA*

Predictions of scalar mixing and the scalar dissipation rate from large-eddy simulations of a piloted non-premixed methane/air diffusion flame (Sandia flame D) using the Lagrangian-type flamelet model are presented. The results obtained for the unconditionally filtered scalar dissipation rate are qualitatively compared with general observations of scalar mixing from experiments in non-reactive and reactive jets. In agreement with experimental data, provided the reaction zone has an inward direction, regions of high scalar dissipation rate are organized in layerlike structures, inwardly inclined to the mean flow and aligned with the instantaneous reaction zone. The analysis of single-point time records of the mixture fraction reveals ramplike structures, which have also been observed experimentally and are believed to indicate large-scale turbulent structures. The probability density function (pdf) of the instantaneous resolved scalar dissipation rate at stoichiometric mixture evaluated at cross sections normal to the nozzle axis is shown to be described accurately by a lognormal pdf with  $\sigma = 1$ . A new model for the conditionally averaged scalar dissipation rate has been proposed and is shown to account for local deviations from the simple mixing layer structure. The stabilizing effect of the pilot flame in the present configuration is also discussed. Finally, the influence of the resolved fluctuations of the scalar dissipation rate on the flame structure is investigated, revealing only a weak influence on temperature and nitric oxide predictions. However, the model requires further refinement for situations in which local extinction events become important.

### Introduction

The mixing of scalars in turbulent flows is a very interesting problem which provides a fundamental understanding of the basic processes involved in non-premixed combustion problems and has been investigated by many in this field. A comprehensive review of experimental findings has recently been provided by Pitts et al. [1].

In non-premixed combustion, chemical reactions occur only if fuel and oxidizer are mixed at the molecular level. Although turbulent mixing is responsible for stirring the reactants at large scales, it contributes to the molecular scalar mixing only indirectly, increasing the scalar variances and thereby the scalar gradients. Molecular mixing essentially occurs at the smallest turbulent scales by removal of the scalar variance. The rate of molecular scalar mixing is represented by the scalar dissipation rate, which can be identified as the most important parameter in the description of non-premixed combustion.

Because combustion can occur only if the reactants are mixed on the molecular level, the scalar dissipation rate provides a measure of the maximum possible chemical reaction rate. This is the basic idea of the eddy break-up model [2]. Assuming infinitely

fast chemistry, it has been shown by Bilger [3] that the turbulent reaction rate is linearly proportional to the scalar dissipation rate at stoichiometric conditions,  $\chi_{st}$ . For finite-rate chemistry, the scalar dissipation rate appears as a parameter in most of the commonly applied combustion models such as the flamelet model [4,5], the transported probability density function model [6,7], and the conditional moment closure model [8].

The influence of the scalar dissipation rate,  $\chi$ , on the structure of diffusion flames has been discussed by Peters [4]. In general, the scalar dissipation rate at the stoichiometric mixture fraction describes the departure from chemical equilibrium. If the stoichiometric scalar dissipation rate in a steady laminar diffusion flame exceeds a critical value,  $\chi_q$ , the flame will be quenched. However, it has been found in experiments [9,10] and numerical simulations [11–13] that the flame structure cannot instantaneously follow changes in  $\chi_{st}$  and that in the case of a fluctuating scalar dissipation rate, instantaneous values of  $\chi_{st}$  can by far exceed  $\chi_q$  without quenching the flame. On the other hand, it is possible for the mean scalar dissipation rate to be smaller than  $\chi_q$  and yet the flame may be quenched by fluctuations above this limit. In situations where local quenching occurs, it might therefore be of great importance to

accurately model the fluctuations of the scalar dissipation rate.

For the modeling of the scalar dissipation rate, large-eddy simulations have the advantage of resolving the major part of the turbulent motion. Only the fluctuations which occur on smaller length scales than the filter width, typically given by the spacing of the numerical discretization, have to be modeled. The modeling effort of the basic quantities such as subgrid scale stresses and variances is supported by the concept of a turbulent energy cascade in two different ways. First, most of the turbulent energy is in the resolved scales. Second, the energy cascade concept suggests that subgrid quantities can be universally related to the resolved field. In contrast, since the dissipation of scalar variance occurs essentially at the smallest scales, the major part of the scalar dissipation rate has to be modeled. Following the energy cascade concept, the scalar dissipation rate is, similar to the turbulent kinetic energy dissipation rate, a universal quantity describing the scalar variance transport in wavenumber space, and knowledge of the resolved-scale field should hence be beneficial in the determination of the scalar dissipation rate as a fluctuating quantity.

In this paper, we describe and evaluate the modeling of the scalar dissipation rate and its fluctuations in large-eddy simulations (LES) for non-premixed combustion using the Lagrangian-type flamelet model [14,15]. The predictions of the unconditional mean scalar dissipation rate from an LES of a piloted turbulent diffusion flame (Sandia flame D [16,17]) is discussed and compared to general and mainly qualitative observations from several experiments. The influence of resolved fluctuations of the modeled conditional scalar dissipation rate on the chemical flame structure is investigated by comparing the results of calculations, which include the fluctuations of the scalar dissipation rate, with results for the same configuration obtained by using time-averaged values for the scalar dissipation [18].

We first give a brief review of the Lagrangian-type flamelet model as a combustion model for LES and present a new model for the evaluation of the conditional mean scalar dissipation rate. We then discuss the results for the unconditional resolved scalar dissipation rate, and finally the influence of the resolved fluctuations of the conditional mean scalar dissipation rate.

## Model Formulation

### Large-Eddy Simulation

The system of equations to be solved is given by the spatially filtered continuity, momentum, and mixture fraction equations provided, for instance, by

Moin et al. [19]. The subgrid stresses and the velocity-mixture fraction covariance appearing in the momentum equations and in the mixture fraction equation are expressed by eddy-viscosity-type models, where the eddy viscosity is given by the Smagorinsky model, the eddy diffusivity,  $D_t$ , by the assumption of a constant turbulent Schmidt number,  $Sc_t = 0.4$  [18]. Following Pierce and Moin [19], the mixture fraction variance is given by

$$\widetilde{Z}''^2 = C_Z \Delta^2 (\nabla \widetilde{Z})^2 \quad (1)$$

The Smagorinsky coefficient and the coefficient  $C_Z$  are computed from the solution of the resolved scales by applying the dynamic procedure [20]. No model constants have to be specified in the computation of the flow field. The simulation was performed in a spherical coordinate system with 192 cells in the downstream direction, 110 cells in the cross-flow direction, and 48 cells in the azimuthal direction. The inflow conditions were prescribed according to the experimental conditions. Detailed information on the numerical procedure has been given in Ref. [18].

### Lagrangian-Type Flamelet Model

In the present simulations, the Lagrangian-type flamelet model was employed to describe turbulence/chemistry interactions. The model was developed in the framework of Reynolds averaged simulations [14,15] and was recently applied in LES [18]. The model follows the conserved scalar approach, implying that the temperature and the species mass fraction can be related to the mixture fraction. Thus, density-weighted filtered quantities are given by

$$\tilde{\phi} = \int_0^1 \phi(Z) \tilde{P}(Z) dZ \quad (2)$$

where  $\phi$  stands for the temperature,  $T$ , and the species mass fractions,  $Y_i$ .  $\tilde{P}(Z)$  is the subgrid scale Favre probability density function (pdf) of the mixture fraction,  $Z$ , which is presumed to be a  $\beta$ -function, whose shape is determined by the resolved mixture fraction and its subgrid scale variance. The function  $Y_i$  is given by the solution of the unsteady flamelet equations. For the species mass fractions, for example, these are given as

$$\frac{\partial Y_i}{\partial \tau} - \rho \frac{\chi}{2} \frac{\partial^2 Y_i}{\partial Z^2} - \dot{m}_i = 0 \quad (3)$$

Here,  $\tau$  is the Lagrangian flamelet time,  $\rho$  is the density,  $\dot{m}_i$  is the chemical production rate per unit volume, and following Ref. [14],  $\chi$  is given by the conditional scalar dissipation rate  $\langle \chi | Z \rangle (\tau)$ . Lewis numbers of the chemical species have been assumed to be unity. Lagrangian flamelet particles are assumed to be introduced at the nozzle exit and travel downstream essentially with the axial velocity at stoichiometric mixture fraction. Then,  $\tau$  can be related

to the physical space coordinate in the axial direction  $x$  as

$$\tau = \int_0^x \frac{1}{\langle \tilde{u}_{\tilde{z}} | \tilde{Z}_{st} \rangle (x', t)} dx' \quad (4)$$

where  $\langle \tilde{u}_{\tilde{z}} | \tilde{Z}_{st} \rangle$  denotes the velocity of the stoichiometric mixture fraction surface in the axial direction. The resolved mass fractions can then be determined as a function of time and space with equations 2, 3, and 4, provided the conditional scalar dissipation rate is given as a function of the flamelet time,  $\tau$ , and the mixture fraction,  $Z$ .

### Scalar Dissipation Rate

The unconditionally filtered scalar dissipation rate is expressed in terms of the eddy diffusivity and the gradient of the resolved mixture fraction using the first-order model given by Girimaji and Zhou [21] as

$$\tilde{\chi} = 2(D_Z + D_t) (\nabla \tilde{Z})^2 \quad (5)$$

where  $D_Z$  is the molecular diffusivity of the mixture fraction.

As pointed out earlier, the temporal development of the scalar dissipation rate appearing in equation 3 is unknown and has to be related to the unconditional mean given by equation 5. A common approach to achieve this is to presume the functional dependence of the scalar dissipation rate on the mixture fraction as  $\langle \chi | Z \rangle = \langle \chi_{st} \rangle f(Z)$ , using analytic expressions for the function  $f(Z)$  as suggested in the literature [4,14,22]. Then, it is sufficient to determine the value conditioned on stoichiometric mixture.  $\langle \chi_{st} \rangle$  can then be determined by introducing the expression for  $\langle \chi | Z \rangle$  in the equation for the filtered scalar dissipation rate,  $\tilde{\chi}$ , which can be written as

$$\tilde{\chi}(\mathbf{x}, t) = \int_{Z=0}^1 \langle \chi | Z \rangle (x, t) \tilde{P}(Z, \mathbf{x}, t) dZ \quad (6)$$

It is demonstrated below that the function  $f(Z)$  cannot be represented by the commonly applied expressions for unsteady mixing layers or counterflow diffusion flames, since in the present study a piloted flame is considered.

Here, a new model for the computation of the conditional average of the scalar dissipation rate, which has to be specified as a function of the axial distance from the nozzle as  $\langle \chi | Z \rangle (x, t)$ , is proposed. This model is similar to the approach used by Bushe and Steiner [23] for the estimation of chemical source terms. The term  $\langle \chi | Z \rangle (x, t)$  is computed by the inversion of the integral in equation 6. Writing equation 6 for each computational cell in a chosen plane normal to the nozzle axis gives

$$\tilde{\chi}_i(x, t) = \int_{Z=0}^1 \langle \chi | Z \rangle (x, t) \tilde{P}_i(Z, x, t) dZ, \quad (7)$$

$$i = 1, \dots, N_c(x)$$

Here,  $N_c(x)$  is the number of cells in the plane considered. If the continuous function  $\langle \chi | Z \rangle (Z, x, t)$  in

equation 7 is approximated by a discrete representation in terms of the mixture fraction as  $\langle \chi | Z_j \rangle (x, t)$ ,  $j = 1, \dots, N_Z$ , where  $N_Z$  denotes the number of values used to represent the mixture fraction space, the integral in equation 7 can be approximated by a sum using, for example, the trapezoidal integration rule as

$$\tilde{\chi}_i(x, t) \approx \sum_{j=1}^{N_Z} A_{ij} \langle \chi | Z \rangle (Z_j, x, t), \quad (8)$$

$$j = 1, \dots, N_Z$$

where the coefficient matrix  $A_{ij}$  contains the discretized pdf  $\tilde{P}_i(Z_j, x, t)$  and the coefficients of the numerical integration scheme.

Equation 8 represents a system of  $N_c(x)$  equations for  $N_Z$  unknowns. For  $N_c(x) > N_Z$ , this can be solved by minimizing the resulting error of the overdetermined system via a least squares approach.

An alternative method to compute the conditional scalar dissipation rate has been proposed by Janicka and Peters [24]. In the transport equation of the mixture fraction pdf [7], the conditional scalar dissipation rate appears in the term representing molecular mixing. If the mixture fraction pdf is prescribed, this equation can be used to determine  $\langle \chi | Z \rangle$ . The underlying assumptions of this approach, which include the use of modeled values of the unconditional mean and assumed  $\beta$ -function shape of the mixture fraction pdf, are very similar to the model presented here. In contrast to this, the pdf transport equation method in principle provides averages over one computational cell, while the method proposed in this work is an average over a larger number of cells. However, for small values of the mixture fraction pdf, the determination of the conditional scalar dissipation rate from the pdf transport equation becomes singular, which makes its application difficult, particularly in LES, where the subgrid pdf is non-zero only in a very narrow range around the mean.

## Results and Discussion

In this section, the predicted results for scalar mixing and the scalar dissipation rate from an LES of a piloted non-premixed methane/air diffusion flame (Sandia flame D) with a Reynolds number of  $Re = 22000$  are presented and discussed. The instantaneous conditional scalar dissipation rates, which are obtained in the LES from equation 8, have been averaged in time and then used in the solution of the flamelet equations. This assumption is discussed below.

Experimental data for axial velocity and root mean square (RMS) has been determined by Hassel [25], while data for the mean and RMS of the temperature, and mean and conditional mean mass fractions of the chemical species  $\text{CH}_4$ ,  $\text{O}_2$ ,  $\text{H}_2$ ,  $\text{H}_2\text{O}$ ,  $\text{CO}$ ,

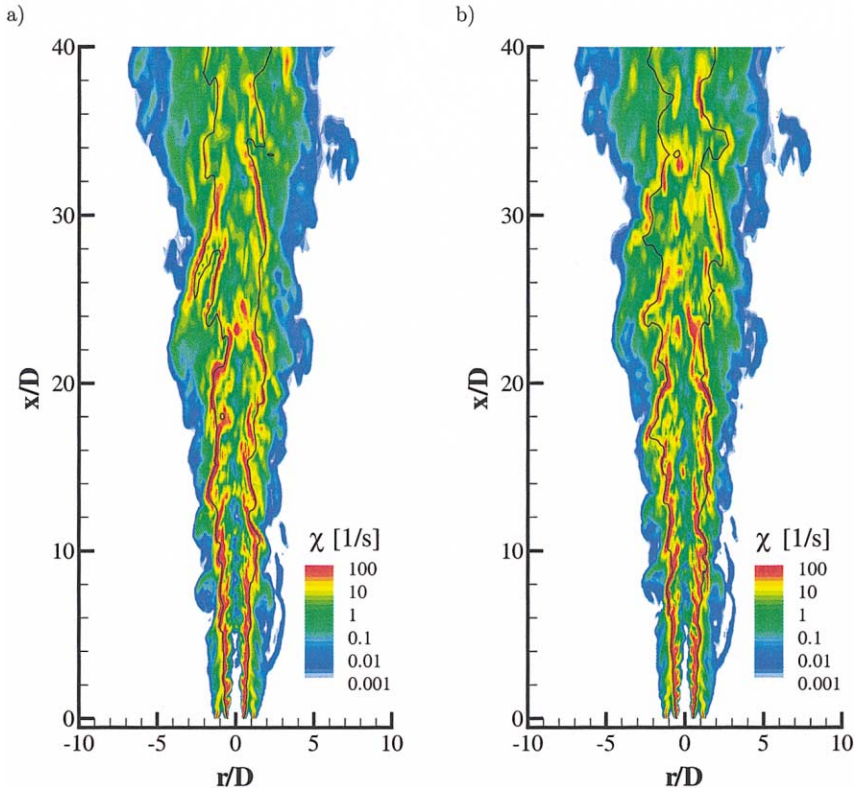


FIG. 1. Resolved instantaneous scalar dissipation rate distribution. Results in (b) are at a time 20 ms later than those in (a).

$\text{CO}_2$ , OH, and NO have been given by Barlow et al. [16,17]. Comparison of the predicted results with the experimental data has been presented and discussed further in Ref. [18]. In general, the agreement of predictions and experimental data is considered very good.

#### *Unconditionally Filtered Scalar Dissipation Rate*

##### Spatial $\bar{\chi}$ -distribution

Figure 1 shows instantaneous distributions of the unconditionally filtered scalar dissipation rate,  $\bar{\chi}$ , obtained from equation 5. Figure 1b shows a realization at a time approximately 20 ms later than that in 1a. The figures are presented at the same point in time as the temperature distributions given in Ref. [18]. The stoichiometric contour, which indicates the approximate location of the reaction zone, is also indicated. Regions of high scalar dissipation rate appear in layerlike structures, which are directed inward. In general, these layers are well aligned with the stoichiometric contour, when this is directed inward. Since both the stoichiometric contour and the

high scalar dissipation rate layers cannot be inclined to the mean flow over a long distance, the stoichiometric contour diverges outward again to the next surrounding dissipation layer. This usually occurs at much higher angles relative to the axis of the jet. Since the inwardly directed stoichiometric contours appear at high scalar dissipation rate, the corresponding temperature distribution is very narrow, as corroborated by Ref. [18]. In contrast, the outwardly directed contours are associated with broad temperature regions.

Similar behavior has been observed by Feikema et al. [26] in measurements of the scalar dissipation rate in a non-reacting turbulent jet. They found that the scalar dissipation rate appears in layers, which are inclined at approximately  $45^\circ$  to the flow. Rehm and Clemens [27,28] found that the minimum compressive strain in turbulent jet flames appears in similar layers, which are also inclined at  $45^\circ$  to the flow and aligned with the reaction zone. Rehm and Clemens [28] have also shown from experiments in non-reacting jets that the minimum compressive strain layers are well aligned with the scalar dissipation rate layers. In experiments of reactive jets,

they also observed the broadening of the reaction zone in instances where this is directed away from the jet axis. All these findings are consistent with the current simulation. However, on average the inclination angle of the dissipation layers in Fig. 1 seems to be smaller than  $45^\circ$  to the direction of the flow.

Single-point time records of  $\tilde{Z}$  and  $\tilde{\chi}$

Single-point time records of the mixture fraction and the scalar dissipation rate at the centerline position at  $x/D = 30$  are given in Fig. 2. As shown in Fig. 2 and also by Pitts et al. [1] for non-reacting jet experiments, the scalar dissipation rate fluctuates at a much higher frequency than the mixture fraction. Also, the mean duration of a peak at high scalar dissipation rate appears to be much longer than a peak at low scalar dissipation rate. Donbar et al. [10] found that for a turbulent jet flame with a Reynolds number  $Re = 18,600$ , which is very similar to the present case, that the strain rate fluctuates at approximately 10 kHz. The frequency of the scalar dissipation rate fluctuations at  $x/D = 30$  shown in Fig. 2 can be estimated to be 2.5 kHz. This frequency however, varies strongly with the nozzle distance.

It should be noted here that even the shortest fluctuations appearing in Fig. 2 are well resolved in time, such that the time-step of the calculation does not impose any filtering. The frequency that can be resolved by the computational mesh might be estimated by the average cell size in the axial direction and the time averaged axial velocity as  $f_{Res} \approx 10$  kHz. Since it has been found in the reacting jet experiments of Donbar et al. [10] and also in simulations of counterflow diffusion flames by Saitoh and Otsuka [9] that the flame chemistry does not respond to fluctuations in the strain rate higher than 10 kHz, it appears that the spatial filtering is not restrictive for the use of the predicted scalar dissipation rate in chemistry calculations.

Figure 2 also reveals one other very important mixing aspect which is not directly related to the

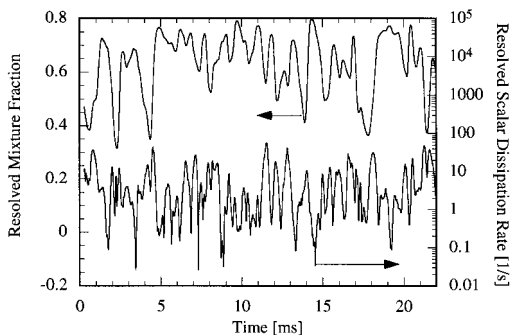


FIG. 2. Time records of the resolved mixture fraction and the scalar dissipation rate on the centerline at  $x/D = 30$ .

scalar dissipation, but should still be discussed here. Pitts et al. [1] have investigated large-scale turbulent structures in a non-reacting jet. As one of the most important proofs of the formation of these structures, they discuss the observation of ramplike structures in one-point time records of scalars in turbulent jets. These ramplike structures can also be observed in the resolved mixture fraction record shown in Fig. 2. In general, the increase of the mixture fraction occurs much more rapidly than the following decrease. This seems to corroborate that the current simulations are capable of describing large-scale mixing phenomena, which are believed to be very important for the overall structure and development of the scalar field.

The pdf of  $\tilde{\chi}$

The pdf of the scalar dissipation rate has been investigated in many studies [1,29,30]. It has been found that the distribution of  $\chi$  is log-normal. In terms of the density-weighted filtered quantities, this can be expressed as

$$\tilde{P}(\tilde{\chi}) = \frac{1}{\tilde{\chi}\sqrt{2\pi}} \exp\left(-\frac{(\ln\tilde{\chi} - \mu)^2}{2\sigma^2}\right) \quad (9)$$

Here,  $\mu$  and  $\sigma$  are parameters of the pdf, which essentially represent the mean and the fluctuation about the mean, respectively. From non-reacting jet experiments, Effelsberg and Peters [29] have found the parameter  $\sigma$  to have a value close to unity. The evaluation of the pdf of  $\tilde{\chi}_{st}$  using all computational cells in the particular cross-section is presented in Fig. 3 for  $x/D = 15$  and  $x/D = 30$ . Also shown is the pdf evaluated from equation 9 with  $\sigma = 1$  and the appropriate values for  $\mu$  to match the mean scalar dissipation rate, viz.  $\mu = 4.7$  and  $3.2$  for  $x/D = 15$  and  $30$ , respectively. The comparison shows that

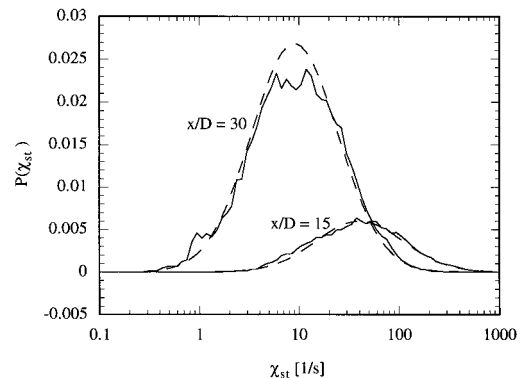


FIG. 3. The pdf of the stoichiometric resolved scalar dissipation rate at  $x/D = 15$  and  $x/D = 30$  (solid lines) compared to log-normal pdfs (dashed lines), with  $\sigma = 1$  from equation 9.

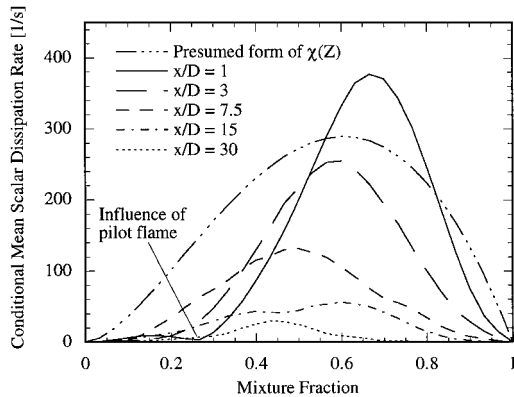


FIG. 4. Conditional scalar dissipation rate at different downstream locations. Also shown is a commonly presumed form of the mixture fraction dependence of the scalar dissipation rate.

the distribution of  $\tilde{\chi}_{st}$  at both positions is almost perfectly log-normal, and also that  $\sigma = 1$  seems to be a very good approximation for the case investigated. The same value of  $\sigma$  is observed at  $x/D = 45$ .

#### Conditional Mean Scalar Dissipation Rate

Results for the conditional mean scalar dissipation rate at different downstream locations determined from equation 8 are shown in Fig. 4. The comparison with a presumed shape of  $\chi(Z)$  from Ref. [14] indicates that this simple function is not applicable in the present case. Within the pilot stream, which is at  $Z = 0.27$ , the scalar gradient, and hence the scalar dissipation rate, is zero. Even at far downstream locations, the shape of the scalar dissipation rate is still influenced by the pilot flame.

The computed shape at  $x/D = 1$  provides an interesting explanation of the stabilizing effect of a pilot flame. The pilot causes the scalar dissipation rate to be zero at the pilot mixture fraction, which in turn also causes the scalar dissipation rate at stoichiometric mixture fraction ( $Z_{st}^* = 0.35$ ) to be small. However, by interdiffusion with the surrounding mixing layer this value strongly increases with downstream direction. Also, the same diffusive effect causes the scalar dissipation rate generally to decrease strongly with downstream direction [31]. Hence, in the present case,  $\chi_{st}$  first increases until approximately  $x/D = 7.5$ , and then decreases. If the maximum value stays smaller than the extinction limit,  $\chi_{st,q}$ , the flame stabilizes at the pilot. However, if it exceeds  $\chi_{st,q}$ , the flame will exhibit local extinction or even blow off. This also explains why it is favorable to have the pilot mixture fraction close to the stoichiometric mixture fraction, which keeps  $\chi_{st}$  lower, and also to have a broad pilot flow, because

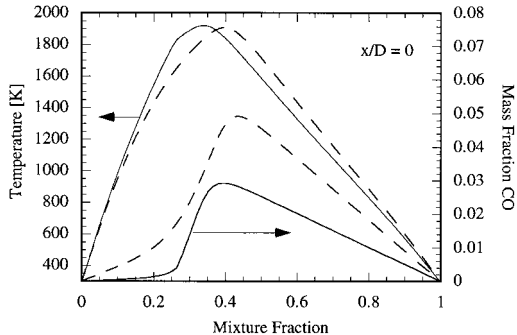


FIG. 5. Influence of the mixture fraction dependence of the scalar dissipation rate on the flamelet solution at the nozzle exit. Calculation using  $\chi(Z)$  from equation 8 (solid lines) compared to solution with  $\chi(Z)$  (dashed lines) presumed according to Ref. [14].

then the increase of  $\chi$  around the pilot will be much slower.

The influence of the scalar dissipation rate model on the initial conditions for the unsteady flamelet calculation, which is assumed to be the steady flamelet solution with  $\chi(Z)$  evaluated from equation 8 at  $x/D = 0$ , is given in Fig. 5. The flamelet solution for the temperature and the CO mass fraction are compared to the solution using the presumed  $\chi(Z)$  of Ref. [14]. Because of the influence of the pilot, the flame is substantially shifted to the lean side. Also, as shown in Fig. 4, the presumed function overestimates the scalar dissipation in the lean part of the flame, leading to a substantial overprediction of the CO mass fraction.

#### Influence of Resolved Scalar Dissipation Rate Fluctuations

The influence of the scalar dissipation rate fluctuations, which are resolved by equation 8, are investigated next. As mentioned above, the pdf of the unconditional scalar dissipation rate clearly reveals a log-normal shape with  $\sigma = 1$ . Because the conditional scalar dissipation rate given by equation 8 is a spatial conditional average, which has for the present study and for the results presented in Ref. [18] been performed over all computational cells in cross sections normal to the jet axis, the pdf of  $\langle\chi\rangle$  is much narrower than the pdfs shown in Fig. 3. This, however, can be substantially improved by sampling over smaller areas. In order to analyze the influence of the resolved fluctuations on the flame structure, 250 different instantaneous scalar dissipation rate and mixture fraction fields were recorded from the calculations presented in Ref. [14]. These calculations were performed using the time-averaged scalar dissipation rate. Using these data, 250 unsteady flamelet calculations were performed, and the resolved

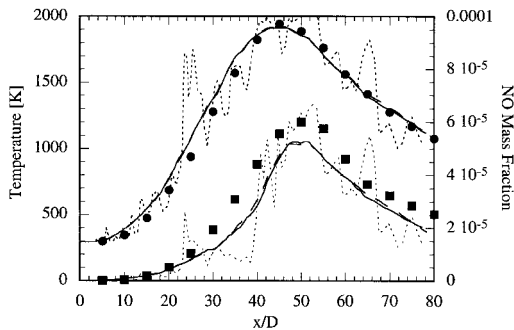


FIG. 6. Ensemble-averaged temperature and NO mass fraction determined as the average over multiple instantaneous realizations (solid lines) compared to a calculation using a time average of the scalar dissipation rate (dashed lines). Also given is an example for one instantaneous realization (dotted line).

temperature and mass fractions were evaluated using equation 2. The results were ensemble averaged, and the temperature and the NO mass fraction of these calculations are compared along the centerline to the calculations using the time average of the scalar dissipation rate and the experimental data given by Barlow et al. [16,17] in Fig. 6. Also given in Fig. 6 is one example of an instantaneous solution of temperature and NO mass fraction. This solution shows temperature fluctuations, which can be of the order of 700 K. However, almost no differences in the results of both methods can be observed, indicating that the resolved fluctuations of the scalar dissipation rate influence the flame structure only very weakly, and also that the strong fluctuations in the instantaneous solution given in Fig. 6 are essentially caused by fluctuations in the resolved mixture fraction and its subgrid scale variance. Both methods yield good agreement with the experimental data for the present case. However, if local extinction events start to become important, the pdf of the scalar dissipation rate has to be determined much more accurately, and averages over complete cross sections can no longer be used.

## Conclusions

The present study provides a discussion of scalar mixing and the scalar dissipation rate in large-eddy simulations. The results from an LES of the Sandia flame D have been used to compare the predictions of the mixture fraction field and the scalar dissipation rate with mostly qualitative experimental data. In agreement with experimental data, it has been found that regions of high scalar dissipation rate are organized in layerlike structures that are inwardly inclined to the mean flow and aligned with the reaction zone.

The fluctuation frequency of the scalar dissipation rate has been discussed in the context of the spatial and temporal resolution of the current simulation, and the findings are that the resolution used in the present investigation is not restrictive for the predictions of the scalar dissipation rate. Single-point time records of the mixture fraction have been found to reveal ramplike structures, which are also evident in experimental data for non-reacting jets. Pitts et al. [1] regarded this as one of the most important proofs for the occurrence of large-scale turbulent structures in turbulent jets.

The pdf of the stoichiometric scalar dissipation rate was found to be described accurately by a log-normal pdf with a value of  $\sigma = 1$ . The ratio of the integral time scales of scalar and velocity fluctuations, which is commonly used in Reynolds-averaged turbulence models to determine the unconditionally averaged scalar dissipation rate, was evaluated using the resolved velocity and scalar field.

A model for the conditional scalar dissipation rate has been suggested that accounts for the influence of local deviations from a simple mixing layer structure. Furthermore, this model has been demonstrated to account for the strong influence of a pilot in the near-field of a turbulent jet flame.

Finally, the influence of the fluctuations resolved by the model for the conditional scalar dissipation rate on the flame structure was investigated by comparing averages over simulations using instantaneous scalar dissipation rate histories with a simulation using the time-averaged scalar dissipation rate. The results for temperature and NO mass fraction are not influenced by the scalar dissipation rate fluctuations. However, the model would need to be refined for instances in which local extinction events become important.

## Acknowledgments

Support by the U.S. Department of Energy within the ASCI program is acknowledged. The authors also thank George Kosály for many helpful discussions.

## REFERENCES

1. Pitts, W. M., Richards, C. D., and Levenson, M. S., *Large- and Small-Scale Structures and Their Interactions in an Axisymmetric Jet*, NIST internal report NISTIR 6393, National Institute of Standards and Technology, Gaithersburg, MD, 1999.
2. Spalding, D. B., *Proc. Combust. Inst.* 13:649–657 (1971).
3. Bilger, R. W., *Combust. Sci. Technol.* 110:155–170 (1976).
4. Peters, N., *Prog. Energy Combust. Sci.* 10:319–339 (1984).
5. Peters, N., *Proc. Combust. Inst.* 21:1231–1250 (1986).

6. Pope, S. B., *Prog. Energy Combust. Sci.* 11:119–192 (1985).
7. O'Brien, E. E., in *Turbulent Reacting Flows*, (P. A. Libby and F. A. Williams, eds.), Springer, 1980, p. 185.
8. Klimenko, A. Y., and Bilger, R. W., *Prog. Energy Combust. Sci.* 25:595–687 (1999).
9. Saitoh, T., and Otsuka, Y., *Combust. Sci. Technol.* 12:135–146 (1976).
10. Donbar, J. M., Driscoll, J. F., and Carter, D. C., *Combust. Flame*, in press (2000).
11. Barlow, R. S., and Chen, J.-C., *Proc. Combust. Inst.* 24:231–237 (1992).
12. Haworth, D. C., Drake, M. C., Pope, S. B., and Blint, R. J., *Proc. Combust. Inst.* 24:589–597 (1988).
13. Mauss, F., Keller, D., and Peters, N., *Proc. Combust. Inst.* 25:693–698 (1990).
14. Pitsch, H., Chen, M., and Peters, N., *Proc. Combust. Inst.* 27:1057–1064 (1998).
15. Pitsch, H., *Combust. Flame*, in press, (1999).
16. Barlow, R. S., and Frank, J. H., *Proc. Combust. Inst.* 27:1087–1095 (1998).
17. [www.ca.sandia.gov/tdf/Workshop.html](http://www.ca.sandia.gov/tdf/Workshop.html), Sandia National Laboratory, 1998 (updated June 7, 2000).
18. Pitsch, H., and Steiner, H., unpublished work (1999).
19. Pierce, C. D., and Moin, P., *Phys. Fluids A* 10:3041–3044 (1998).
20. Moin, P., Squires, K., Cabot, W., and Lee, S., *Phys. Fluids A* 3:2746–2757 (1991).
21. Girimaji, S. S., and Zhou, Y., *Phys. Fluids A* 8:1224–1236 (1996).
22. Kim, J. S., and Williams, F. A., *SIAM J. Appl. Math.* 53:1551–1566 (1993).
23. Bushe, W. K., and Steiner, H., *Phys. Fluids A* 11:1896–1906 (1999).
24. Janicka, J., and Peters, N., *Proc. Combust. Inst.* 19:367–374 (1982).
25. Hassel, E., [www.ca.sandia.gov/tdf/Workshop.html](http://www.ca.sandia.gov/tdf/Workshop.html), Sandia National Laboratory, 1998 (updated June 7, 2000).
26. Feikema, D. A., Everest, D., and Driscoll, J. F., *AIAA J.* 34:2531–2538 (1996).
27. Rehm, J. E., and Clemens, N. T., *Proc. Combust. Inst.* 27:1113–1120 (1998).
28. Rehm, J. E., and Clemens, N. T., “The Association of Scalar Dissipation Rate Layers and OH Zones with Strain, Vorticity, and 2-D Dilatation Fields in Turbulent Nonpremixed Jets and Jet Flames,” AIAA paper 99-0676, Thirty-Seventh AIAA Aerospace Sciences Meeting and Exhibit, Reno, NV, Jan. 11–14, 1999.
29. Effelsberg, E., and Peters, N., *Proc. Combust. Inst.* 22:693–700 (1988).
30. Dahm, W. J. A., and Buch, K. A., *Phys. Fluids A* 1:1290–1293 (1989).
31. Peters, N., and Williams, F. A., *AIAA J.* 21:423–429 (1983).

## COMMENTS

*William Mell, University of Utah, USA.*

1. Did you also implement a quasi-steady version of the flamelet model? If so, how did it perform compared to your transient model?
2. What boundary conditions did you use for the laminar flamelet model? In particular, were transient effects important?
3. Did you consider regimes in which buoyancy played a greater role (rather than momentum) in the flow? It seems likely that in such a situation the axial velocity (which gives the Lagrangian time) may not be as representative of the flamelets at a given axial position.

*Author's Reply.*

1. Predictions using a quasi-steady model have been shown to be more accurate if radiation is neglected. For the investigated configuration, the application of the quasi-steady model leads thereby to an overprediction of the temperature. This leads to an overprediction of the NO mass fraction by approximately a factor of 2. However, for the conclusions of the present paper regarding the scalar mixing process, the use of a quasi-steady model will show hardly any influence.
2. Using the models proposed in the present paper, the predicted conditional scalar dissipation rate becomes small if the pdf of the mixture fraction goes to zero.

This can be seen in Fig. 4. In the region of zero scalar dissipation rates, the diffusion term in the flamelet equation is zero. This implies that the boundary conditions of the flamelet solution are homogeneous reactor solutions at an effective maximum mixture fraction.

3. We did not consider a configuration where buoyancy is important. However, the Lagrangian time can still be determined from the axial velocity, which would change accordingly if the momentum flux were dominated by buoyancy.

•

*A. Y. Klimeuto, The University of Queensland, Australia.* I am certain that the topic of the presentation, investigation into the influence of fluctuations of the conserved scalar-dissipation on combustion, is most important for flamelet modeling. However, I think that one question needs some clarification. The subgrid model used by the authors ignores the subgrid fluctuations which can be expected to be most significant for the scalar dissipation. Can this factor affect the conclusions of the present work?

*Author's Reply.* In the present model, the subgrid part of the scalar dissipation rate is considered by the use of a subgrid model. Because of the subgrid filtering, the pdf

of the scalar dissipation rate and also the frequency of its fluctuations might be influenced. It is shown in Fig. 3 that the resolved pdf is in good agreement with experimental findings. This suggests that the filtering only influences the tails of the pdf. It is also mentioned in the paper that the present simulation can resolve a frequency of 10 kHz. It has been shown in experiments (Ref. [10] in this paper) and simulations of counterflow diffusion flames (Ref. [9] in this paper) that the flame chemistry does not respond to higher frequencies.

- 

*Andrew Pollard, Queen's University, Canada.* Can you confirm that the scalar dissipation is coincident with regions of high axial vorticity (i.e., braids between azimuthal vortex rings)?

*Author's Reply.* Obviously, the regions of high scalar dissipation rate are located between large-scale azimuthal vortical structures. However, from the observations we made in this study there is not clear evidence that these structures appear in rings, which would be connected by secondary axial vortices. This might still be the case, but we have not looked explicitly into these details.

H. STEINER & W. K. BUSHE

Large eddy simulation of a turbulent reacting jet with  
conditional source-term estimation.

*Phys. Fluids* **13** (2001), 754–769

# Large eddy simulation of a turbulent reacting jet with conditional source-term estimation

H. Steiner<sup>a)</sup> and W. K. Bushe<sup>b)</sup>

*Center for Turbulence Research, Stanford University, Stanford, California 94305-3030*

(Received 30 November 1999; accepted 4 December 2000)

The Conditional Source-term Estimation (CSE) method was recently proposed to close the chemical source terms occurring in the spatially filtered transport equations of species and enthalpy for Large Eddy Simulation (LES) of nonpremixed reacting flows [W. K. Bushe and H. Steiner, *Phys. Fluids* **11**, 1896 (1999)]. The model is based on the Conditional Moment Closure hypothesis, which provides fairly accurate predictions for the conditional averages of the chemical reaction rates as functions of the conditionally averaged composition vector and temperature with the mixture fraction being an appropriate conditioning variable. In CSE the conditionally averaged composition vector and temperature are obtained by mapping the corresponding spatially filtered scalar fields resolved by the LES into the conditioning (i.e., mixture fraction) space. After the conditional averages of the chemical reaction rates are approximated in mixture fraction space, these are mapped into the physical space to close the source terms in the LES transport equations for the reactive scalars. The present simulation of a turbulent reacting jet is the first test of this new closure in a self-sustained predictive LES. A two-step reduced chemical kinetic mechanism for methane-air flames was used. The results of the simulation, which are in reasonable agreement with available experimental data, prove the model's predictive capabilities as well as its robustness and feasibility for LES. © 2001 American Institute of Physics. [DOI: 10.1063/1.1343482]

## I. INTRODUCTION

In the foreseeable future, the requirements of true Direct Numerical Simulation (DNS) of turbulent reacting flows at technically relevant Reynolds numbers will exceed by far the computational resources available. Rather than resolving all physically relevant scales, as is required in DNS, Large Eddy Simulation (LES) resolves only the large scale motion of the flow while modeling the small scale motion, which tends to be more isotropic and is therefore easier to model. The governing equations of LES are obtained by applying a spatial filter to the transport equations of mass, momentum, species concentration (or mass fraction), and energy. This filtering operation can be generally defined by

$$\begin{aligned}\bar{F}(\mathbf{x}, t) &= \int_D F(\mathbf{x}', t) G(\mathbf{x} - \mathbf{x}') d\mathbf{x}' \\ &= \int_D F(\mathbf{x} - \mathbf{x}', t) G(\mathbf{x}') d\mathbf{x}',\end{aligned}\quad (1)$$

where  $\bar{F}$  denotes the filtered value of some quantity  $F$  in space  $\mathbf{x}$  and time  $t$ ,  $G$  is the spatial filter function, and  $D$  is the domain of the flow. As a result of its defining properties given by Eq. (1), the filter function  $G$  commutes with spatial

and temporal derivatives.<sup>1</sup> This is strictly valid only if the width of the filtering kernel is uniform in space. However, LES of inhomogeneous flows, e.g., boundary layer flow, where dynamically important length scales strongly depend on position, suggests a filtering operation with variable filter width, which in general does not commute with the spatial derivatives. It was shown that the commutation error due to a nonuniform filter width is of the order of the grid spacing squared ( $\epsilon_{\text{comm}} \sim O[\Delta x_i^2]$ ).<sup>2</sup> This error is still acceptable, if a second-order accurate scheme is used to discretize the LES equations. The same reasoning justifies the use of the unfiltered, i.e., physical, boundary conditions for LES, although the boundary conditions for the filtered fields are not necessarily the same as those for the unfiltered fields. The difference between the boundary conditions for the filtered and the unfiltered fields is also of the order  $O[\Delta x_i^2]$ .<sup>3</sup>

In reacting flows with nonconstant density the filtering operation (1) is usually weighted with the density yielding density-weighted, or Favre-filtered, quantities denoted by the “ $\sim$ ” symbol

$$\tilde{F} = \frac{\overline{\rho F}}{\bar{\rho}}. \quad (2)$$

In most applications of LES, the actual form of the filter function is implicitly determined by the choice of numerical scheme used rather than being chosen explicitly by the user, although methods which use explicit filters have been proposed.<sup>2,3</sup> A top-hat filter, which is defined in the  $i$ th direction of the physical space by

<sup>a)</sup> Author to whom correspondence should be addressed; present address: Institut für Strömungslehre und Wärmeübertragung, Technical University Graz, Inffeldgasse 25, A-8010 Graz, Austria; fax: +43 (316) 873 7356; electronic mail: f321stei@mbox.tu-graz.ac.at

<sup>b)</sup> Present address: Department of Mechanical Engineering, University of British Columbia, 2324 Main Mall, Vancouver, BC, V6T 1Z4, Canada; fax: (604) 822-2403; electronic mail: wkb@mech.ubc.ca

$$G_i(x_i - x_i') = \begin{cases} 1/\Delta_i, & \text{for } \|x_i - x_i'\| \leq \Delta_i/2 \\ 0, & \text{elsewhere} \end{cases}$$

was adopted in the present work. The filter with  $\Delta_i$  is typically related to the grid size  $\Delta x_i$  in the  $i$ th direction. In order to account for the contribution of the subgrid-scale fluctuations to the fluxes of momentum, species mass fraction, and enthalpy, the molecular viscosity and diffusivities are augmented by an “eddy viscosity” and “eddy diffusivities,” respectively. Several subgrid-scale models for these turbulent transport coefficients have been suggested and successfully applied in many flow configurations.<sup>1</sup> In particular, dynamic models—which, unlike the original Smagorinsky model,<sup>4</sup> do not require a model constant to be set prior to the simulation—have become a well established approach.<sup>5,6</sup>

In the case of reacting flows the spatially filtered chemical source terms represent an additional challenge to LES. The chemical reaction rates are in general given by Arrhenius-type equations

$$\dot{\omega}_k = A_k T^{n_k} \exp\left(-\frac{E_k}{RT}\right) \prod_{j=1}^J \left(\frac{\rho Y_j}{W_j}\right)^{\nu_{jk}}, \quad (3)$$

which are highly nonlinear functions of temperature  $T$ , density  $\rho$ , and the participating reactive species mass fractions  $Y_j$ .  $J$  denotes the total number of the reactive species,  $W_j$  is the molecular weight of species  $j$ , and  $\nu_{jk}$  is the stoichiometric coefficient of species  $j$  in reaction  $k$ .  $A_k$  is the frequency factor,  $n_k$  is the pre-exponential temperature exponent,  $E_k$  is the activation energy of reaction  $k$ , and  $R$  is the universal gas constant. Substituting the corresponding spatially filtered quantities  $\bar{\rho}$ ,  $\bar{Y}_j$ , and  $\bar{T}$  into Eq. (3) will generally lead to unacceptably erroneous predictions for the filtered reaction rates  $\dot{\omega}_k$ ; thus, a model must be provided for  $\dot{\omega}_k$ . In the context of turbulent nonpremixed combustion, where the fuel and oxidizer have to be mixed together before they can react, the mixture fraction  $Z$ , which represents the local fraction of gas originating from the feed fuel stream, is an important parameter on which the reaction rates and the resulting chemical composition strongly depend. Therefore, many proposed closure models rely on the mixture fraction  $Z$  and its probability density function (PDF) describing the state of mixedness.

LES resolves only spatially filtered quantities involving a filtering operation as shown in Eq. (1). Correspondingly, in the framework of LES the state of mixedness, which accounts for the unresolved subgrid-scale fluctuations  $Z''$  around the filtered scalar  $\bar{Z}$ , is appropriately described by a “filtered density function” (FDF).<sup>7</sup> The density-weighted FDF is defined as

$$\bar{P}(\zeta; \mathbf{x}, t) = \frac{1}{\bar{\rho}(\mathbf{x}, t)} \int_D \rho(\mathbf{x}', t) \delta[\zeta - Z(\mathbf{x}', t)] G(\mathbf{x} - \mathbf{x}') d\mathbf{x}', \quad (4)$$

where  $\zeta$  denotes the random variable in the mixture fraction domain,  $\delta$  is the delta function, and  $Z(\mathbf{x}', t)$  represents an instantaneous value of the mixture fraction at the location  $\mathbf{x}'$  and time  $t$ . The FDF can be obtained through a transport

equation as suggested in the FDF-transport methods.<sup>7,8</sup> Alternatively, the shape of the FDF can be presumed. In this case the presumed FDF can, for instance, be specified in terms of its first and second moment ( $\bar{Z}$ ,  $\bar{Z}^2$ ) given at every computational grid point. In the last years several mixture fraction based models using a presumed FDF have been proposed for LES.

Assuming chemical equilibrium<sup>9</sup> offers the benefit that the chemical composition as well as the thermodynamic state are completely specified by the mixture fraction only (“mixed=burned”). However, as this approach implies infinitely fast chemistry, it is applicable only to flames with very fast reactions, whose time scale is negligibly small in comparison to the smallest flow time scale. In addition, no formation of any intermediate species can be accounted for. The steady-state Laminar Flamelet Model<sup>10,11</sup> allows for non-equilibrium chemistry with very detailed kinetics. It considers the flame as an ensemble of laminar flamelets strained by the turbulent flow field. The laminar flamelets are computed as the steady-state solutions of a laminar diffusion flame in mixture fraction space with the scalar dissipation rate, which represents the diffusive and convective transport normal to the stoichiometric mixture fraction, as varying parameter. Due to the steady-state assumption for the flamelet solutions in mixing space this model is basically not capable of predicting unsteady effects like ignition or extinction. The Lagrangian Flamelet Model, which was proposed for LES of a reacting jet in a recent work,<sup>12</sup> attempts to account for transient effects on the flame in  $Z$  space. This model solves the unsteady laminar flamelet equations in a Lagrangian type flamelet time, which can be regarded as the residence time of a flamelet in the physical flow field. Both the flamelet time and the time-dependent scalar dissipation rate are obtained using the resolved velocity and mixture fraction fields provided by the LES in the physical domain. While this approach does not require any steady-state assumption when solving the flamelet equations in mixture fraction, it still assumes that the individual laminar flamelets do not vary with time in the physical flow domain. The flamelet solutions are supplied to the LES as functions only of the downstream location, where they remain constant in time. The assumed PDF method proposed by Frankel *et al.*<sup>13</sup> for nonequilibrium chemistry requires the specification of an assumed joint PDF to close the spatially filtered reaction terms. As the dimensionality of this joint PDF increases with the number of reactive scalars, this approach is basically restricted to very simple chemistry. In the case of a multistep kinetic scheme with several reactive scalars it would become inhibitive troublesome to parameterize the then highly multivariate PDF appropriately.

The Conditional Source-term Estimation (CSE) method used in the present work was developed as a mixture fraction based model for nonequilibrium chemistry, which does not require any steady-state assumptions either in mixing space or in physical space. Moreover, the model should be able to handle more complex multistep, reduced though, chemistry rather than simple artificial one-step mechanisms, which were frequently used in test computations.

The present LES considers a piloted methane–air jet flame with the Reynolds number  $Re=22\,400$ . The feed stream consists of 25% (vol.) methane and 75% (vol.) air. The coflowing oxidizer stream is pure air, and the stoichiometric mixture fraction is  $Z_{\text{stoic}}=0.352$ . The pilot stream surrounding the inner fuel jet resembles the hot product composition of a premixed methane–air flame with  $Z_{\text{pilot}}=0.27$ . This flame, known as the ‘‘Sandia D-Flame,’’ has been intensively investigated experimentally.<sup>14,15</sup> While the partial premixedness of the feed fuel stream might be considered as a further complication for the simulation in comparison to a purely nonpremixed situation, the dilution of the fuel jet with air is sufficiently far below the flammable limit such that the flame can still be regarded as a typical diffusion flame. In addition, the dilution makes very accurate measurements of this methane–air flame possible, and a large amount of reliable and well documented experimental data for the individual species concentrations are available in physical space as well as in mixture fraction space. The LES of this flame attempts to assess the predictive capabilities of the recently proposed CSE method,<sup>16</sup> as well as the method’s robustness and computational cost. Previous to this work, the CSE model has only been validated in *a priori* tests against DNS, where it gave promising results.

## II. FORMULATION

### A. LES transport equations

The LES set of equations is obtained by applying a density-weighted spatial filter as given in Eq. (2) to the differential transport equations for mass, momentum, species, and enthalpy:

$$\frac{\partial \bar{\rho}}{\partial t} + \nabla \cdot (\bar{\rho} \tilde{\mathbf{u}}) = 0, \quad (5)$$

$$\frac{\partial \bar{\rho} \tilde{\mathbf{u}}}{\partial t} + \nabla \cdot (\bar{\rho} \tilde{\mathbf{u}} \tilde{\mathbf{u}}) = -\nabla \bar{p} + \nabla \cdot (\bar{\sigma} + \bar{\tau}), \quad (6)$$

$$\frac{\partial \bar{\rho} \tilde{Y}_j}{\partial t} + \nabla \cdot (\bar{\rho} \tilde{\mathbf{u}} \tilde{Y}_j) = \nabla \cdot (\bar{\rho} D_{l,j} \nabla Y_j + \bar{q}) + \bar{\Omega}_j, \quad (7)$$

$$\frac{\partial \bar{\rho} \tilde{h}}{\partial t} + \nabla \cdot (\bar{\rho} \tilde{\mathbf{u}} \tilde{h}) = \nabla \cdot (\bar{\kappa}_l \nabla T + \bar{s}) + \sum_{j=1}^J (\bar{\Omega}_j h_{0,j}). \quad (8)$$

Here,  $\bar{\rho}$ ,  $\tilde{\mathbf{u}}$ ,  $\tilde{h}$ , and  $\tilde{T}$  are the filtered density, velocity vector, enthalpy, and temperature.  $\tilde{Y}_j$  is the mass fraction of species  $j$ ,  $h_{0,j}$  is the enthalpy of formation of species  $j$ .  $\bar{\sigma}$  and  $\bar{\tau}$  are the molecular viscous and subgrid-scale stress tensor, respectively,  $D_{l,j}$  is the molecular diffusivity of the species  $j$ ,  $\bar{\kappa}_l$  is the thermal conductivity,  $\bar{q}$  and  $\bar{s}$  the subgrid-scale fluxes of species and heat, respectively.

Due to the fairly high Froude number of the jet flow considered in the present study the buoyancy forces are small in comparison to the inertial forces. The magnitude of the buoyancy effects relative to momentum effects is represented by the inverse of the densimetric Froude number

$$Fr^{-1} = \frac{\left(1 - \frac{\rho_f}{\rho_0}\right) g D}{U_0^2} \approx 2.5 \times 10^{-5} \ll 1,$$

where  $g$  is the gravitational acceleration,  $U_0$  is the bulk velocity of the jet,  $D$  is the nozzle diameter,  $\rho_f$  is the minimum density attainable in the flame, and  $\rho_0$  is the density of the reference state given by  $T_0=298$  K and  $p_0=1$  atm in the coflowing pure air stream. Estimating the downstream length of the nonbuoyant region in jet diameters

$$\left(\frac{x}{D}\right)_{\text{nb}} = 0.5 Fr^{1/2} \left(\frac{\rho_f}{\rho_0}\right)^{1/4} \approx 63$$

following a proposal by Chen and Rodi<sup>17</sup> for round, vertical turbulent buoyant jets, indicates that buoyancy is practically negligible in the considered jet flame (according to the experiment the visible flame length is about  $x/D=67$ ). It was therefore neglected in Eq. (6).

The velocities occurring in the jet flow are small in comparison to the speed of sound. Thus, the flow is in the low Mach number regime, and the spatial pressure derivative term  $\mathbf{u} \cdot \nabla p$  as well as the viscous dissipation  $\sigma : \nabla \mathbf{u}$  were omitted in Eq. (8). Moreover, as we are dealing with an open diffusion flame (such that the bulk pressure is constant) the temporal pressure derivative  $\partial \bar{p} / \partial t$  was omitted in Eq. (8), as well. The unresolved subgrid-scale convective fluxes are modeled using eddy viscosity and eddy diffusivity models, respectively:

$$\bar{\tau} = -\bar{\rho}(\overline{\mathbf{u}\mathbf{u}} - \tilde{\mathbf{u}}\tilde{\mathbf{u}}) = \bar{\rho} \tilde{\nu}_t (\nabla \tilde{\mathbf{u}} + (\nabla \tilde{\mathbf{u}})^T - \frac{2}{3}(\nabla \cdot \tilde{\mathbf{u}})\mathbf{I}), \quad (9)$$

$$\bar{q} = -\bar{\rho}(\overline{\mathbf{u}Y_j} - \tilde{\mathbf{u}}\tilde{Y}_j) = \bar{\rho} \tilde{D}_{t,j} \nabla \tilde{Y}_j, \quad (10)$$

$$\bar{s} = -\bar{\rho}(\overline{\mathbf{u}h} - \tilde{\mathbf{u}}\tilde{h}) = \tilde{\kappa}_t \nabla \tilde{T}. \quad (11)$$

Therein,  $\tilde{\nu}_t$  is the eddy viscosity;  $\tilde{D}_{t,j}$  is the eddy diffusivity of species  $j$ ;  $\tilde{\kappa}_t$  is the thermal eddy conductivity; and  $\mathbf{I}$  is the identity matrix. All the turbulent transport coefficients  $\tilde{\nu}_t$ ,  $\tilde{D}_{t,j}$ , and  $\tilde{\kappa}_t$  are computed using the dynamic model proposed for compressible flows.<sup>6</sup>

As the subgrid-scale contributions arising from the nonlinearities in the molecular viscous and diffusive fluxes are small when compared to convective turbulent subgrid-scale terms given by Eqs. (9)–(11),<sup>18</sup> these contributions were omitted resulting in the following approximations:

$$\begin{aligned} \bar{\sigma} &= \bar{\rho} \nu_l (\nabla \mathbf{u} + (\nabla \mathbf{u})^T - \frac{2}{3}(\nabla \cdot \mathbf{u})\mathbf{I}) \\ &\approx \bar{\rho} \tilde{\nu}_l (\nabla \tilde{\mathbf{u}} + (\nabla \tilde{\mathbf{u}})^T - \frac{2}{3}(\nabla \cdot \tilde{\mathbf{u}})\mathbf{I}), \\ \bar{\rho} D_{l,j} \nabla Y_j &\approx \bar{\rho} \tilde{D}_{l,j} \nabla \tilde{Y}_j, \quad \bar{\kappa}_l \nabla T \approx \tilde{\kappa}_l \nabla \tilde{T}. \end{aligned}$$

The filtered molecular viscosity is assumed to be a function of the filtered temperature following a power law,<sup>19,20</sup> where again the subgrid-scale fluctuations of the temperature are neglected:

$$\bar{\mu} = \bar{\rho} \tilde{\nu}_l \sim \tilde{T}^{0.7}.$$

Constant specific heats  $c_p$  and  $c_v$ , unity Lewis number, and a constant molecular Schmidt number were assumed for all species:

$$Le_j = \frac{\bar{\kappa}_l}{\bar{\rho} c_p \bar{D}_{l,j}} = 1, \quad Sc_j = \frac{\bar{\nu}_l}{\bar{D}_{l,j}} = 0.7. \quad (12)$$

It should be noted at this point that the assumptions concerning the molecular transport coefficients and the specific heats are strictly valid only for gaseous mixtures, where the properties of the individual components do not differ markedly. Due to the great variety of different species participating in a combustion process the assumption (12) has surely to be regarded as a rather crude approximation from a physical point of view. It permits, however, a considerable simplification of the analytical formulation. Many mixture fraction based models make the unity Lewis number assumption associated with equal molecular diffusivities of all scalars, because, under this assumption, the conserved scalar can be expressed as a linear combination of species mass fractions and/or temperature. However, in nonunity Lewis number flows with significantly differing molecular diffusivities, it is possible to simply regard the conserved scalar more as a random variable whose sample space ranges from  $Z=0$  in pure oxidizer and  $Z=1$  in pure fuel. This would require solving an extra transport equation and storing the conserved scalar in a simulation; to minimize computational cost in our simulations, we have elected to make the assumption (12) for this test case. The assumption (12) is not essential to the present method though. The rate of change of species mass fraction due to chemical reaction  $\bar{\Omega}_j$ , appearing as source term in Eqs. (7) and (8), is a linear combination of the different reaction rates in which species  $j$  participates:

$$\bar{\Omega}_j = W_j \sum_{k=1}^K (\nu'_{jk} - \nu''_{jk}) \bar{\omega}_k. \quad (13)$$

Therein,  $K$  is the total number of reactions and  $\nu'_{jk}$  and  $\nu''_{jk}$  are the stoichiometric coefficients for species  $j$  in reaction  $k$ . The CSE method was used to close the chemical reaction terms  $\bar{\omega}_k$  in Eq. (13). A very detailed description of this closure model can be found in previous work.<sup>16</sup> The general concept of the CSE method will be outlined in the following section (II B). Its actual application to a methane–air kinetic mechanism will be described in Sec. III B.

### B. CSE closure method

The CSE model is based on Conditional Moment Closure (CMC), a method which was first proposed independently by Bilger and Klimenko.<sup>21,22</sup> In CMC, the chemical source terms can be closed using the first order accurate CMC hypothesis, which reads

$$\langle \dot{\omega}_k | \zeta \rangle(\mathbf{x}, t) \approx f_k(\langle \rho | \zeta \rangle, \langle T | \zeta \rangle, \langle Y_j | \zeta \rangle), \quad (14)$$

where  $\langle \cdot | \zeta \rangle$  denotes the average of some random variable  $(\cdot)$  over an ensemble of realizations of the flow field being investigated conditioned on the mixture fraction having some value  $\zeta$ ;  $f_k$  is the Arrhenius-type equation (3) for reaction  $k$  evaluated with the conditionally averaged density  $\langle \rho | \zeta \rangle$ ,

temperature  $\langle T | \zeta \rangle$ , and mass fractions  $\langle Y_j | \zeta \rangle$ . The spatial and time dependence of the conditional averages on the right hand side (RHS) of Eq. (14) was omitted for brevity. The CMC hypothesis (14) has proven to give a good approximation when compared to data from experiments and DNS,<sup>23,24</sup> particularly when the activation energy is small and for steadily burning flames (without extinction or ignition). The CMC method solves a transport equation for the conditional averages in space, time, and in mixture fraction space, adding a further dimension to the problem, which makes the computational cost exceedingly high for three-dimensional flows.

The CSE model proposes a way to incorporate the CMC hypothesis (14) in LES without having to solve transport equations for the conditional averages as is required in CMC. In the context of LES the conditional filtered average of some random variable  $f$  is defined by

$$\overline{f | \zeta}(\mathbf{x}, t) = \frac{\int_D \rho(\mathbf{x}', t) f(\mathbf{x}', t) \delta[\zeta - Z(\mathbf{x}', t)] G(\mathbf{x} - \mathbf{x}') d\mathbf{x}'}{\bar{\rho}(\mathbf{x}, t) \bar{P}(\zeta; \mathbf{x}, t)}, \quad (15)$$

where  $\bar{P}(\zeta; \mathbf{x}, t)$  is the FDF as specified in Eq. (4). The integration of (15) over the mixture fraction space yields the spatially filtered counterpart  $\tilde{f}$

$$\tilde{f}(\mathbf{x}, t) = \int_0^1 \overline{f | \zeta}(\mathbf{x}, t) \bar{P}(\zeta; \mathbf{x}, t) d\zeta. \quad (16)$$

Averaging the conditional filtered mean over some arbitrary ensemble  $A$  of  $M$  discrete points in the flow field yields the ensemble average of the conditional filtered mean

$$\langle \overline{f | \zeta} \rangle(t; A) = \frac{1}{M} \sum_{m=1}^M \overline{f | \zeta}(\mathbf{x}_m, t). \quad (17)$$

It has been observed that the conditional averages of mass fractions and temperature do not vary significantly on planes across a shear layer.<sup>24</sup> Thus, these planes can be assumed to be statistically homogeneous for the conditional averages. Applying this homogeneity assumption to the conditional filtered means implies that the conditional filtered averages do not change on these planes. Thus, if the ensemble  $A$  in Eq. (17) is comprised of points  $\mathbf{x}_m$ :  $m = 1, \dots, M$ , being all located on a homogeneous surface, the conditional filtered average at every sample point  $m$  is

$$\overline{f | \zeta}(\mathbf{x}_m, t) = \langle \overline{f | \zeta} \rangle(t; A). \quad (18)$$

With the conditional filtered means being dependent on time but not on space, Eq. (16) can be rewritten as

$$\tilde{f}(\mathbf{x}_m, t) = \int_0^1 \langle \overline{f | \zeta} \rangle(t; A) \bar{P}(\zeta; \mathbf{x}_m, t) d\zeta \quad (19)$$

on every homogeneous surface. In the present flow configuration planes at constant distance  $x$  downstream of the nozzle of the jet were assumed to be surfaces of statistical homogeneity for the conditional filtered averages as shown in Fig. 1. Given a presumed functional form of the FDF  $\bar{P}(\zeta; \mathbf{x}_m, t)$  in terms of the mean and variance

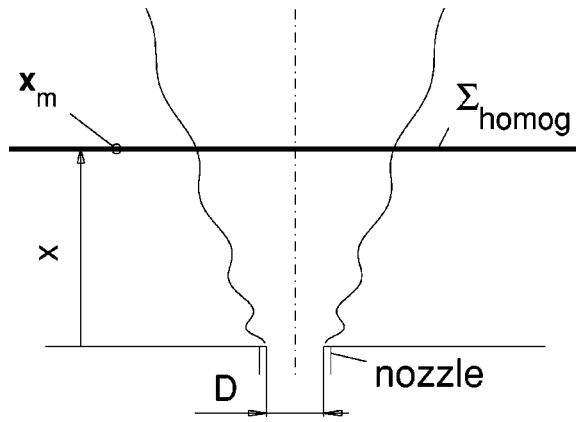


FIG. 1. Planes  $\Sigma_{\text{homog}}$  across the jet's shear layer on which statistical homogeneity for the conditional averages is assumed.

$$\tilde{P}(\zeta; \mathbf{x}_m, t) = \tilde{P}(\zeta; \tilde{Z}(\mathbf{x}_m, t), \tilde{Z}^{n2}(\mathbf{x}_m, t)),$$

as well as the spatially filtered scalars  $\tilde{f}(\mathbf{x}_m, t)$ , which are provided by the filtered scalar transport equations (7) and (8), the integral equation (19) can be rewritten at every LES grid point  $\mathbf{x}_m: m=1, \dots, M$ , on each of these homogeneous planes. This constitutes a system of  $M$  linear equations for the conditional filtered average  $\overline{\langle f | \zeta_n \rangle}$  over discrete intervals  $\Delta \zeta_n: n=1, \dots, N$  in mixture fraction space on each plane. The solution of each overdetermined ( $M > N$ ) linear system of equations using a linear regularization technique provides the conditional filtered averages as a function of the downstream location  $x$  and time  $t$ . Inserting these conditional averages into the RHS of Eq. (14) yields approximations for the conditional filtered mean reaction rates

$$\overline{\langle \dot{\omega}_k | \zeta \rangle}(x, t) \approx f_k(\overline{\langle \rho | \zeta \rangle}(x, t), \overline{\langle T | \zeta \rangle}(x, t), \overline{\langle Y_j | \zeta \rangle}(x, t)). \quad (20)$$

Their unconditional spatially filtered counterparts  $\overline{\dot{\omega}_k}(\mathbf{x}_m, t)$  occurring in Eqs. (7) and (8) through Eq. (13) can then be calculated using

$$\overline{\dot{\omega}_k}(\mathbf{x}_m, t) = \overline{\rho}(\mathbf{x}_m, t) \int_0^1 \frac{\overline{\langle \dot{\omega}_k | \zeta \rangle}(x, t)}{\overline{\langle \rho | \zeta \rangle}(x, t)} \tilde{P}(\zeta; \mathbf{x}_m, t) d\zeta. \quad (21)$$

The assumption of the statistical homogeneity for the conditional filtered means of the ensemble  $A$  is essential to the method. If the conditional filtered means of the ensemble  $A$  is not homogeneous, Eq. (19) does not represent adequately all points of the ensemble. The solution of Eq. (19) for the conditional filtered average may produce poor approximations for the unconditional source terms at certain points of the ensemble. Therefore, a realistic selection of the statistically homogeneous ensembles requires some *a priori* information about the structure of the particular flow field considered. For example, in wall-bounded flows, points near cooled walls should not be sampled together with points far away from walls.

The experimental data of the piloted jet flame<sup>14,15</sup> show that the conditional averages do not change very rapidly downstream of the axis of the jet. This rather slow down-

stream variation makes it possible to “thicken” the surfaces on which statistical homogeneity for the conditional averages can be assumed. Thus, rather than using the LES points located on every single plane as illustrated in Fig. 1, all the LES points on a layer of several neighboring planes can be taken as the statistical sample of size  $M$  to establish the linear system by writing the integral equation, Eq. (19), at sample point  $\mathbf{x}_m: m=1, \dots, M$ . Solving the linear systems obtained with these larger multiplane samples did not give significantly different results for the conditional averages compared with results obtained with the smaller single-plane samples. Unfortunately, having to invert a linear system on fewer successive layers of neighboring planes does not reduce the computational cost. The larger sample size involves larger linear systems making the inversion procedure, which is based on a least squares method, computationally more expensive. The higher computational expense per sample outweighs the savings due to a smaller total number of samples.

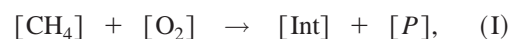
As no steady-state condition for the flame was assumed *a priori*, the linear system obtained from Eq. (19) at  $m=1, \dots, M$  LES sample points has to be inverted at every time step to obtain the conditional averages evolving in time. This principle can be relaxed however in cases where the flame eventually reaches a steady state and the conditional averages do not change noticeably in time any more. In such cases the conditional averages need to be computed at every time step only until they reach a steady state. From that point onwards, the integral in Eq. (21) can be evaluated using the same steady-state solutions of the conditional averages, then varying only with the jet's downstream distance  $x$ . This simplification could be made for the particular test case considered in the present study to save computational cost. It is, however, noted again that the CSE method basically does not require any steady-state assumption for the conditional filtered averages.

### III. METHANE–AIR CHEMISTRY

The use of a very detailed chemical mechanism for methane–air diffusion flames involves a large number of reactive species and elementary reactions. While the CSE closure model is generally applicable to arbitrarily complex kinetic mechanisms, it should be noted that every additional reaction requires at least one more transport equation, adding to the computational cost. A strongly reduced scheme, a two-step mechanism, was determined to be an appropriate choice for the present first test of CSE in a predictive LES, in that this reduced mechanism gives reasonably good predictions of methane–air flame properties while requiring minimal computational effort.

#### A. Reduced kinetic mechanism

Based on steady-state and partial-equilibrium assumptions for various elementary steps in the complex methane–air reaction kinetics the detailed mechanism can be systematically reduced to the following two-step kinetic scheme:<sup>25</sup>



The molar composition of the intermediate species [Int] and of product [P] is defined as

$$[\text{Int}] = \frac{4}{3}[\text{H}_2] + \frac{2}{3}[\text{CO}] \quad \text{and} \quad [P] = \frac{2}{3}[\text{H}_2\text{O}] + \frac{1}{3}[\text{CO}_2]$$

in mole  $\text{cm}^{-3}$ , respectively. The rates for reaction (I) and (II) are given by

$$\dot{\omega}_I = k_{11f}[\text{CH}_4][\text{H}], \quad (22)$$

$$\dot{\omega}_{II} = k_5[\text{O}_2][\text{H}][M]. \quad (23)$$

The steady-state assumption for the hydrogen radical [H] gives

$$[\text{H}] = (K_1 K_2)^{1/2} K_3 \frac{[\text{O}_2]^{1/2} [\text{H}_2]^{3/2}}{[\text{H}_2\text{O}]} \Theta \left[ 1 - \exp\left(-\frac{T}{1000}\right)^5 \right], \quad (24)$$

where the quantity  $\Theta$  is calculated following a proposal by Peters:<sup>26</sup>

$$\Theta = \exp\left[-\left(\frac{15}{4}\right)^{1/2} \frac{k_{11f}[\text{CH}_4]}{k_{1f}[\text{O}_2]}\right]. \quad (25)$$

The rate coefficients  $k_{1f}$ ,  $k_5$ ,  $k_{11f}$  as well as the equilibrium constants  $K_1$ ,  $K_2$ ,  $K_3$  refer to the skeletal methane–air mechanism as listed in the literature;<sup>27</sup> units in Eqs. (22)–(25) are mole, centimeter, gram, second, and Kelvin. The third body concentration in Eqs. (22) and (23) is

$$[M] = 6.5[\text{CH}_4] + 6.5[\text{H}_2\text{O}] + 1.5[\text{CO}_2] + [\text{H}_2] + 0.75[\text{CO}] + 0.4[\text{O}_2] + 0.4[\text{N}_2]. \quad (26)$$

The rates of change in the participating mass fractions due to the chemical reactions expressed in terms of  $\dot{\omega}_I$  and  $\dot{\omega}_{II}$  are

$$\dot{\Omega}_{\text{CH}_4} = -W_{\text{CH}_4} \dot{\omega}_I, \quad (27)$$

$$\dot{\Omega}_{\text{O}_2} = -W_{\text{O}_2} (\dot{\omega}_I + \dot{\omega}_{II}), \quad (28)$$

$$\dot{\Omega}_{\text{Int}} = W_{\text{Int}} (\dot{\omega}_I - \dot{\omega}_{II}), \quad (29)$$

$$\dot{\Omega}_P = W_P (\dot{\omega}_I + 2 \dot{\omega}_{II}), \quad (30)$$

with  $W_{\text{CH}_4}$ ,  $W_{\text{O}_2}$ ,  $W_{\text{Int}}$ , and  $W_P$  being the molecular weights of fuel, oxidizer, intermediate species, and product, respectively. The source term in the transport equation for enthalpy (8) reads

$$\dot{\Omega}_T = \sum_j (\dot{\Omega}_j h_{0,j}) = \dot{\omega}_I Q_I + \dot{\omega}_{II} Q_{II}, \quad (31)$$

with  $j = \text{CH}_4, \text{O}_2, \text{Int}, P$ ,

where the reactive heat release due to reactions I and II is linearly composed of the enthalpies of formation of fuel, intermediate species, and product as follows:

$$Q_I = h_{0,\text{CH}_4} - \overbrace{\frac{2}{3}h_{0,\text{CO}}}^{-h_{0,\text{Int}}} - \overbrace{\frac{2}{3}h_{0,\text{H}_2\text{O}} - \frac{2}{3}h_{0,\text{CO}_2}}^{-h_{0,P}}, \quad (32)$$

$$Q_{II} = h_{0,\text{Int}} - 2 h_{0,P}. \quad (33)$$

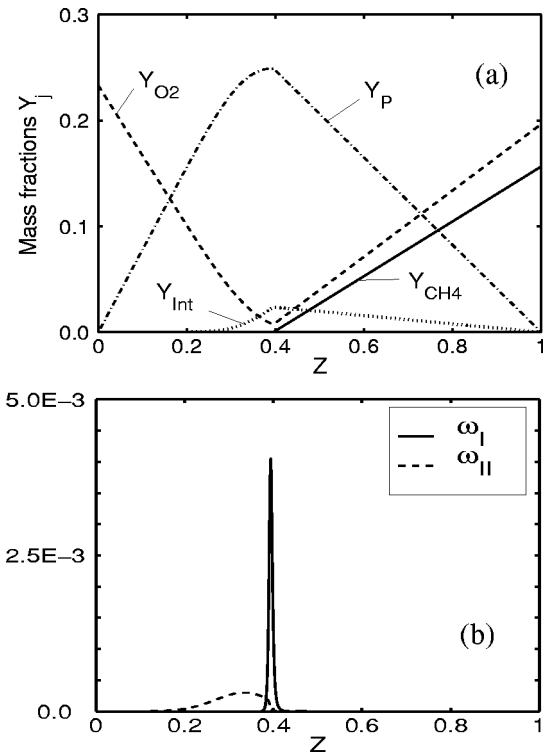


FIG. 2. Steady-state laminar flamelet solution using two-step mechanism with a scalar dissipation rate  $\chi = 33 \text{ s}^{-1}$ : (a) species mass fractions of fuel  $Y_{\text{CH}_4}$ , oxidizer  $Y_{\text{O}_2}$ , intermediate  $Y_{\text{Int}}$ , and product  $Y_P$ ; (b) chemical reaction rates  $\dot{\omega}_I$  and  $\dot{\omega}_{II}$  in mole  $\text{s}^{-1} \text{cm}^{-3}$ .

The numerical values of  $Q_I$  and  $Q_{II}$  are  $291 \times 10^3$  and  $511 \times 10^3 \text{ J mol}^{-1}$ , respectively. The concentration of the radical [H], as is specified in Eqs. (24) and (25), is very sensitive to temperature and fuel concentration  $[\text{CH}_4]$ . The decrease of temperature together with the increase of the fuel mass fraction on the rich side of the diffusion flame gives  $[\text{H}] = 0$ , shutting off the chemistry so oxidizer can leak through the reaction zone to the fuel rich side as is the case at high strain rates. On the lean side, however, the reaction rate  $\dot{\omega}_I$  drops to zero only if the fuel is burned completely (fuel cannot leak to the lean side). By allowing  $\text{O}_2$  leakage but not  $\text{CH}_4$  leakage in highly strained flames, this two-step mechanism qualitatively exhibits behavior found in the experiment.<sup>25</sup> Moreover, in the present case, the feed fuel stream is diluted with air. The shut off of the reactions as the H radical concentration drops to zero on the rich side prevents the flame from penetrating too far into the partially premixed fuel zone. The diffusion flame structure in mixture fraction ( $Z$ ) space for the two-step chemistry is shown in Figs. 2(a) and 2(b). These results were obtained from the steady-state solution of the laminar flamelet equations for all participating species mass fractions  $Y_j$  and temperature  $T$ . Having assumed unity Lewis number, constant specific heats, and Schmidt numbers, the laminar flamelet equations are written as<sup>11</sup>

$$\frac{\partial Y_j}{\partial t} - \frac{\chi}{2} \frac{\partial^2 Y_j}{\partial Z^2} = \frac{\dot{\Omega}_j}{\rho}, \quad j = \text{CH}_4, \text{O}_2, \text{Int}, P, \quad (34)$$

$$\frac{\partial T}{\partial t} - \frac{\chi}{2} \frac{\partial^2 T}{\partial Z^2} = \frac{\dot{\Omega}_T}{\rho}. \quad (35)$$

The scalar dissipation rate was set to  $\chi = 2D_Z(\nabla Z)^2 = 32 \text{ s}^{-1}$ . It is evident from Figs. 2(a) and 2(b) that the fuel consumption occurs in a very narrow zone around the peak of reaction rate  $\dot{\omega}_I$  and virtually no fuel leaks to the lean side. Adjacent to this very thin layer of fuel consumption is the broader zone of reaction rate  $\dot{\omega}_{II}$  in which intermediate and oxidizer are reacted to product. While being totally reacted by  $\dot{\omega}_{II}$  on the lean side, intermediate can diffuse through the reaction zone toward the rich side. On the other hand, the leakage of oxidizer to the rich side is inhibited by the dilution of the fuel stream with air.

Concerning the aforementioned flame structure, at higher strain rates it should be noted that the considered piloted flame is far away from extinction, which is crucial for the applicability of model being based only on the mixture fraction as is used in the present LES. The main criteria for choosing the present two-step mechanism were that it handles the partial premixedness of the fuel feed well and that its computational cost does not make the closure model exceedingly expensive. Considering a case where the flame is close to extinction due to high strain rates would require, in the first place, a modification of the chemical closure model. The CSE model would likely have to account for strain, e.g., by introducing a second conditioning variable.

## B. CSE closure for two-step chemistry

Invoking the CMC closure hypothesis (14) with the present two-step chemistry yields for the conditional filtered averages of rate (I) and (II)

$$\overline{\dot{\omega}_I | \zeta} = f_I(\overline{T | \zeta}, \overline{Y_{\text{CH}_4} | \zeta}, \overline{Y_{\text{O}_2} | \zeta}, \overline{Y_{\text{Int}} | \zeta}, \overline{Y_P | \zeta}), \quad (36)$$

$$\overline{\dot{\omega}_{II} | \zeta} = f_{II}(\overline{T | \zeta}, \overline{Y_{\text{CH}_4} | \zeta}, \overline{Y_{\text{O}_2} | \zeta}, \overline{Y_{\text{Int}} | \zeta}, \overline{Y_P | \zeta}), \quad (37)$$

where  $f_I$  and  $f_{II}$  include all the functional dependencies described in Eqs. (22)–(26). For the case of low Mach number for which thermodynamic pressure  $p_0$  is constant, the conditional density can be expressed in terms of temperature and chemical composition using the equation of state

$$\overline{\rho | \zeta} = \frac{p_0}{\overline{T | \zeta} \sum_j \overline{Y_j | \zeta} \frac{R}{W_j}}, \quad \text{with } j = \text{CH}_4, \text{O}_2, \text{Int}, P, \quad (38)$$

and does not appear in Eqs. (36) and (37). Similar to the CMC hypothesis (36)–(37), the fluctuations around the filtered conditional means are assumed to be small in Eq. (38) as well.

Rather than solving an integral equation as given by Eq. (19) for every conditional filtered mean quantity needed in  $f_I$  and  $f_{II}$ , the conditional filtered averages for the species mass fractions and temperature can be rewritten as functions of two conditional variables which represent the consumption of fuel and oxidizer by the reaction, respectively. These two new variables, the fuel-consumption variable  $C_1$  and the oxidizer-consumption variable  $C_2$ , are defined in physical

(LES) space as the difference of the actual fuel and oxidizer mass fractions to the corresponding chemically inert mixed states  $\tilde{Y}_{\text{CH}_4}^*$  and  $\tilde{Y}_{\text{O}_2}^*$ , respectively,

$$\tilde{C}_1 = \tilde{Y}_{\text{CH}_4}^* - \tilde{Y}_{\text{CH}_4}, \quad (39)$$

$$\tilde{C}_2 = \tilde{Y}_{\text{O}_2}^* - \tilde{Y}_{\text{O}_2}. \quad (40)$$

The quantities  $\tilde{Y}_{\text{CH}_4}^*$  and  $\tilde{Y}_{\text{O}_2}^*$ , which are associated with  $\tilde{C}_1 = 0$  and  $\tilde{C}_2 = 0$ , respectively, represent mixing of fuel and oxidizer without any chemical reaction; they are linear functions of the mixture fraction  $\tilde{Z}$  only. In the mixing configuration of the present jet simulation they read

$$\tilde{Y}_{\text{CH}_4}^* = \tilde{Z} Y_{\text{CH}_4,1}, \quad (41)$$

$$\tilde{Y}_{\text{O}_2}^* = \tilde{Y}_{\text{O}_2,2} + \tilde{Z} (Y_{\text{O}_2,1} - Y_{\text{O}_2,2}), \quad (42)$$

where  $Y_{\text{CH}_4,1}$  and  $Y_{\text{O}_2,1}$  is the methane and oxygen mass fraction in the feed fuel stream, respectively, and  $Y_{\text{O}_2,2}$  is the oxygen mass fraction in the oxidizer stream. Having assumed no differential diffusion, i.e., unity Lewis number, the spatially filtered mixture fraction  $\tilde{Z}$  is defined as a linear combination of the individual filtered species mass fractions

$$\tilde{Z} = \frac{1}{Y_{\text{CH}_4,1} + \frac{2W_{\text{CH}_4}}{W_{\text{O}_2}}(Y_{\text{O}_2,2} - Y_{\text{O}_2,1})} \times \left[ \tilde{Y}_{\text{CH}_4} - \frac{2W_{\text{CH}_4}}{W_{\text{O}_2}}(\tilde{Y}_{\text{O}_2} - Y_{\text{O}_2,2}) - \frac{W_{\text{CH}_4}}{W_P} \tilde{Y}_P \right]. \quad (43)$$

The coefficients in Eq. (43) were determined so that the linear combination of the transport equations for  $\tilde{Y}_{\text{CH}_4}$ ,  $\tilde{Y}_{\text{O}_2}$ , and  $\tilde{Y}_P$  has no chemical source term and the boundary conditions— $\tilde{Z} = 0$  in the pure feed oxidizer stream and  $\tilde{Z} = 1$  in the pure feed fuel stream—are satisfied. The present definition (43) was chosen in accordance with the definition of  $Z$  used in the experiment, where  $Z$  also measures the mixing between the partially premixed fuel feed jet and the co-flow and not the local methane/air mixing. This definition of  $Z$  has the advantage that the stoichiometric mixture fraction is ( $Z_{\text{stoic}} = 0.352$ ), such that the FDFs are easy to resolve numerically.

The product and intermediate mass fractions can be expressed as linear combinations of  $\tilde{C}_1$ ,  $\tilde{C}_2$ , and  $\tilde{Z}$ :

$$\tilde{Y}_P = \frac{2W_P}{W_{\text{O}_2}} \tilde{C}_2 - \frac{W_P}{W_{\text{CH}_4}} \tilde{C}_1 - \frac{W_P}{W_{\text{CH}_4}} \left( \frac{2W_{\text{CH}_4}}{W_{\text{O}_2}} - 1 \right) \tilde{Y}_{\text{O}_2}^*, \quad (44)$$

$$\begin{aligned} \tilde{Y}_{\text{Int}} = & \left( \frac{W_P}{W_{\text{CH}_4}} + 1 \right) \tilde{C}_1 - \left( \frac{2W_P}{W_{\text{O}_2}} - 1 \right) \tilde{C}_2 \\ & + \frac{W_P}{W_{\text{CH}_4}} \left( \frac{2W_{\text{CH}_4}}{W_{\text{O}_2}} - 1 \right) \tilde{Y}_{\text{O}_2}^*. \end{aligned} \quad (45)$$

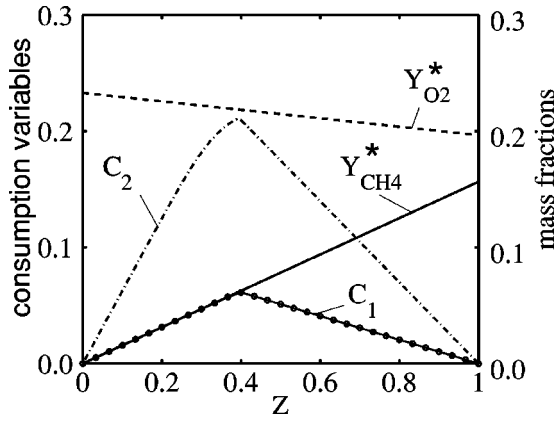


FIG. 3. Fuel-consumption variable  $C_1$  and oxidizer-consumption variable  $C_2$  for the steady-state laminar flamelet solution shown in Fig. 2 and chemically inert mixing lines of fuel  $Y_{\text{CH}_4}^*$  and oxidizer  $Y_{\text{O}_2}^*$ .

For the temperature the analogous linear functional dependence  $\tilde{T} = \tilde{T}(\tilde{C}_1, \tilde{C}_2, \tilde{Z})$  is obtained by incorporating Eqs. (39)–(45) into the equation for the total enthalpy

$$c_p(\tilde{T} - T_0) + \sum_j (\tilde{Y}_j - \tilde{Y}_j^*) \frac{h_{0j}}{W_j} = 0, \quad (46)$$

with  $j = \text{CH}_4, \text{O}_2, \text{Int}, P,$

where  $T_0$  is the reference temperature and the quantities with the asterisk again represent the chemically inert mixed state. Translating the unconditional quantities  $\tilde{Y}_j(\tilde{C}_1, \tilde{C}_2, \tilde{Z})$  and  $\tilde{T}(\tilde{C}_1, \tilde{C}_2, \tilde{Z})$  from physical space into conditioning, or mixture fraction, space, the corresponding conditional filtered quantities are obtained as linear combinations of the conditional filtered fuel-consumption and oxidizer-consumption variable  $\overline{C_1 | \zeta}$  and  $\overline{C_2 | \zeta}$ , respectively:

$$\overline{Y_{\text{CH}_4} | \zeta} = \overline{Y_{\text{CH}_4} | \zeta^*} - \overline{C_1 | \zeta}, \quad (47)$$

$$\overline{Y_{\text{O}_2} | \zeta} = \overline{Y_{\text{O}_2} | \zeta^*} - \overline{C_2 | \zeta}, \quad (48)$$

$$\overline{Y_{\text{Int}} | \zeta} = \left( \frac{W_P}{W_{\text{CH}_4}} + 1 \right) \overline{C_1 | \zeta} - \left( 2 \frac{W_P}{W_{\text{O}_2}} - 1 \right) \overline{C_2 | \zeta}, \quad (49)$$

$$\overline{Y_P | \zeta} = 2 \frac{W_P}{W_{\text{O}_2}} \overline{C_2 | \zeta} - \frac{W_P}{W_{\text{CH}_4}} \overline{C_1 | \zeta}, \quad (50)$$

$$\overline{T | \zeta} = T_0 + \frac{Q - Q_{\text{II}}}{W_{\text{CH}_4}} \overline{C_1 | \zeta} + \frac{Q_{\text{II}}}{W_{\text{O}_2}} \overline{C_2 | \zeta}, \quad (51)$$

with the molecular weights of the individual mass species being  $W_{\text{CH}_4} = 16$ ,  $W_{\text{O}_2} = 32$ ,  $W_{\text{Int}} = 64/3$ , and  $W_P = 80/3 \text{ g mol}^{-1}$ . The chemically inert straight mixing lines  $-\overline{Y_{\text{CH}_4} | \zeta^*}$  in Eq. (47) and  $\overline{Y_{\text{O}_2} | \zeta^*}$  in Eq. (48)—as well as the functional shape of fuel-consumption variable  $C_1$  and oxidizer-consumption variable  $C_2$  in mixture fraction ( $Z$ ) space—can be seen in Fig. 3. The displayed curves of  $C_1(Z)$  and  $C_2(Z)$  correspond to the steady-state laminar flamelet solution shown in Fig. 2(a).

Using Eqs. (47) and (48) an integral equation similar to Eq. (16) can be written for the two conditional filtered variables  $\overline{C_1 | \zeta}$  and  $\overline{C_2 | \zeta}$

$$\tilde{Y}_{\text{CH}_4}^* - \tilde{Y}_{\text{CH}_4} = \int_0^1 \overline{C_1 | \zeta} \tilde{P}(\zeta; \mathbf{x}, t) d\zeta, \quad (52)$$

$$\tilde{Y}_{\text{O}_2}^* - \tilde{Y}_{\text{O}_2} = \int_0^1 \overline{C_2 | \zeta} \tilde{P}(\zeta; \mathbf{x}, t) d\zeta, \quad (53)$$

where the shape FDF at grid point  $\mathbf{x}$  and time  $t$  was assumed to be a  $\beta$  function,<sup>9</sup> which is specified by the instantaneous spatially filtered mean  $\tilde{Z}(\mathbf{x}, t)$  and variance  $\tilde{Z}''^2(\mathbf{x}, t)$

$$\tilde{P}(\zeta; \mathbf{x}, t) = \frac{\zeta^{a-1} (1-\zeta)^{b-1}}{\beta(a, b)}, \quad a = \tilde{Z} \left[ \frac{\tilde{Z}(1-\tilde{Z})}{\tilde{Z}''^2} - 1 \right],$$

$$b = a \left( \frac{1}{\tilde{Z}} - 1 \right).$$

Therein, the spatially filtered mixture fraction  $\tilde{Z}$  is expressed as a linear combination of the filtered species mass fractions as given in Eq. (43). The filtered variance  $\tilde{Z}''^2$  is modeled using a dynamic procedure.<sup>28</sup> Thus, it is not necessary to solve an extra transport equation for either the filtered mean or the filtered variance of the mixture fraction.

As outlined in Sec. II B, statistical homogeneity of the conditional averages is assumed on planes of constant downstream distance from the nozzle (see Fig. 1), and Eq. (18) can be applied to all conditional filtered means including  $\overline{C_1 | \zeta}$  and  $\overline{C_2 | \zeta}$ . At every LES sample point  $\mathbf{x}_m$ :  $m = 1, \dots, M$ , located on each of these homogeneous planes the integral equations (52) and (53) are rewritten as

$$(\tilde{Y}_{\text{CH}_4}^* - \tilde{Y}_{\text{CH}_4})_m = \sum_{n=1}^N \langle \overline{C_1 | \zeta_n} \rangle \tilde{P}_{n,m} \Delta \zeta_n, \quad (54)$$

$$(\tilde{Y}_{\text{O}_2}^* - \tilde{Y}_{\text{O}_2})_m = \sum_{n=1}^N \langle \overline{C_2 | \zeta_n} \rangle \tilde{P}_{n,m} \Delta \zeta_n, \quad (55)$$

where the integrals are approximated as sums over  $N$  discrete intervals  $\Delta \zeta_n$  using a trapezoidal scheme.  $\tilde{P}_{n,m}$  represent the discretized FDF at point  $m$  and  $\langle \overline{C_{1,2} | \zeta_n} \rangle$  are the discretized conditional filtered means, respectively. Equations (54) and (55) constitute a linear system of  $M$  equations for the  $N < M$  discrete unknowns  $\langle \overline{C_1 | \zeta_n} \rangle$  and  $\langle \overline{C_2 | \zeta_n} \rangle$  in conditioning space at each node  $\zeta_n$  with  $n = 1, \dots, N$ . The  $\zeta$  grid was specified with  $N = 41$  points, which are strongly clustered around the stoichiometric mixture fraction at  $\zeta = Z_{\text{stoic}} = 0.352$  in order to increase the resolution in the reaction zone. The accuracy of the chosen discretization in  $\zeta$  space was checked by solving the laminar flamelet equations (34)–(35) on the given  $\zeta$  grid for the reduced two-step chemistry and comparing the results with the corresponding laminar flamelet solution obtained on a further refined  $\zeta$  grid. The solutions obtained on the two different grids showed no significant difference. The linear system (54)–(55) constitutes a Fredholm equation of the first kind which has to be inverted; this was solved for  $\langle \overline{C_1 | \zeta_n} \rangle$  and  $\langle \overline{C_2 | \zeta_n} \rangle$  using a linear

regularization method.<sup>29</sup> The number of grid points located on each plane at a constant distance downstream from the nozzle determines the maximum sample size of  $M$ ; in the present case that maximum value was  $M = 4032$ . Calculations were made both with the maximum and half of the maximum sample size. The results of the inversion did not vary significantly, however the model's computational cost in the latter case was reduced by half, hence all results shown in the following sections were obtained with  $M = 2016$  sample points on each homogeneous plane. The chosen sample points are located on radial grid lines going outward from the center line of the jet through the reaction layer into the coflowing oxidizer stream. The individual grid rays are randomly chosen. Inserting the solutions for the conditional filtered averages  $\langle C_1 | \zeta \rangle$  and  $\langle C_2 | \zeta \rangle$  into the RHS of Eqs. (47)–(51) provides the conditionally averaged temperature and species mass fractions needed for the closure hypothesis in Eqs. (36) and (37) on each plane. The integration of these conditional filtered averages with the FDF over  $\zeta$  gives the unconditional spatially filtered values for the reaction rates  $\dot{\omega}_I$  and  $\dot{\omega}_{II}$  at every point  $\mathbf{x}_m$ :

$$\dot{\omega}_I(\mathbf{x}_m, t) = \bar{\rho}(\mathbf{x}_m, t) \int_0^1 \frac{\langle \dot{\omega}_I | \zeta \rangle}{\langle \rho | \zeta \rangle} \bar{P}(\zeta; \mathbf{x}_m, t) d\zeta, \quad (56)$$

$$\dot{\omega}_{II}(\mathbf{x}_m, t) = \bar{\rho}(\mathbf{x}_m, t) \int_0^1 \frac{\langle \dot{\omega}_{II} | \zeta \rangle}{\langle \rho | \zeta \rangle} \bar{P}(\zeta; \mathbf{x}_m, t) d\zeta. \quad (57)$$

Expressing the thermodynamic state in terms of two consumption variables reduces the computational cost considerably because only two integral equations (52) and (53) have to be inverted. The left hand side of these equations is obtained from the filtered fields of the mass fractions of fuel and oxidizer. Only two scalar transport equations (7) have to be solved for  $\bar{Y}_{\text{CH}_4}$  and  $\bar{Y}_{\text{O}_2}$ , whose source terms  $\bar{\Omega}_{\text{CH}_4}$  and  $\bar{\Omega}_{\text{O}_2}$  are related to  $\dot{\omega}_I$  and  $\dot{\omega}_{II}$  by Eqs. (27) and (28), respectively. The spatially filtered instantaneous values of the remaining scalars involved in the two-step mechanism, i.e., intermediate species  $\bar{Y}_{\text{Int}}$ , product  $\bar{Y}_P$ , and temperature  $\bar{T}$ , are calculated by computing the corresponding conditional averages  $\langle Y_{\text{Int}} | \zeta \rangle$ ,  $\langle Y_P | \zeta \rangle$ , and  $\langle T | \zeta \rangle$  as functions of  $\langle C_1 | \zeta \rangle$  and  $\langle C_2 | \zeta \rangle$  according to Eqs. (49)–(51) and substituting them into the integrals

$$\bar{Y}_{\text{Int}}(\mathbf{x}_m, t) = \int_0^1 \langle Y_{\text{Int}} | \zeta \rangle \bar{P}(\zeta; \mathbf{x}_m, t) d\zeta, \quad (58)$$

$$\bar{Y}_P(\mathbf{x}_m, t) = \int_0^1 \langle Y_P | \zeta \rangle \bar{P}(\zeta; \mathbf{x}_m, t) d\zeta, \quad (59)$$

$$\bar{T}(\mathbf{x}_m, t) = \int_0^1 \langle T | \zeta \rangle \bar{P}(\zeta; \mathbf{x}_m, t) d\zeta. \quad (60)$$

#### IV. RESULTS

The computational code used for the present LES is based on a code originally developed for DNS of non-reacting, round, free jets in the low Mach number limit.<sup>30</sup>

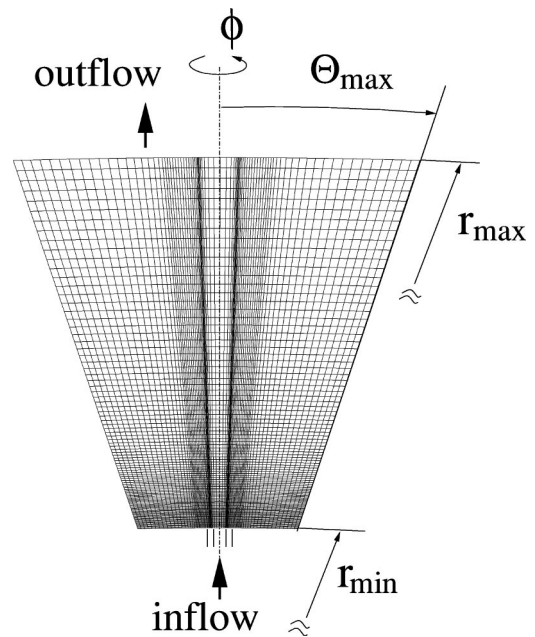


FIG. 4. Computational grid in spherical coordinates (for better visibility only every second grid line is displayed).

The LES version of that code was obtained by implementing dynamic subgrid-scale models for the unresolved turbulent transport and the CSE closure model for the chemical reaction terms. The LES was performed on a computational grid shown in schematic form in Fig. 4. It is given in spherical coordinates with  $192 \times 84 \times 48$  points in streamwise  $r$ , cross-stream  $\Theta$ , and azimuthal  $\Phi$  direction of the jet. The grid is refined in the streamwise and cross-stream direction to increase the spatial resolution in the region close to the orifice as well as in the shear layer. As the numerical integration scheme employs a finite volume method, which is second-order accurate in space, the local mesh refinement was also needed to reduce the effect of the numerical dissipation inherent in second-order schemes. The numerical dissipation might otherwise excessively dampen the contributions of the subgrid scale models. Due to the high density ratio (the ratio of reference density in the coflowing air to the minimum density in the flame is  $\rho_0/\rho_{\text{min}} \approx 7$ ) the LES transport equations for momentum and the scalars are integrated in time using the predictor–corrector–projection scheme.<sup>31</sup> Thereby, the numerical solution is advanced in time using a second-order Adams–Bashford scheme in the predictor-step, which is followed by a corrector step using a semi-implicit Crank–Nicholson scheme. The advective fluxes in the scalar transport equations were obtained with a Total Variation Diminishing (TVD) scheme to avoid spurious oscillations in the vicinity of strong gradients which occur particularly in the shear layer of the jet close to the nozzle, where large amounts of unmixed fuel meet the oxidizer from the coflow. To overcome stability problems due to an eventual stiffness of the kinetic mechanism, a timestep splitting technique is used<sup>32</sup> when computing the source terms in conditioning space. Equations (56) and (57) are evaluated with the conditional filtered source terms averaged in time over the flow timestep  $\Delta t^n = t^{n+1} - t^n$ , which read

$$\left( \frac{\overline{\langle \dot{\omega}_k | \zeta \rangle}}{\overline{\langle \rho | \zeta \rangle}} \right)^t_{(x,t^n)} = \frac{1}{\Delta t^n} \int_{t^n}^{t^{n+1}} \left( \frac{\overline{\langle \dot{\omega}_k | \zeta \rangle}}{\overline{\langle \rho | \zeta \rangle}} \right) (x, \theta) d\theta, \quad (61)$$

where  $\langle \dot{\omega}_k | \zeta \rangle(x, \theta)$  is evaluated at every subimestep according to the CMC hypothesis given in Eq. (20). The time integral in (61) is computed using an ordinary differential equation solver from the package ODEPACK.<sup>33</sup>

At the inflow boundary, all the required mean quantities are specified according to the experimental data given for the fuel jet, pilot, and coflowing air stream, respectively. Velocity fluctuations were superimposed on the measured mean profiles  $\langle u_{in} \rangle$  to mimic turbulent inflow conditions. The mean velocity profile was perturbed with several rotating helical as well as oscillating axisymmetric modes.<sup>34</sup>

A convective boundary condition is used for the outflow boundary at  $r = r_{max}$ .<sup>35</sup>

$$\frac{\partial \tilde{u}_i}{\partial t} + U_{con} \frac{\partial \tilde{u}_i}{\partial r} = 0.$$

Therein, the convection velocity  $U_{con}$  is the mean outflow velocity averaged over the azimuthal direction  $\phi$ . The convective boundary condition convects vortical structures out of the computational domain through the outflow boundary, thereby stabilizing the simulation. Although this procedure is nonphysical in elliptic problems, it can still be applied to flows of convective nature like free flow without disturbing the upstream solution,<sup>30</sup> however, the region immediately adjacent to the outflow boundary has to be disregarded in the analysis of the numerical results.

A traction-free condition is used at the lateral boundary at  $\Theta = \Theta_{max}$ .<sup>36</sup> The traction-free boundary condition is given by

$$\sigma_{ij} n_j = 0,$$

where  $\sigma_{ij}$  is the stress tensor and  $n_j$  is the unit normal vector on the boundary. Unlike the no-slip or free-slip conditions it allows for a flux of ambient fluid across the lateral boundary. Thus, it is well suited to capture the entrainment in a spreading jet.

An instantaneous temperature field is shown in Fig. 5 to illustrate the structure of the piloted jet flame. The cold inner fuel jet is surrounded by a hot coannular pilot stream, which keeps the flame attached to the nozzle. The region close to the nozzle is evidently dominated by small scale structures emerging from the boundary layers, while the region further downstream is dominated by larger structures. The profile of the time-averaged mixture fraction and temperature—the latter normalized with the inflow temperature of the coflowing air stream  $T_0 = 291$  K—on the centerline and radial distribution at various locations downstream the nozzle are shown in Figs. 6 and 7, respectively. The agreement with the experimental data is reasonable, implying that the heat release is predicted fairly accurately by the model.

Figures 8 and 9 show the radial distribution of time-averaged species mass fractions at various locations downstream of the nozzle. The agreement of the LES results with the experiment is good. There is, however, an underprediction of intermediate species and an overprediction of prod-

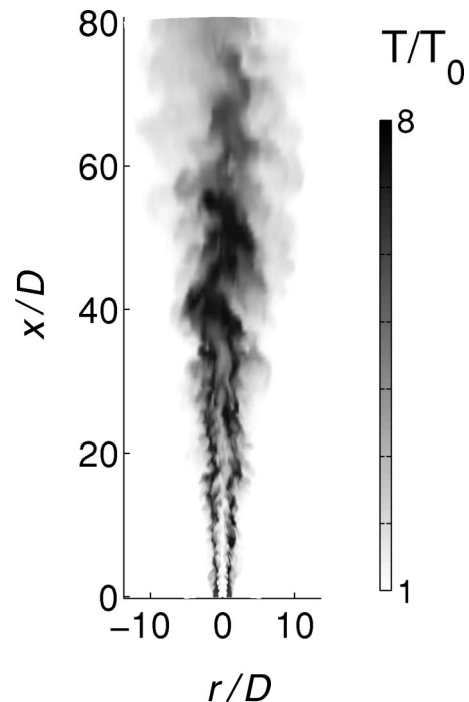


FIG. 5. Instantaneous temperature field normalized with reference temperature  $T_0 = 291$  K.

uct, which is most significant at  $x/D = 30$ . This is a result of discrepancies in the prediction of the conditional averages; as shown in Figs. 10 and 11, the conditional filtered averages computed according to the procedure described in Eqs. (47)–(53) also exhibit the aforementioned disagreement for the intermediate species and product at the corresponding downstream locations. Some part of these discrepancies can be attributed to the extreme simplicity of the chemical kinetic mechanism which was applied in the present LES as derived in the literature<sup>25</sup> without adjusting any of the mechanism’s parameters. Although this two-step mechanism mimics qualitatively the structure of methane–air diffusion flames very well, it is conceivable that simplifying the very complex methane–air chemistry to just two reactions will give quantitatively less accurate predictions than the full detailed

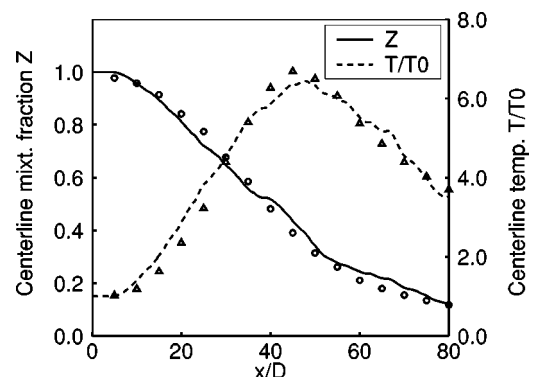


FIG. 6. Mixture fraction  $Z$  and temperature  $T/T_0$  normalized with the reference temperature  $T_0 = 291$  K at the centerline of the jet vs downstream distance in nozzle diameters  $D$ ; (—) LES result for mixture fraction; (---) is LES result for temperature; symbols denote the experimental data.

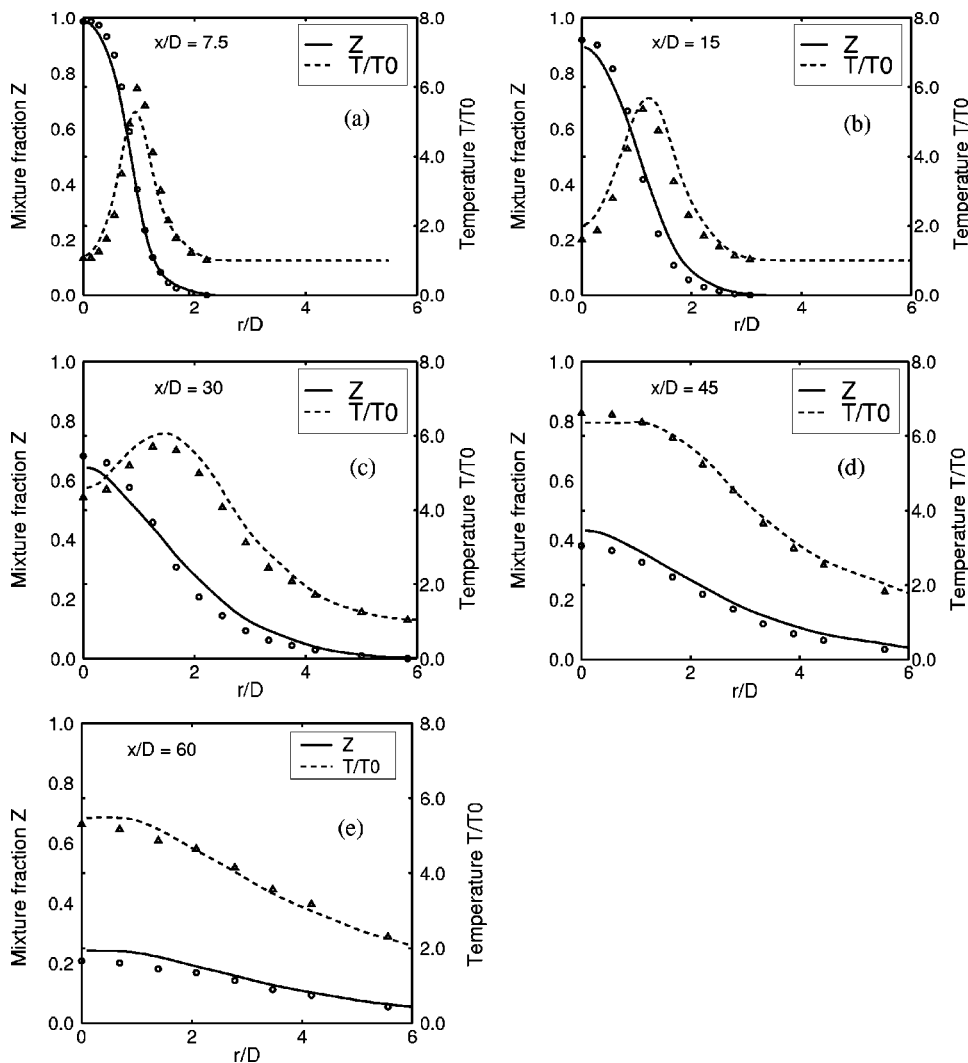


FIG. 7. Mixture fraction  $Z$  and temperature  $T/T_0$  normalized with the reference temperature  $T_0=291$  K vs radial direction in jet diameters  $D$  at different downstream locations: (a) at  $x=7.5$ , (b) at  $x=15$ , (c) at  $x=30$ , (d) at  $x=45$ , (e) at  $x=60$  diameters downstream of the nozzle; (—) LES results for  $Z$ ; (---) LES results for  $T/T_0$ ; symbols denote the measurements.

mechanism. In deriving the two-step mechanism one of the major reduction steps involves the partial equilibrium assumption for the water–gas shift



Applied to the present flame this partial equilibrium evidently causes an underprediction of the concentrations of  $[\text{CO}]$ , the principal intermediate species. Using a more detailed chemical kinetic mechanism would help to overcome this problem. It should be noted, however, that computational cost is an important issue in the choice of a chemical mechanism to be employed in CSE. As already pointed out above, every further reaction accounted for requires at least one more scalar transport equation in the resolved physical space plus one more mapping procedure [Eq. (52)] for the corresponding conditional average in mixture fraction space. The main objective of the present LES was to assess the feasibility and predictive capabilities of the CSE method in a self-sustained LES. The two-step mechanism was chosen as the least computationally expensive methane–air mechanism that can be applied to the particular configuration given in the present jet flame. Applying very detailed chemistry was determined to be beyond the scope of this study. A close examination of the experimental data on the rich side of the

flame unveils something else that should not be overlooked: the partial premixedness of the feed fuel stream. The experimental data of the conditional averages of the intermediate species and product shown in Figs. 10(b), 10(d), 11(b), and 11(d) exhibit a slight hump on the fuel side of the diffusion flame around mixture fraction  $Z=0.6$ . Assuming rather a physical background than experimental uncertainties as a possible reason for this hump, it can be concluded that there is some reactive formation of intermediate species and product in this partially premixed fuel region. The CSE method, like any other mainly mixture fraction based model, is designed for nonpremixed combustion. Thus, it is conceivable that the occurrence of a premixed reaction zone might contribute to the disagreement of the model's predictions with the experiment on the partially premixed rich side, as well.

## V. DISCUSSION

The test simulation of a piloted jet reported here shows that the CSE method is a tool with satisfactory predictive capabilities to be employed in a predictive self-sustained LES of diffusion flames. Nevertheless, the discrepancies found between the predictions of the LES and the experimental data unveil the limitations and shortcomings of the

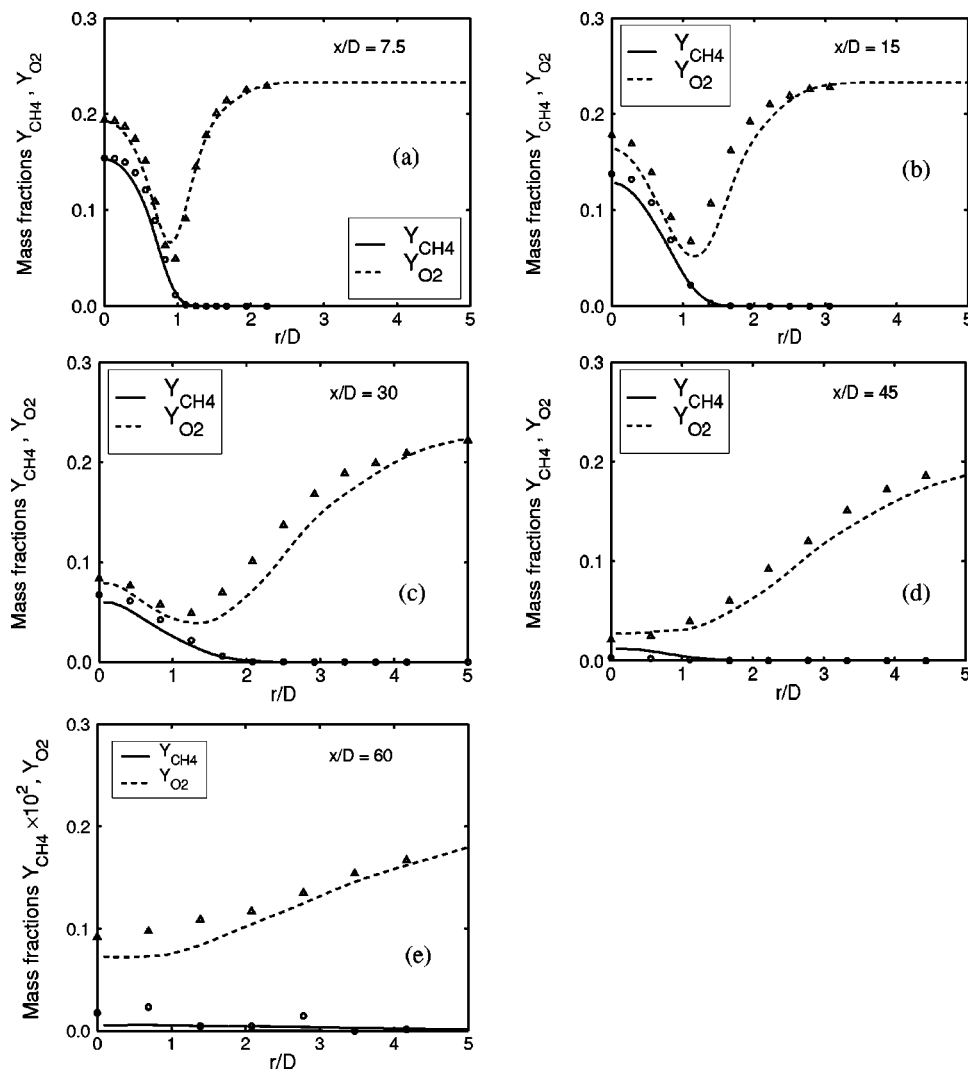


FIG. 8. Species mass fractions of fuel  $Y_{\text{CH}_4}$  and oxidizer  $Y_{\text{O}_2}$  vs radial direction in jet diameters  $D$  at different downstream locations: (a) at  $x=7.5$ , (b) at  $x=15$ , (c) at  $x=30$ , (d) at  $x=45$ , (e) at  $x=60$  diameters downstream of the nozzle; (—) LES results for  $Y_{\text{CH}_4}$ ; (---) LES results for  $Y_{\text{O}_2}$ ; symbols denote the measurements.

CSE model as well as those of the strongly reduced kinetic mechanism. The quality of the results obtained with the present CSE model depends mainly on the validity of the following assumptions:

- (1) The reactions depend solely on one conditioning variable.
- (2) The conditional reaction terms can be approximated by the CMC hypothesis to first-order accuracy (14), i.e., the conditional fluctuations around the conditional averages are negligible.
- (3) Surfaces of homogeneity for the conditional averages, where Eq. (18) applies, can be specified in the flow field.
- (4) The uncertainties in the numerical solution of the integral equation (19) are small.

The flame considered in the present study is far enough away from extinction that the conditional fluctuations around the conditional averages can be neglected and the first two assumptions are satisfied. The free unbounded jet configuration is characterized by a dominant motion of fluid downstream of the axis of the jet. There are no walls, which may lead to recirculation zones or heat transfer from the gas. Thus, planes of constant downstream distance to the nozzle can be

realistically assumed to be homogeneous surfaces for the conditional averages. Dealing with other more complicated configurations, e.g., wall-bounded or swirling, jets that have significant back flow and/or wall effects would complicate the selection of homogeneous surfaces in that this selection would surely have to account for the greater complexity of the flow field (e.g., regions with a considerable heat loss to the walls, or regions with larger pockets of recirculating hot burned gas will have to be treated separately owing to their different statistics in mixing space). In such complex cases, surfaces constituted by particles with the same residence time might be a more appropriate, though numerically more expensive, choice. Moreover, if extinction is important, a second conditioning variable will have to be added to the mixture fraction. This additional variable could be related to the scalar dissipation rate. The CSE procedure would be as described in previous work.<sup>16</sup>

The assumption of the shape of the filtered probability density functions is inherent in all presumed PDF methods and is not a constraint for the CSE method *per se*. CSE can alternatively be applied with a transported PDF approach as well.

As chemical reaction rates are in general very sensitive

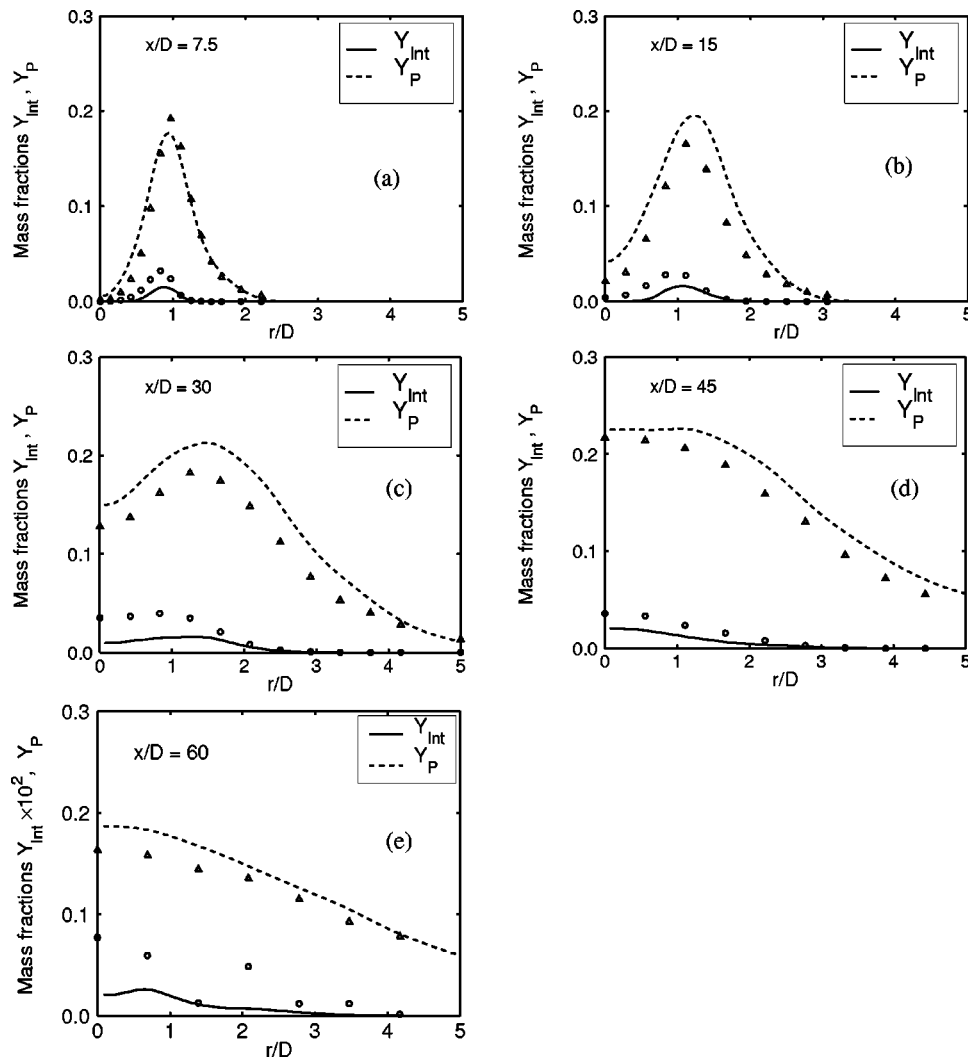


FIG. 9. Species mass fractions of intermediate  $Y_{\text{Int}}$  and product  $Y_P$  vs radial direction in jet diameters  $D$  at different downstream locations: (a) at  $x = 7.5$ , (b) at  $x = 15$ , (c) at  $x = 30$ , (d) at  $x = 45$ , (e) at  $x = 60$  diameters downstream of the nozzle; (—) LES results for  $Y_{\text{Int}}$ ; (---) LES results for  $Y_P$ ; symbols denote the measurements.

to variations in the participating reactive scalars, the accuracy of the numerical solution procedure for the conditional averages as proposed by the CSE method is an important issue. The reaction zones have to be resolved sufficiently well in mixture fraction space, which requires strong clustering of points in the stoichiometric region when discretizing the integral equations. The quality of the resolution in conditioning space can be tested best by computing a laminar flamelet solution on the chosen grid. Generally, more detailed chemistry requires more points in mixing space.

The CSE method's uncertainties, which are primarily related to the latter two items given above, can be estimated by comparing the spatially filtered fuel mass fraction  $\bar{Y}_j$  provided by the LES transport equation (7) with the spatially filtered value obtained with the integral equation (19) for the same species. For example, rewriting Eq. (19) for fuel reads

$$\bar{Y}_{\text{CH}_4}(\mathbf{x}_m, t) = \int_0^1 \langle Y_{\text{CH}_4} | \zeta \rangle \bar{P}(\zeta; \mathbf{x}_m, t) d\zeta, \quad (63)$$

where the conditional average  $\langle Y_{\text{CH}_4} | \zeta \rangle$  is computed according to Eq. (47) as a function of  $\langle C_1 | \zeta \rangle$ . Figure 12 shows the results of this comparison obtained at all points of the computational domain at some instant in time. The mass frac-

tions provided by the transport equation are denoted by  $\bar{Y}_{\text{CH}_4}^{\text{transp.}}$  and plotted on the abscissa. The mass fractions obtained with Eq. (63) at the corresponding grid points are denoted by  $\bar{Y}_{\text{CH}_4}^{\text{CSE}}$  and plotted on the ordinate. The width of the scatter around the straight line with unity slope gives a qualitative estimate of the uncertainties due to the inversion procedure of Eq. (54) and the homogeneity assumption invoking Eq. (18) on each plane at constant downstream distance. The relative standard error obtained for all points, where  $\bar{Y}_{\text{CH}_4}$  is significant ( $\geq 1 \times 10^{-2}$ ),  $\sigma_{\text{rel}}$  is about 8%. Unfortunately, it is not possible to distinguish clearly which part of the deviations is caused by the numerics of the inversion procedure and which part is due to the homogeneity assumption. Test calculations were made with chemically inert mixing fields. There, the inversion procedure proved to be very accurate—inserting the solution of Eq. (54) into Eq. (47) produced the straight mixing lines for the conditional filtered averages in mixing space which read for fuel

$$\langle Y_{\text{CH}_4} | \zeta \rangle = \zeta Y_{\text{CH}_4,1}. \quad (64)$$

Concerning the kinetic mechanism, the results of the present LES make it evident that the simple two-step methane–air

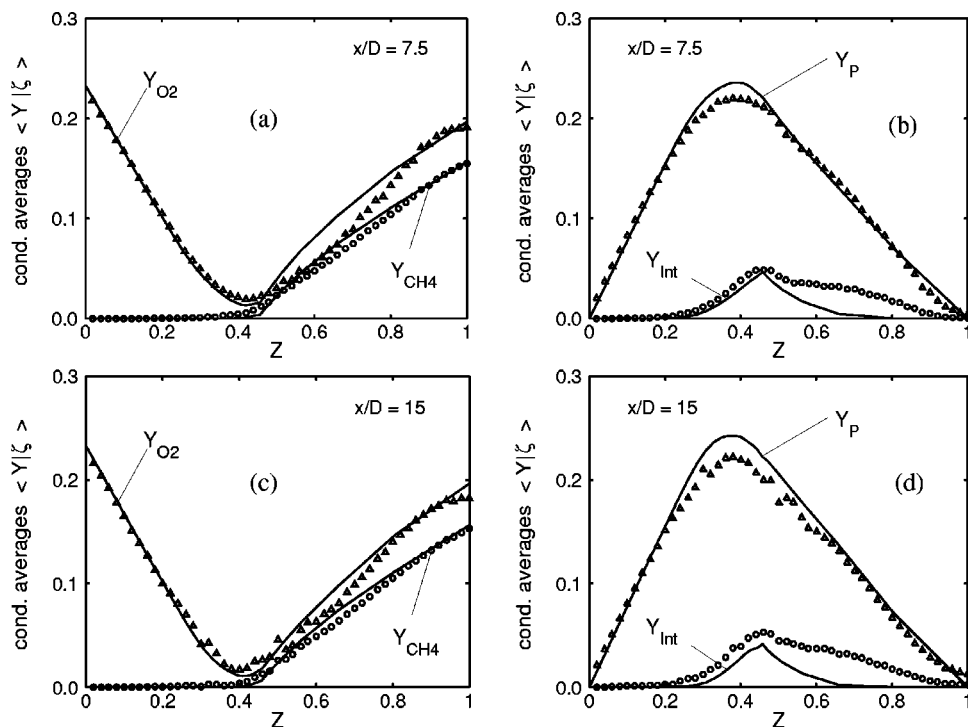


FIG. 10. Conditional averages of species mass fractions of fuel  $\langle Y_{CH_4} | Z \rangle$ , oxidizer  $\langle Y_{O_2} | Z \rangle$ , intermediate  $\langle Y_{Int} | Z \rangle$ , and product  $\langle Y_P | Z \rangle$ : (a), (b) at  $x = 7.5$  diameters downstream of the nozzle; (c), (d) at  $x = 15$  diameters downstream of the nozzle; (—) CSE results; symbols denote the measurements.

mechanism clearly has its limits in producing quantitatively accurate predictions for all the species involved. In particular, the disagreement of the intermediate species with the experiment suggests the application of a more detailed chemistry for future work. Full or large skeletal kinetic mechanisms have to be ruled out as they would make the LES with CSE closure too computationally expensive. A compromise between very accurate chemistry and computational cost has to be made.

### VI. CONCLUSION

The closure problem for the reactive source terms imposes an enormous challenge to LES of reacting flows. The CSE method was developed with the objective of providing a generally applicable closure model for LES of nonpremixed combustion. As long as surfaces of homogeneity for the conditionally averaged composition vector and temperature (which the method needs as input quantities) can be speci-

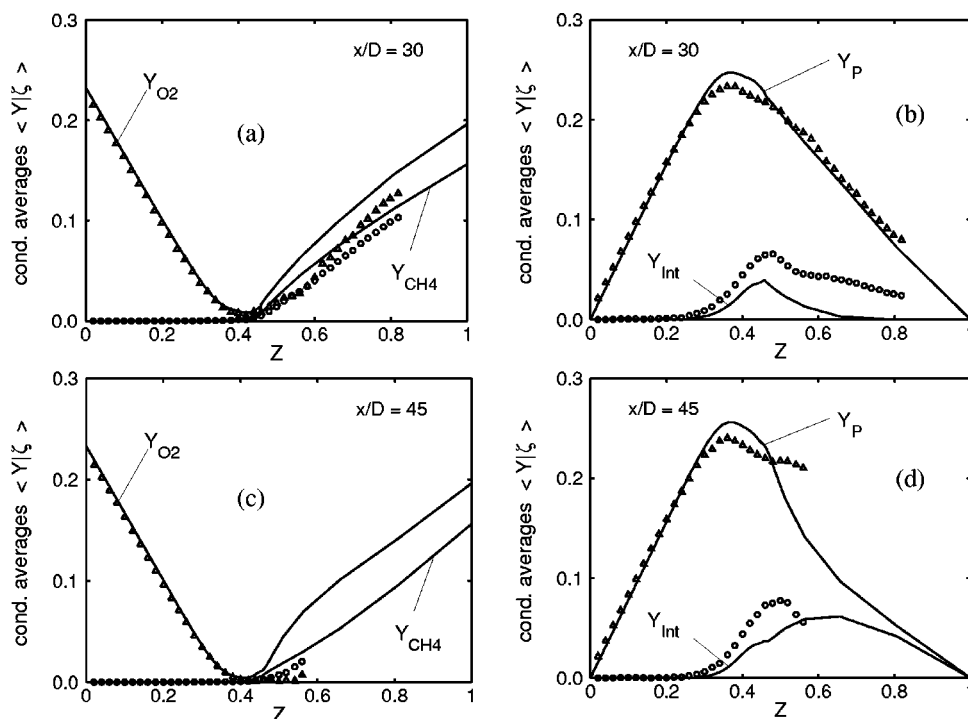


FIG. 11. Conditional averages of species mass fractions of fuel  $\langle Y_{CH_4} | Z \rangle$ , oxidizer  $\langle Y_{O_2} | Z \rangle$ , intermediate  $\langle Y_{Int} | Z \rangle$ , and product  $\langle Y_P | Z \rangle$ : (a), (b) at  $x = 30$  diameters downstream of the nozzle; (c), (d) at  $x = 45$  diameters downstream of the nozzle; (—) CSE results; symbols denote the measurements.

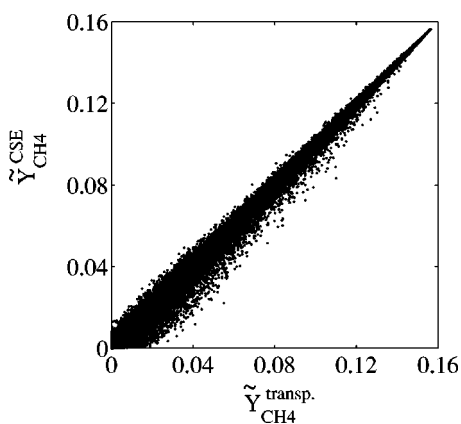


FIG. 12. Spatially filtered species mass fraction for fuel from CSE procedure  $\bar{Y}_{\text{CH}_4}^{\text{CSE}}$  vs spatially filtered species mass fraction for fuel from LES transport equation  $\bar{Y}_{\text{CH}_4}^{\text{transp.}}$ .

fied, the model can be applied to diffusion flames with any given flow configuration and chemistry. The model does not require “infinitely fast reactions” or steady-state assumptions for the conditional averages. As it relies on information from the instantaneous flow field provided by the LES transport equations, it is capable of accounting for unsteady effects of the turbulent motion on the reaction rates. The present LES of a piloted turbulent jet flame proved the CSE method to be an appropriate closure model for nonpremixed flames. The discrepancies found between the numerical results and the experimental data unveiled the limitations of the strongly reduced kinetic mechanism applied in the present LES as well as the limitations and shortcomings of the CSE method itself. The latter are related mainly to the statistical homogeneity assumption required by the method, the dependence of just one single conditioning variable, and the problem of obtaining sufficiently accurate solutions in conditioning space. Summing up, it can be said that CSE is a very feasible approach to get closure for the spatially filtered reaction terms in LES of diffusion flames. To obtain good results, it requires, however, some *a priori* knowledge of the structure of the flowfield in physical space as well as the knowledge of the flame structure in conditioning space for the given chemistry.

## ACKNOWLEDGMENTS

The authors wish to thank R. W. Bilger, G. Kořaly, A. Kerstein, N. Peters, J. Ferziger, H. Pitsch, and the staff at the Center for Turbulence Research for their useful suggestions and discussions as well as the NASA-Ames Research Center for providing the required computing resources. H.S. gratefully acknowledges financial support from the FWF, Austria.

- <sup>1</sup>M. Lesieur and O. Mětais, “New trends in large-eddy simulations of turbulence,” *Annu. Rev. Fluid Mech.* **28**, 45 (1996).
- <sup>2</sup>S. Ghosal and P. Moin, “The basic equations of large eddy simulation of turbulent flows in complex geometry,” *J. Comput. Phys.* **118**, 22 (1995).
- <sup>3</sup>O. V. Vasilyev, T. S. Lund, and P. Moin, “A general class of commutative filters for LES in complex geometries,” *J. Comput. Phys.* **146**, 82 (1998).
- <sup>4</sup>J. Smagorinsky, “General circulation experiments with the primitive equations, I. The basic experiment,” *Mon. Weather Rev.* **91**, 99 (1963).

- <sup>5</sup>M. Germano, U. Piomelli, P. Moin, and W. H. Cabot, “A dynamic subgrid-scale eddy viscosity model,” *Phys. Fluids A* **3**, 1760 (1991).
- <sup>6</sup>P. Moin, K. Squires, W. Cabot, and S. Lee, “A dynamic subgrid-scale model for compressible turbulence and scalar transport,” *Phys. Fluids A* **3**, 2746 (1991).
- <sup>7</sup>P. J. Colucci, F. A. Jaber, P. Givi, and S. B. Pope, “Filtered density function for large eddy simulation of turbulent reacting flows,” *Phys. Fluids* **10**, 499 (1998).
- <sup>8</sup>S. B. Pope, “PDF methods for turbulent reactive flows,” *Prog. Energy Combust. Sci.* **11**, 119 (1985).
- <sup>9</sup>A. W. Cook and J. J. Riley, “A subgrid model for equilibrium chemistry in turbulent flows,” *Phys. Fluids* **6**, 2868 (1994).
- <sup>10</sup>A. W. Cook, J. J. Riley, and G. Kořaly, “A laminar flamelet approach to subgrid-scale chemistry in turbulent flows,” *Combust. Flame* **109**, 332 (1997).
- <sup>11</sup>N. Peters, “Laminar diffusion flamelet models,” *Prog. Energy Combust. Sci.* **10**, 319 (1984).
- <sup>12</sup>H. Pitsch and H. Steiner, “Large-eddy simulation of a piloted methane/air diffusion flame (Sandia flame D),” *Phys. Fluids* **12**, 2541 (2000).
- <sup>13</sup>S. H. Frankel, V. Adumitroaie, C. K. Madnia, and P. Givi, “Large eddy simulation of turbulent reacting flows by assumed pdf methods,” *FED* **162**, 81 (1993).
- <sup>14</sup>R. S. Barlow and J. H. Frank, “Effects of turbulence on species mass fractions in methane/air jet flames,” *Twenty-Seventh Symposium (International) on Combustion*, The Combustion Institute, Paper 4A10, 1998.
- <sup>15</sup>Information available at: [www.ca.sandia.gov/tdf/Workshop.html](http://www.ca.sandia.gov/tdf/Workshop.html)
- <sup>16</sup>W. K. Bushe and H. Steiner, “Conditional moment closure for large eddy simulation of non-premixed turbulent reacting flows,” *Phys. Fluids* **11**, 1896 (1999).
- <sup>17</sup>C. J. Chen and W. Rodi, *Vertical Turbulent Buoyant Jets—A Review of Experimental Data* (Pergamon, New York, 1980).
- <sup>18</sup>A. W. Vreman, B. J. Geurts, and J. G. M. Kuerten, “Subgrid-modelling in LES of compressible flow,” in *Direct and Large-Eddy Simulation I*, edited by P. R. Voke, L. Kleiser, and J.-P. Cholle (Kluwer Academic, Dordrecht, 1994), p. 133.
- <sup>19</sup>G. A. Bird, *Molecular Gas Dynamics and the Direct Simulation of Gas Flows* (Clarendon, Oxford, 1994).
- <sup>20</sup>F. M. White, *Viscous Fluid Flow* (McGraw-Hill, New York, 1991).
- <sup>21</sup>R. W. Bilger, “Conditional moment closure for turbulent reacting flow,” *Phys. Fluids A* **5**, 436 (1993).
- <sup>22</sup>A. Yu. Klimenko, “Multicomponent diffusion of various admixtures in turbulent flow,” *Fluid Dynamics* **25**, 327 (1990).
- <sup>23</sup>R. W. Bilger, “Conditional moment closure modelling and advanced laser measurements,” in *Turbulence and Molecular Processes in Combustion*, edited by T. Tekeno (Elsevier, New York, 1993).
- <sup>24</sup>W. K. Bushe, R. W. Bilger, and G. R. Ruetsch, “Incorporating realistic chemistry into direct numerical simulations of turbulent non-premixed combustion,” *Annual Research Briefs*, Center for Turbulence Research, NASA Ames/Stanford University, 1997, p. 195.
- <sup>25</sup>F. A. Williams, “Overview of asymptotics for methane flames,” in *Reduced Kinetic Mechanism and Asymptotic Approximations for Methane-Air Flames*, edited by M. D. Smooke (Springer, New York, 1991), p. 68.
- <sup>26</sup>N. Peters, “Numerical and asymptotic analysis of systematically reduced reaction schemes for hydrocarbon flames,” in *Numerical Simulation of Combustion Phenomena*, edited by R. Glowinski, B. Larroutour, and R. Temam, *Lecture Notes in Physics*, Vol. 241 (Springer, New York, 1995), p. 90.
- <sup>27</sup>M. D. Smooke and V. Giovangigli, “Formulation of the premixed and nonpremixed test problems,” in *Reduced Kinetic Mechanism and Asymptotic Approximations for Methane-Air Flames*, edited by M. D. Smooke (Springer, New York, 1991), p. 1.
- <sup>28</sup>C. D. Pierce and P. Moin, “A dynamic model for subgrid-scale variance and dissipation rate of a conserved scalar,” *Phys. Fluids* **10**, 3041 (1998).
- <sup>29</sup>W. H. Press, S. A. Teukolsky, W. T. Vetterling, and B. P. Flannery, *Numerical Recipes in Fortran* (Cambridge University Press, Cambridge, 1992).
- <sup>30</sup>B. J. Boersma, G. Brethouwer, and F. T. M. Nieuwstadt, “A numerical investigation on the effect of the inflow conditions on the self-similar region of a round jet,” *Phys. Fluids* **10**, 899 (1998).
- <sup>31</sup>H. N. Najm, P. S. Wyckoff, and O. M. Knio, “A semi-implicit numerical scheme for reacting flow,” *J. Comput. Phys.* **143**, 381 (1998).

- <sup>32</sup>E. S. Oran and J. P. Boris, *Numerical Simulation of Reactive Flow* (Elsevier, New York, 1987).
- <sup>33</sup>A. C. Hindmarsh, "Odepack, a systematized collection of ode solvers," in *Scientific Computing*, edited by R. S. Stepleman *et al.* (North-Holland, Amsterdam, 1983), p. 55.
- <sup>34</sup>I. Danaila and B. J. Boersma, "DNS of forced jet at low Reynolds numbers," *Proceedings of the 1998 Summer Program*, Center for Turbulence Research (NASA Ames/Stanford University Press, Stanford, CA, 1998), p. 141.
- <sup>35</sup>K. Akselvoll and P. Moin, "Large-eddy simulation of turbulent confined coannular jets," *J. Fluid Mech.* **315**, 387 (1996).
- <sup>36</sup>P. M. Gresho, "Incompressible fluid dynamics: Some fundamental formulations issues," *Annu. Rev. Fluid Mech.* **23**, 413 (1991).

P 5

W. K. BUSHE & H. STEINER

Laminar flamelet decomposition for conditional  
source-term estimation

*Phys. Fluids* **15** (2003), 1564–1575

# Laminar flamelet decomposition for conditional source-term estimation

W. Kendal Bushe<sup>a)</sup>

Department of Mechanical Engineering, University of British Columbia, Vancouver, British Columbia V6T-1Z4, Canada

Helfried Steiner

Department for Fluid Mechanics and Heat Transfer, Technical University Graz, Inffeldgasse 25, A-8010 Graz, Austria

(Received 4 September 2002; accepted 28 February 2003; published 5 May 2003)

A new decomposition approach to conditional source-term estimation (CSE) is proposed and discussed. The new approach is tested in the *a priori* sense using direct numerical simulations (DNS). It is found that—where CSE had previously been found to provide closure for chemical source-terms with arbitrary chemistry in the large eddy simulation paradigm—it can provide this closure in the Reynolds averaged Navier–Stokes paradigm as well. Using the proposed decomposition improves the predictions of CSE considerably. Only the assumptions that gradients in conditional averages are small and that the probability density function of mixture fraction can be adequately approximated using a presumed functional form are needed. The computational cost of the new laminar flamelet decomposition approach to CSE is also substantially lower than that of the original approach. © 2003 American Institute of Physics. [DOI: 10.1063/1.1569483]

## I. INTRODUCTION

Recently, a new approach for obtaining closure for chemical source terms in large eddy simulations (LES) of nonpremixed turbulent reacting flows was proposed<sup>1</sup> which takes advantage of the now well-established chemical source-term closure used in conditional moment closure (CMC) methods.<sup>2–5</sup> In conditional source-term estimation (CSE)—as the method has come to be known—conditional filtered means are assumed to be homogeneous for some user-prescribed ensemble of computational grid-cells. By assuming a form for the filtered density function of the mixture fraction (such as the  $\beta$ -function<sup>6</sup>), it becomes possible to invert integral equations for the conditional averages of species mass fractions and temperature and density. These can then be substituted into the reaction rate expressions to obtain approximations for conditional reaction rates, which are then mapped back onto the LES computational grid, such that the filtered chemical source-terms are obtained in closed form.

CSE was originally proposed as a closure for LES; here, traditional CMC methods have the problem that they require the addition of the conditioning variable (mixture fraction in the nonpremixed flame context) as an independent variable—effectively requiring a solution in four “dimensions” for a three-dimensional flow field. In order to capture the effect of vortex-stretching on the cascade of energy from large scales to smaller scales, a LES calculation must solve the flow-field in three dimensions; to use CMC in LES, one would have to solve in four dimensions. Another drawback to CMC is that many terms in the CMC transport equations are unclosed. The CSE approach circumvents both of these

problems, which allows us to use the CMC closure for the chemical source-term without requiring closure for other terms and without requiring an additional dimension in the simulation.

The method has been compared (in the *a priori* sense) to DNS results obtained using one-step chemistry<sup>7</sup> and found to give good predictions of filtered reaction rates.<sup>1</sup> The method has subsequently been modified somewhat and included into a LES code; the code has been used to simulate the “Sandia D-flame.”<sup>8,9</sup> That work has demonstrated three important features: (1) The method is a practical solution to the chemical closure problem for LES; (2) the method provides closure for the chemical source-terms at an acceptably low computational cost; and (3) the method can be used for predictive calculations of nonpremixed turbulent reacting flows.<sup>10</sup>

While the CSE method as described in the above-noted works is successful in providing a closed-form solution in turbulent nonpremixed flows, there have been several shortcomings that have been identified. First, CSE requires solution of transport equations for many scalars—however, many scalars participate in the chemical reactions for a given problem. Second, the inversion of the integral equations have been found, under many circumstances, to lead to poor approximations for the conditional averages of species mass fractions and temperature—approximations that resemble solutions to the spatially degenerate CMC equation where the conditional scalar dissipation rate is excessively high (as if the diffusivity were too large). Finally, our previous work with the method has been applied only to LES; in principal, the closure should also work in the Reynolds averaged Navier–Stokes (RANS) context, however, this has yet to be proven.

In this paper, a new modification to the CSE method is proposed in which unsteady laminar flamelet solutions are

<sup>a)</sup> Author to whom correspondence should be addressed. Telephone: 604-822-3398; fax: 604-822-2403; electronic mail: wkb@mech.ubc.ca

used to provide basis functions to approximate the conditional averages. The method is tested against DNS which uses realistic chemistry for methane oxidation.<sup>11</sup> For this *a priori* test, rather than using spatially filtered means, the method will be applied to ensemble averaged means which will demonstrate the applicability of the method to RANS problems.

## II. BACKGROUND

CSE is a means for circumventing the chemical closure problem. In LES and RANS, transport equations are being solved for the averages (either spatial averages in the case of LES or time/ensemble averages in RANS) of fluid properties such as density, temperature, and composition (usually in the form of mass fractions of chemical species). The chemical source-terms which appear in these transport equations are linear combinations of chemical reaction rates which are themselves highly nonlinear functions of the instantaneous local density, temperature, and composition. Evaluating the reaction rate expressions with the average density, temperature, and mass fractions (first moment closure) generally results in very poor predictions of the mean reaction rates. That is, if the reaction rate expression  $\dot{\omega}(\rho, T, Y_K)$  is evaluated using mean density, temperature and mass fractions, the approximation

$$\overline{\dot{\omega}(\rho, T, Y_K)} \approx \dot{\omega}(\bar{\rho}, \bar{T}, \bar{Y}_K) \quad (1)$$

(where  $\bar{\Theta} \equiv \overline{\rho\Theta}/\bar{\rho}$  denotes the Favre average of the random scalar field  $\Theta$ ), is generally not acceptable.

The underlying philosophy of CSE is to approximate conditional averages of density, temperature, and mass fractions by inverting integral equations for these properties and to use these approximations to close the chemical source-term in conditioning space. Several recent findings have driven the development of this method. It has been found that the chemical closure hypothesis used in CMC provides a good prediction of conditional averages of reaction rates given good estimates of conditional averages of density, temperature and mass fractions,<sup>11</sup> with the mixture fraction being the conditioning variable. Also it has been found that conditional averages of temperature and mass fractions tend to be weak functions in space.<sup>11</sup> Finally, it has been found that the probability density function (PDF)—or, in LES, the filtered density function (FDF)—of mixture fraction in a nonpremixed system can be well approximated using a  $\beta$ -function evaluated such that the first two moments of the mixture fraction are matched.<sup>6</sup>

In RANS (and in LES) transport equations are to be solved for the average temperature  $\bar{T}$ , mass fractions  $\bar{Y}_K$  of chemical species and, in some cases, also the average density  $\bar{\rho}$ . In RANS, the average can either be a time-average or an ensemble average; in LES the average is a spatial filtering operation. In CSE,<sup>1</sup> the integral

$$\bar{T}(x_k, t) = \int_0^1 \overline{T(x_k, t) | \zeta} \bar{P}(\zeta; \bar{Z}(x_k, t), \widetilde{Z}''^2(x_k, t)) d\zeta, \quad (2)$$

is written [where  $\bar{P}(\zeta)$  is the Favre FDF or PDF of mixture fraction, depending on how the conditional average is defined] for the temperature with similar integrals written for density and mass fractions. The Favre average temperature is known at many discrete points in space. The Favre average of the mixture fraction can often be obtained as a linear combination of mass fractions, although the transport equation for the mean mixture fraction is often solved separately. In RANS, an additional transport equation for the Favre variance of the mixture fraction is frequently solved to close terms representing turbulent mixing in the RANS equation for the average mixture fraction. If the  $\beta$ -function is assumed for the form of the Favre PDF of the mixture fraction, such that the Favre average and variance of mixture fraction are matched, then only the conditional average of the temperature in Eq. (2) is unknown. For a user-supplied ensemble of discrete realizations of this integral over which the conditional average can be assumed to be constant, such that, for that ensemble

$$\overline{T(x_k, t) | \zeta} = T | \zeta, \quad (3)$$

it is possible to invert this integral using a technique such as linear regularization<sup>12</sup> and obtain a mean conditional average of temperature for the ensemble. Substituting this approximation for the conditional average of the temperature, and similarly obtained approximations for the conditional averages of density and species mass fractions, into the reaction rate expressions provides an approximation to the conditional average of the reaction rates

$$\overline{\dot{\omega}(\rho, T, Y_K) | \zeta} \approx \dot{\omega}(\rho | \zeta, T | \zeta, Y_K | \zeta). \quad (4)$$

Closure for the unconditional average of the reaction rates can now be obtained by integrating

$$\bar{\omega}(x_k, t) = \bar{\rho} \int_0^1 \frac{\overline{\dot{\omega} | \zeta} \bar{P}(\zeta; \bar{Z}(x_k, t), \widetilde{Z}''^2(x_k, t))}{\bar{\rho} | \zeta} d\zeta, \quad (5)$$

at each point in the ensemble of computational grid-points.

This method was found to provide good predictions of reaction rates when compared to DNS, but it was found to be necessary to include a second conditioning variable (scalar dissipation of mixture fraction) to obtain predictions of local extinction phenomena.<sup>1</sup> The need to include a second conditioning variable was found to be a result of the effect of large variations in scalar dissipation on the conditional averages, leading to significant conditional variances in mass fractions and temperature. These variations are somewhat correlated with the instantaneous scalar dissipation. Thus, adding scalar dissipation as a second conditioning variable has been found to reduce the variations significantly.

Instantaneous local scalar dissipation is by no means the ideal second conditioning variable. Local extinction may be caused by high local scalar dissipation, but extinction events have been found to lag in time behind peaks in scalar dissipation.<sup>11</sup> Re-ignition of local extinction events does not necessarily coincide with the abatement of local scalar dissipation; these events also show a significant time-lag.<sup>11</sup> Thus, the ideal second conditioning variable would have to include some kind of time-integral of the local, instantaneous scalar

dissipation. Unfortunately, the local, instantaneous scalar dissipation is not actually being resolved in either a RANS or LES simulation. How one might obtain a time-history of a scalar field that is not being resolved is unclear. Ultimately, the inclusion of a second conditioning variable has been found to involve a prohibitively high computational cost, thus the issue of selecting an appropriate variable seems to be irrelevant.

Another shortcoming that has been identified in the CSE approach is in how the integrals are inverted. The regularization approach used in the previous *a priori* tests worked well for the single-step chemistry in the DNS database against which CSE was compared, however, it has been found that the smoothing matrix necessary to obtain an acceptable solution to the inverse problem causes the conditional average to take on an overly diffusive character—as if it were the result of a CMC calculation where the scalar dissipation is too large. In one-step chemistry, this behavior has a negligible effect on the closure of the source-terms, however for more complex chemistry the effect leads to unacceptable errors in the reaction rate predictions.

One way to circumvent this problem is to invert integral equations for reaction progress variables rather than for individual species mass fractions, temperature and density directly.<sup>10</sup> Progress variables generally do not exhibit the sharp gradients in mixture fraction space that individual species mass fractions do. The smoothness of the progress variables as functions of mixture fraction mitigates the effect of the smoothing matrix considerably. Unfortunately, this approach has the drawback that it may be necessary to neglect differential diffusion to obtain useful expressions for the progress variables.

### III. FORMULATION

An alternative means of circumventing the effect of the smoothing matrix is to use a decomposition approach. In a decomposition approach, the conditional average would be approximated by forming a linear combination of basis functions. These basis functions could be chosen such that they might have the sharp gradients that one expects to find in conditional averages of species mass fractions. Rather than estimating the conditional average at each discrete point in mixture fraction directly, one would solve for the coefficient vector to be multiplied by the basis function matrix.

For example, the conditional average of the temperature would be estimated using

$$\overline{T|Z=\zeta} = \sum_{i=1}^n a_i \Theta_i(\zeta), \quad (6)$$

where  $\Theta_i(\zeta)$  would be the *i*th basis function and  $a_i$  would be the coefficient by which that basis function would be weighted. Now the integral equation becomes

$$\tilde{T} = \int_0^1 \sum_{i=1}^n a_i \Theta_i(\zeta) \tilde{P}(\zeta; \tilde{Z}, \tilde{Z}''^2) d\zeta, \quad (7)$$

and we would invert this equation for the coefficient vector  $a_i$ .

One obvious choice for basis functions is a library of steady laminar flamelet solutions.<sup>13</sup> Unfortunately, a steady laminar flamelet solution cannot hope to capture the physics underlying a local extinction or ignition event. An alternative would be to use a library of solutions to the *unsteady* laminar flamelet equation<sup>14</sup> (or solutions to the spatially degenerate CMC equation<sup>15</sup>). This choice has several appealing features. As solutions to the unsteady laminar flamelet equation, these functions would represent physically realizable conditions for the flame. These solutions would likely exhibit many of the same features (i.e., sharp gradients in species mass fractions) to be expected in the conditional average of a mass fraction in a turbulent flame. By choosing unsteady solutions, it is possible to include solutions that arise from ignition and extinction phenomena—although other features, such as the edge-flame phenomenon,<sup>16</sup> would not be represented in such a library. Including flamelet solutions which include ignition and extinction might eliminate the need for a second conditioning variable.

This last point is perhaps the most attractive feature of the decomposition approach. In a sense, the coefficient vector  $a_i$  plays the role of the probability density function of scalar dissipation. Now, rather than having to calculate the double-conditional average and assume some form for the PDF of scalar dissipation, one can use a pre-computed library and calculate the coefficient vector from the given flow field. This should require a very small computation compared to that required to invert the two-condition CSE equation.

The relationship between the decomposition approach and double-condition CSE is worth exploring. We note that

$$\overline{T|Z=\zeta} = \int_0^\infty \overline{T|Z=\zeta, c=\chi} P(c) dc. \quad (8)$$

Comparing Eqs. (6) and (8), we can see that, if the integration in Eq. (8) is evaluated using a simple trapezoidal rule and it can be assumed that  $\Theta_i(\zeta) = \overline{T|Z=\zeta; c=\chi}_i$ , then the coefficient vector becomes  $a_i = P(\chi_i) d\chi_i$ .

Further savings in computational time may also be afforded by recognizing that, if the coefficient vector  $a_i$  is taken to be  $P(\chi) d\chi$ , then the conditional average of the chemical source terms can be expressed as linear combinations of those from the flamelet library

$$\overline{\omega_j|Z=\zeta} = \sum_{i=1}^n a_i \omega_{ij}(\zeta). \quad (9)$$

This would avoid having to compute each chemical reaction rate at each time step.

Practically, it can be expected that a different coefficient vector for  $a_i$  will result from inverting the integral for each different scalar in the system. This is because it would be impossible to include a flamelet solution for every single realizable condition in the system; it would be even more difficult to conceive of including a flamelet for every possible realization in a system where the flame is not in the flamelet regime. Nevertheless, one possible means of taking advantage of the available computational savings is to invert a much larger system of integrals (including several scalars)

for the same coefficient vector. Here, there would likely be a trade-off between the computation saved by not having to compute many exponential functions in the chemical reaction rates and the additional computation required to invert a much larger system of equations. An alternative would be to choose only one scalar—such as the temperature—and invert the integral for the coefficient vector using only that one scalar.

Here again, an enormous computational savings can be realized: if we are only using the temperature to obtain the coefficient vector  $a_i$ , then it would be unnecessary to solve individual transport equations for species mass fractions. The conditional averages of these would now be given by

$$\overline{Y_j|Z=\zeta} = \sum_{i=1}^n a_i Y_{ij}(\zeta), \quad (10)$$

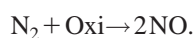
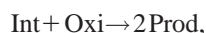
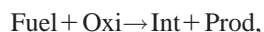
and the *unconditional* averages (for which we previously would have had to solve transport equations) would given by

$$\bar{Y}_j = \int_0^1 \sum_{i=1}^n a_i Y_{ij}(\zeta) \bar{P}(\zeta; \bar{Z}, \widetilde{Z''^2}) d\zeta. \quad (11)$$

As was mentioned above, there are many different conceivable strategies for performing the flamelet decomposition described herein. We will examine several different possibilities in the next section.

#### IV. RESULTS

In order to test the ideas discussed above, we have performed a number of *a priori* tests using a relatively new DNS database.<sup>11</sup> The database consists of several independent simulations of a decaying, shear-free, temporal mixing layer. The code which was used to create the database uses a sixth order Padé differentiation scheme in space<sup>17</sup> and a third order Runge–Kutta algorithm for time integration.<sup>16</sup> The domain used was periodic in two directions and in–out-flow was allowed in the third direction at either end of the domain using the Navier–Stokes characteristic boundary conditions of Poinso and Lele.<sup>18</sup> The flow field was initialized with a turbulent field obtained from a forced, statistically stationary incompressible simulation using a pseudo-spectral code<sup>19</sup> and the initial scalar fields were initialized with a planar, laminar flame. A two-step reduced chemical kinetic mechanism representative of methane–oxygen combustion was used<sup>20,21</sup> with a third step added to be representative of nitric oxide formation; hence the kinetic mechanism is



The mechanism used in creating the DNS database is unable to predict ignition—the reaction rates depend strongly on the concentration of a radical species which would be zero initially in an ignition problem, leading to reaction rates that are identically zero. However, the DNS database did include several significant local extinction events. One consequence of extinction is that a single, unsteady flamelet or a

spatially degenerate CMC calculation<sup>15</sup> fails to predict accurately the average species mass fractions and temperatures as functions of time in an *a priori* test<sup>22</sup>—that is, where the CMC calculation started from the same initial conditions as were used in the DNS and the scalar dissipation (needed to close the diffusion term in the equation) was extracted directly from the DNS. Specifically, it was found that the formation rates of intermediate species and NO are underpredicted significantly whenever extinction is occurring. One global conditional average of temperature inevitably fails to represent the much lower temperature in regions where extinction has occurred. It should be stressed that, while the global average of scalar dissipation decays in the database with time, it was found that extinction events occurred only locally where the instantaneous scalar dissipation exceeded that necessary for extinction.<sup>11</sup> Because of the presence of extinction in the DNS database, it represents an opportunity to test models purporting to predict local extinction.

A library was prepared, consisting of solutions to the unsteady flamelet equation,<sup>14</sup> starting with the same initial condition as was used to initialize the DNS, and steadily increasing the scalar dissipation rate linearly with time until extinction occurred and the mass fractions returned to a completely unreacted, mixing-only state. The library consists of 45 flamelets, with approximately half of them taken from between the time of onset of extinction to the point where the solution had relaxed to that of pure mixing. The flamelets were essentially chosen arbitrarily with the intent that the library should contain realizations of as broad a scope as possible. Other than that the flamelets are placed in a chronological order in the library, there is no other significance attached to the actual time or scalar dissipation; as such, we refer to them only with “Flamelet #.” The temperature and rates of the three different reactions are shown in Fig. 1.

The CSE method provides closure for the chemical reaction rates, which comprise the chemical source-terms in the averaged transport equations. The inputs to the method are the mean mass fractions, temperature, and density and the mean and variance of mixture fraction. It is common practice to use Favre averaging in numerical simulation of reacting flows, so, for the *a priori* tests, we elected to use Favre averages and variances for each of these quantities. The DNS data were averaged at each stage across the mixing layer which provided the Favre averages and variance at 241 points for each time at which data were available. The Favre PDF of mixture fraction was estimated using a  $\beta$ -PDF at each of these 241 points. The output from CSE is the mean reaction rate, although at interim stages, the conditional averages of the reaction rates are estimated; thus, we are able to compare both conditional and unconditional averages of the reaction rates.

We have tested three different approaches to CSE: First, CSE using the original formulation (we will refer to this as CSE0); second, CSE with flamelet decomposition where conditional averages are calculated for all scalars and reaction rates are calculated with first conditional moment closure (we will refer to this as CSEFD1); and third, CSE with flamelet decomposition where the coefficient vector is obtained from the inverting the integral for temperature only

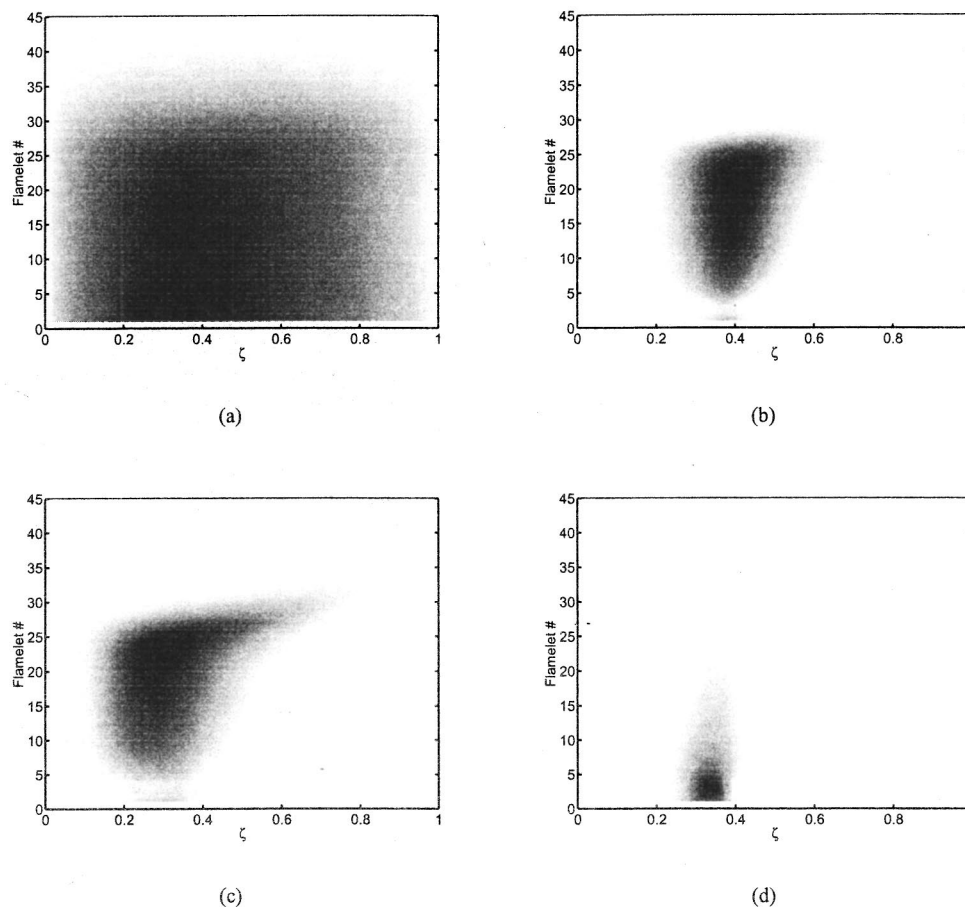


FIG. 1. Surface plots of flamelet library; flamelets are shown in order of increasing scalar dissipation with dark regions corresponding to the maximum and light regions corresponding to the minimum. (a) Temperature: 300–2000 K; (b)  $\omega_I$ :  $0-5 \times 10^5 \text{ s}^{-1}$ ; (c)  $\omega_{II}$ :  $0-3 \times 10^5 \text{ s}^{-1}$ ; (d)  $\omega_{III}$ :  $0-2 \times 10^12 \text{ s}^{-1}$ .

and reaction rates are obtained from the flamelet library directly (we will refer to this as CSEFD2). The first method provides a baseline, the second provides what we anticipate should be a significant improvement to the prediction of the conditional averages of the scalars and the third provides the least computationally intensive approach.

Figure 2 shows a comparison of the actual conditional average of the scalar mass fractions and the temperature with that calculated using CSE0 and CSEFD1. The new flamelet decomposition method improves the prediction of the conditional averages of all of the scalars. The greatest improvement is for the intermediate species. Here, because the regularization method in the original CSE method is attempting to find a smooth function that best fits the data, it is very difficult to obtain a solution to match the two abrupt changes in the slope of the curve. Flamelet decomposition does not suffer from this problem.

Figure 3 shows a comparison of the actual conditional average of the three different chemical reaction rate with those calculated using CSE0, CSEFD1, and CSEFD2. The original CSE method fails to capture both the trend and the magnitude of the reaction rate; there are ways of improving this comparison, including making use of *a priori* information to tune the regularization matrix and inverting equations for reaction progress variables rather than for individual species mass fractions. At best, however, one would be tuning

the regularization matrix to obtain a solution like that obtained (without any tuning) with the new CSEFD1 model. We can see that, even using the improved approximations to the conditional averages of the mass fractions given by CSEFD1, first conditional moment closure for the conditional averages of the chemical reaction rates is still found lacking.

Clearly, of the tested models, CSEFD2 provides the best approximation to the conditional averages of chemical reaction rates. For reaction I, CSEFD2 provides a nearly perfect representation of the rate on the lean side of the peak, and is slightly better than CSEFD1 for the rich side (although both methods slightly under-predict the rate here). For reactions II and III, the prediction with CSEFD2 is better than with any other method tested. CSEFD1 under-predicts both reaction rates quite significantly; there are two reasons for this: (1) These two rates are quite sensitive to the intermediate mass fraction, and (2) first conditional moment closure, particularly for reaction III, has been found (in previous work<sup>11</sup>) to under-predict these rates in the presence of local extinction phenomena. The significant improvement in the prediction of reaction rate III given by CSEFD2 is evidence of the ability of this method to account for the effects of local extinction.

Figure 4 compares the three different methods to DNS in real space. The chemical source terms in Reynolds averaged transport equations for species mass fraction and temperature

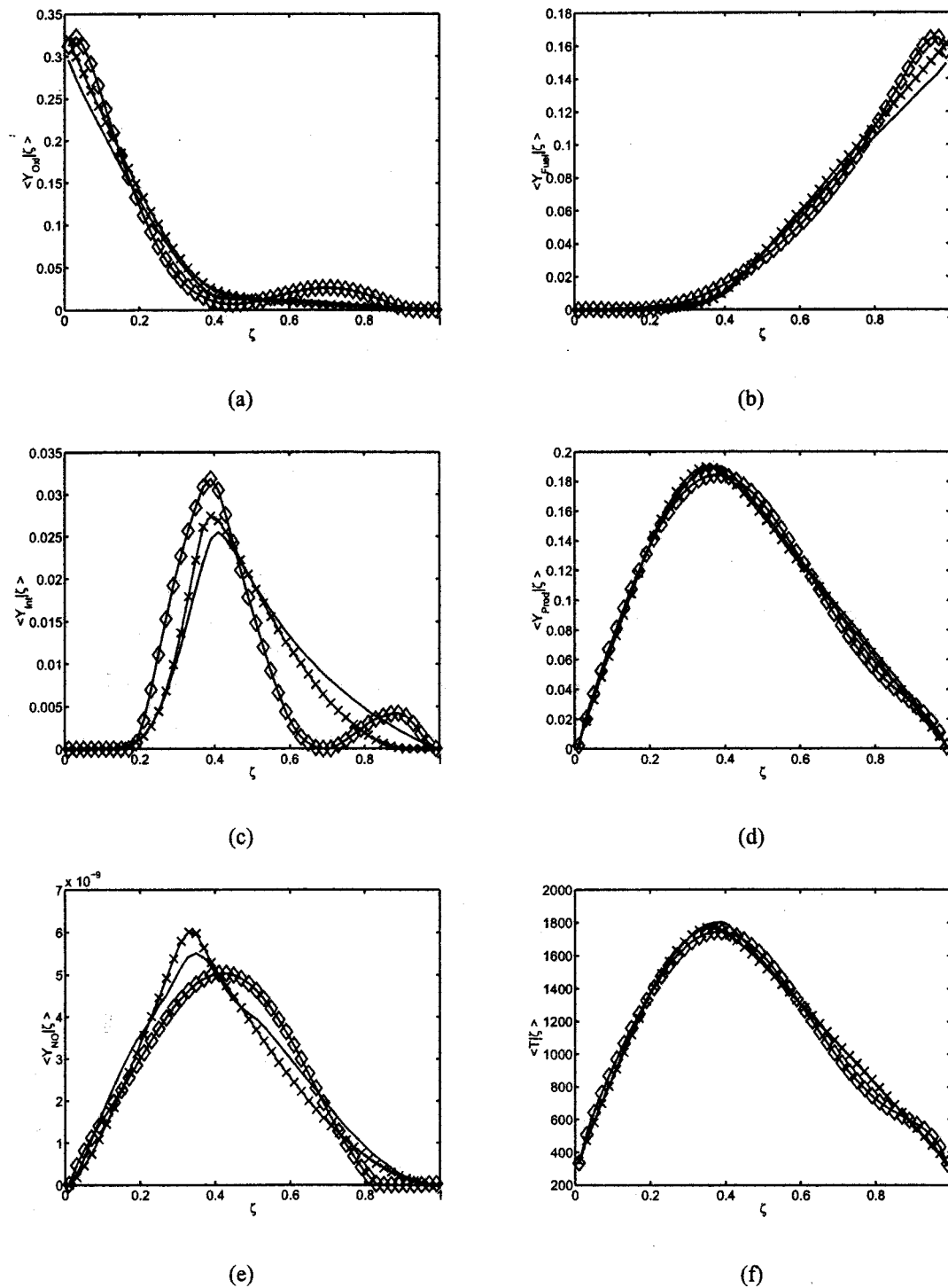


FIG. 2. Comparison between conditional averages of the mass fractions and temperature calculated with the original CSE model (CSE0:  $\diamond$ ) and the new CSE model with flamelet decomposition (CSEFD1:  $\times$ ) to actual conditional averages from DNS (solid lines).

(or energy) would be linear combinations of the mean chemical source terms shown here. As such, this is a final test of the method's ability to provide closure for the mean chemical source-terms in these transport equations.

As one would expect, the poor predictions of the conditional averages given by CSE0 and CSEFD1 translate into poor predictions of the unconditional averages. While the prediction given by CSEFD2 is also somewhat lacking, it is clearly the best of the models tested. If one integrates the

reaction rate across the mixing layer to get a global reaction rate, CSEFD2 predicts this global mean within 20% for all three reaction rates at all the times for which the model was tested. There appears to be no bias in this error. CSE0 and CSEFD1 were in error on this global mean by over 40%; for reaction rate III, this was always an under-prediction.

To better understand the nature of the errors in the CSEFD2 model, we have performed an additional two tests designed to establish the effects of assuming the form of the

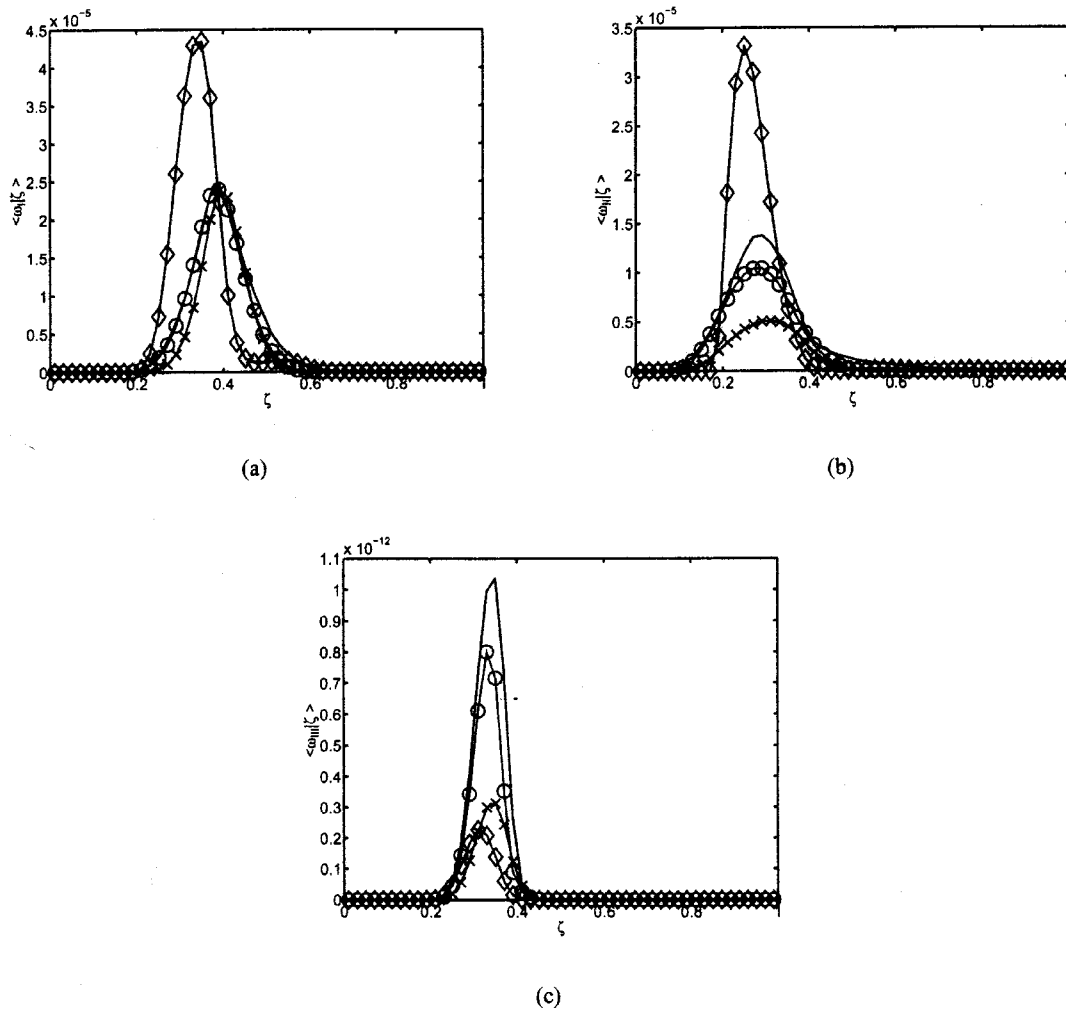


FIG. 3. Conditional averages of chemical reaction rates calculated with the original CSE model (CSE0:  $\diamond$ ) and the new CSE model with flamelet decomposition (CSEFD1:  $\times$ ; CSEFD2: lines with  $\circ$ ) compared to actual conditional averages from DNS (solid lines).

PDF of mixture fraction and assuming the conditional averages are homogeneous across the mixing layer. First, we take the actual, global conditional average from the DNS and convolve it with the presumed form of the PDF. This results in a prediction of the mean reaction rate which is essentially the best prediction possible given the two underlying assumptions made in CSE. As is seen in Fig. 5, there is a significant discrepancy between this “best possible prediction” and the actual reaction rate. Furthermore, the discrepancy is very similar to that seen with CSEFD2; indeed, judging solely from the appearance of this comparison, it would be hard to say which of the two estimates of the reaction rates would best represent the actual average reaction rates.

The second test is also quite illuminating. Here, we use the actual Favre PDF from the DNS data: It is used as an input to the CSEFD2 algorithm in place of the presumed form and it is convolved with the actual, global conditional average from the DNS. The results of this test are shown in Fig. 6. Here, both predictions of the average reaction rate are improved considerably, however, there is still a significant discrepancy. We conclude that *both* the assumption of homogeneity in the conditional averages across the layer and the

presumed form for the PDF contribute to the inaccuracy of the model for prediction of the reaction rates.

## V. DISCUSSION

We find that the new method for obtaining the conditional averages of scalars (CSEFD1) represents a significant improvement over the original CSE model, however the best predictions of the reaction rates were given by CSEFD2. The important distinction between the methods is that CSEFD2 is likely to be by far the least expensive computationally. The new method requires storing only the conditional averages of the chemical reaction rates and the temperature from an unsteady flamelet calculation made prior to performing the calculation of the flow field. Rather than having to invert several integral equations, we need only to invert one (for temperature). Subsequently, the conditional reaction rates are estimated with two matrix multiply operations. As such, we expect the new version of the model to be considerably less computationally intensive than the original version, which has already been proven to have an acceptably low computational cost.

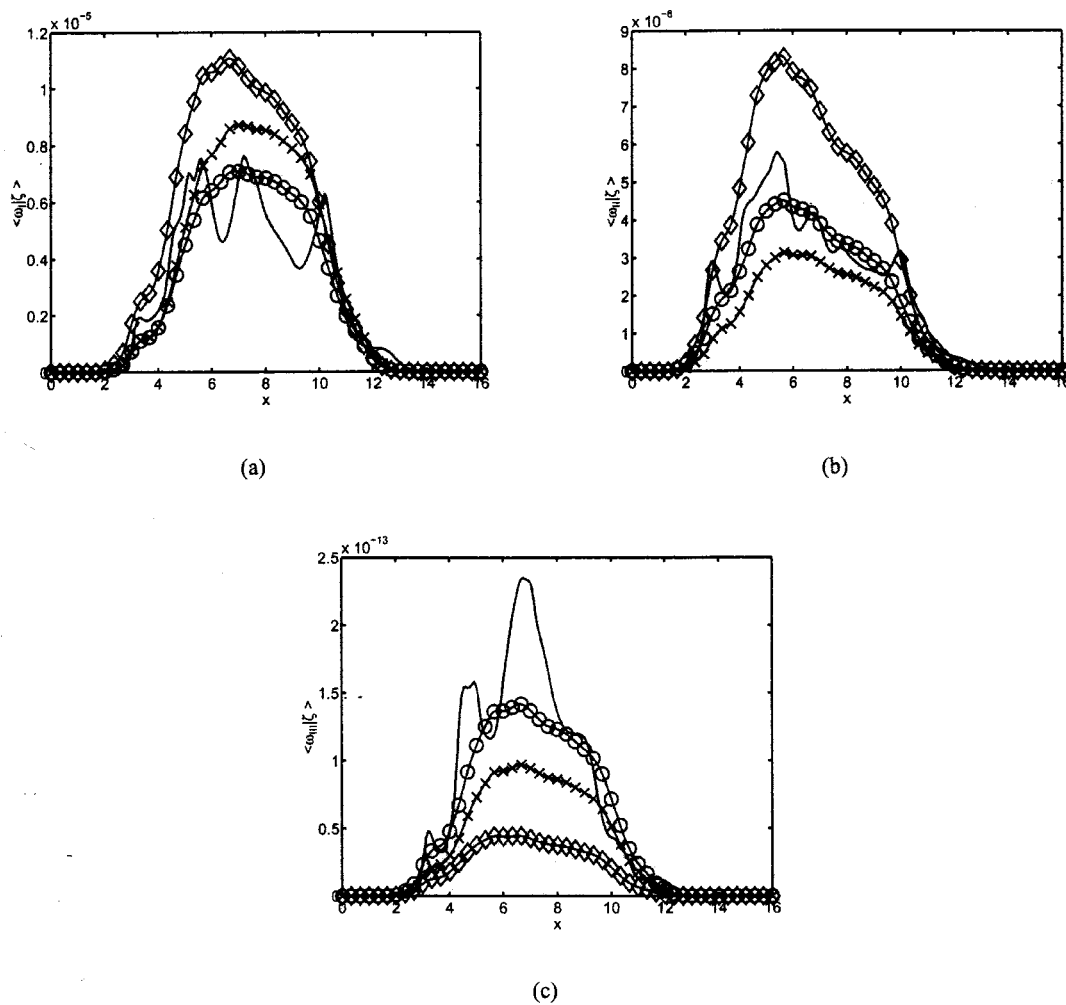


FIG. 4. Reynolds averages of chemical reaction rates calculated with the original CSE model (CSE0:  $\diamond$ ) and the new CSE model with flamelet decomposition (CSEFD1:  $\times$ ; CSEFD2:  $\circ$ ) compared to actual Reynolds averages from DNS (solid lines).

The new version of the model retains all of the advantages of the previous version and adds two significant new abilities: (1) We should now be able to use the model for simulations of flames with ignition, extinction and reignition phenomena; and (2) in addition to being able to use arbitrarily complex chemistry, we can now take advantage of the latest advances in flamelet modelling, such as the ability to account for differential diffusion.<sup>14</sup> It should be noted that, like the original CSE model, the present new version also requires the assumption of statistical homogeneity for the conditional averages when solving the integral equation [Eq. (7)]. One of the important accomplishments of the *a priori* test shown here is that we have now shown CSE to provide acceptable predictions of chemical rates not just for simple chemistry but also for more complex chemistry. Hence, our confidence in the previous comparison to the Sandia experiments is much greater.

Clearly, the laminar flamelet decomposition (LFD) approach for CSE proposed here borrows many useful concepts from the more classical flamelet models, however, there are significant differences worth noting. First, the new method has not required making any assumption about the relation of the characteristic length or time scales of chemistry to those

of the turbulent flow field. Rather, we are using the CMC closure for the chemical source-term—a closure which is in no way confined to the flamelet regime. Second, unlike in a classical flamelet closure, we are not assuming the form of the PDF of the scalar dissipation; rather, we are (in a sense) calculating this PDF from the simulation results at each time step. Finally, unlike in a classical flamelet model, we do not tabulate flamelets and subsequently look them up in the library based on the local scalar dissipation in the flow-field calculation: We simply tabulate them in order of increasing scalar dissipation and attempt to find the linear combination of flamelets which leads to the best approximation of the conditional average of the temperature extracted from the flow-field calculation.

There is an indication presented here that the new method can provide an avenue to account for extinction processes, however, it should be pointed out that an unsteady flamelet model cannot be expected to predict some important phenomena associated with extinction and ignition—specifically, in order to predict the propagation of triple-flames with a flamelet method, it is necessary to use a much more complicated flamelet model. One alternative might be to use a two-condition CMC method<sup>23,24</sup> and tabulate solu-

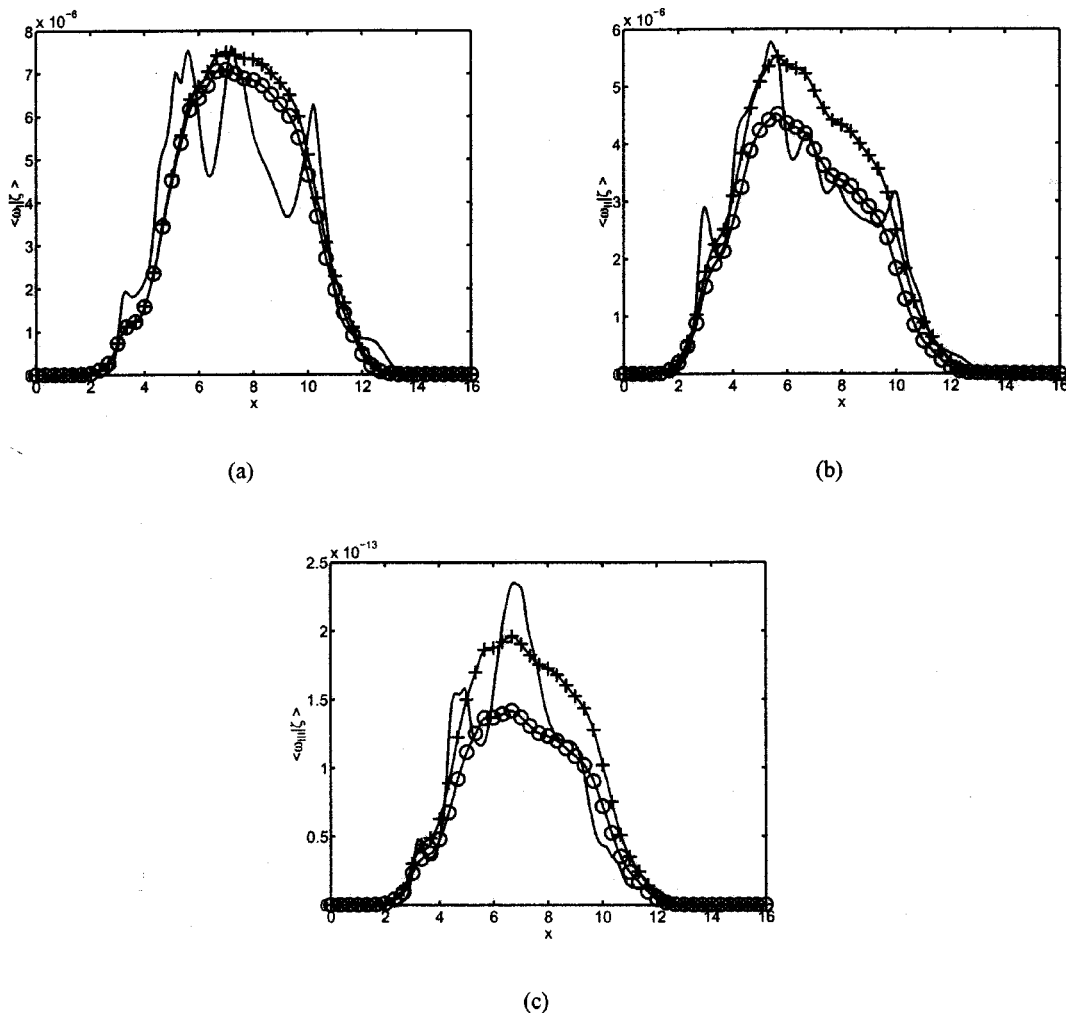


FIG. 5. Reynolds averages of chemical reaction rates calculated with the new CSE model with flamelet decomposition (CSEFD2:  $\circ$ ) and with the actual conditional average of reaction rate from DNS convolved with local presumed PDF ( $+$ ) compared to actual Reynolds averages from DNS (solid lines).

tions using that model for use as a library of basis functions in place of the unsteady flamelet solutions used here. The flamelet library used in this work would be broadly applicable to many flows, however, the LFD/CSE combination presented herein will still be unable to cope with wall-quenching, a process which would make the assumption of spatial homogeneity in the conditional averages break down. Here, a CMC simulation for a simple flow past a flat plate (where the spatial dimension normal to the plate could be retained) might provide a set of basis functions that could represent this quenching process. These possibilities will have to be examined in future work.

While the LFD method is a solution born out of numerical constraints, we have argued that it has a physical interpretation: The coefficient vector  $a_i$  performs the role of the PDF of  $\chi$ , being equivalent to the quantity  $P(\chi)d\chi$ . There is a limitation to this physical interpretation, in that, if  $a_i$  actually is  $P(\chi_i)d\chi_i$ , then we must get  $a_i \geq 0$ . Using a simple regularization procedure (as we have done here) does not guarantee this. In Fig. 7, we plot  $a_i$  for the same case as was discussed in the previous section and find that  $a_i$  is negative for several of the flamelets (numbers 25–34). What effect having negative elements in the coefficient vector may have

in actual applications of CSEFD2 to RANS or LES is unclear. There is no physical meaning that could be attached to negative elements in the coefficient vector. When we use a coefficient vector with negative elements in the CSEFD2 model, we are essentially subtracting, rather than adding, the forward reaction rate for some of the flamelets in the library. This is not the same as adding the *reverse* reaction rate: Ordinarily, reverse reaction rates have very different rate expressions from the positive rates.

One means of enforcing non-negativity in the coefficient vector is to simply truncate the vector at 0 and rescale it. The rescaling operation is straightforward: Having truncated the vector at 0, we can use a least-squares approach to obtain the optimum scaling factor which minimizes the error in the prediction of temperature. That is, first we set

$$a_i = \max(0, a_i),$$

and then we rescale that vector to

$$a^* = a_i \times \frac{\sum_j \tilde{T}_j \int_0^1 \sum_{i=1}^n a_{t,i} \Theta_i(\zeta) \tilde{P}_j(\zeta; \tilde{Z}, \tilde{Z}''^2) d\zeta}{\sum_j (\int_0^1 \sum_{i=1}^n a_{t,i} \Theta_i(\zeta) \tilde{P}_j(\zeta; \tilde{Z}, \tilde{Z}''^2) d\zeta)^2} \quad (12)$$

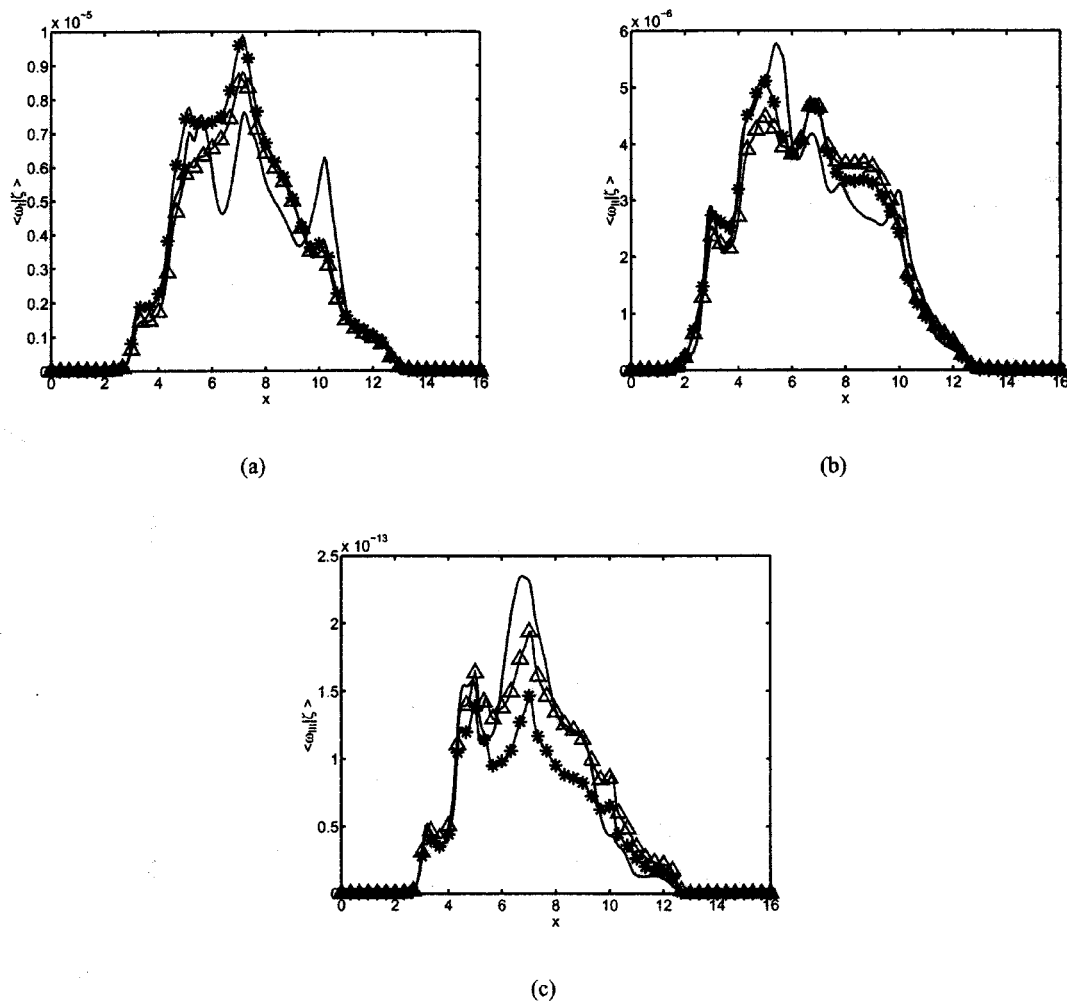


FIG. 6. Reynolds averages of chemical reaction rates calculated with the new CSE model with flamelet decomposition using PDF from DNS (CSEFD2: \*) and actual conditional average of reaction rate from DNS convolved with PDF from DNS ( $\Delta$ ) compared to actual Reynolds averages from DNS (solid lines).

This is the second curve in Fig. 7; the effect of rescaling is to reduce slightly the magnitude of the nonzero elements of the truncated vector. We find that this truncation and rescaling operation has very little effect on the CSEFD2 model's pre-

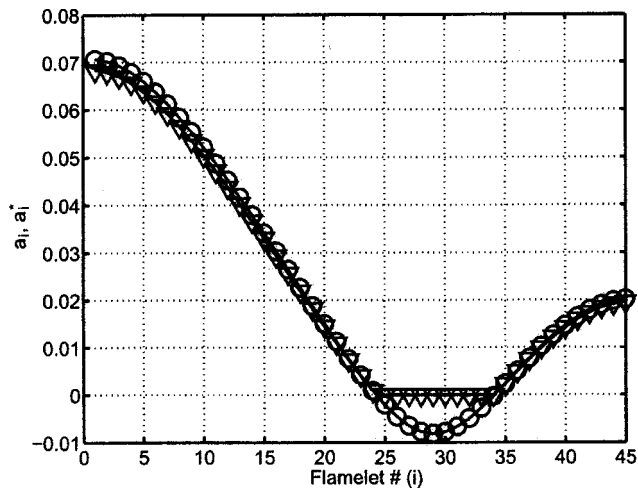


FIG. 7. Coefficient vector calculated from inversion of integral equation for temperature: Original vector  $a_i$  ( $\circ$ ) and vector after truncation and rescaling  $a_i^*$  ( $\nabla$ ).

diction of reaction rates. This is shown in Fig. 8 where the averages of the reaction rate predictions obtained with  $a_i$  and  $a_i^*$  are compared—and can be seen to be nearly indistinguishable from one another. It is possible to use an iterative procedure to ensure  $a \geq 0$  in the inversion process, however we have found that this does not change the ultimate result of the test significantly. Instead, the primary effect of enforcing this constraint is to increase the computational cost of the method considerably—to a level that might be unacceptably high for large-scale CFD applications. We suggest that it would be prudent to maintain a physical consistency in the model—despite the fact that the effect appears to be minimal.

### VI. CONCLUSIONS

We have proposed a new decomposition approach to conditional source-term estimation and compared the new approach to DNS in the *a priori* sense. We have found the following features.

- (i) Conditional source-term estimation can provide closure for chemical source-terms with arbitrary chemistry in *both* the LES and RANS paradigms.

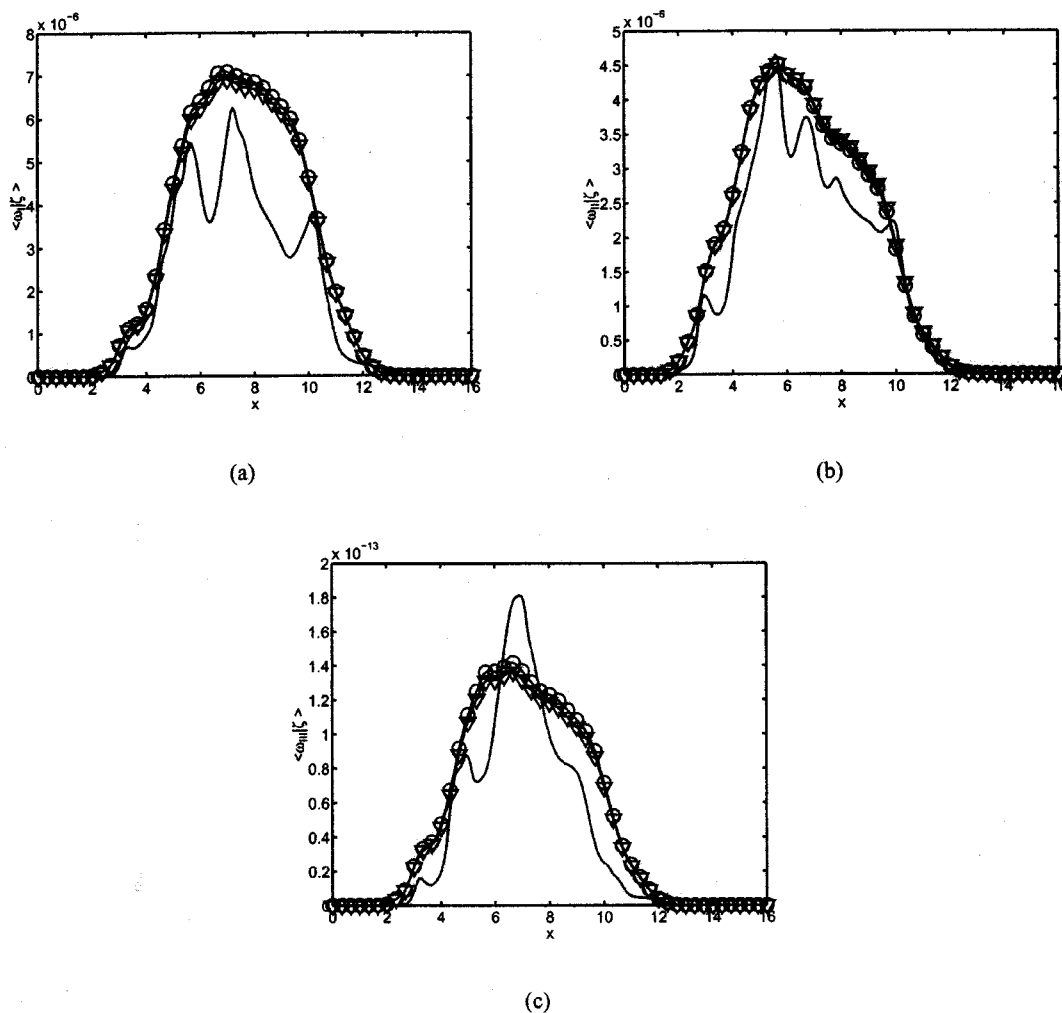


FIG. 8. Comparison to actual Reynolds averages of chemical reaction rates from DNS (solid lines) of the Reynolds averages calculated with new CSE model using flamelet decomposition and original coefficient vector (○) and using modified coefficient vector (▽).

- (ii) Only assumptions about small gradients in conditional averages and about the PDF of mixture fraction are needed—even for the new laminar flamelet decomposition presented here; closure for the source-terms is still based on the closure used in first-moment CMC methods which is not constrained to the laminar flamelet regime.
- (iii) Using LFD improves the predictions of CSE considerably.
- (iv) The computational cost of the new LFD approach to CSE is significantly lower than that of the original approach. Using CSEFD2, in particular, could lead to a cost reduction—both in storage and CPU time—of several orders of magnitude if a large, detailed chemical kinetic mechanism is required.

<sup>1</sup>W. K. Bushe and H. Steiner, "Conditional moment closure for large eddy simulation of nonpremixed turbulent reacting flows," *Phys. Fluids* **11**, 1896 (1999).

<sup>2</sup>R. W. Bilger, "Conditional moment closure for turbulent reacting flow," *Phys. Fluids A* **5**, 436 (1993).

<sup>3</sup>R. W. Bilger, "Conditional moment closure modelling and advanced laser measurements," in *Turbulence and Molecular Processes in Combustion*, edited by T. Takeno (Elsevier Science, New York, 1993), p. 267.

<sup>4</sup>A. Yu. Klimenko, "Multicomponent diffusion of various admixtures in turbulent flow," *Fluid Dyn.* **25**, 327 (1990).

<sup>5</sup>A. Yu. Klimenko and R. W. Bilger, "Conditional moment closure for turbulent combustion," *Prog. Energy Combust. Sci.* **25**, 595 (1999).

<sup>6</sup>A. W. Cook and J. J. Riley, "A subgrid model for equilibrium chemistry in turbulent flows," *Phys. Fluids* **6**, 2868 (1994).

<sup>7</sup>J. H. Chen, S. Mahalingam, I. K. Puri, and L. Vervisch, "Effect of finite-rate chemistry and unequal Schmidt numbers on turbulent nonpremixed flames modeled with single-step chemistry," in *Proceedings of the 1992 Summer Program* (Center for Turbulence Research, NASA Ames/Stanford University, Stanford, CA, 1992), p. 367.

<sup>8</sup>R. S. Barlow, "Turbulent diffusion flame workshop," <http://www.ca.sandia.gov/tdf/Workshop.html> (1996).

<sup>9</sup>R. S. Barlow and J. H. Frank, "Effects of turbulence on species mass fractions in methane/air jet flames," in *Twenty-Seventh Symposium (International) on Combustion* (The Combustion Institute, Pittsburgh, 1998), Paper 4A10.

<sup>10</sup>H. Steiner and W. K. Bushe, "Large eddy simulation of a turbulent reacting jet with conditional source-term estimation," *Phys. Fluids* **13**, 754 (2001).

<sup>11</sup>W. K. Bushe and R. W. Bilger, "Direct numerical simulation of nonpremixed combustion with realistic chemistry," *Annual Research Briefs* (Center for Turbulence Research, NASA Ames/Stanford University, Stanford, CA, 1998), p. 3.

<sup>12</sup>W. H. Press, S. A. Teukolsky, W. T. Vetterling, and B. P. Flannery, *Numerical Recipes in Fortran* (Cambridge University Press, Cambridge, UK, 1992).

<sup>13</sup>N. Peters, "Laminar diffusion flamelet models in non-premixed turbulent

- combustion," *Prog. Energy Combust. Sci.* **10**, 319 (1984).
- <sup>14</sup>H. Pitsch and N. Peters, "Unsteady flamelet formulation for non-premixed combustion considering differential diffusion effects," *Combust. Flame* **123**, 358 (2000).
- <sup>15</sup>N. S. A. Smith, "Development of the conditional moment closure method for modelling turbulent combustion," Ph.D. thesis, Department of Mechanical and Mechatronic Engineering, University of Sydney, Sydney, Australia, October 1994.
- <sup>16</sup>G. R. Ruetsch, L. Vervisch, and A. Liñán, "Effects of heat release on triple flames," *Phys. Fluids* **7**, 1447 (1995).
- <sup>17</sup>S. Lele, "Compact finite difference schemes with spectral-like resolution," *J. Comput. Phys.* **103**, 16 (1992).
- <sup>18</sup>T. Poinso and S. Lele, "Boundary conditions for direct simulations of compressible viscous flows," *J. Comput. Phys.* **101**, 104 (1992).
- <sup>19</sup>G. R. Ruetsch and M. R. Maxey, "Small-scale features of the vorticity and passive scalar fields in homogeneous isotropic turbulence," *Phys. Fluids A* **3**, 1587 (1991).
- <sup>20</sup>F. A. Williams, "Overview of asymptotics for methane flames," in *Reduced Kinetic Mechanism and Asymptotic Approximations for Methane–Air Flames*, edited by M. D. Smooke (Springer-Verlag, Berlin, 1991), p. 68.
- <sup>21</sup>N. Swaminathan and R. W. Bilger, "Direct numerical simulation of turbulent nonpremixed hydrocarbon reaction zones using a two-step reduced mechanism," *Combust. Sci. Technol.* **127**, 167 (1998).
- <sup>22</sup>W. K. Bushe and R. W. Bilger, "Conditional moment closure modeling of turbulent nonpremixed combustion with reduced chemistry," *Annual Research Briefs* (Center for Turbulence Research, NASA Ames/Stanford University, Stanford, CA, 1999), p. 139.
- <sup>23</sup>R. W. Bilger, "Conditional moment methods for turbulent reacting flow using Crocco variable conditions," Charles Kolling Laboratory Report, Department of Mechanical Engineering, The University of Sydney, TN F-99, 1991.
- <sup>24</sup>W. K. Bushe, "Conditional moment closure methods for autoignition problems," Ph.D. thesis, Cambridge University, Cambridge, UK, December 1995.

H. STEINER, A. KOBOR & L. GEBHARD

A wall heat transfer model for subcooled boiling flow

*Int. J. Heat Mass Transfer* **48** (2005), 4161–4173

# A wall heat transfer model for subcooled boiling flow

Helfried Steiner <sup>\*</sup>, Alexander Kobor, Ludwig Gebhard

*Institute of Fluid Mechanics and Heat Transfer, Technical University Graz, Inffeldgasse 25, A-8010 Graz, Austria*

Received 18 August 2004; received in revised form 8 February 2005

## Abstract

High compactness, low weight and little space requirement are gaining attention as prominent design criteria in the development of modern cooling systems in many applications. The resulting demand for highest possible heat transfer rates has lead to the very promising concept of providing for a controlled transition from pure single-phase convection to subcooled boiling flow in thermally highly loaded regions. For its application in modern engineering design this approach requires a realistic modeling of the complex phenomena associated with the two-phase flow heat transfer. The present work proposes for the computation of the specific wall heat transfer rate a modified superposition model, where the total heat flux is assumed to be additively composed of a forced convective and a nucleate boiling component. Since the present model requires only local input quantities, it is well suited to CFD of geometrically very complex coolant flows, where the definition of global length or velocity scales would be impractical. The wall heat fluxes predicted by the present model were compared against experimental data which were obtained by in-house measurements with water being the working fluid. The overall agreement is very good, particularly, in the partially nucleate boiling regime, where the effect of the bulk flow rate on the heat transfer is significant. Deviations are primarily observed at higher wall superheats, where a strong two-way coupling between the motion of the liquid and the motion of the bubbles as well as considerable bubble–bubble interactions typically occur.

© 2005 Elsevier Ltd. All rights reserved.

*Keywords:* Convective flow boiling; Flow-induced suppression; Subcooling

## 1. Introduction

In the development of modern cooling systems, be it for internal combustion engines, or, for microprocessors, the increasing output of specific power combined with a most compact space- and weight saving design leads to increasingly high thermal loads on the heating

surfaces. Thus, wherever a high coolant power with limitations on the available surface area for the heat transfer, the mass flow rate of the liquid coolant as well as the acceptable wall temperatures is to be achieved, a controlled transition to the nucleate boiling regime offers an attractive solution. The concept of exploiting the markedly enhanced heat transfer rates associated with the highly complex phenomenon of evaporation is also a big challenge to the CFD of coolant flows. The computationally very costly concept of direct numerical simulation, which attempts to resolve all physically relevant scales, is applicable only to strongly simplified cases like single bubble configurations (see [1–3]). For engineering

<sup>\*</sup> Corresponding author. Tel.: +43 316 873 7344; fax: +43 316 873 7356.

E-mail address: [steiner@fluidmech.tu-graz.ac.at](mailto:steiner@fluidmech.tu-graz.ac.at) (H. Steiner).

### Nomenclature

$b$	model constant [-]
$c$	specific heat [J/kg K]
$C_s$	constant [-]
$d_{\text{hyd}}$	hydraulic diameter [m]
$F$	force [N]
$g$	gravitational acceleration [ $\text{m/s}^2$ ]
$G$	specific mass flow rate [ $\text{kg/m}^2 \text{ s}$ ]
$G_s$	$= (du/dy)(y/u)$ shear rate [-]
$h$	heat transfer coefficient [ $\text{W/m}^2 \text{ K}$ ]
$h_{\text{lg}}$	latent heat [J/kg]
$k$	thermal conductivity [ $\text{W/m K}$ ]
$K$	constant [-]
$m, n$	constants [-]
$p$	pressure [ $\text{N/m}^2$ ]
$q$	specific heat transfer rate [ $\text{W/m}^2$ ]
$r$	radius [m]
$S$	suppression factor [-]
$T$	temperature [ $^{\circ}\text{C}$ ]
$t$	time [s]
$u$	velocity [m/s]
$u_{\tau}$	$= \sqrt{\tau_w/\rho}$ wall friction velocity [m/s]
$V$	volume [ $\text{m}^3$ ]
$x$	axial coordinate [m]
$y$	wall normal coordinate [m]
$y^+$	$= \rho u_{\tau} y / \mu_1$ non-dimensional distance [-]

### Greek symbols

$\alpha$	thermal diffusivity [ $\text{m}^2/\text{s}$ ]
$\kappa, \chi$	constants [-]

$\mu$	dynamic viscosity [ $\text{kg/m s}$ ]
$\rho$	mass density [ $\text{kg/m}^3$ ]
$\Phi$	correction factor [-]
$\Psi$	constant [-]
$\sigma$	surface tension [ $\text{kg/s}^2$ ]
$\tau$	shear stress [ $\text{N/m}^2$ ]
$\Theta$	angle [rad]
$\zeta$	mass fraction [-]

### Subscripts

b	bulk
bcy	buoyancy
d	drag
du	bubble growth
D	departure
fc	forced convection
flow	flow-induced
g	vapour phase
l	liquid phase
L	lift-off
nb	nucleate boiling
onb	onset of boiling
$p$	constant pressure
s	saturation
sl	shear lift
sub	subcooling
tp	two-phase
trans	transition
w	wall

flow configurations, where the technique of direct numerical simulation has to be ruled out for its high computational cost, computationally feasible and at the same time accurate boiling models have to be provided to obtain reliable numerical results.

The location of subcooled boiling occurring in a channel heated from beneath is sketched for in Fig. 1. The subcooled boiling region extends downstream from a certain location  $B$ , where the wall superheat  $T_w - T_s$  is sufficient to initiate and sustain nucleate boiling, while the temperature of the bulk liquid  $T_b$  remains below the local saturation temperature  $T_s$ . The corresponding subcooled boiling segment in the flow boiling curve is schematically shown in Fig. 2. The lower boundary at point  $B$  marks the onset temperature  $T_{\text{onb}}$  of the partially developed boiling (PDB), where the boiling curve starts to deviate from the dashed-dotted extension of the almost straight single-phase line. The heat transfer in the PDB regime is basically dominated by two effects, the macroconvection due to the motion of the bulk liquid and the latent heat transport associated with the

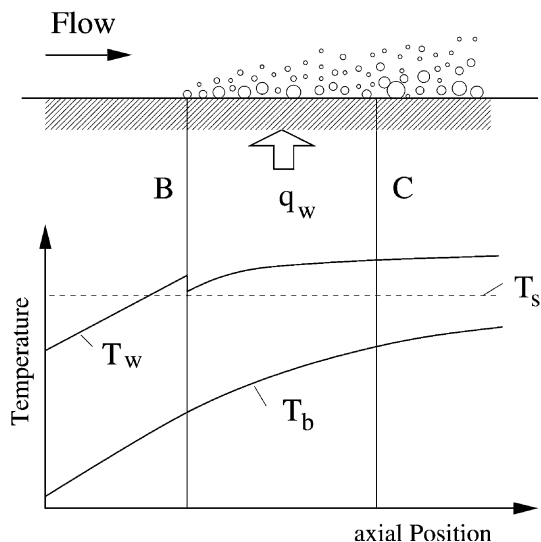


Fig. 1. Subcooled flow boiling domain in a heated channel.

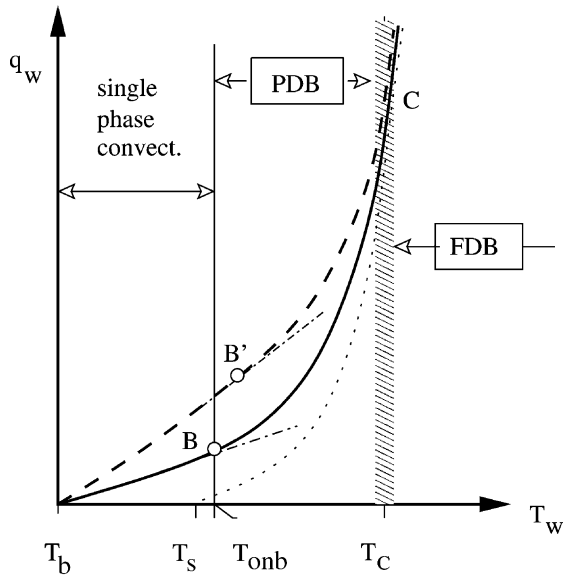


Fig. 2. Flow boiling curves for two bulk velocities: dashed line (---) denotes the higher velocity; dotted line (···) denotes the pool boiling curve.

evaporation of the liquid microlayer between the bubble and the heater wall. The important contribution of the macroconvection in the PDB region can be seen from the different paths of the two flow boiling curves representing two different flow rates in comparison to the path of the pool boiling curve, which is associated with zero bulk velocity, being all depicted in Fig. 2. With increasing bulk velocity the onset of nucleate boiling is typically shifted to higher wall superheats, such that the nucleate boiling sets in at point  $B'$  instead of  $B$  in case of the higher flow rate, as schematically shown in the diagram. At higher wall superheats the influence of the macroconvection becomes less and less pronounced, and the evaporating effect prevails. Accordingly, the flow boiling curves approach the pool boiling curve. The transition to the fully developed boiling (FDB) regime can be localized at a certain position  $C$  downstream from the location  $B$  as shown in Fig. 1. The corresponding point in the boiling curve diagram shown in Fig. 2 is located at temperature  $T_C$ . Beyond this temperature  $T_C$  there is a merger of the different flow boiling curves for varying bulk velocity, which indicates that they become practically independent of the actual flow rate.

As already pointed out above the large number and the wide diversity of influences which may essentially affect the nucleate flow boiling practically rule out a strict mathematical description of this phenomenon. Therefore, one has to rely on empirical, or, semi-empirical correlations to capture the basic mechanisms which significantly contribute to the total effective heat transfer. Many models suggested for subcooled flow boiling

assume the total wall heat flux  $q_w$  to be superimposed of two additive contributions, which can be written as

$$q_w = q_{fc} + q_{nb}. \quad (1)$$

The first term  $q_{fc}$  is due to forced convection, the latter  $q_{nb}$  is due to nucleate boiling. This concept of additive contributions was first introduced by Rohsenow [4]. In this approach Rohsenow subtracted from the experimentally measured values for the total wall heat flux a convective single phase contribution and attributed the residual term to nucleate boiling. He could further successfully correlate this nucleate boiling component using an equation he had originally proposed for saturated pool boiling. In later approaches due to Bowring [5], Bergles and Rohsenow [6] the subcooled boiling contribution was correlated using a simple power law

$$T_w - T_s = \Psi q_{nb}^m, \quad (2)$$

where  $\Psi$  and  $m$  are empirical constants to be determined in experiments. Since the system pressure is of major importance for the onset of boiling a prominent class of the power law correlations involves the reduced pressure  $p_{red}$  as a key correlation parameter. An early correlation of this type was introduced by Mostinskii [7]. Cooper [8], Leiner and Gorenflo [9] and Leiner [10], proposed formulations, which account for surface roughness, as well.

Rather than assuming the additive composition (1) an alternative group of models suggests a geometrical combination of the basic contributions. Models of this type formulate the effective heat transfer coefficient as some product function which can be generally written as

$$h_{tp} = h_{fc} \Phi_{tp}, \quad (3)$$

where the  $\Phi_{tp}$  represents a correction function due to nucleate boiling. Correlations of this type as suggested by Kandlikar [11], or, by Shah [12], mostly distinguish between the partially and the fully developed boiling regime. Accordingly, they propose different correlations for each regime, which in turn requires an a priori specification of the point of transition from the PDB to the FDB regime.

Among the superposition models of type (1) the model proposed by Chen [16] is widely used today especially in engineering applications in the automotive industry. Chen's model was originally developed for saturated boiling flow. Later, it was extended by Butterworth [17] to the subcooled regime, where it also produced results with acceptable accuracy. In his approach Chen advanced his predecessors' superposition models by accounting explicitly for the interaction between the liquid and the vapour phase. In particular, he distinguished two competing effects on the outcome of total wall heat flux, the enhanced convective transport due to bubble agitation, and the flow-induced

suppression of the nucleate boiling. To the first effect Chen attributed minor importance in the subcooled boiling regime, and, therefore, it need not be explicitly accounted for. The latter flow-induced suppression effect is modelled by Chen in terms of a suppression factor which reduces the nucleate boiling component especially in the PDB regime. Basically, the introduction of such a suppression factor in order to bridge the region between pure single-phase forced convection and fully developed nucleate boiling has the advantage that it circumvents the determination of the point of transition from PDB to the FDB regime, which mostly relies on a lot of empiricism. On the other hand the suppression factor proposed by Chen depends on the bulk flow Reynolds number as the only correlation parameter, which bears two drawbacks. First, imposing only the bulk flow Reynolds number as correlation parameter the suppression model is practically based on a single-phase bulk flow quantity, which makes it incapable to account for important effects like the influence of the liquid phase flow field on the near-wall motion of the bubbles, or, the influence of the wall superheat. The correlation is therefore expected to be very case dependent. Secondly, in the CFD of complex flow geometries it is hardly possible to define a reasonable bulk flow Reynolds number. The boiling departure lift-off (BDL) model, which is presented in this work, was devised to improve Chen's superposition approach, in that it attempts to model the flow-induced suppression on a physically sounder base. The suggested correlation for the flow-induced suppression depends only on local flow quantities which are in general knowns in the numerical solution of the liquid phase flow field. The impact of the subcooling, which is very pronounced at small flow rates combined with low superheats, is accounted as well through an additional parameter. The predictive capability of the BDL model is evaluated by comparing its predictions with experimental data. These data have been obtained in-house in boiling flow experiments. A detailed description of the experimental apparatus used for these measurements is given in Section 2. The description of the mathematical formulation for the BDL model is presented in Section 3.

## 2. Experimental setup

The present experimental apparatus was designed to investigate subcooled convective boiling at conditions, which are typically met in liquid coolant systems of internal combustion engines. The forced convective flow loop is schematically shown in Fig. 3. The flow is generated by a pump feeding a tank, where the working fluid is preheated to sustain a certain bulk temperature in the test section. The operating pressure is set to a fixed level using a pressure control vessel. The velocity of the bulk

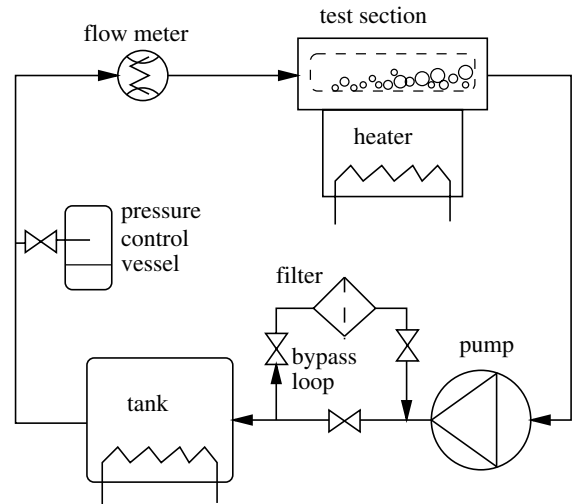


Fig. 3. Schematic diagram of the entire convective boiling flow loop.

flow is controlled by means of an inductive flow meter, whose output is used to adjust the volumetric flow rate via the speed of the feeding pump and/or the flow-rate through the by-pass loop. The present configuration allows the bulk velocity to be varied within the range of  $0.05 \leq u_b \leq 2.0$  m/s. The absolute operating pressure can be set within the range  $1.0 \leq p \leq 2.0$  bar. Small bubbles as well as particle contaminations are sieved out by a filter.

Fig. 4 gives a schematic view inside the test section of the channel. The test section is a square duct with a

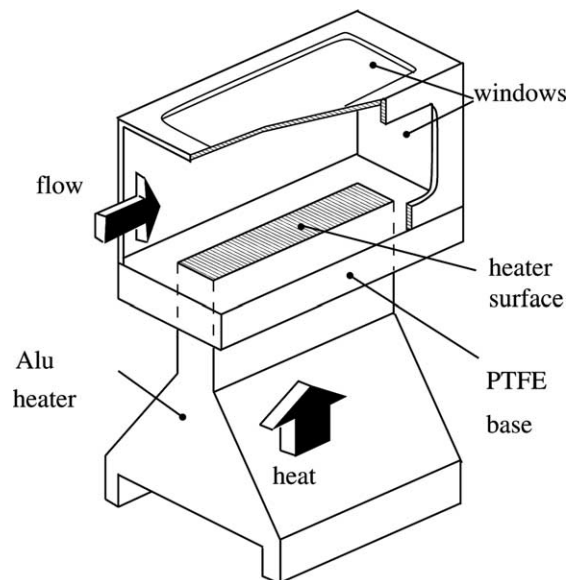


Fig. 4. Test section of the experimental facility.

height of 40 mm and a width of 30 mm. The heat flux into the channel is generated by heating coils located at the bottom of the aluminium heater from where it is conducted to the top of the heater. At the upper surface, whose length is 60 mm and width is 10 mm, respectively, the heat is transferred to the working fluid flowing through the channel. The wall temperature as well as the wall heat flux are determined based on measurements of the temperature using several K-type thermocouples appropriately distributed in the solid heater. The base plate of the test section, where the top of the aluminium heater is built in, is made of PTFE. The outstandingly low thermal conductivity ( $\lambda_{\text{PTFE}} = 0.23 \text{ W/m K}$ ) of this material should guarantee the lowest possible heat loss of the heater to the surrounding structure. Due to thermal durability restrictions of the PTFE base plate the maximum heater surface temperature was limited to  $T_w = 160 \text{ }^\circ\text{C}$ . Below this temperature the observed thermal deformations of the PTFE-structure always remained within an acceptable range. Windows made of glass are embedded in the top as well as the side walls of the test channel to make the heater surface optically accessible. Using the present configuration the total error in the experimentally obtained heat fluxes are mainly due to measurement and position errors of the thermocouples, as well as the uncertainties in the actual thermal conductivity of the heater material (aluminium alloy) and in the heat losses to the surroundings of the heater. A worst-case estimation turned out a total error for the heat flux ranging from  $\pm 5\%$  in the convective regime to  $\pm 2\%$  in the nucleate boiling regime always referring the value actually obtained from the measurements. The error in the measured surface temperatures amounts to  $\pm 0.15 \text{ }^\circ\text{C}$ . The inductive flow meter measures the flow rate with high accuracy, such that the relative error is only  $\pm 0.5\%$  of the displayed value.

### 3. Mathematical formulation of the subcooled boiling flow model

The BDL model invokes an additive ansatz as suggested by Chen [16] for the total wall heat flux

$$q_w = q_{\text{fc}}\Phi + q_{\text{nb}}S, \tag{4}$$

where the two correction parameters  $\Phi$  and  $S$  modify the forced convection heat flux  $q_{\text{fc}}$  and the nucleate boiling heat flux  $q_{\text{nb}}$ , respectively. Both heat fluxes are computed following Chen’s proposal. Accordingly, the first is written as

$$q_{\text{fc}} = h_{\text{fc}}(T_w - T_b), \tag{5}$$

where the transfer coefficient  $h_{\text{fc}}$  is calculated using the Dittus–Boelter equation

$$Nu_{\text{fc}} = \frac{h_{\text{fc}}d_{\text{hyd}}}{\lambda_l} = 0.023Re_1^{0.8}Pr_1^{0.4} \tag{6}$$

involving the bulk flow Reynolds number and the Prandtl number of the liquid phase

$$Re_1 = \frac{\rho_l u_b d_{\text{hyd}}}{\mu_l}, \quad Pr_1 = \frac{\mu_l c_{p,l}}{\lambda_l},$$

respectively. The nucleate boiling heat flux

$$q_{\text{nb}} = h_{\text{nb}}(T_w - T_s) \tag{7}$$

is obtained using a correlation due to Forster and Zuber [18]

$$h_{\text{nb}} = 0.00122 \frac{\lambda_l^{0.79} c_{p,l}^{0.45} \rho_l^{0.49}}{\sigma^{0.5} \mu_l^{0.29} h_{\text{fg}}^{0.24} \rho_g^{0.24}} \Delta T_s^{0.25} \Delta p_s^{0.75}, \tag{8}$$

where the saturation pressure difference corresponding to the superheat temperature is written as

$$\Delta p_s = p_s(T_w) - p_s(T_s).$$

The factor  $\Phi$  occurring in Eq. (4) represents the enhancement of the convective component due to bubble agitation. Chen [16] derived a graphic relationship for  $\Phi$  as a dependent of the inverse of the Martinelli number  $X_{tt}$ , which reads

$$\left(\frac{1}{X_{tt}}\right) = \left(\frac{\zeta_g}{1 - \zeta_g}\right)^{0.9} \left(\frac{\rho_l}{\rho_g}\right)^{0.5} \left(\frac{\mu_g}{\mu_l}\right)^{0.1}, \tag{9}$$

where  $\zeta_g$  denotes mass fraction of the vapour. Butterworth [17] fitted this relationship  $\Phi = \Phi(1/X_{tt})$  with

$$\begin{aligned} \zeta_g > 0.1 : \Phi &= 2.35 \left(\frac{1}{X_{tt}} + 0.213\right)^{0.736} \\ \zeta_g \leq 0.1 : \Phi &= 1. \end{aligned} \tag{10}$$

In subcooled boiling flow the vapour mass fractions are typically small, such that  $\zeta_g \leq 0.1$  applies and  $\Phi$  can be assumed unity.

The essential difference between Chen’s approach and the present BDL concept consists in the modeling of the modification of the nucleate boiling component in terms of the factor  $S$  in Eq. (4). Chen introduced this parameter  $S$  as a flow-induced suppression factor, which he correlated as an empirical function of the product  $Re_1\Phi^{1.25}$ . This correlation was later fitted by Butterworth [17] with the expression

$$S_{\text{Chen}} = \frac{1}{1 + 2.53 \times 10^{-6} (Re_1\Phi^{1.25})^{1.17}}. \tag{11}$$

For subcooled boiling flow, where  $\Phi \approx 1$ , the factor  $S_{\text{Chen}}$  obviously depends on the bulk flow Reynolds number only. In contrast to Chen’s bulk-flow dependent, hence, basically global, approach the BDL model attempts to model the flow-induced suppression based on the local dynamics of a vapour bubble subject to the surrounding flow field near the heater surface. Thereby, the BDL model utilizes a concept which was originally proposed by Zeng et al. [19] to compute the

size of a bubble at the point of detachment from the heater surface. According to the hypothesis of Zeng and his coworkers the whole process of vapor bubble detachment basically evolves in three different stages, as schematically shown in Fig. 5. At the first stage the bubble is attached to its nucleation site, and it is inclined by the angle  $\theta$  due to the hydrodynamic flow forces. The attached bubble is growing until it reaches a critical departure volume  $V_D$ , where the bubble is dragged off its nucleation site. At the point of departure the volume equivalent departure radius is defined as

$$r_D = \left( \frac{3V_D}{4\pi} \right)^{\frac{1}{3}}$$

The departure from the nucleation site marks the beginning of the stage II, where the departed bubble slides in upright posture ( $\theta = 0$ ) along the heater surface. Thereby, the bubble still keeps growing in size until it reaches a bubble volume, where the buoyancy force is sufficiently high to make the bubble lift-off from the surface. At the point of the bubble's lift-off the stage III begins and the corresponding lift-off volume  $V_L$  determines the volume equivalent lift-off radius defined as

$$r_L = \left( \frac{3V_L}{4\pi} \right)^{\frac{1}{3}}$$

The departure radius  $r_D$  as well as the inclination angle  $\theta$  are mathematically obtained by solving the momentum balance equations right at the instant of departure, which are written in the  $x$ - and  $y$ -direction as

$$0 = F_d + F_{du} \sin \theta, \tag{12}$$

$$0 = F_{bcy} + F_{du} \cos \theta + F_{sl}, \tag{13}$$

respectively. Therein, ought to the small density ratio  $\frac{\rho_g}{\rho_l} \ll 1$  the inertial forces were neglected, such that the Eqs. (12) and (13) basically represent a static force balance. All the forces which are assumed to be relevant at the point of departure, and, therefore, have to be

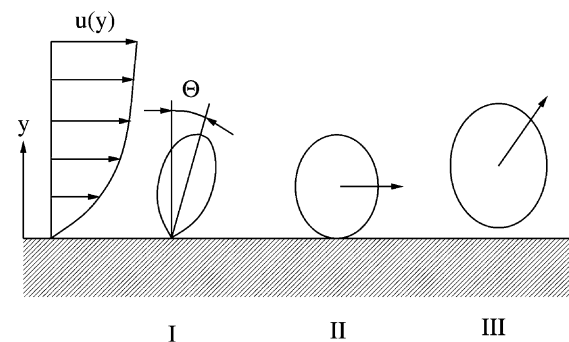


Fig. 5. Three stages of a vapor bubble departing from the heater surface: (I) instant of departure from the nucleation site, (II) sliding bubble, (III) instant of lift-off.

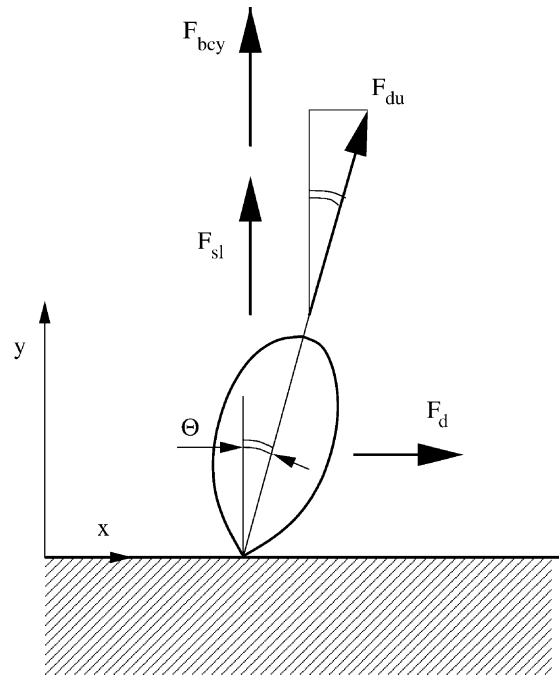


Fig. 6. Force balance at a vapor bubble at the instant of departure from its nucleation site.

accounted for are schematically shown in Fig. 6. The considered forces are the drag force  $F_d$ , the shear-lift force  $F_{sl}$ , the buoyancy force  $F_{bcy}$ , and the bubble growth force  $F_{du}$ . The surface tension force was assumed to be negligibly small at the moment of departure and omitted. The drag force and the shear-lift force are given by

$$F_d = 6\pi\mu_l u r \left\{ \frac{2}{3} + \left[ \left( \frac{12}{Re_b} \right)^n + 0.796^n \right]^{-\frac{1}{n}} \right\}, \tag{14}$$

with  $n = 0.65$

and

$$F_{sl} = \frac{3.877}{2} \rho_l u^2 \pi r^2 G_s^{\frac{1}{2}} \left( \frac{1}{Re_b^2} + 0.014 G_s^2 \right)^{\frac{1}{4}}, \tag{15}$$

where

$$Re_b = \frac{\rho_l u 2r}{\mu_l} \quad \text{and} \quad G_s = \left. \frac{du}{dy} \right|_{y=r} \frac{r}{u}$$

denote the bubble Reynolds number and the shear rate, respectively. As for the velocity  $u$  as well as its spatial derivative  $\frac{du}{dy}$ , whose values at the location  $y = r$  are needed in Eqs. (14) and (15), the presence of the vapour bubbles is neglected such that Reichardt's analytical expression for single-phase flow

$$\begin{aligned}
 u^+ &= \frac{u}{u_\tau} \\
 &= \frac{1}{\kappa} \ln(1 + \kappa y^+) \\
 &\quad + C \left[ 1 - \exp\left(-\frac{y^+}{\chi}\right) - \frac{y^+}{\chi} \exp\left(-\frac{y^+}{3}\right) \right] \quad (16)
 \end{aligned}$$

can be used to provide the velocity profile of the liquid phase. Eq. (16) is written as a non-dimensional function of the wall coordinate

$$y^+ = \frac{\rho_1 u_\tau y}{\mu_1}$$

with the wall friction velocity

$$u_\tau = \left( \frac{\tau_w}{\rho_1} \right)^{\frac{1}{2}}$$

being determined by the wall shear stress  $\tau_w$ . The constants are set to  $\kappa = 0.41$ ,  $\chi = 11$ , and  $C = 7.4$ , respectively.

The buoyancy force is given by

$$F_{\text{bcy}} = \frac{4}{3} r^3 \pi g (\rho_l - \rho_g) \quad (17)$$

The bubble growth force  $F_{\text{du}}$  is modeled following Zeng et al. [21], who considered a hemispherical bubble expanding in an inviscid liquid. They proposed the equation

$$F_{\text{du}} = -\rho_l \pi r^2 \left( \frac{3}{2} C_s \dot{r}^2 + r \ddot{r} \right), \quad (18)$$

where the empirical constant  $C_s$  was introduced to account primarily for the presence of the wall. Based on a comparison with experimental data available to them the authors suggested to set  $C_s = \frac{20}{3}$ . The temporal evolution of the bubble radius  $r(t)$ , as well as its temporal derivatives  $\dot{r}$  and  $\ddot{r}$  needed in Eq. (18), are obtained assuming a diffusion controlled bubble growth model due to Zuber [20], which reads

$$r(t) = \frac{2b}{\sqrt{\pi}} Ja \sqrt{\alpha_l t}, \quad (19)$$

involving the Jakob number

$$Ja = \frac{\rho_l c_{p,l} (T_w - T_s)}{\rho_g h_g},$$

the thermal diffusivity of the liquid phase  $\alpha_l$ , and the empirical constant  $b$ .

The lift-off radius of the bubble  $r_L$  is obtained by solving the momentum balance equations (12) and (13) under the assumption that at the instant of lift-off there is no slip in the velocity between the bubble and the surrounding liquid phase. This implies a zero drag and shear-lift force, and a zero inclination angle,  $\Theta = 0$ ,  $F_d = 0$ ,  $F_{sl} = 0$ , respectively, such that  $r_L$  is obtained upon the solution of

$$0 = F_{\text{bcy}} + F_{\text{du}} \quad (20)$$

The predicted bubble radii were compared to experimental data measured at a given wall superheat  $\Delta T_s = 29^\circ\text{C}$  for four different velocities  $u_b = 0.05, 0.39, 0.77, 1.17$  m/s, respectively. Thereby, the growth rate parameter occurring in Eq. (19) was set to  $b = 0.21$ . The wall friction velocities  $u_\tau$  needed as input by the model in Eq. (16) were obtained from LDA measurements of the axial velocity component in the plane of symmetry of the test channel right before the beginning of the heater surface. The bubble radii were measured optically using video records. The results of these bubble size measurements are depicted as vertical bars in Fig. 7. Bubble size data taken from a recent very detailed experimental investigation on the bubble dynamics in subcooled boiling flow made by Maurus [22] are shown as well. Maurus measured the bubble radii distribution functions near the wall at a subcooling of  $\Delta T_{\text{sub}} = 20^\circ\text{C}$ , which is comparable to the subcooling of the present in-house measurements being  $\Delta T_{\text{sub}} = 16^\circ\text{C}$ . It is important to note that the open symbols in Fig. 7 represent the median bubble radii from Maurus' measurements with varying bulk flow rate and a constant wall heat flux of  $q_w = 0.77$  MW/m<sup>2</sup>. This heat flux is considerably higher than in the present experiments, where the bubble size data were obtained at a heat flux in the range of  $q_w = 0.40$ – $0.45$  MW/m<sup>2</sup>. The higher heat flux evidently leads to larger bubble radii in Maurus' data as well as to a slower decrease in bubble size with increasing velocity. The here manifested dependence of the mean bubble size on heat flux is also confirmed by

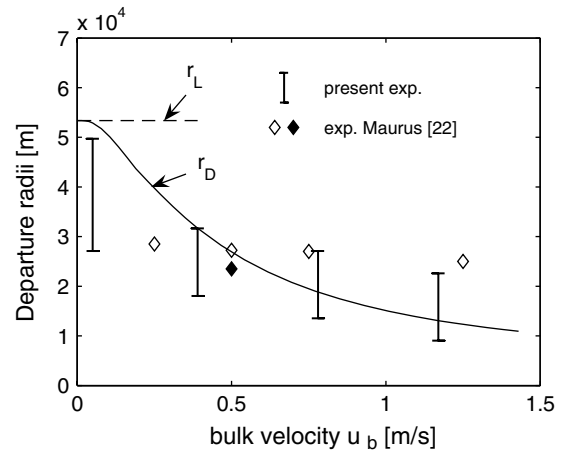


Fig. 7. Full line, ‘—’, predicted departure radii  $r_D$ ; dashed line, ‘- -’, predicted lift-off radius  $r_L$ ; bars, ‘|’, denote the range of the departure radii at a given bulk velocity  $u_b$  measured in the present experiments; symbols denote the median bubble radii experimentally obtained by Maurus [22] at a given wall heat flux  $q_w$ : open diamonds, ‘◇’,  $q_w = 0.77$  MW/m<sup>2</sup>; filled diamond, ‘◆’,  $q_w = 0.37$  MW/m<sup>2</sup>.

a further set of Maurus' measurements, where the heat flux was varied and the specific mass flow rate was kept constant at  $G = 500 \text{ kg/m}^2 \text{ s}$ . Referring to these measurements the filled symbol represents the median bubble radius obtained for  $q_w = 0.37 \text{ MW/m}^2$  which is very close to the range in our own present experiments. It becomes evident that due to the lower heat flux the bubble median radius lies notably below the corresponding value obtained for  $q_w = 0.77 \text{ MW/m}^2$  (represented by the open symbol above). Ought to the comparable magnitude of the imposed heat flux the agreement with the present in-house measurements is better for this case as well.

The comparison of the model predictions for the departure radii with the corresponding experimental data exhibits a good agreement for the higher velocities, while deviations occur at the lowest velocity considered. Both modelled radii become equal, i.e.,  $r_D = r_L$ , in the limit of zero bulk velocity. With increasing flow rate the departure radius  $r_D$  decreases markedly relative to the lift-off radius  $r_L$ . The widening gap between these two radii with increasing bulk velocity evidently reflects the influence of the local velocity field on the bubble detachment process from the surface. Based on this consideration the BDL model correlates the flow-induced suppression in terms of the ratio  $\frac{r_D}{r_L}$ , and the corresponding suppression factor is proposed as

$$S_{\text{flow}} = \frac{r_D}{r_L}. \quad (21)$$

According to its definition  $S_{\text{flow}}$  is supposed to represent the flow-induced deviation of the bubble departure radius from the corresponding pool boiling limit, which is associated with zero bulk velocity, where  $r_D = r_L$  and, hence,  $S_{\text{flow}} = 1$ . The present formulation for the computation of  $r_D$  and  $r_L$  does not explicitly account for subcooling. Thus, the obtained radius  $r_L$  basically represents the lift-off radius in the saturated boiling regime and not in the subcooled boiling regime as it is considered in the present configuration. This also explains the overprediction for the bubble sizes in the very low velocity range shown in Fig. 7. It is reasonable to assume that even at very small flow rates the advection of subcooled bulk liquid is sufficient to maintain a subcooled thermal boundary layer, where the departing bubbles are typically smaller than in the saturated case. Accordingly, the experimentally measured departure radii tend towards a limit markedly below the predicted lift-off radius  $r_L$  representing the saturated case.

The BDL model accounts for the effect of subcooling by introducing the factor

$$S_{\text{sub}} = \frac{T_w - T_s}{T_w - T_b}. \quad (22)$$

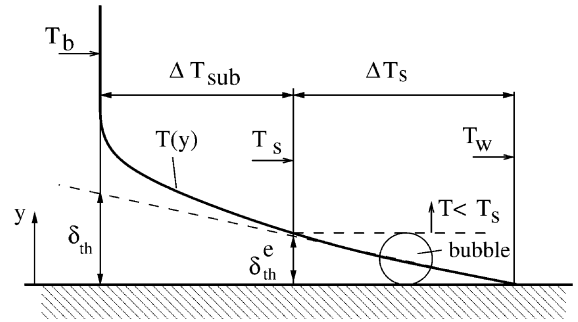


Fig. 8. Superheated thermal boundary layer in subcooled boiling.

The present definition of (22) is based on the concept of a so-called “extrapolated superheat layer thickness” suggested by Wiebe and Judd [23]. As it can be seen in the sketch of the superheated boundary layer in Fig. 8, the extrapolated superheat layer thickness,  $\delta_{\text{th}}^e$ , is defined as the height of intersection between the tangent to the temperature profile at the wall and the bulk temperature  $T_b$ . It is written as

$$\delta_{\text{th}} = \frac{T_w - T_b}{\left. \frac{dT}{dy} \right|_w} \quad (23)$$

and is supposed to reflect closely the superheated layer, which strongly governs the whole process of bubble nucleation, growth and departure. It further becomes evident from Fig. 8 that due to the subcooling a considerable portion of  $\delta_{\text{th}}$  exhibits a temperature lower than the saturation temperature  $T_s$ . The growing vapor bubbles cannot protrude into this subcooled layer, because condensation sets in at the bubble tip, once it reaches the zone, where  $T < T_s$ . Considering this limitation on the bubble size due to the subcooling an “effective extrapolated superheat layer thickness”

$$\delta_{\text{th}}^e = \frac{T_w - T_s}{\left. \frac{dT}{dy} \right|_w} \quad (24)$$

can be defined replacing in (23) the bulk temperature  $T_b$  by the saturation temperature  $T_s$ . The factor  $S_{\text{sub}}$  given by (22) is then obtained as the ratio  $\delta_{\text{th}}^e/\delta_{\text{th}}$  representing thus a measure for the subcooling. The factor  $S_{\text{sub}}$  is at maximum unity in the case of saturated boiling, where  $T_b = T_s$ , and it decreases to zero for increasing subcooling  $\Delta T_{\text{sub}} = T_s - T_b$ .

It is noted that in the choice of the empirical parameter  $b$  occurring in (19) the value  $b = 0.21$  yielded the best fit to the experimentally measured bubble radii. Basically, this model constant is supposed to account for the asphericity of the bubbles and is of the order of unity. Zeng et al. [19] considered flow boiling data for the refrigerant R113 and obtained the best overall

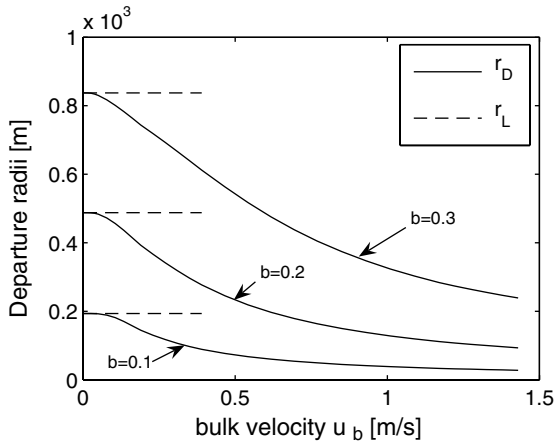


Fig. 9. Predicted departure and lift-off radii for a varying model parameter  $b$ .

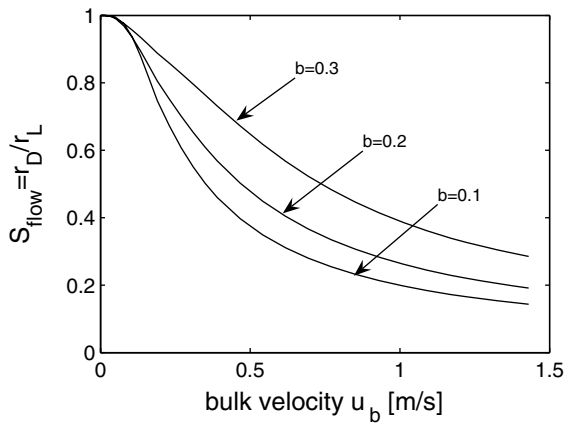


Fig. 10. Flow-induced suppression factor  $S_{\text{flow}}$  obtained for a varying model parameter  $b$ .

agreement with  $b = 1$ . The sensitivity of the predictions for the bubble size to a variation of  $b$  and its effect on the resulting suppression factor  $S_{\text{flow}}$  is illustrated in Figs. 9 and 10, respectively. It becomes evident that the model parameter  $b$  essentially determines the level of the predicted bubble lift-off radius. The suppression factor  $S_{\text{flow}}$  represents by definition the flow-induced decrease of the departure radius relatively to the corresponding lift-off radius. Depending thus on the ratio of the predicted radii and not explicitly on the predicted individual numerical values, the factor  $S_{\text{flow}}$  is to some extent less sensitive to the choice of  $b$ . As it can be seen from Fig. 10, there is, however, still the tendency that smaller values for  $b$  basically produce a smaller flow-induced suppression factor  $S_{\text{flow}}$ .

Substituting the two suppression factors defined in Eqs. (21) and (22) as total suppression into Eq. (4) the total wall heat flux is then rewritten as

$$q_w = q_{\text{fc}} + q_{\text{nb}} S_{\text{flow}} S_{\text{sub}} \tag{25}$$

#### 4. Comparison of the model predictions with experiments

Using the experimental setup described in Section 2 several flow boiling curves for a given absolute pressure and a given bulk velocity were measured. The thereby considered individual pressure–velocity combinations are summarized in Table 1. In all considered cases the temperature of the bulk liquid was kept constant at  $T_b = 95\text{ °C}$ , which implies a subcooling of  $\Delta T_{\text{sub}} = 16\text{ °C}$  in the case  $p = 1.5\text{ bar}$  and  $\Delta T_{\text{sub}} = 25\text{ °C}$  in the case  $p = 2.0\text{ bar}$ , respectively. The heater wall temperature was varied within the interval  $95\text{ °C} \leq T_w \leq 150\text{ °C}$ . The slowest velocity in the lower pressure case ( $p = 1.5\text{ bar}$ ) was chosen deliberately small, i.e.,  $u_b = 0.05\text{ m/s}$ , to come as closest to the pool boiling limit as it was possible in

Table 1

Pressures and velocities of the bulk liquid considered in the boiling flow experiments

Absolute pressure $p$ [bar]	Velocity of the bulk liquid $u_b$ [m/s]		
1.5	0.05	0.39	1.17
2.0	0.20	0.39	1.17

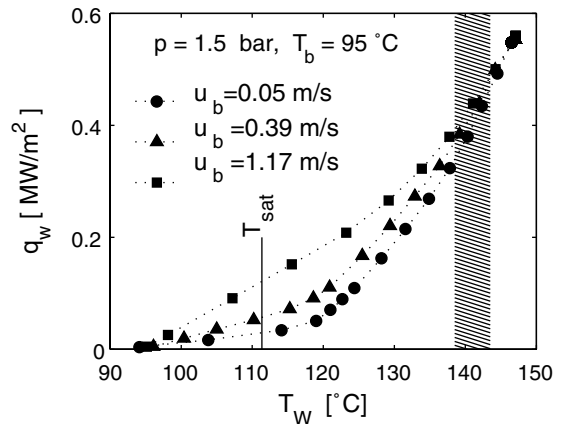


Fig. 11. Experimentally measured flow boiling curves at  $p = 1.5\text{ bar}$  absolute operating pressure and three different absolute velocities of the bulk flow,  $u_b = 0.05$ ,  $u_b = 0.39$ ,  $u_b = 1.17\text{ m/s}$ , respectively.

the present experimental facility. As already noted in the former section the individual wall friction velocities  $u_\tau$  associated with each bulk velocity  $u_b$  and required as model input were obtained using LDA measurements of the axial velocity profiles at the entrance of the heated test section. Fig. 11 shows all the boiling curves measured at  $p = 1.5$  bar plotted into one single graph to illustrate the individual flow boiling regimes as already discussed schematically in Fig. 2. The approximately linear sections to the left of the curves indicate pure single-phase convection. Above the saturation temperature  $T_s$  the curves start to deviate from the single-phase linearity which marks the onset of the partially developed boiling regime (PDB). The notably different paths of the individual boiling curves demonstrate the strong influence of the flow rate in this temperature range. Looking at the wall temperatures, above which a non-linear increase of the heat flux can be observed, makes evident that the nucleate boiling sets in at about  $\Delta T_s = 3$  °C wall superheat in the slow velocity case,  $u_b = 0.05$  m/s, while the onset of boiling is located at about  $\Delta T_s = 15$  °C in the high velocity case,  $u_b = 1.17$  m/s. With increasing wall superheat the individual curves converge in the region around  $T_w = 140$  °C (pattern-shaded interval), which indicates the transition to the fully developed boiling regime. There, the effect of the bulk flow rate is obviously insignificant and the total heat flux is dominated by velocity independent nucleate boiling mechanisms. As a consequence, irrespectively of the macroscopic flow velocity all boiling curves practically merge into one single branch.

Figs. 12 and 13 show the comparison between the total wall heat fluxes predicted by the BDL model with the corresponding experimental data at the two considered levels of the operating pressure, respectively. In all diagrams the saturation temperature  $T_s$  is marked by a thin vertical line. In addition to the results of the present BDL approach the heat fluxes predicted by other widely used models, due to Chen [16], Shah [12] and Kandlikar [11] are depicted as well.

The overall agreement between the predictions of the BDL model and the experimental data is good. Particularly in the high velocity case,  $u_b = 1.17$  m/s, the BDL model predicts the shift of the onset of nucleate boiling to higher wall superheats accompanied by a relative reduction of the boiling component in the total heat flux very accurately. This indicates that the BDL model is capable to capture the strong flow induced suppression of the nucleate boiling in the PDB regime very well. For higher wall superheats, however, approaching the FDB regime, the agreement becomes worse especially in case of the lowest velocity considered ( $u_b = 0.05$  m/s). This discrepancy can be explained by the fact that the present BDL model basically relies on the dynamics of a single bubble subject to a surrounding subcooled liquid flow field, which is assumed to remain unaffected by the

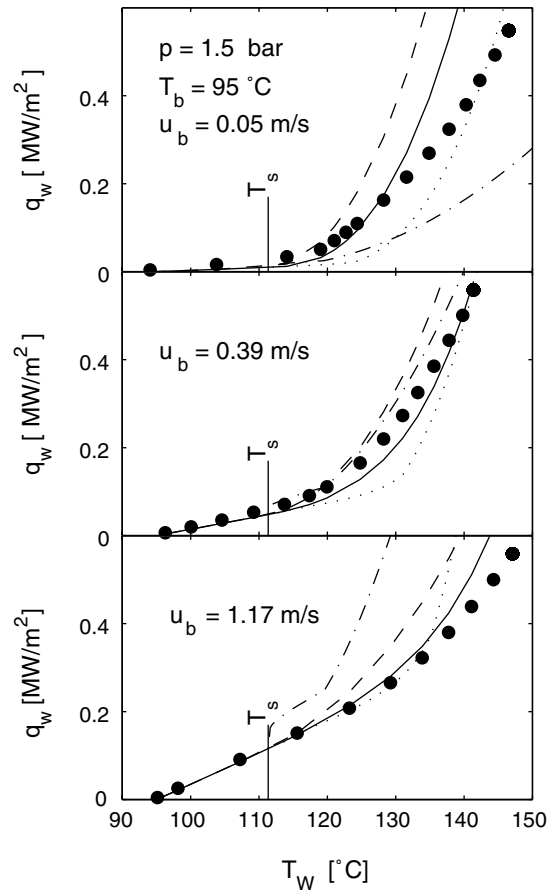


Fig. 12. Predicted flow boiling curves at  $p = 1.5$  bar and three different velocities of the bulk flow, respectively: full line, '—', BDL; dashed line, '---', Chen; dashed dotted line '---' Shah; dotted line '···' Kandlikar; symbols, '●', measurements.

presence of the vapour phase. Hence, it is conceivable that the predictions of the model are less accurate once phenomena related to the very complex multi-bubble dynamics become important. Due to the high bubble number densities, which are typically found on the heater surface in the FDB regime, a strong bubble–bubble interaction as well as a notable two-way coupling between the motion of the bubbles and the liquid phase occur. In such a regime bubbles tend to coalesce forming larger structures on the surface. Moreover, the motion of the bubbles pronouncedly affects the surrounding flow field of the liquid phase and vice versa. Considering these highly complex multi-phase flow phenomena there is certainly scope for further development of the present model in order to improve its accuracy particularly in the FDB regime.

The comparison with the results which were obtained with the models proposed by other authors and are also plotted in Figs. 12 and 13 reveals that

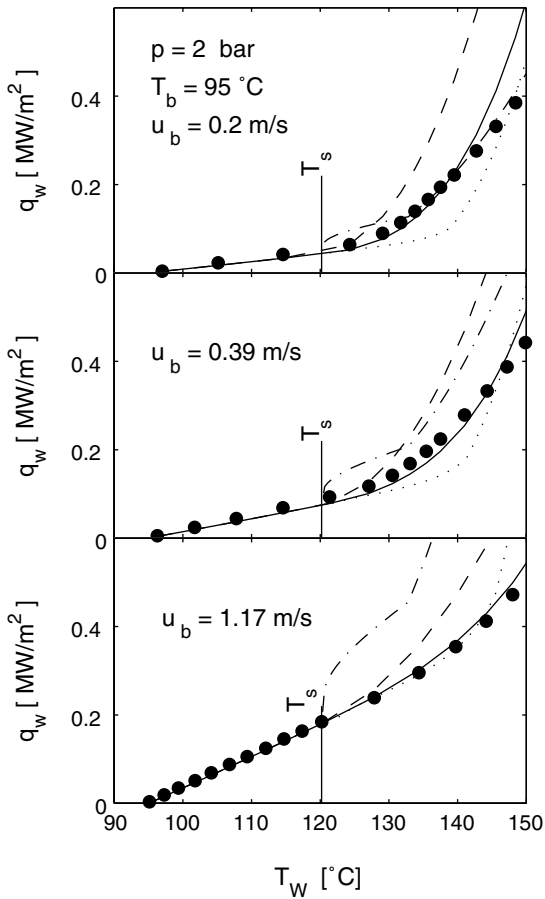


Fig. 13. Predicted flow boiling curves at  $p = 2.0$  bar and three different velocities of the bulk flow, respectively: full line, ‘—’, BDL; dashed line, ‘---’, Chen; dashed dotted line ‘-·-·-’ Shah; dotted line ‘····’ Kandlikar; symbols, ‘●’, measurements.

Chen’s approach generally overpredicts the heat fluxes. This tendency towards overpredictions, which is also observed with many other Chen-type additive superposition correlations, can be explained by two main reasons. First, the empirical function for the suppression factor given in Eq. (11) used in Chen’s model is obviously calibrated for saturated boiling, where the nucleate boiling heat transfer is typically higher than in subcooled boiling. Second, since the factor  $S_{\text{Chen}}$  depends on the bulk flow Reynolds number only, it practically represents a pure bulk flow quantity. It is therefore insensitive to local quantities like the wall superheat or wall shear stress, which can be expected to have a significant effect on a local phenomenon like the nucleate boiling heat transfer in a wall shear layer. As it was already pointed out in the former section, it was essentially these two shortcomings which motivated the authors to develop Chen’s ansatz further to the present BDL proposal. The comparison with the

corresponding results of the BDL model demonstrates that the predictive capability of Chen’s superposition ansatz could be considerably improved by introducing an alternative model for the suppression of the nucleate boiling component as proposed in the BDL concept.

The results obtained using Shah’s model [12] show a very good agreement in the FDB region in the case, at  $p = 2.0$  bar and  $u_b = 0.2$  m/s. In the PDB regime the agreement is generally rather poor especially for the higher velocities, where considerable overpredictions are observed. The kink in the boiling curves marks the transition from the PDB to the FDB regime which is in Shah’s model located at the superheat  $\Delta T_s = 0.5 \cdot \Delta T_{\text{sub}}$ . At this in principle arbitrarily determined point of transition the formulation switches from the correlation suggested for the PDB to the correlation suggested for the FDB regime which typically leads to an abrupt turn in the boiling curve. The approach due to Kandlikar [11] also prescribes a change in the formulation at the point of the transition from the PDB to the FDB regime. The location of this transition is determined in terms of the heat flux at the intersection between the extension of the single-phase line and the FDB curve multiplied by the factor 1.4. As shown in the results Kandlikar’s proposal for locating the point of transition leads to accurate predictions in the PDB regime in the high velocity case. At the lower velocities the region which is dominated by single-phase convection extends too far into the nucleate boiling region, as the considerable underpredictions in the PDB regime make evident.

In order to evaluate the performance of the BDL model in the case of stronger subcooling its predictions were also compared against experimental data obtained by Bibeau and Salcudean [13]. They carried out their

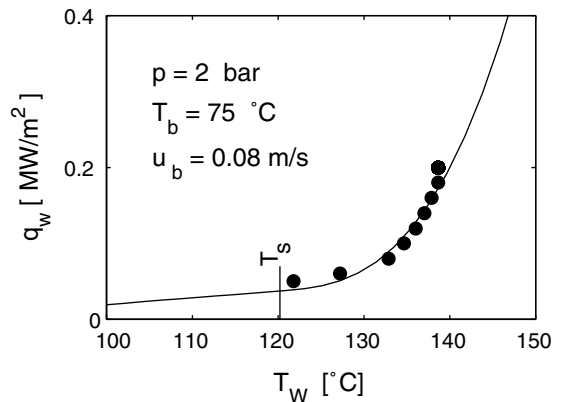


Fig. 14. Comparison at stronger subcooling; full line, ‘—’, BDL; symbols, ‘●’, measurements by Bibeau and Salcudean [13].

flow boiling measurements using an annular test section with the inner surface heated. The pressure was  $p = 2$  bar and the bulk velocity was  $u_b = 0.08$  m/s. The temperature of the bulk flow was  $T_b = 75$  °C, which implies a subcooling of  $\Delta T_{\text{sub}} = 45$  °C. As it is shown in Fig. 14, the predictions produced by the BDL model agree very well with the experiments. Due to the low flow rate the flow-induced suppression is considerably small, and, hence, the corresponding suppression factor  $S_{\text{flow}}$  does not deviate much from unity. Thus, the total suppression  $S$  is mainly due to effect of the subcooling. It turns out that the in the present case very dominant effect of subcooling is estimated very well in terms of the corresponding model parameter  $S_{\text{sub}}$  as given by Eq. (22).

## 5. Conclusion

In the present study a Chen-type superposition model is proposed to compute the effective wall heat flux in subcooled boiling flow. The proposed BDL model modifies the nucleate boiling contribution by introducing two suppression factors accounting for the effect of the flow forces and of the subcooling of the thermal boundary layer. The comparison with experimental data using water as working fluid shows good agreement especially in the partially developed boiling (PDB) regime. This good agreement in the PDB region, where the bulk flow rate exerts a significant effect on the nucleate boiling, indicates that the model captures the flow-induced suppression very well. Notable deviations occur primarily in the vicinity of the fully developed boiling (FDB) regime. These discrepancies clearly demonstrate the limits of the present model and give the scope for a further development. Thereby, the focus will have to be put on the consideration of the bubble–bubble as well as the bubble–liquid interactions, which are of great importance in the FDB regime.

## Acknowledgements

The authors gratefully acknowledge the financial support from the Forschungsförderungsfond der gewerblichen Wirtschaft Österreich, the AVL List GmbH/Graz, the BMW Motoren GmbH/Steyr, and the Kplus Virtual Vehicle Competence Centre/Graz.

## References

- [1] R. Mei, W. Chen, J.F. Klausner, Vapour bubble growth in heterogeneous boiling. I. Formulation, *Int. J. Heat Mass Transfer* 38 (1995) 909–919.
- [2] R. Mei, W. Chen, J.F. Klausner, Vapour bubble growth in heterogeneous boiling. II. Growth rate and thermal fields, *Int. J. Heat Mass Transfer* 38 (1995) 921–934.
- [3] W. Chen, R. Mei, J.F. Klausner, Vapour bubble growth in highly subcooled heterogeneous boiling, in: J.C. Chen (Ed.), *Convective Flow Boiling*, Taylor & Francis, Washington, DC, 1996, pp. 91–98.
- [4] W.M. Rohsenow, Heat transfer with evaporation, in: *Heat Transfer—A Symposium held at the University of Michigan During the Summer of 1952*, University of Michigan Press, 1953, pp. 101–150.
- [5] R.W. Bowring, Physical model based on bubble detachment and calculation of steam voidage in the subcooled region of a heated channel, OECD Halden Reactor Project Report HPR-10, 1962.
- [6] A.E. Bergles, W.M. Rohsenow, The determination of forced convective surface boiling and heat transfer, Paper 63-HT-22 presented at the 6th National Heat Transfer Conference of the ASME-AIChE, Boston, 11–14 August 1963.
- [7] J.L. Mostinskii, Calculation of heat transfer and critical heat fluxes in liquids, *Teploenergetika* 10 (1963) 66.
- [8] M.G. Cooper, Saturation and nucleate pool boiling—A simple correlation, *Inst. Chem. Eng. Symp. Ser.* 86 (1984) 785.
- [9] W. Leiner, D. Gorenflo, Methods of predicting the boiling curve and a new equation based on the thermodynamic similarity, in: V.K. Dhir, A.E. Bergles (Eds.), *Pool and External Flow Boiling*, ASME, New York, 1992, pp. 99–103.
- [10] W. Leiner, Heat Transfer and convective pool boiling—General correlations based on the thermodynamic similarity, *Int. J. Heat Mass Transfer* 91 (1994) 763–769.
- [11] S.G. Kandlikar, Heat transfer characteristics in partial boiling, fully developed boiling, and significant void flow regions of subcooled flow boiling, *Trans. ASME J. Heat Transfer* 120 (1998) 395–401.
- [12] M. Shah, A general correlation for heat transfer during subcooled boiling in pipes and annuli, *ASHRAE Trans.* 83 (Part 1) (1977) 205–217.
- [13] E.L. Bibeau, M. Salcudean, A study of bubble ebullition in forced-convective subcooled nucleate boiling at low pressure, *Int. J. Heat Mass Transfer* 37 (1994) 2245–2259.
- [14] J.C. Chen, A correlation for boiling heat transfer to saturated fluids in convective flow, ASME preprint 63 HT34 presented at the 6th National Heat Transfer Conference, Boston, 1963.
- [15] D. Butterworth, The correlation of cross flow pressure drop data by means of a permeability concept, UKAEA Report AERE-R9435, 1979.
- [16] H.K. Forster, N. Zuber, Dynamics of vapor bubbles and boiling heat transfer, *AIChE J.* 1 (1955) 531–535.
- [17] L.Z. Zeng, J.F. Klausner, D.M. Bernhard, R. Mei, A unified model for the prediction of bubble detachment diameters in boiling systems—II. Flow boiling, *Int. J. Heat Mass Transfer* 36 (1993) 2271–2279.
- [18] N. Zuber, The dynamics of vapour bubbles in nonuniform temperature fields, *Int. J. Heat Mass Transfer* 2 (1961) 83–98.
- [19] L.Z. Zeng, J.F. Klausner, R. Mei, A unified model for the prediction of bubble detachment diameters in boiling systems—I. Pool boiling, *Int. J. Heat Mass Transfer* 36 (1993) 2261–2270.

- [22] R. Maurus, Bestimmung des Blasenverhaltens beim unterkühlten Strömungssieden mit der digitalen Bildfolgenanalyse, Doct. thesis, TU Munich, 2003.
- [23] J.R. Wiebe, R.L. Judd, Superheat layer thickness measurements in saturated and subcooled nucleate boiling, *Trans. ASME J. Heat Transfer* 93 (1971) 455–461.

F. RAMSTORFER, B. BREITSCHÄDEL, H. STEINER & G. BRENN

Modeling of the near-wall velocity field of the liquid in subcooled  
boiling flow

*ASME International Heat Transfer Conference (Proc.),*  
July 17<sup>th</sup> – 22<sup>th</sup>, 2005, San Francisco, USA.

## MODELLING OF THE NEAR-WALL LIQUID VELOCITY FIELD IN SUBCOOLED BOILING FLOW

Franz Ramstorfer

Bernd Breitschädel

*The Virtual Vehicle Research Company, Inffeldgasse 21a,  
8010 Graz, Austria*

Helfried Steiner

Günter Brenn

*Institute of Fluid Mechanics and Heat Transfer, Graz University of Technology, Inffeldgasse 25f,  
8010 Graz, Austria*

### ABSTRACT

The subject of the present work is the modelling of the liquid streamwise flow velocity in the two-phase boundary layer in subcooled boiling flow under the influence of the vapor bubbles. Subcooled boiling flow experiments were carried out in a horizontal test channel in order to investigate the interaction between the bubbles and the liquid phase. The heater surface was located at the bottom of the test channel. The near-wall liquid flow velocity was measured using a two-component laser-Doppler anemometer. Based on the experimental data a model is proposed to describe the impact of the gaseous phase on the motion of the liquid in the subcooled boiling regime. It was observed that the axial velocity profiles near the wall follow a logarithmic law similar to that used in turbulent single-phase flow over rough surfaces. Based on this finding it is suggested to model the influence of the bubbles on the liquid flow analogously to the effect of a surface roughness. The correlation developed for an equivalent surface roughness associated with the bubbles yields good agreement of the modeled axial velocity profiles with the experimental data.

### INTRODUCTION

In modern internal combustion engines, increasing specific power, accompanied by a decrease in size and weight of the engines, leads to increasing thermal loads, especially in the cylinder head. Convective single-phase transport is not sufficient to transfer the heat from the structure into the coolant. Hence, the wall temperature increases and subcooled boiling occurs. The bubbles grow in the superheated zone near the wall and collapse in regions where the temperature is lower than the saturation temperature. Due to this phase change in the coolant,

the heat flux from the structure into the liquid is increased significantly.

Many models proposed for the heat transfer in subcooled boiling flow assume the total wall heat flux  $q_w$  to be composed of two additive contributions, which can be written as

$$q_w = q_{\text{conv}} + q_{\text{nb}}, \quad (1)$$

where the term  $q_{\text{conv}}$  is due to forced convection and the term  $q_{\text{nb}}$  is due to nucleate boiling. This concept of additive contributions was first introduced by Rohsenow [1]. Among the superposition models of type Eq. (1), the approach due to Chen [2] is widely used today, especially in engineering applications in the automotive industry. Recently, Steiner *et al.* [3] presented a superposition approach which modifies Chen's concept for the flow-induced suppression of the nucleate boiling component. While Chen correlated the flow-induced suppression only with the bulk flow Reynolds number, the modified approach [3] models the suppression dependent on the local superheat, subcooling, and wall shear stress. Since the local quantities are in general known in numerical simulations of convective flows, the model is well suited for CFD of geometrically complex coolant flows.

Another class of models assumes the total wall heat flux as a geometrical combination of the basic contributions. Models of this type, as proposed by e.g. Kandlikar [4] and Shah [5], formulate the effective heat transfer rate as a product, which can be generally written as

$$q_w = q_{\text{conv}} \Psi_{\text{tp}}, \quad (2)$$

where  $\Psi_{tp}$  represents a mostly empirically determined enhancement function due to nucleate boiling.

Most superposition as well as multiplicative models proposed for the total wall heat flux in subcooled boiling flow assume that the liquid flow field is unaffected by the presence of the vapor bubbles. It was, however, shown in a recent experimental work of Maurus [6] that the motion of bubbles can significantly interact with the liquid phase flow. Using a PIV measurement technique, Maurus investigated the bubble-laden flow in the two-phase region for varying heat fluxes, flow rates and subcooling.

To date, most model approaches considering the effect of the gaseous phase on the motion of the liquid have been developed for the non-boiling case, where bubbles are injected through porous walls into the flow. Gabillet *et al.* [7] considered a horizontal channel with a porous injection plate located at the bottom. Moursali *et al.* [8] investigated a turbulent bubbly boundary layer developing along a vertical wall. Due to the different physics of bubble formation and growth, and due to the absence of bubble collapse, a successful extension of the models derived for the unheated bubbly flow to subcooled boiling flow cannot be taken for granted.

It is the subject of the present work to investigate the impact of the motion of the bubbles on the liquid phase in a subcooled boiling channel flow. Based on experimental observations it is attempted to derive an appropriate model for the near-wall velocity field. Accounting for the effect of the motion of the bubbles should also provide a physically sounder basis for the modelling of the wall heat flux.

## NOMENCLATURE

### Latin symbols

$C$	integration constant [-]
$C_{kr}$	roughness constant [-]
$d$	bubble diameter [mm]
$D_h$	hydraulic diameter [m]
$k_r$	physical height of the roughness [m]
$\tilde{k}_r$	modeled height of the roughness [m]
$Nu$	Nusselt number [-]
$p$	pressure [N/m <sup>2</sup> ]
$q$	heat flux [W/m <sup>2</sup> ]
$Re$	channel Reynolds number [-]
$T$	temperature [°C]
$u$	velocity component in streamwise direction [m/s]
$u_\tau$	wall friction velocity [m/s]
$v$	velocity component in wall-normal direction [m/s]
$y$	distance from the heated wall [mm]

### Greek symbols

$\varepsilon$	accuracy threshold [-]
$\zeta$	model parameter [-]
$\eta$	model parameter [-]
$\kappa$	von Kármán constant [-]
$\lambda$	thermal conductivity [W/mK]
$\nu$	kinematic viscosity [m <sup>2</sup> /s]
$\tau$	shear stress [N/m <sup>2</sup> ]
$\Psi_{tp}$	enhancement function [-]

### subscripts

lph	single-phase
b	bulk

conv	convective
dep	departure
m	measured
nb	nucleate boiling
ref	reference
sat	saturation
sub	subcooling
w	wall
rms	root mean square
<i>superscripts</i>	
+	quantities in wall units
n	counter of iteration step

## EXPERIMENTAL SETUP

The experimental facility basically consists of a closed loop and produces a forced convective flow driven by a pump. The working fluid passes through a heated test section, which is schematically shown in Fig. 1. The bulk velocity, the bulk temperature of the liquid and the operating pressure at the inlet of the section are controlled. In the present configuration the bulk velocity can be varied within the range of  $0.05 \text{ m/s} \leq u_b \leq 2.0 \text{ m/s}$ . The absolute operating pressure can be set within the range  $1.0 \text{ bar} \leq p \leq 2.0 \text{ bar}$ . The square cross section of the test channel has the dimensions  $36 \text{ mm} \times 36 \text{ mm}$ . The heat flux into the channel is generated by heating coils located at the bottom of the aluminum heater from where the heat is conducted to the top of the heater. At the upper surface (grey shaded in Fig. 1), with length  $65 \text{ mm}$  and width  $10 \text{ mm}$ , the heat is transferred to the working fluid flowing through the channel.

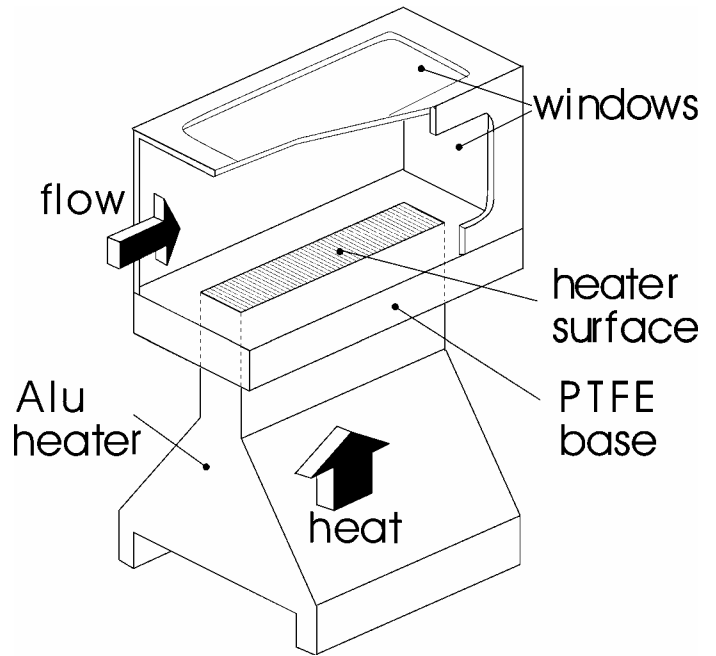


Fig. 1. Test section of the experimental facility.

The wall temperature and the wall heat flux are determined based on measurements of the temperature using several K-type thermocouples appropriately distributed in the solid heater. The base plate of the test section, where the top of the aluminum heater is built in, is made of PTFE. The very low thermal conductivity of PTFE should guarantee the lowest possible heat

loss from the heater to the surrounding structure. Due to thermal durability restrictions of the PTFE base plate, the maximum heater surface temperature was limited to  $T_w = 160\text{ }^\circ\text{C}$ . Windows made of glass are embedded in the top as well as in the side walls of the test channel to make the heater surface optically accessible.

In the experimental part of the work, the size and dynamics of the bubbles were investigated using a high-speed camera. A 2D laser-Doppler anemometer from DANTEC was used for the liquid velocity measurements. The argon-ion laser used as light source has a maximum power of 200 mW. The focal length of the lens in the fiber optic probe is 310 mm, and the beam spacing is 60mm. The laser-Doppler anemometer was used in the back-scattering mode. Laser-Doppler anemometry has been extensively used for local velocity measurements in transparent single-phase flow because of its high accuracy, good spatial resolution, and non-intrusive features. In general, small seeding particles following the flow serve as the scattering centers for the laser light. In the case of flow boiling experiments, no seeding particles may be added to the liquid, since they might affect the boiling process. Instead, the vapor bubbles, which move closely at the velocity of the liquid phase, are used as scattering centers. No additional seeding is therefore required. For the present experiments, the consequence that the data rate is low in regions of the flow field populated sparsely with bubbles, was not a problem. It is noted that using the vapor bubbles as tracer particles one inherently assumes the slip between the bubbles and the liquid phase to be negligibly small. In the present work the validity of this assumption could be shown by comparing the bubble relaxation time based on the bubble drag force with the relevant turbulent flow time scale. The latter turned out to be about three orders of magnitude higher.

## EXPERIMENTAL RESULTS

Using the experimental setup described above, several near-wall velocity profiles in the axial and the wall-normal direction for a given heat flux and a given bulk velocity were measured. In all considered cases the working fluid was a mixture of ethylene glycol and water with a mixing ratio of 40/60 vol. %. The bulk inlet temperature was kept constant at a subcooling of  $\Delta T_{\text{sub}} = T_{\text{sat}} - T_b = 22\text{ }^\circ\text{C}$  at the absolute pressure of  $p = 1.5\text{ bar}$ . By varying the wall heat flux  $q_w$  a maximum wall superheat of  $40\text{ }^\circ\text{C}$  was achievable. The bulk velocity was set within the range of  $0.2\text{ m/s} \leq u_b \leq 0.8\text{ m/s}$ . The Reynolds number based on the bulk flow quantities can be written as

$$\text{Re} = \frac{u_b D_h}{\nu}, \quad (3)$$

where  $D_h$  denotes the hydraulic diameter, which is equal to the side length of the square cross section of the channel, and  $\nu$  is the kinematic viscosity of the bulk liquid at the inlet of the test section. The chosen velocity range corresponds to a range of Reynolds numbers from 11260 to 45030. It is noted that all measured heat fluxes are presented here in non-dimensionalized form for confidentiality reasons. Figure 2 shows the non-dimensional wall heat flux  $q_w/q_{\text{ref}}$  as a function of the corresponding wall superheat  $T_w - T_{\text{sat}}$  obtained from the measurements for three different bulk velocities  $u_b$ . In all

considered experimental cases the saturation temperature was the same. The strong deviation from the single-phase macro-convection in the boiling regime ( $T_w > T_{\text{sat}}$ ) illustrates the enhanced heat transfer rate associated with nucleate boiling. It becomes further evident that, at higher wall superheats, the different flow boiling curves follow almost the same path, illustrating the vanishing influence of the flow rate on the total heat flux.

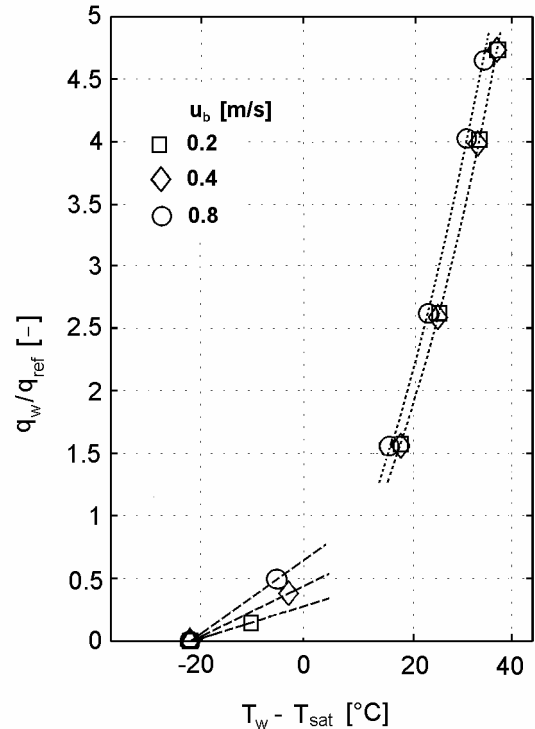


Fig. 2. Measured non-dimensional wall heat flux  $q_w/q_{\text{ref}}$  vs. the wall superheat  $T_w - T_{\text{sat}}$  at different bulk velocities  $u_b$ . The dashed lines represent the single-phase macro-convection, and the dotted lines the flow boiling branch.

The LDA measurements carried out to investigate the interaction of the bubbles and the liquid phase were performed at the conditions shown in Fig. 2. Figures 3 to 5 show the near-wall velocity profiles obtained in these experiments. The mean values of the velocity components  $u$  and  $v$  in the streamwise and the wall-normal directions, respectively, as well as the rms values of the corresponding fluctuations,  $u_{\text{rms}}$  and  $v_{\text{rms}}$ , are plotted against the wall-normal distance  $y$ . All displayed velocity profiles are scaled with the bulk velocity  $u_b$ . The bubbles evidently affect the flow considerably in the superheated near-wall layer. This influence becomes more pronounced with increasing boiling activity on the surface associated with an increasing wall heat flux.

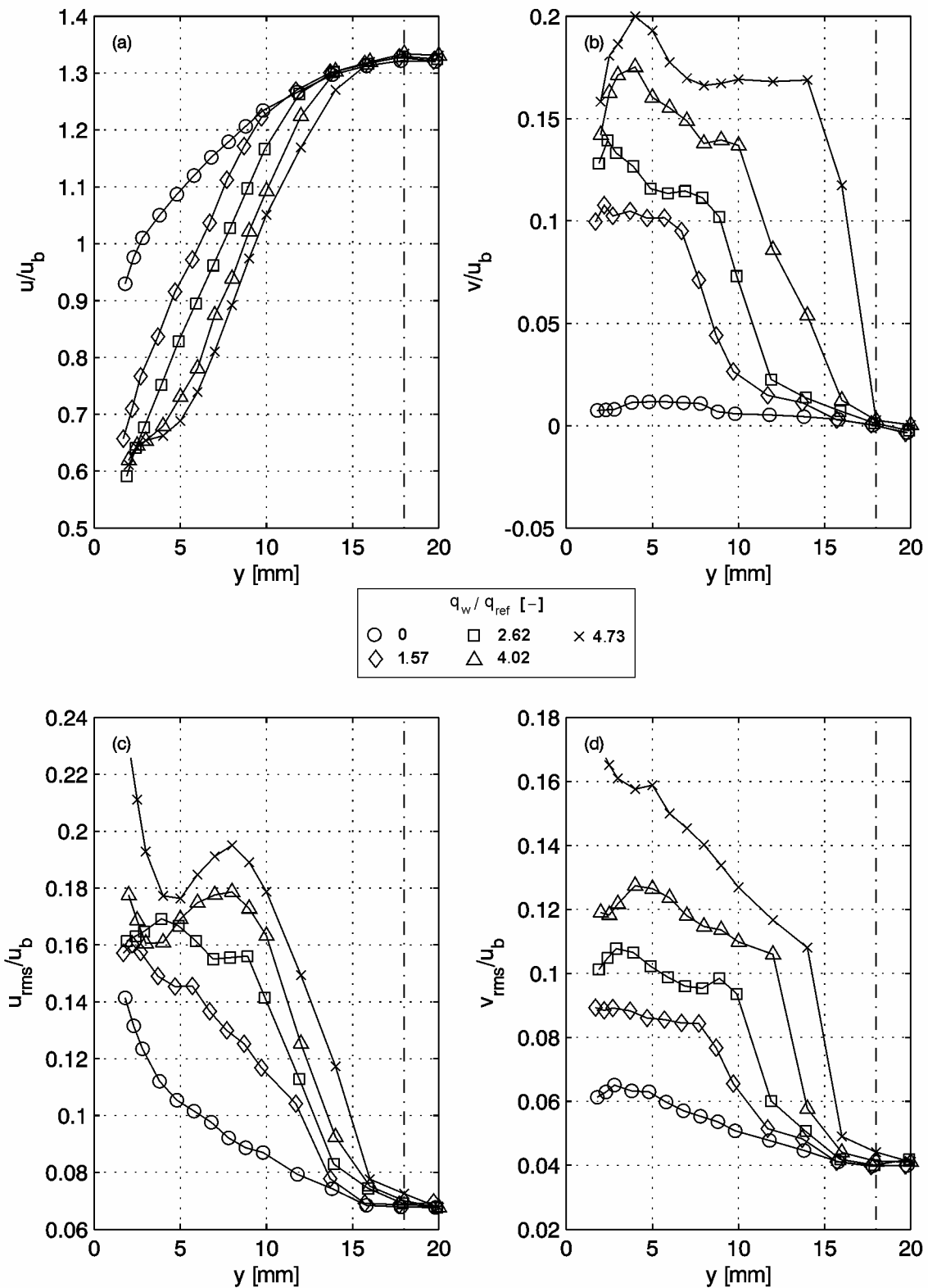


Fig. 3. Results of the LDA measurements at a bulk velocity of  $u_b = 0.2$  m/s and varying non-dimensional wall heat fluxes  $q_w / q_{ref}$ . The dashed-dotted line marks the center of the test channel.

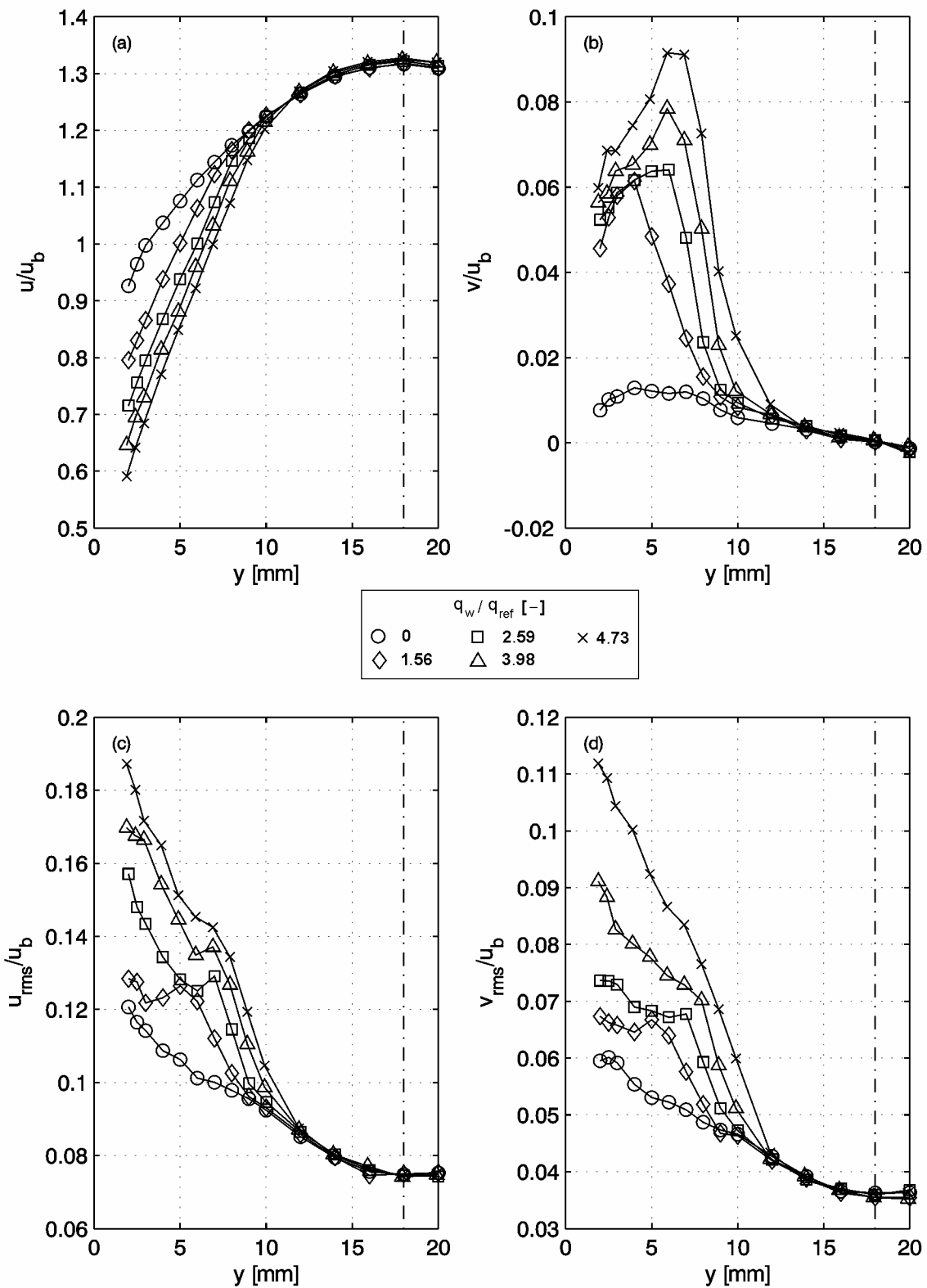


Fig. 4. Results of the LDA measurements at a bulk velocity of  $u_b = 0.4$  m/s and varying non-dimensional wall heat fluxes  $q_w / q_{ref}$ . The dashed-dotted line marks the center of the test channel.

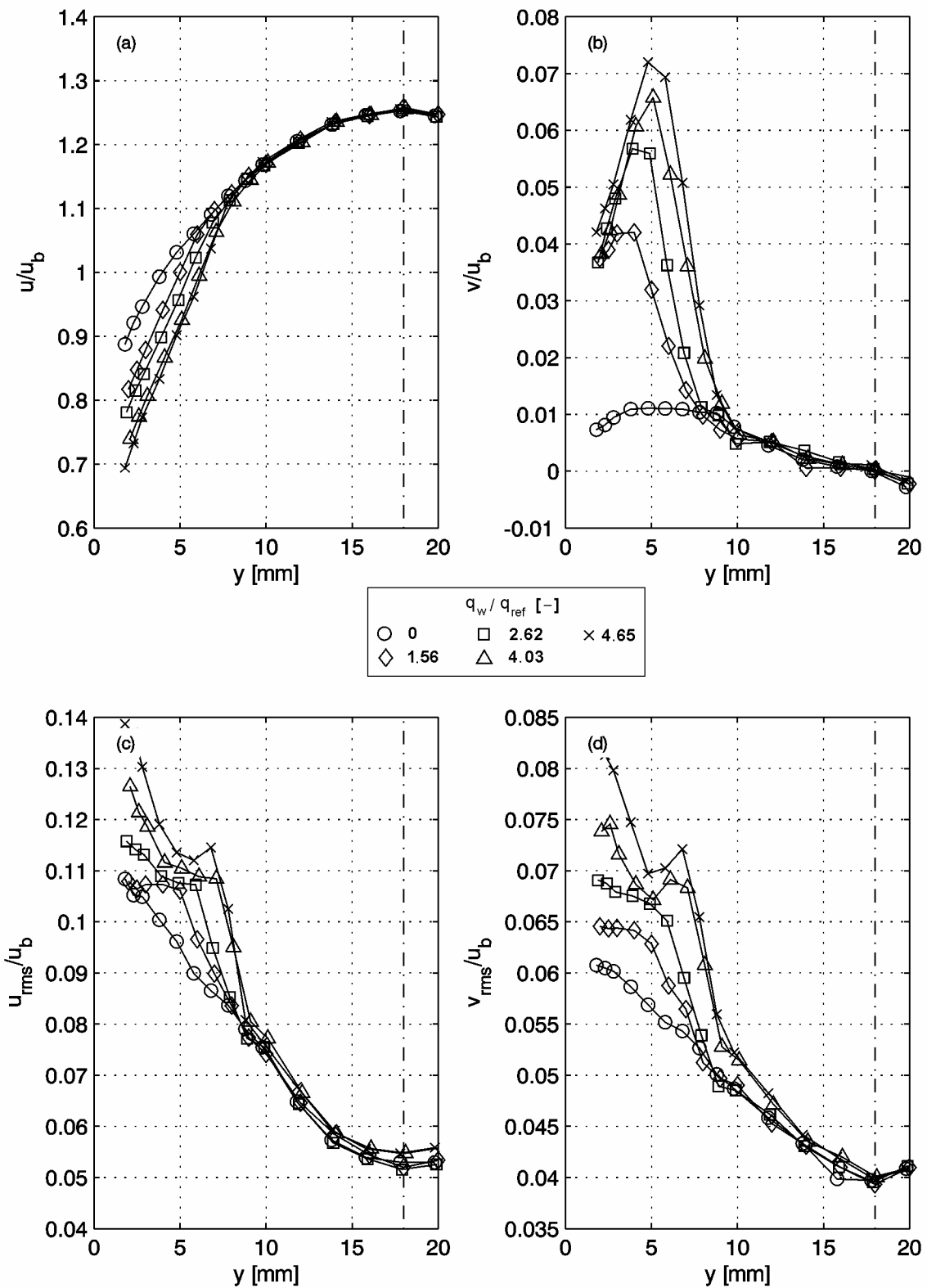


Fig. 5. Results of the LDA measurements at a bulk velocity of  $u_b = 0.8$  m/s and varying non-dimensional wall heat fluxes  $q_w / q_{ref}$ . The dashed-dotted line marks the center of the test channel.

In the core flow region outside the superheated layer, the velocity profiles merge with the single-phase velocity profiles. Figures 3a to 5a show the deceleration in the two-phase region of the mean velocity  $u(y)$  in the streamwise direction. The rise of the bubbles causes an enhancement of the mean wall-normal velocity component  $v(y)$ , as shown in Figs. 3b to 5b. In the cases of low bulk velocities and high heat fluxes, the maximum of the mean wall-normal velocity component is of the same order of magnitude as the streamwise component  $u(y)$ . The present experimental results for the mean velocities confirm the observations made by Maurus [6].

The presence of the bubbles causes a marked increase of the mean turbulent fluctuations  $u_{rms}(y)$  and  $v_{rms}(y)$  in the streamwise and the wall-normal directions in the two-phase region of the flow, as shown in Figs. 3c and d to 5c and d, respectively. The observed increase of the turbulence in the near-wall region leads to enhanced momentum and heat transfer. This microconvection induced by bubble agitation strongly contributes to the increased heat transfer rates achievable in subcooled boiling flow as compared to single-phase convection.

As it is shown in Fig. 3a, at low bulk velocities and high heat fluxes a plateau in the mean axial velocity profile occurs. In this case the buoyancy-driven vertical motion of the bubbles obviously prevails over the streamwise motion of the liquid phase. The observed plateau is produced by clockwise rotating large vortical structures generated by the rise of the bubbles, as shown in Fig. 6.

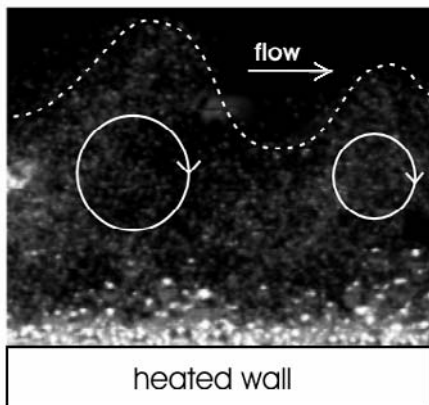


Fig. 6. Observed clockwise rotating vortices in the bubbly layer. The picture was taken at a bulk velocity of  $u_b = 0.2$  m/s and a non-dimensional wall heat flux of  $q_w / q_{ref} = 4.02$ . The dashed line marks the upper boundary of the vortical layer.

The impact of the bubbles on the flow field is supposed to depend strongly on the bubble size distribution at the heated wall. Therefore, the size of the bubbles located at the heater surface was measured using high speed camera recordings at different thermal and flow conditions. Figure 7 shows the median bubble diameter  $d_m$  measured at the wall. A higher wall heat flux evidently leads to larger bubble mean diameters. It becomes further obvious that, at a given heat flux, the mean size is smaller the higher the bulk velocity, reflecting the influence of the local velocity field on the bubble detachment process from the heated surface.

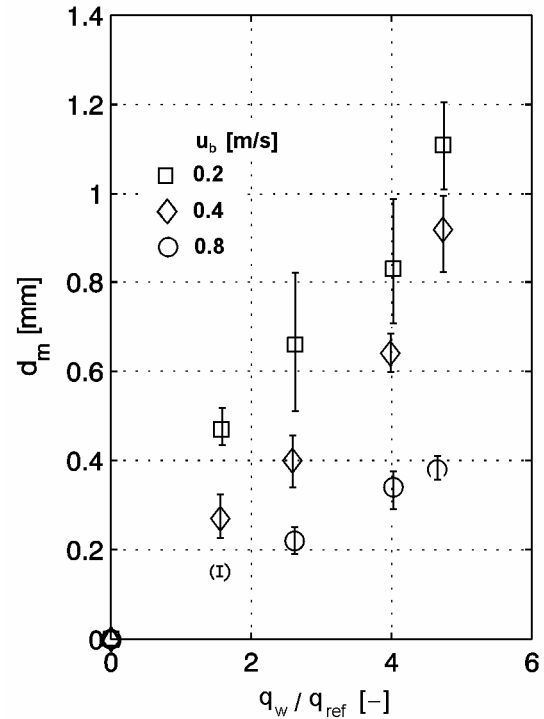


Fig. 7. Measured bubble diameters  $d_m$  at different bulk velocities  $u_b$ . The rms fluctuations around the statistical median value are denoted with an error bars.

## MODELLING

As already noted in the previous section, most models proposed for the liquid velocity field in bubble-laden boundary layer flows were developed for non-boiling flow. The non-boiling bubbly flow, where bubbles are mostly introduced through porous walls, inherently differs from boiling flows by essential aspects of the whole process of bubble formation and detachment in the superheated boundary layer as well as the bubble collapse occurring in subcooled regions, where  $T < T_{sat}$ . As it is shown in the present work, the model formulations proposed for non-boiling bubbly flows can be nonetheless extended to boiling flow, if the physics of the vapor bubble formation and detachment is incorporated into the mathematical description of the bubble-laden superheated wall layer.

The present model is based on a formulation originally proposed by Gabillet *et al.* [7], who investigated horizontal boundary layer flows of water densely populated by air bubbles injected through a porous wall. Gabillet *et al.* observed that the presence of bubbles in the wall layer has an effect on the liquid phase flow, which is very similar to the effect of surface roughness. They therefore suggested a logarithmic law of the wall, which is commonly used for turbulent flows over rough walls, to capture the impact of the bubbles on the near-wall flow. The present model extends this analogy to subcooled boiling flow, where the bubble layer is generated by evaporation on the superheated wall. The adopted log-law for turbulent flows over rough walls generally reads

$$u^+ = \frac{1}{\kappa} \ln(y^+) + C - \Delta u^+, \quad (4)$$

where  $u^+ = u/u_\tau$  and  $y^+ = y u_\tau / \nu$  are written in the so-called wall units involving the wall friction velocity  $u_\tau = \sqrt{\tau_w / \rho}$ .

$C = 5.3$  and  $\kappa = 0.41$  are constants. The last term on the RHS of Eq. (4) represents the offset of  $u^+$  due to the wall roughness with respect to the log-law for the hydrodynamically smooth surface, where  $\Delta u^+ = 0$ . This offset is a function of the so-called roughness Reynolds number

$$k_r^+ = \frac{k_r u_\tau}{\nu} \quad (5)$$

involving the physical roughness height of the surface  $k_r$ . For the functional dependence  $\Delta u^+(k_r^+)$ , different regimes are distinguished [9]:

- hydrodynamically smooth,  $k_r^+ < 2.25$  :

$$\Delta u^+ = 0 \quad (6)$$

- transitional regime,  $2.25 \leq k_r^+ < 90$  :

$$\Delta u^+ = \frac{1}{\kappa} \ln(1 + C_{kr} k_r^+) \cdot \sin\{0.4258(\ln k_r^+ - 0.811)\} \quad (7)$$

- fully rough regime  $k_r^+ \geq 90$  :

$$\Delta u^+ = \frac{1}{\kappa} \ln(1 + C_{kr} k_r^+) \quad (8)$$

$C_{kr}$  is a roughness constant and depends on the type of roughness. For sand-grain roughness, a value of  $C_{kr} = 0.5$  is used.

Applying a best fit of the log-law given by Eq. (4) to the measured streamwise velocity profiles shown in Figs. 3a to 5a yields for each profile  $u(y)$  a corresponding pair of  $u_\tau$  and  $k_r$ . All considered experimental data points lie within the  $y^+$  range  $30 < y^+ < 200$ , where the log-law is basically applicable. The results obtained for each individual  $u(y)$  profile are summarized in Tab. 1. The measured streamwise velocity profiles rescaled in wall units and the applied log-law profiles are plotted in Fig. 8. The log-law evidently matches well the experimental data in the region close to the wall. It is noted that the profiles which exhibit a plateau in the near-wall region as shown in Fig. 3a had to be excluded from this analysis. In this case the buoyancy-induced vertical bubble motion is too strong to allow for a simple log-law modeling, which requires a dominant motion along the wall.

The roughness heights  $k_r$  fitted from the experimental data basically represent an equivalent roughness associated with the vapor bubble layer on the heater surface. This equivalent roughness height  $k_r$  has to be provided by the model to determine the near-wall velocity profile using Eq. (4).

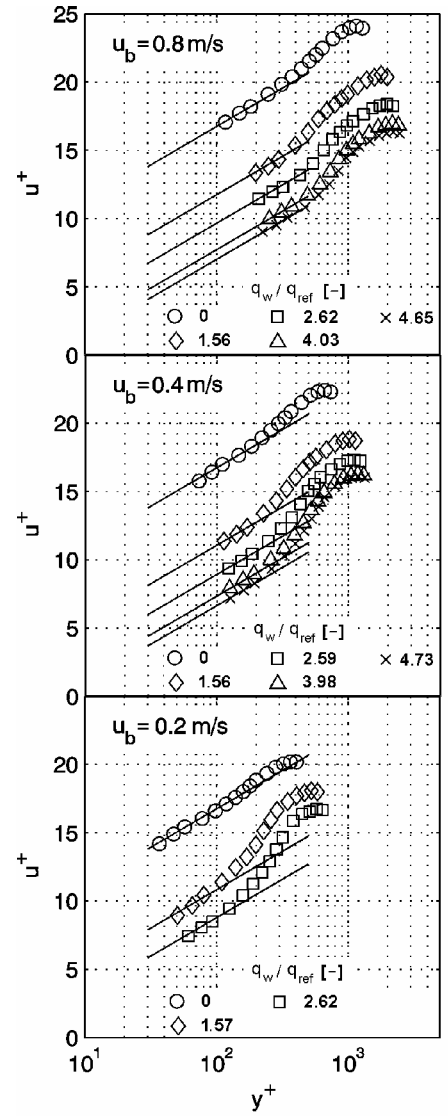


Fig. 8. The logarithmic law of the wall (Eq. (4)) compared to the measured velocity profiles in wall units for different bulk velocities  $u_b$  and non-dimensional wall heat fluxes  $q_w / q_{ref}$ . Solid line, '—', log-law for rough surfaces.

The present model assumes the bubble-equivalent roughness height to depend essentially on two quantities: the median bubble size and the contribution of the nucleate boiling heat flux,  $q_{nb}$ , to the total heat flux  $q_w$ . Accordingly, it proposes the correlation

$$\tilde{k}_r = \eta d_{dep} \left( \frac{q_{nb}}{q_w} \right)^\zeta = \eta d_{dep} \left( 1 - \frac{q_{conv}}{q_w} \right)^\zeta, \quad (9)$$

where  $d_{dep}$  denotes the bubble diameter at the instant of departure from the nucleation site. This diameter represents the bubble mean size and is computed as predominantly dependent on the wall superheat ( $T_w - T_{sat}$ ) and the wall friction velocity  $u_\tau$  according to the bubble detachment model of Zeng *et al.* [10].

$u_b$ [m/s]	$q_w/q_{ref}$ [-]	$u_\tau$ [m/s]	$k_r$ [mm]
0.2	0	0.0131	0
0.2	1.57	0.0147	1.00
0.2	2.62	0.0159	1.71
0.4	0	0.0235	0
0.4	1.56	0.0280	0.49
0.4	2.59	0.0305	0.85
0.4	3.98	0.0326	1.4
0.4	4.73	0.0330	1.85
0.8	0	0.0416	0
0.8	1.56	0.0490	0.23
0.8	2.62	0.0545	0.38
0.8	4.03	0.0593	0.66
0.8	4.65	0.0615	0.85

Tab. 1. Wall friction velocity and roughness height determined by a least-square fit of the log-law to the measured velocity profiles  $u(y)$  for different bulk velocities and non-dimensional wall heat fluxes.

Figure 9 shows the diameters predicted by this model for all cases listed in Tab. 1, as compared to the corresponding experimental data presented in Fig. 7. The agreement is very good. The ratio of the nucleate boiling component to the total heat flux,  $q_{nb}/q_w$ , has been introduced to account for the fact that, at high nucleate boiling activity associated with high wall superheats, the near wall layer which is populated by bubbles becomes thicker than the mean size of the single bubbles detaching from the wall. It ranges between zero and unity, as can be immediately seen from Eq. (1). The quantities  $\eta$  and  $\zeta$  in Eq. (9) are empirical parameters.

In Fig. 10 the predictions for the equivalent roughness  $\tilde{k}_r$  using the correlation given by Eq. (9) are compared against the roughness heights  $k_r$  listed in Tab. 1 which were obtained from the best fit of the log-law in Eq. (4) to the measured velocity profiles. Using the empirical parameters  $\eta = 2.5535$  and  $\zeta = 0.1741$ , good agreement is achieved.

It is noted that the increase of the wall friction velocity  $u_\tau$  due to the bubble-equivalent surface roughness inherently leads to an increase of the convective component  $q_{conv}$  in the total heat flux. In the present computation of  $\tilde{k}_r$  using Eq. (9), where  $q_{conv}$  is required as an input quantity, the enhanced convective component is estimated invoking the Reynolds analogy between the wall heat transfer and the wall friction, which yields the relation

$$\frac{Nu_{conv}}{Nu_{conv,1ph}} = \left( \frac{u_\tau}{u_{\tau,1ph}} \right)^2, \quad (10)$$

where the Nusselt number is based on the hydraulic diameter of the channel,  $D_h$ , and the thermal conductivity of the bulk liquid  $\lambda_b$ . The wall friction velocity  $u_{\tau,1ph}$  and the Nusselt number  $Nu_{conv,1ph}$  refer to the single-phase convection regime, and they are both obtained from measured points  $(q_w, T_w)$  with  $T_w < T_{sat}$ .

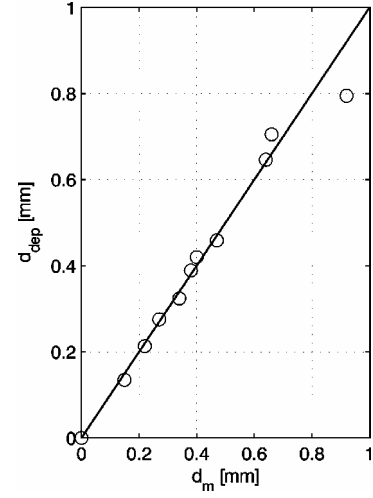


Fig. 9. Predicted bubble departure diameters  $d_{dep}$  in comparison with experimental data.

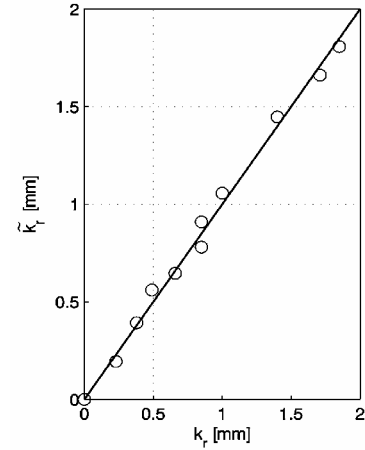


Fig. 10. Predicted roughness heights  $\tilde{k}_r$  in comparison with experimental data ( $\eta = 2.5535$ ,  $\zeta = 0.1741$ ).

The Nusselt number  $Nu_{conv,1ph}$  is obtained from the measured total wall heat flux,  $q_w$ , which is equal to  $q_{conv}$  in the single-phase regime, as

$$Nu_{conv,1ph} = \frac{q_w}{(T_w - T_b)} \cdot \left( \frac{D_h}{\lambda_b} \right) \quad \text{with } T_w < T_{sat}. \quad (11)$$

The obtained Nusselt numbers  $Nu_{conv,1ph}$  for the considered data points in the single-phase regime are summarized in Tab. 2.

$u_b$ [m/s]	$T_w - T_b$ [°C]	$q_w/q_{ref}$ [-]	$Nu_{conv,1ph}$ [-]
0.8	17.7	0.500	217.7
0.4	20.0	0.395	152.2
0.2	11.0	0.150	105.6

Tab. 2. Measurement points for the evaluation of the Nusselt numbers  $Nu_{conv,1ph}$ .

Substituting the wall friction velocities, which can be taken directly from the best-fit results listed in Tab. 1, into Eq. (10) finally yields  $Nu_{conv}$ . The convective heat flux component in the subcooled boiling regime is then computed as  $q_w = Nu_{conv} (T_w - T_b) (\lambda_b / D_h)$ , with  $T_w > T_{sat}$ .

When applying the present model to CFD of subcooled boiling flow, the computational procedure essentially consists of an iterative loop for the calculation of the bubble-equivalent surface roughness  $\tilde{k}_r$ . The iterative procedure is schematically shown in Fig. 11 for the case with a given superheated wall temperature  $T_w > T_{sat}$ .

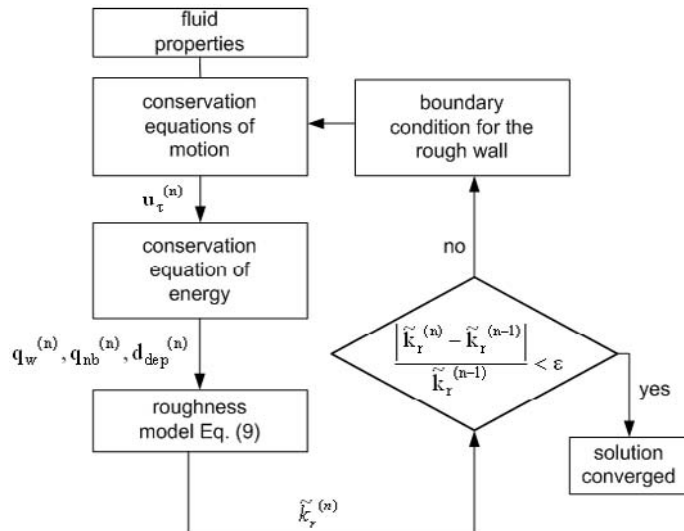


Fig. 11. Implementation scheme of the roughness model for CFD. The superscript (n) denotes the counter of each iteration step, and  $\epsilon$  is the accuracy threshold.

It becomes obvious that the velocity boundary condition is iteratively obtained in dependence on the surface roughness determined by the local boiling activity.

## CONCLUSIONS

Subcooled flow boiling experiments were carried out in a horizontal test channel in order to investigate the near-wall liquid motion under the influence of the vapor bubbles. The experiments yielded the size and dynamics of the bubbles with a high-speed camera. A 2D laser-Doppler anemometer was used to measure the near-wall velocity field of the liquid flow. The main effects of the gaseous phase on the motion of the liquid phase are the deceleration of the mean velocity in the streamwise direction and the enhancement of the mean wall-normal velocity component. It was also observed that the turbulence is markedly increased in the two-phase region. At low liquid flow rates, the buoyancy-driven motion of the bubbles becomes dominant and leads to a plateau in the mean axial velocity profile.

It was found that the axial velocity profiles near the wall follow a logarithmic law similar to that used in turbulent single-phase flow over rough surfaces. Based on these findings, a modelling was proposed which captures the influence of the bubbles on

the liquid flow in analogy to a surface roughness effect. The proposed model correlates an equivalent surface roughness with the bubble size and the wall heat flux, such that the modified logarithmic law of the wall for rough surfaces can be applied. The proposed correlation for an equivalent surface roughness associated with the bubble layer yields good agreement of the predicted axial velocity profiles with experimental data.

## ACKNOWLEDGMENTS

The authors wish to thank the K plus Kompetenzzentren-Programm of the Austrian Federal Ministry for Transport, Innovation, and Technology (BMVIT), Technologie Impulse Gesellschaft (TIG), Das Land Steiermark, Stadt Graz, and Die steirische Wirtschaftsförderung (SFG) for their financial support. Additionally we gratefully acknowledge financial support from AVL List GmbH.

## REFERENCES

- [1] Rohsenow, W.M., 1953, "Heat transfer with evaporation", Heat Transfer - A Symposium held at the University of Michigan during the summer of 1952, Univ. of Michigan Press, pp. 101-150.
- [2] Chen, J.C., 1963, "A correlation for boiling heat transfer to saturated fluids in convective flow, ASME preprint 63 HT34 presented at the 6th National Heat Transfer Conference, Boston
- [3] Steiner, H., Kobor, A., and Gebhard, L., 2004, "A wall heat transfer model for subcooled boiling flow", Proc. ASME - ZSIS International Thermal Science Seminar II, Bled, Slovenia, pp. 643-650.
- [4] Kandlikar, S.G., 1998, "Heat transfer characteristics in partial boiling, fully developed boiling, and significant void flow regions of subcooled flow boiling", Trans. ASME J. Heat Transfer, 120, pp. 395-401.
- [5] Shah, M., 1977, "A general correlation for heat transfer during subcooled boiling in pipes and annuli", ASHRAE Trans. 83, Part 1, pp. 205-217.
- [6] Maurus, R., 2003, "Bestimmung des Blasenverhaltens beim unterkühlten Strömungssieden mit der digitalen Bildfolgenanalyse", Ph.D. thesis, TU München.
- [7] Gabillet, C., Colin, C., Fabre, J., 2002, "Experimental study of bubble injection in a turbulent boundary layer", Int. J. Multiphase Flow, 28, pp.553-578.
- [8] Moursali, E.M., Marié, J.L., Bataille, J., 1995, "An upward turbulent bubbly boundary layer along a flat plate", Int. J. Multiphase Flow, 21, pp. 107-117.
- [9] Cebeci, T., and Bradshaw, P., 1977, Momentum Transfer in Boundary Layers, Hemisphere, Washington, DC.
- [10] Zeng L. Z., Klausner J. F., Bernhard D. M. and Mei R., 1993, "A unified model for the prediction of bubble detachment diameters in boiling systems - II. Flow boiling", Int. J. Heat Mass Transfer, 36, pp. 2271-2279.